From coherent to single-particle quantum walks

Der Naturwissenschaftlichen Fakultät der Universität Paderborn

zur

Erlangung des Doktorgrades Dr. rer. nat.

vorgelegt von

Thomas Nitsche

Erklärung der Selbstständigkeit

Hiermit versichere ich, die vorliegende Arbeit selbstständig verfasst und keine anderen als die angegebenen Quellen und Hilfsmittel benutzt sowie die Zitate deutlich kenntlich gemacht zu haben.

Paderborn, den 10.09.2019 Thomas Nitsche

1. Gutachterin:	Prof. Dr. Christine Silberhorn
2. Gutachter:	Prof. Dr. Thomas Zentgraf
Vertreter des Mittelbaus:	Dr. Matthias Reichelt
Vorsitzender der Prüfungskommission:	Prof. Dr. Wolf Gero Schmidt

Datum der Abgabe: 10.09.2019

Contents

1 Abstract

In this work we present the implementation and study of time-multiplexed optical quantum networks. These incorporate the preparation of single-photon states, their manipulation in a dynamically reconfigurable circuitry and mode-resolving detection. With such a system we achieve versatile simulation capabilities for both wave-like as well as particle-like phenomena.
The input states are generated in a parametric down-conversion (PDC) process engineered to be compatible with the time-multiplexing fibre network as well as to yield indistinguishable and pure photons which are required for quantum interference with high visibility.
Employing fast-switching electro-optic modulators (EOMs), we can dynamically reconfigure the circuitry in terms of the splitting, routing and inhomogeneous losses to which the photons are subjected. In this way, we can probe the effect of projective measurements during the evolution.
The detection unit resolves the external (time bins) as well as the internal modes (polarisation), allowing for mode-dependent intensity and coincidence measurements.
For describing the photon's evolution we adopt the formalism of discrete-time quantum walks.
Examining wave-like behaviour with coherent states, we investigate topologically-protected edge states as well as the effect of projective measurements.
Probing particle-like effects with single-photon states, we conduct experiments revealing the interplay between the coherence properties of synthesized modes, the degree of mode resolution in the detection and the time-multiplexed quantum interference.

2 Zusammenfassung

In dieser Arbeit präsentieren wir die Implementierung und Untersuchung von zeitgemultiplexten optischen Quantennetzwerken. Diese beinhalten die Präparierung von Einzelphotonen-Zuständen, ihre Weiterverarbeitung in einem dynamisch rekonfigurierbaren Netzwerk und moden-auflösende Detektion. Mit einem solchen System erlangen wir vielseitige Möglichkeiten im Bereich der Simulation von sowohl teilchenartigen als auch wellenartigen Phänomenen.
Die Eingangszustände werden in einem parametrischen Fluoreszenzprozess (englisch: parametric down-conversion, PDC) erzeugt, der dahingehend optimiert wurde, dass er einerseits kompatibel mit dem verwendeten Zeitmultiplex-Netzwerk ist und andererseits ununterscheidbare und reine Photonen liefert und somit Quanteninterferenz mit hoher Visibilität erlaubt.
Durch den Einsatz schneller elektro-optischer Modulatoren (EOMs) können wir das Verhalten der Photonen hinsichtlich Aufspaltung, Propagation und inhomogener Verluste dynamisch beeinflussen. Auf diese Weise können wir die Auswirkungen projektiver Messungen untersuchen.
Mit der Detektionseinheit lassen sich sowohl die externen (Zeitslots) als auch die internen Moden (Polarisation) auflösen, so dass moden-abhängige Intensitäts- und Koinzidenzmessungen möglich sind.
Die Beschreibung der Zeitentwicklung der Photonen erfolgt über den Formalismus eines Quantenspaziergangs mit diskreten Zeitschritten.
Im Rahmen der Untersuchung von wellenartigen Phänomenen mit kohärenten Zuständen implementieren wir sowohl topologisch geschützte Randzustände als auch eine Simulation projektiver Messungen.
Teilchenartige Phänomene untersuchen wir dagegen mit Einzelphotonen-Zuständen. Hier zeigt sich im Experiment das Zusammenspiel zwischen den Kohärenzeigenschaften der Moden, der Moden-Auflösung während der Detektion und der zeitgemultiplexten Quanteninterferenz.

3 Introduction

In the last decades the interest in quantum effects has been intensified by the prospect of building a quantum computer, i.e. a device that is capable of harnessing the complexity of quantum systems for computational tasks and simulation of quantum systems [1]. In this regard, one can harness quantum mechanical processes to achieve computational tasks such as the famous examples of prime factorization [2] or search algorithms [3]. On the other hand, they can be used to simulate quantum mechanical systems such as molecules which are hard to compute classically due to their computational complexity. Possible implementations and applications of a quantum computer are manifold and giving an extensive overview would thus go beyond the scope of this thesis.

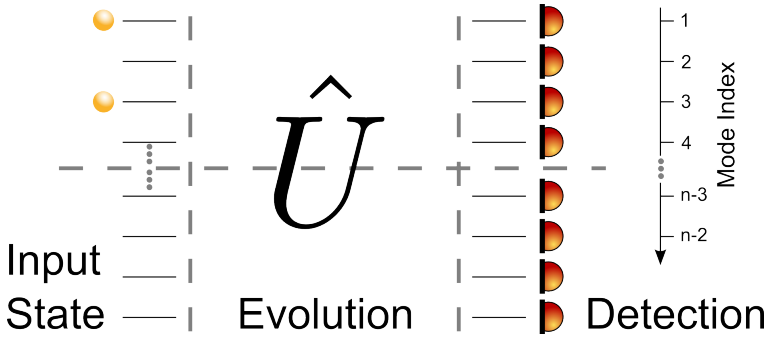

Figure 3.1: The three major components relevant in studying a quantum network: The input states, in this instance two photons, are subjected to an evolution (marked by $\hat{U}$ for unitary) and eventually detected.

We can, however, resort to representing such a device as a quantum network, which is an appropriate way for at least certain instances, e.g. linear optics quantum computing [4]. Such a network can be split it up into three major components (see Figure 3.1): We start with an input state, e.g. in the given instance two photons, that occupies a certain number of modes. Here, the term mode denotes basis states of a Hilbert space in that the photons could be distinguishable. For example, distinct modes can be different positions in space or time as well as certain frequencies.
Subsequently, the input state undergoes an evolution (represented by $\hat{U}$ in Figure 3.1) during which it is transformed. A straightforward example of such an evolution would be directing photons to certain spatial positions via beam splitters.
Eventually, the state is detected. While one might naively assume this to be the most boring part, the way a quantum mechanical system is measured might have significant

consequences on the outcome.
In this work, we will present the implementation of a fully-fledged quantum network comprising all three components: input state generation, evolution and detection. Eventually, we will present an experiment that relies on a high degree of control in all three of these. For the first time, we implement a time-multiplexed optical network combining approximative single-photon input states with a dynamically reconfigurable circuit allowing for implementing a different operation on each of the modes. The results of the experiments made possible by these features offer valuable insights into the interplay of coherence and quantum interference.
In order to describe the evolution section, we adopt the framework of quantum walks, which are considered as a universal computational primitive [5] resp. architecture for universal quantum computation [6]. Furthermore,they play an important role in quantum simulation [7].
Considering the input states, we can think of different scenarios: a classical particle exhibits a rest mass but not a wave function. In contrast, a particle such as an electron exhibits a rest mass and a wave function. Light presents an interesting case in this regard as it can show particle-like behaviour in certain instances, but does not possess a rest mass.
The state's evolution described in the quantum walk framework shows an interesting interplay with the input state: Originally, the term "Quantum walk" was coined to describe the evolution of a massive particle in a wave picture, i.e. with probability amplitudes according to wave-particle duality [8]. The wave-like description also holds for fields of light. It, however, depends on the concrete scenario whether the particle-like aspect of light become relevant. For instance, a quantum walks starting with photons in only a single mode can be simulated with coherent states which are in quantum optics usually considered to be classical states. On the other hand, analysing coincidence counts for a case with single photons in multiple input states clear reveals their particle nature. At this point we see that detection is indeed a crucial part of a quantum network.
It remains the question why we should complicate matters by examining effects that only occur for multiple quantum particles. An answer going to back to our initial motivation is that the aforementioned approaches to quantum computation rely on genuine quantum states in distinct input modes, i.e. they cannot be conducted with coherent input states. Looking at a broader picture, we will see that certain quantum walk protocols require quantum states in multiple input modes, while realising single-input-mode scenarios suffices for others. In the present work, we will investigate instances of both: In chapter 6 we present the investigation of various topological phenomena with coherent input states. In addition, chapter 7 is devoted to the simulation of measurement-induced dynamics with coherent states via the implementation of absorptive sinks.
In order to make our experimental platform presented in chapter 4 a fully-fledged quantum network, we enhance the well-established time-multiplexing architecture [9, 10, 11, 12] such that it becomes compatible with an approximative single-photon source and experimentally verify the performance: The signature of photons in multiple input modes depends on

their indistinguishability and purity, both of which can be tested in a Hong-Ou-Mandel (HOM) interference experiment as described in chapter 5. HOM-interference provides the foundation for the implementation of a time-multiplexed HOM-dip with an additonal mode structure which is presented in chapter 8. In this experiment, we exploit the high degree of control we have for state preparation, state evolution as well as detection to exert coherent control of quantum interference. Furthermore, we show that the amount of information retrieved during detection has a crucial impact on the results. Eventually, we will draw a conclusion and give an outlook in chapter 9.
In the current chapter, we will introduce the fundamentals resorting to the threefold representation of a quantum network: To start with, we will present parametric down-conversion as the process with which we generate approximative single-photon states in section 3.1. The evolution of the state is described in the frameworks of quantum walks which will be presented in section 3.2. Eventually, the experimental signatures of a single photon presented in section 3.3 are related to detection schemes that allow to distinguish single photon from classical states of light.
Furthermore, we will put our work into context by describing the state of the art in section 3.2 and by sketching how to classify experiments in terms of required input states in section 3.5.

3.1 Fundamentals Part 1: Parametric Down-Conversion

We can generate approximative single-photon states with the help of spontaneous parametric down-conversion (SPDC) and more precisely type-II SPDC. A detailed account on parametric down-conversion (PDC) can be found in the corresponding chapter of the referenced book [13].
On an abstract level, type-II SPDC is a two-mode squeezing operation described by the Hamiltoninan $\hat{H}_{\mathrm{SPDC}}$ with $\hat{a}_{s,i}^{\dagger}$ and $\hat{a}_{s,i}$ denoting the creation and annihilation operators for the two modes called signal resp. idler:

$$\hat{H}_{\mathrm{SPDC}} = r \cdot (\hat{a}_s^{\dagger}\hat{a}_i^{\dagger} + \hat{a}_s\hat{a}_i) \tag{3.1}$$

The SPDC state ψ_{SPDC} is obtained by applying the corresponding unitary $\hat{U}_{\mathrm{SPDC}}$ on the vacuum. $\hat{U}_{\mathrm{SPDC}}$ is defined as the matrix exponential of $\hat{H}_{\mathrm{SPDC}}$:

$$|\psi_{\mathrm{SPDC}}\rangle = \hat{U}_{\mathrm{SPDC}}\,|0{,}0\rangle = e^{-i\hat{H}_{\mathrm{SPDC}}}\,|0{,}0\rangle \tag{3.2}$$

In SPDC photons are generated by the interaction of incident pump light and a non-linear medium. This interaction can be thought of as inducing dipols in the material, which will in turn also irradiate an electro-magnetic field. Creating a significant output from

these fields requires the contribution from the individual dipoles to interfere constructively. With $\vec{k}_p, \vec{k}_s$ and $\vec{k}_i$ being the wave vectors of pump, signal and idler, perfect constructive interference needs the phase-mismatch Δk to be zero, which can also be interpreted as the result of momentum conservation:

$$\Delta k = |\vec{k}_s + \vec{k}_i - \vec{k}_p| = \frac{n_s \cdot \omega_s}{c} + \frac{n_i \cdot \omega_i}{c} - \frac{n_p \cdot \omega_p}{c} \tag{3.3}$$

Fulfilling the above equation, i.e. the phase-matching condition, can in principle be achieved by non-collinear propagation of signal and idler (see Figure 3.2, (b)). This possibility is lost for PDC inside a waveguide confining the propagation of the light. In this case phase-matching can be accomplished by periodically poling the crystal and thus adding a quasi-momentum $\vec{k}_{\mathrm{QPM}} = \frac{2\pi}{\Lambda}$ (Figure 3.2, (c)) with Λ being the poling period. Confining the light fields in waveguides allows, on the other hand, to increase the effective length over which the PDC process takes place in comparison to a non-waveguided, i.e. bulk, sample where this parameter is related to the Rayleigh length of the pump beam. The resulting advantages are twofold: On the one hand, a longer effective length increases the brightness, i.e. the number of generated PDC photons per pump power. On the other hand, it offers new possibilities in engineering the spectral properties of the PDC process via the effective length of the sample. This spectral engineering will be treated in detail in section 5.4, while in the following we will briefly introduce the relevant terms in relation to the spectral aspects of PDC.

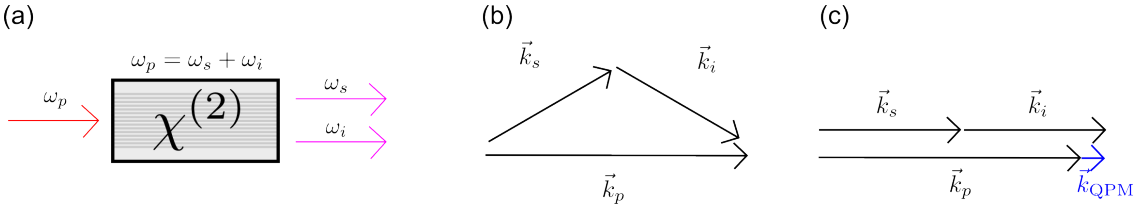

Figure 3.2: (a): Illustration of the SPDC process: Photons from bright pump beam with frequency ω_p decay inside a $\chi^{(2)}$-non-linear medium with a probability on the order of magnitude of 10^{-7} into a signal and an idler photon at frequencies ω_s resp. ω_i. (b): Illustration of the phase-matching condition that requires the wave vectors of the involved photons to match up. Note that this can in general be achieved by non-collinear propagation. (c): Illustration of the phase-matching condition for a PDC process inside a periodically-poled crystal with waveguides: The waveguides force the photons into collinear propagation, however, the periodical poling leads to a quasi-momentum $\vec{k}_{\mathrm{QPM}}$ that can be engineered such that the wave vectors again match up.

In order to obtain an expression for the spectral properties, we sum up the contributions of the individual dipols for the whole length L of the crystal. This corresponds to the integration over a rectangle in space and thus yields a sinc-function depending on

$\Delta k(\lambda_s, \lambda_i)$, the so called phase-matching function $\Phi(\lambda_s, \lambda_i)$:

$$\Phi(\lambda_s, \lambda_i) \propto \mathrm{sinc}[\Delta k(\lambda_s, \lambda_i) \cdot L/2] \tag{3.4}$$

An additional constraint is imposed on the generated state by energy conservation:

$$\omega_p = \omega_s + \omega_i \tag{3.5}$$

This condition is represented in the function $\alpha(\omega_s + \omega_i)$ for the pump distribution, which can also be expressed in terms of the wavelengths λ_s and λ_i .
Since both momentum and energy conservation have to be fulfilled by the PDC process, the correlation of signal wavelength λ_s and idler wavelength λ_i is given by the product of the phase-matching function $\Phi(\lambda_s, \lambda_i)$ and the pump distribution $\alpha(\lambda_s, \lambda_i)$. We call this product the joint-spectral amplitude (JSA) $f(\lambda_s, \lambda_i)$:

$$f(\lambda_s, \lambda_i) = \Phi(\lambda_s, \lambda_i)\alpha(\lambda_s, \lambda_i) \tag{3.6}$$

The JSA is important in the context of this work as it can be related to the purity of the photons generated in a PDC process and thus to the HOM-dip visibility (elaborated on in section 5.4).
Considering its photon-number statistics, a two-mode SPDC state is not an ideal single-photon state, but exhibits exponential photon-number statistics and can in the photon-number-basis (Fock-basis) be written in the following way [14]:

$$|\psi_{\mathrm{PDC}}\rangle = \sqrt{1 - |\lambda|^2} \sum_{n=0}^{\infty} \lambda^n \, |n,n\rangle \tag{3.7}$$

Note that n generally denotes the photon number and specifically the corresponding component of the Fock-state when written in brackets. λ is defined as $\lambda = -e^{i\phi} \cdot \tanh r$ where r and ϕ are related to the squeezing parameter ξ by the relation $\xi = r \cdot e^{i\phi}$. Since the relative weight of higher photon-number contributions scales exponentially with n, a single-photon state is more closely approximated as λ gets smaller.
An experimental setting where photon-number information on the idler is not available corresponds to the mathematical operation of tracing out the photon number in the idler subsystem, i.e. summing over the diagonal elements of the subsystem. Such a setting is usually realised when either the idler is not detected or detected with non-photon-number-resolving bucket detectors. The operation will turn the density matrix ρ_{her} of the PDC state after the detection of the idler into an incoherent sum of components with different

photon numbers and thereby reduce its purity:

$$\begin{aligned}\rho_{\mathrm{her}} = \mathrm{Tr_i}\{\rho\} &= (1-|\lambda|^2)\sum_{n_\mathrm{i}=0}^{\infty} \mathbb{1}_x \otimes \langle n_\mathrm{i}^{'}| \sum_{n_\mathrm{i}=0}^{\infty} \lambda^{n_\mathrm{i}} \sum_{n_\mathrm{s}=0}^{\infty} \lambda^{n_\mathrm{s}} |n_\mathrm{i}, n_\mathrm{s}\rangle \langle n_\mathrm{i}, n_\mathrm{s}| n_\mathrm{i}^{'}\rangle \otimes \mathbb{1} \\ &= (1-|\lambda|^2)\sum_{n_\mathrm{i}=0}^{\infty} \lambda^{n_\mathrm{i}} \sum_{n_\mathrm{s}=0}^{\infty} \lambda^{n_\mathrm{s}} |n_\mathrm{s}\rangle \langle n_\mathrm{s}| = (1-|\lambda|^2)\sum_{n=0}^{\infty} \lambda^{2n} |n\rangle \langle n|\end{aligned} \tag{3.8}$$

Here, n_i and n_s denote the components of the Fock-state of the idler resp. the signal. Since PDC sources constitutes a photon-pair sources, we can identify $n_\mathrm{i} = n_\mathrm{s} = n$.
As the detection of the idler photon heralds the presence of the signal photon, we call the PDC state after the detection of the idler a heralded PDC state. The incoherent sum in (3.8) reduces the purity of the state associated to ρ_{her} and thus the visibility of quantum interference between two heralded PDC as will be discussed in section 3.3, where (3.27) links the purity of the two states involved to the visibility.
The relative weight of higher photon numbers according to (3.8) scales with λ^n, so that the higher-order terms vanish for values of λ approaching 0. Consequently, decreasing λ will increase the purity of interfering states and thereby also increase the visibility. Identifying $|\lambda| = |\tanh(r)|$ and $r = \mathrm{arcsinh}(\sqrt{\bar{n}})$ and noting that tanh as well as arcsinh are monotonous functions, we find that a small value of λ corresponds to a low mean photon number $\bar{n}$.
$\bar{n}$ is given by the sum over the photon numbers n with their respective probabilities p_n which can be expressed according to (3.8):

$$\bar{n} = \sum_{n=0}^{\infty} n \cdot p_n = \sum_{n=0}^{\infty} n \cdot (1-|\lambda|^2) \cdot |\lambda|^{2n} \tag{3.9}$$

We will see in the chapters to come that the mean photon number $\bar{n}$ is an important parameter determining both the experimentally observed visibilities of quantum interference as well as the achievable rates of measurement events.

3.2 Fundamentals Part 2: Quantum Walks

3.2.1 Random Walk vs. Quantum Walk

The term "quantum walk" was first coined in the sense of "quantum random walk" [8]. It is consequently derived from the classical random walk in which a classical particle undergoes movements in random directions. The Galton board presents a very illustrative example for such a setting. It is a pyramidal arrangement of pins (see Figure 3.3, (a)) where the particle, or a walker in a more general case, has at each pin a 50 % chance of going left and a 50 % chance of going right. Consequently, the probability to find the

walker in a certain bin x for a certain step n is given by a binomial distribution $P_n(x)$ centered around the bin in the middle ($x = 0$, see Figure 3.10, (b)):

$$P_n(x) = \frac{1}{2^n} \begin{pmatrix} n \\ (n+x)/2 \end{pmatrix} \tag{3.10}$$

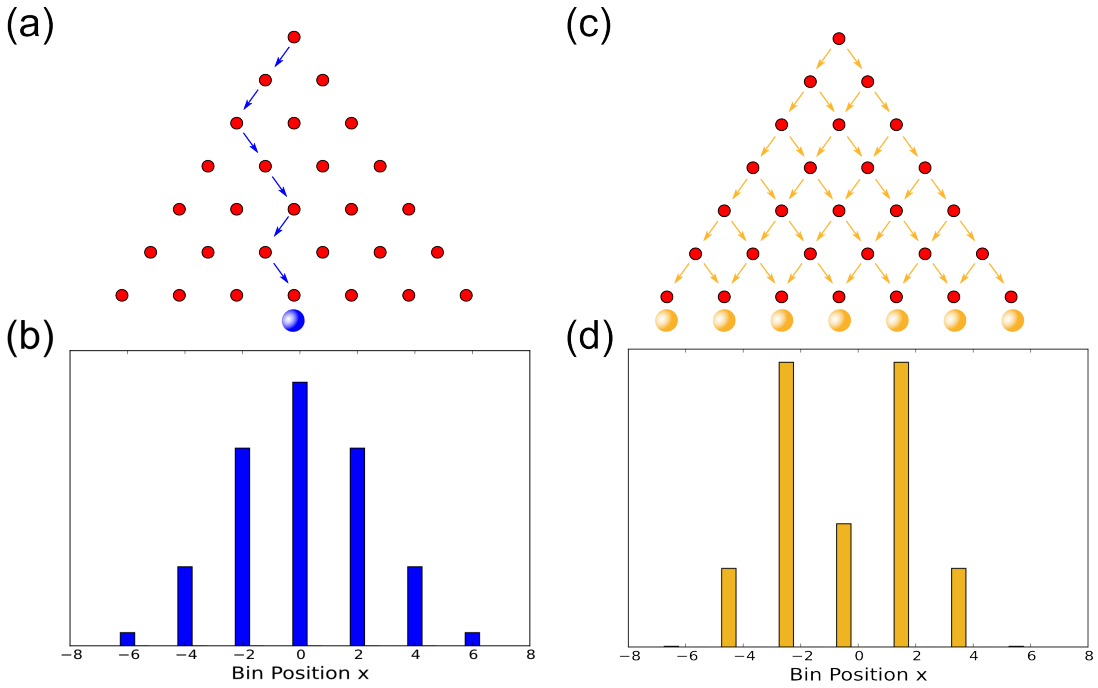

Figure 3.3: (a): Example of a possible trajectory of a classical particle on a Galton board in random walk over six steps. (b): The corresponding probability for each bin as given by a binomial distribution. (c): Illustration of the evolution in a quantum walk: In contrast to its classical pendant, here the walker travels along all possible paths simultaneously. The different components interfere with each other, consequently the resulting probability distribution as shown in (d) looks qualitatively different from the classical case.

While classical random walks play an important role in explaining phenomena [15] in fields as diverse as economics [16, 17] or biology [18, 19, 20], this model is insufficient when considering quantum particles. Here, we also have to account for their wave-aspect [8], making the wave function $|\Psi\rangle$ the key to accessing probability distributions. In the particle picture this would correspond to the walker taking all paths simultaneously with the individual pulses interfering with each other (Figure 3.3, (b)). The resulting probability distribution (Figure 3.3, (d)) thus differs qualitatively from its classical pendant. We will see in the following how this probability distribution can be derived.
Since the theoretical framework has been described in detail in previous works (e.g.

[21, 22]), the treatment in the following is limited to the key aspects.

3.2.2 Continuous-time vs. Discrete-time Quantum Walk

Once the description of a system via its wave function has been adopted, the Schrödinger equation assigns fundamental importance for its time-evolution to the Hamiltonian $\hat{H}$. In its integral formulation the Schrödinger equation allows for the identification of a unitary time-evolution operator $\hat{U}(t,t_0)$:

$$|\Psi(t)\rangle = \hat{U}(t,t_0)\,|\Psi(t_0)\rangle = T\exp^{-\frac{i}{\hbar}\int_{t_0}^{t}\hat{H}(t)\mathrm{d}t}\,|\Psi(t_0)\rangle \tag{3.11}$$

The time-ordering operator T accounts for possible time dependencies of the Hamiltonian. For the concrete expression of $\hat{U}$, we distinguish between the two main settings for the evolution of the wave function: In a continuous-time quantum walk it is described by a tight-binding Hamiltonian involving couplings constants between modes. In a discrete-time quantum walk, on the other hand, we assume an evolution over a number n of discrete time steps, each of them being described by a unitary operator consisting of a coin operation $\hat{C}$ and a subsequent step operation $\hat{S}$:

$$|\Psi(n+1)\rangle = \hat{U}\,|\Psi(n)\rangle = \hat{S}\hat{C}\,|\Psi(n)\rangle = (\hat{S}\hat{C})^n\,|\Psi(n=0)\rangle \tag{3.12}$$

In this work we will concentrate on discrete-time quantum walks as this is the concept appropriate for the description of our experimental system. An extensive account on the relation of discrete- and continuous-time quantum walks from view-point of mathematical physics can be found in [23, 24].
In a discrete-time quantum walk, the step operation $\hat{S}$ in the external or position degree of freedom is conditioned on the internal or coin state of the walker. The Hilbert space $\mathcal{H}$ for the walker's wave function is thus given as the tensor product of the disjunct position and coin subspaces $\mathcal{H}_\mathrm{x}$ and $\mathcal{H}_\mathrm{c}$:

$$\mathcal{H} = \mathcal{H}_\mathrm{x} \otimes \mathcal{H}_\mathrm{c} \tag{3.13}$$

Consequently, the walker's wave function for a quantum walk along a line can be written in the following way with A_x and A_c being the complex probability amplitudes for the individual modes in the position resp. coin space:

$$|\Psi\rangle = \sum_{x\in\mathbb{Z}}\sum_{c\in\{H,V\}} A_x A_c\,|x\rangle\otimes|c\rangle \equiv \sum_{x\in\mathbb{Z}}\sum_{c\in\{H,V\}} A_{x,c}\,|x\rangle\otimes|c\rangle \tag{3.14}$$

As illustrated by Figure 3.3, (d), a walk starting at a single position can occupy $n+1$ positions after n steps and can thus be expressed in a Hilbert space of dimensionality $n+1$. The coin space, on the other hand, comprises in our setting the two basis states of horizontal polarisation $|H\rangle = (1,0)^{\mathrm{T}}$ and vertical polarisation $|V\rangle = (0,1)^{\mathrm{T}}$. As a consequence, the overall Hilbert space according to (3.13) is of dimensionality $2 \cdot (n+1)$. Once the wave function is known, the probability distribution can be calculated as the square of its absolute.

3.2.3 Coin vs. Step Operation

In order to determine the wave function, we need to known how to describe the operations governing its evolution.
Operations on the coin degree of freedom can be described with 2×2 unitary matrices equivalent to the Jones-matrices of the corresponding optical components. In certain instances these are connected to the Pauli-matrices σ_x, σ_y and σ_z. We start by linking the rotation $R_x(\theta)$ described by the σ_x matrix with the rotation $\hat{R}_{\mathrm{EOM}}$ effected by the electro-optic modulators (EOM) used in the experiment (elaborated on in section 4.3.2):

$$\begin{aligned} R_x(\theta) \propto e^{-i\sigma_x \cdot \theta} &= \sum_{n=0}^{\infty} \frac{(-i\sigma_x \cdot \theta)^n}{n!} = \sum_{n=0}^{\infty} (-1)^n \left[\frac{(i\sigma_x \cdot \theta)^{2n+1}}{(2n+1)!} + \frac{(i\sigma_x \cdot \theta)^{2n}}{(2n)!} \right] \\ &= \sum_{n=0}^{\infty} (-1)^n \left[i\sigma_x \frac{\theta^{2n+1}}{(2n+1)!} - \sigma_0 \frac{\theta^{2n}}{(2n)!} \right] = i\sigma_x \cdot \sin(\theta) - \sigma_0 \cdot \cos(\theta) \\ &= \begin{pmatrix} \cos(\theta) & -i\sin(\theta) \\ -i\sin(\theta) & \cos(\theta) \end{pmatrix} \propto \hat{R}_{\mathrm{EOM}}(\theta) \end{aligned} \tag{3.15}$$

In the above derivation we used the fact that the square of σ_x is equal to the identity σ_0. The rotation $\hat{R}_{\mathrm{HWP}}$ implemented by a half-wave plate (HWP) is defined in the following way:

$$\hat{R}_{\mathrm{HWP}}(\theta) \propto \begin{pmatrix} \cos(\theta) & \sin(\theta) \\ \sin(\theta) & -\cos(\theta) \end{pmatrix} \tag{3.16}$$

Assuming position-independent polarisation rotation, the coin operation acting on all positions of the state $|\Psi\rangle$ is obtained as the dyadic product of the coin and the identity operation in the position subspace:

$$\hat{C}_{\mathrm{EOM/HWP}} = \mathbb{1}_x \otimes \hat{R}_{\mathrm{EOM/HWP}}(\theta) \tag{3.17}$$

A position-dependent coin, on the other hand, requires a position-dependent rotation angle

θ_x.
The step operator effects a polarisation-dependent shift in the position space and is defined as follows:

$$\hat{S} = \sum_x \left(|x+1\rangle \langle x| \otimes |H\rangle \langle H| + |x-1\rangle \langle x| \otimes |V\rangle \langle V| \right) \tag{3.18}$$

We see that the polarisation determines in which direction the light is translated in the step operation.
Having defined the coin operation $\hat{C}$ and the step operation $\hat{S}$, we have all the ingredients necessary to describe the evolution of the walker's wave function by the combined effect of these two operators as it is illustrated in Figure 3.4.
The framework laid out above can be used for describe single- as well as multi-particle wave functions. As laid out in appendix B, a single-particle quantum walk can be simulated with coherent light, while it is only in a multi-particle quantum walk that coincidence detection reveals non-classical signatures in the form of photon bunching.

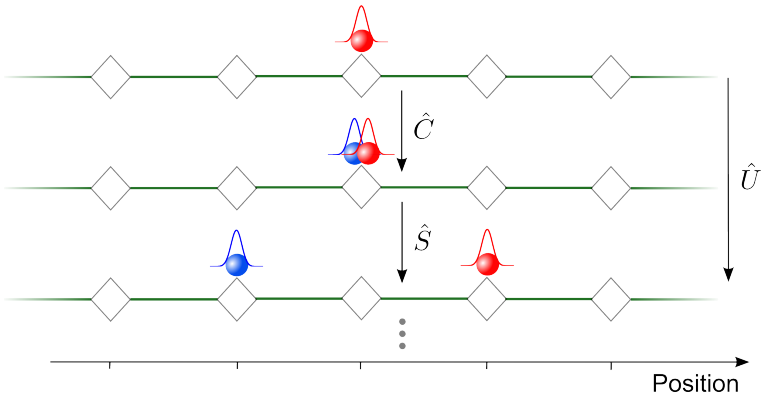

Figure 3.4: Illustration of how the walker is transformed by the one-time application of the unitary $\hat{U}$ for a one-dimensional quantum walk (quantum walk on a line): First, the coin operation $\hat{C}$ turns the internal degree of freedom into a superposition of horizontal (red) and vertical polarisation (blue). Subsequently, the step operation $\hat{S}$ increases the external degree of freedom (position) by one for the horizontal component and decreases it by one for the vertical component. The combined effect of coin and step operation is described by the evolution unitary $\hat{U}$. This operator is applied n times to obtain the quantum walk evolution for n steps.

3.3 Fundamentals Part 3: Experimental Signatures of a Single Photon

A fully-fledged quantum system for simulation and computation requires the possibility to put individual particles in distinct input modes. For an optical system these are particles of light, so called photons.

The wave-particle duality in combination with the fact that photons do not exhibit a mass poses a serious challenge to the notion of an observer-independent reality. It seems that firm statements can only be made on how photons behave in a certain experimental setting. In this sense, we will discuss setups that make a photon reveal itself in its particle-nature, namely the measurements of second-order correlations in subsection 3.3.1 and Hong-Ou-Mandel (HOM) interference in subsection 3.3.2.
Note that it has suggested to altogether abandon the notion of a photon being either a particle or wave [25].

3.3.1 Second-order Correlations Measurements

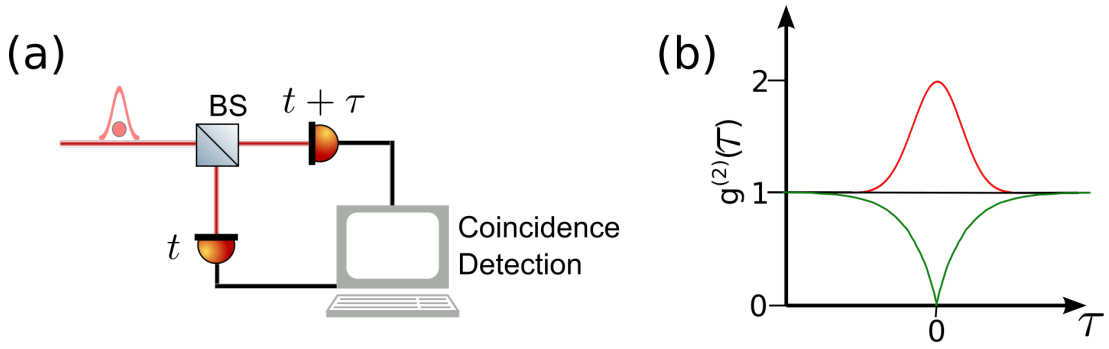

Figure 3.5: (a): Schematic of a Hanbury-Brown Twiss interferometer: The light incident in one mode is split-up at a probabilistic beam splitter (BS). Detectors in the two output modes are used to detect coincidence and single count rates. The setup allows for determining the second-order correlation function $g^{(2)}(\tau)$ depending on the delay τ between the arms (shown in subfigure (b)). (b): $g^{(2)}(\tau)$ for states with super-Poissonian statistics (red curve), Poissonian statistics (black curve) and sub-Poissonian statistics (green curve), exhibiting bunching, no bunching and antibunching.

The experimental signature of a single photon is that it produces exactly one detection event. This characteristic can be tested by correlation measurements in a Hanbury Brown-Twiss interferometer [26, 13] (see Figure 3.5, a), in which we measure correlations between the two output ports of a beam spitter with light incident in one input port. Here, the relevant quantity is the second-order coherence $g^{(2)}$. Considering a single spatial mode, $g^{(2)}$ depending on the delay τ between two photons can be written in the following way with $\hat{a}^\dagger$ and $\hat{a}$ being the creation resp. annihilation operators of single photons [13]:

$$g^{(2)}(\tau) = \frac{\langle \hat{a}^\dagger(t)\hat{a}^\dagger(t+\tau)\hat{a}(t+\tau)\hat{a}(t)\rangle}{\langle \hat{a}^\dagger(t)\hat{a}(t)\rangle^2} \tag{3.19}$$

For $\tau = 0$ the above expression assumes the following form with $\hat{n} = \hat{a}^\dagger \hat{a}$ being the photon-number operator:

$$g^{(2)}(0) = \frac{\langle \hat{n}(t)(\hat{n}(t) - 1) \rangle}{\langle \hat{n}(t) \rangle^2} \tag{3.20}$$

In a Hanbury Brown-Twiss interferometer, we usually measure the probability of coincidences p_{Coinc} in a certain time interval versus the respective probability of single detection events p_{S}. $P(n)$ denotes the probability of a certain photon number n. For a PDC state with low mean photon number the assumption $P(1) \gg P(2) \gg P(n > 2)$ holds and we obtain the following relation [13]:

$$g^{(2)}(0) = \frac{2P(2)}{P(1)^2} = \frac{P_{\mathrm{Coinc}}}{P_{\mathrm{S1}} \cdot P_{\mathrm{S2}}} = \frac{n_{\mathrm{Coinc}}/n_{\mathrm{T}}}{n_{\mathrm{S1}}/n_{\mathrm{T}} \cdot n_{\mathrm{S2}}/n_{\mathrm{T}}} = \frac{n_{\mathrm{Coinc}} \cdot n_{\mathrm{T}}}{n_{\mathrm{S1}} \cdot n_{\mathrm{S2}}} \tag{3.21}$$

In the above equation, we translated the probabilities into the number of the respective counts n_{Coinc},n_{S1} and n_{S2} as well as the number n_{T} of trigger events in the same time interval.
Figure 3.5, (b) shows the correlation function $g^{(2)}(\tau)$ depending on the delay τ between the arms in units of the correlation time τ_{C} resp. the correlation function $g^{(2)}(0)$ for zero delay for different types of sources: For a perfect single photon source emitting one photon at a time and thus exhibiting anti-bunching and sub-poissonian statistics we expect a $g^{(2)}(0)$-value of 0. Coherent light obeying poissonian statistics, on the other hand, has a $g^{(2)}(0)$-value of 1. Thermal light is characterised by bunching and super-poissonian statistics and thus shows a $g^{(2)}(0)$ of 2.
Measurements of the $g^{(2)}(\tau)$ rep. $g^{(2)}(0)$-values consequently constitute a well-established way of verifying whether a light source emits single photons.

3.3.2 HOM-Dip Experiment

Regarding interference, single photons show a distinct behaviour which depends not only on the single-photon character but also on the indistinguishability of these photons.
The description of multi-photon system via a single bosonic multi-photon wavefunction assumes the indistinguishability of the individual photons. Since this assumption is not fulfilled in general, we quantify the indistinguishability I of two photons with density matrices $\hat{\rho}_1$ and $\hat{\rho}_2$ according to the following formula [13]:

$$I(\hat{\rho}_1,\hat{\rho}_2) = 1 - ||\hat{\rho}_1 - \hat{\rho}_2||^2 \tag{3.22}$$

Here, $||\rho_1 - \rho_2||^2$ denotes the operational distance between the two density matrices.

For pure states with $\hat{\rho}_1 = |\psi_1\rangle\langle\psi_1|$ and $\hat{\rho}_2 = |\psi_2\rangle\langle\psi_2|$, I is given by the square of the scalar product of the two states:

$$I(\hat{\rho}_1,\hat{\rho}_2) = |\langle\psi_1|\psi_2\rangle|^2 \tag{3.23}$$

This expression corresponds to the fidelity [27] and allows in principle for a direct calculation of the indistinguishability.
In practice, however, a possibly unbound number of different degrees of freedom could affect its value. An empiric access to the visibility is thus desirable.
Since its first experimental demonstration in 1987 [28], Hong-Ou-Mandel(HOM)-interference has become a well-established workhorse technique for testing the indistinguishability of quantum states [29, 30, 31, 32].

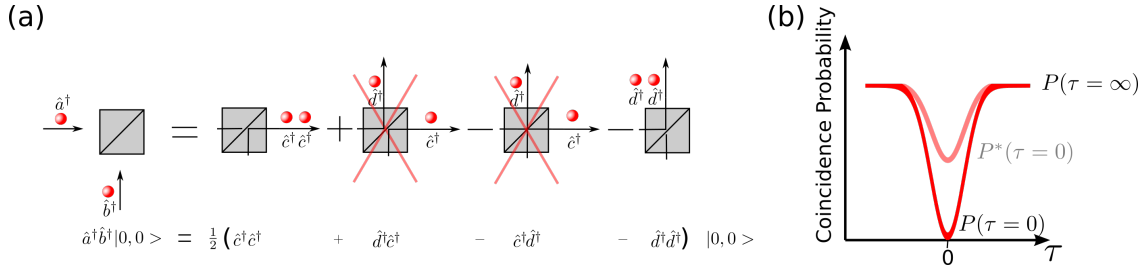

Figure 3.6: (a): Illustration of an HOM dip experiment: Single photons impinge on a beam splitter in both of the input modes a and b. Due to the bosonic nature of the two-photon wavefunction, the terms corresponding to photons in each of the output modes c and d vanish as long as indistinguishability of the two photons is given, i.e. $\hat{c}^\dagger$ and $\hat{d}^\dagger$ do commute. (b): Illustration of the measured coincidence probabilities for perfectly indistinguishable quantum particles (P) as well as for classical (coherent) light (P^*). In first case, the obtained visibility is 1, in the second 0.5.

Figure 3.6, (a) illustrates the principle underlying this experiment: Two photons (one in each of the input mode a and b) of the state $|\phi\rangle$ are brought to interference on a 50:50 beam splitter described by the unitary $\hat{B}$ acting in the following way:

$$\begin{aligned} \hat{B}: \quad \hat{c}^\dagger &= \frac{1}{\sqrt{2}}\left(\hat{a}^\dagger + \hat{b}^\dagger\right) \qquad \hat{d}^\dagger = \frac{1}{\sqrt{2}}\left(\hat{a}^\dagger - \hat{b}^\dagger\right) \\ \Leftrightarrow \quad \hat{a}^\dagger &= \frac{1}{\sqrt{2}}\left(\hat{c}^\dagger + \hat{d}^\dagger\right) \qquad \hat{b}^\dagger = \frac{1}{\sqrt{2}}\left(\hat{c}^\dagger - \hat{d}^\dagger\right) \end{aligned} \tag{3.24}$$

In the above expression the two output modes of the beam splitter are denoted c and d. With this definition the beam splitter transforms an input state with one photon in mode

a and one photon in mode b in the following way:

$$\hat{a}^\dagger \hat{b}^\dagger \left|0,0\right\rangle = \frac{1}{2}\left(\hat{c}^\dagger \hat{c}^\dagger + \hat{d}^\dagger \hat{c}^\dagger - \hat{c}^\dagger \hat{d}^\dagger - \hat{d}^\dagger \hat{d}^\dagger\right)\left|0,0\right\rangle \tag{3.25}$$

In case of perfect indistinguishability of the two photons, $\hat{c}^\dagger$ and $\hat{d}^\dagger$ commute and the terms corresponding to the photons exiting in different modes of the beam splitter cancel out, so that they will both end up in the same output modes. This outcome is a result of the bosonic character of photons. In contrast, fermions would exit in different ports.
In case the two photons are distinguishable in any degree of freedom, the terms corresponding to a photon in each output mode will no longer cancel out perfectly.
Experimentally, distinguishability between the two photons can be deliberately introduced, for example by temporally delaying one of the photons in respect to the other by a certain time τ. When placing detectors in each of the two output modes, we can record coincidences between them, which are associated to both photons exiting in different modes. This allows us to obtain the coincidence probability $P_{\tau=0}$ for zero time delay as well as $P_{\tau=\infty}$ (see Figure 3.6, (b)). In this context, $\tau = \infty$ corresponds to a time delay for which the temporal overlap of the pulses is negligibly small, i.e. the photon exhibit almost perfect temporal distinguishably and thus the terms with photons in both output modes no longer cancel out.
Tuning the temporal overlap will result in a dip in the coincidience probability around $\tau = 0$, when the two photons overlap. The visibility V_{HOM} of this dip is defined as the difference between the maximum $P_{\tau=\infty}$ of the coincidence probability and its minimum $P_{\tau=0}$, divided by the maximum [13]:

$$V_{\mathrm{HOM}} = \frac{P_{\tau=\infty} - P_{\tau=0}}{P_{\tau=\infty}} \tag{3.26}$$

This experimentally obtained visibility can be related to the density matrices [33]:

$$V_{\mathrm{HOM}} = \mathrm{Tr}\left\{\hat{\rho}_1 \hat{\rho}_2\right\} = 1/2\left(\mathrm{Tr}\left\{\hat{\rho_1}^2\right\} + \mathrm{Tr}\left\{\hat{\rho_2}^2\right\} - ||\hat{\rho}_1 - \hat{\rho}_2||^2\right) \tag{3.27}$$

In the above expression, the last term denotes the operational distance which is equivalent to the Hilbert-Schmidt distance [34, 35], so that we can rephrase the formula in the following way:

$$V_{\mathrm{HOM}} = 1/2\left(\mathrm{Tr}\left\{\hat{\rho_1}^2\right\} + \mathrm{Tr}\left\{\hat{\rho_2}^2\right\} - \mathrm{Tr}\left\{(\hat{\rho}_1 - \hat{\rho}_2)^2\right\}\right) \tag{3.28}$$

For pure states with $\mathrm{Tr}\left\{\rho_1^2\right\} = 1$ and $\mathrm{Tr}\left\{\rho_2^2\right\} = 1$, the visibility equals the indistinguisha-

bility [34, 33]:

$$V_{\mathrm{HOM}} = I(\hat{\rho_1},\hat{\rho_2}) = |\langle\psi_1|\psi_2\rangle|^2 \tag{3.29}$$

The temporal delay is not the only parameter introducing distinguishability between two photons, as all imaginable degrees of freedom can have this effect. Deliberately tuning one of them (in this case the temporal delay) allows us to obtain a visibility from which information about indistinguishably in the other degrees of freedom can be inferred.
The different degrees of freedom of a state (such as frequency, photon number, polarisation, etc.) can be considered as subspaces with the corresponding wavefunction ψ_i, so that (3.29) assumes the following form:

$$V_{\mathrm{HOM}} = |\langle\psi_1|\psi_2\rangle|^2 = \prod_n |\langle\psi_{1,i}|\psi_{2,i}\rangle|^2 \tag{3.30}$$

Here, the first index denotes the state and the second index the subspace under consideration. The above formula tells us that the overall visibility is obtained by multiplying the visibilities of the individual subspaces.

3.4 State of the Art

Having briefly laid out the fundamentals for state preparation, evolution and detection, we will in the following take a look at possible physical implementations of systems that allow to investigate an evolution according to a quantum walk formalism.

3.4.1 Interest in Quantum Walks

As already mentioned, an important aspect founding the interest in quantum walks is that they provide a framework allowing to understand the evolution of a state in a quantum network. Consequently, they can be harnessed to describe systems in which quantum computation can be implemented [5, 6]. It has been shown that this is also true for the special case of discrete-time quantum walks [36]. A prominent example of algorithms that can be implemented with quantum walks are search algorithms [37, 38]. Furthermore, quantum walks offer considerable possibilities for the simulation of physical systems [7] as illustrated by various examples such as relativistic wave-packet spreading [39], energy transfer in photosynthetic systems [40, 41], dephasing-assisted transport [42], molecular binding [43], Bloch-oscillating spinor atoms [44] or non-linear Dirac equations and solitons [45].
In addition, quantum walks exhibit symmetries that make them a feasible model system for experimentally accessing topological phenomena [46, 47, 48].
Photonic quantum walks constitute a possible platform for the implementation of boson

sampling [49, 50, 51, 52, 53], a promising experimental testbed for the extended Church-Turing thesis [54]. This application will be elaborated on in section 3.5.1.

3.4.2 Implementations of Quantum Walks

Experimentally, quantum walks can in principle be implemented in any system allowing for the split of a walker's probability amplitude and its coherent propagation. We deliberately speak of a walker here and not of a laser pulse, a photon or a massive particle, as it is only important at this point that its evolution can be described by the spread of a probability amplitude.
In continuous-time quantum walks this split is determined by a coupling constant, while in discrete-time quantum walks it is governed by the coin (internal) degree of freedom. Consequently, systems exhibiting a fixed coupling constant between modes, e.g. arrays of coupled waveguides [55, 56, 57, 58], lend themselves to the implementation of photonic continuous-time quantum walks.
On the other hand, discrete-time quantum walks require operations on the coin degree of freedom. In an experimental setting, the coin state can be constituted by e.g. the fein resp. hyperfein levels of an ion [59, 60] or an atom [61, 62] as well as nuclear spins in molecules [63].
Considering photonic quantum walks, a range of external and internal (for discrete quantum walks) degrees of freedom is available: Choosing the position space as the external degree of freedom seems straight-forwards, but requires experimental resources increasing with the step number, making it infeasible for larger numbers of steps. Photonic quantum walk experiments in the position space have been conducted with laser-written integrated waveguide arrays [64, 65, 66, 67], beam displacer arrangements [68, 69, 70] or actual beam splitter cascades [53].
Harnessing, on the other hand, time as the external degree of freedom allows for time-multiplexing, i.e. using the same physical device for different steps and positions in time, thereby significantly increasing resource-efficiency. Devices such as detectors and optical switches impose constrains on the minimal possible time separation between two positions, usually requiring the implementation of an optical delay e.g. by means of fibres [9, 71, 72]. Such a delay, on the other hand, allows for a dynamic coin operation, i.e. for switching different coins at different positions [10, 73]. In the referenced instances, polarisation constitutes the coin degree of freedom, allowing to make use of fast switching Pockels cells. This capability opens the path to investigating an abundance of phenomena such as disorder and Anderson localisation [74, 10], percolation [12], state transfer and finite graphs [73] and split-step quantum walks exhibiting interesting topological phenomena [75, 76]. The fast switching operation can also be utilised for dynamic in- and outcoupling, enabling experiments relying on inhomogeneous, i.e. position-dependent, losses such as the implementation of sinks for the simulation of measurement-induced dynamics [77]. Eventually, the concomitant possibility of deterministically coupling in and out single photons enables reducing losses to a regime where they are compatible with quantum

input states.
Polarisation is not the only possible coin (internal) degree of freedom, e.g frequency (temporal) modes constitute an alternative coin state [78, 79, 80]. A concrete experimental framework for the implementation of quantum walks with frequency modes, however, still has to be devised.
Orbital angular momentum, on the other hand, has been shown to be a feasible external degree of freedom [81, 82, 83, 84].
Furthermore, it has been proposed to implement quantum walks in Bose-Einstein condensates [85, 86].
An overview over experimental implementations of quantum walks can be found in [87].

3.4.3 Figures of Merit

The applications of quantum walk system in quantum information processing and simulation mentioned above point to figures of merit by which to evaluate the various implementations.
Photonic systems inhibit an inherent disadvantage in comparison to massive particles: Since photons do not interact with each other, harnessing them for quantum information processing and computation is usually based on feeding a quantum state into a linear optical network and the implementation of photonic two-qubit gates has so far only been achieved in a probabilistic way [4, 88, 89] or for a single photon [90, 91]. Concerning the implementation of multiparticle gates, massive particles exhibit an inherent advantage over photons [92], but also require significant effort to isolate the model system from the environment and thus allow for sufficient coherence times. Photons on the other hand do not interact with each other without a mediator and are consequently intrinsically immune to certain environment influences, e.g. blackbody radiation. Photonic implementations of quantum walks are thus inherently more robust and usually exhibit significant advantages in terms of resource efficiency. In the following, we will focus our considerations on photonic systems.
Schemes for universal computation with quantum walks such as [6] require multi-particle input states. One figure of merit is consequently the number of possible occupied input modes. It is closely related to the amount of loss in the system as sensitivity towards loss increases exponentially with the number of particles.
Using quantum walks as a versatile quantum simulator [7] points to the need of high flexibility in generating different input states and dynamically reconfiguring the circuit. Similar requirements are valid for boson sampling (see section 3.5.1).
In the following, we take a closer look at the mentioned figures of merit.
Photonic input states can be generated with single atoms [93, 94], parametric down-conversion (PDC) [95, 27, 29, 32] or quantum dots [96, 97, 53, 52]. Quantum dots can in principle be deterministic on-demand single-photon sources, actual implementations, however, exhibit non-ideal, albeit very good values for indistinguishability, purity and

extraction efficiency [98, 96]. An estimate of the achievable rates for PDC and quantum dot sources is found in section 4.4.3 . While the photon-number statistics of probabilistic PDC sources might look less favourable than that of deterministic quantum dot sources, it can also be made use of, e.g. in schemes for Gaussian boson sampling [99, 100].
The achievable rates of multi-particle experiments will depend exponentially on the generation probability as well as on the Klyshko-efficiency, i.e. the losses, with the photon number being in the exponent. While losses also limit achievable step numbers in single-walker experiments, it is here easier to overcome them by increasing the intensity of the initial state. Furthermore, the achievable rates for single-walker experiments do not exhibit the exponential scaling with the photon number. Integrated platforms [55, 56, 65, 66, 58, 57, 67] face an inherent challenge regarding this aspect, since the walker is subjected to absorption throughout its evolution, i.e. propagation through the material. On the other hand, free-space implementations without feedback-loop are restricted in the number of modes due to their scaling in required components.
Fibre-based feedback-loop architectures [9, 71, 72] make use of the low losses in optical fibres in order to implement quantum walks with large number of modes.
Another figure of merit is the flexibility in reconfiguring the coin setting and/or the graph on which the walk takes place. Regarding the coin, this concerns the possibility of conducting different coin operations at different steps and/or different positions. For implementations utilising space as the external degree of freedom, free-space or integrated [101, 67], this can in principle be done in a straight-forward way. However, this may be connected with considerable effort and resources for large numbers of positions or configurations. Time-multiplexing is also more resource-efficient in this aspect as in the ideal case the same device can be used for all positions and configurations.

3.5 From Coherent Quantum Walks to Single Photon Quantum Walks

We previously pointed out that quantum computing and certain applications in quantum simulation require single particles in multiple input modes, while a coherent states initialised at a single position suffices for others.
In order to discuss which quantum effects require which type of input states, we refer to the four axioms of quantum mechanics as formulated by Nielsen and Chuang [102].
The first axiom states that a quantum mechanical system in a pure state is completely represented by a state vector $|\Psi\rangle$, the wave function, in a Hilbert Space $\mathcal{H}$. According to the second axiom, the evolution of this state is governed by a unitary $\hat{U}$:

$$|\Psi(t)\rangle = \hat{U}\,|\Psi(t_0)\rangle \tag{3.31}$$

The third axiom describes the effect of a projective measurement onto a certain mode m

with the projection operator $\hat{M}_m$:

$$|\Psi_m\rangle = \frac{\hat{M}_m |\Psi\rangle}{\sqrt{\langle\Psi| \hat{M}_m^\dagger \hat{M}_m |\Psi\rangle}} \tag{3.32}$$

The fourth axioms refers to composite systems: Assuming subsystems numbered from 1 to n with system number i prepared in the state ψ_i, we can write the overall state as the tensor product of the individual states:

$$\phi = \psi_1 \otimes ... \otimes \psi_n \tag{3.33}$$

The overall state does not necessarily have to be separable, i.e. we might not be able to write it as a product of two states. Famous examples of non-separable states are the Bell states, for instance the state $|\phi_+\rangle$:

$$|\phi_+\rangle = \frac{1}{\sqrt{2}} (|0,0\rangle + |1,1\rangle) \tag{3.34}$$

Here, the state is written in the computational basis with the basis states $|0\rangle$ and $|1\rangle$. Due to its non-separability it is considered an example of an entangled state.
The fact that a system can be described in accordance with a selection of these axioms does not mean that its evolution cannot simulated with coherent states which are usually treated as classical states in quantum optics: As shown in appendix A, a coherent state behaves in the same way as a single photon for a quantum walk only occupying one initial position. In experiments the simulation of systems obeying the first two axioms with coherent states is well established (see for example [103, 55, 9, 71, 10, 11, 12, 72, 73, 75, 104, 105, 76]). As we demonstrate in chapter 7 of this work, coherent states can also be harnessed to simulate the effects of projective measurements [77].
In spite of evolving according to the first three axioms of quantum mechanics, coherent states are in the quantum optics community considered to be classical. In order to find out why this is the case, we take a closer look at the fourth axiom. Note that although coherence is conventionally regarded as a classical feature, it can nevertheless lead to non-classical correlations [106] or be regarded as a resource [107].
As already mentioned, the wave function describing a composite system can exhibit a mathematical property called inseparability, i.e. it cannot be written as a product of the subsystems, which manifests itself physically by giving rise to non-classical correlations called entanglement [108]. Originally, this property was considered evidence for the incompleteness of quantum-mechanical descriptions [109]. However, empirical evidence with increasing validity strongly suggests that entanglement is indeed an element of physical reality [110, 111, 112, 113].

While a single particle can exhibit non-separability in its different degrees of freedom [114], the non-local quantum correlations described as "spooky action at distance", however, require multiparticle, non-local entanglement [115]. As a consequence, one may regard entanglement and non-locality as different resources [116]. Certain effects requiring only entanglement, but not non-locality can thus be observed in single-particle systems, where entanglement between the different degrees of freedom is present [117, 118, 11, 82, 119]. This leaves us with the possibility to exhibit non-local entanglement as one of the most exclusive criteria for a genuine quantum system. Fulfilling this criterion requires the individual partitions to be separated in a space-like manner, i.e. to be individual particles in individual modes. Note that non-local entanglement is assumed to be possible also for a single particle that can be in either one of two spatially separated modes [120].
While wave-like behaviour of something conventionally thought of as a particle, e.g. an electron, is considered a non-classical "quantum" effect, it is the particle character of photons that the optics community deems to be a quantum feature. Indeed, proposed schemes for photonic quantum computing rely on non-local entanglement [4]. A review of linear optical computing can be found in [121, 122], a review on multiphoton entanglement and interferometry in [123].

3.5.1 Towards Boson Sampling

The dimensionality of the Hilbert space needed for describing a composite quantum system according to the fourth axiom points to the different complexity of single- and multi-particle systems.
Due to the application of the tensor product the dimensionality D_s of the Hilbert space for a single-particle system is the product of the dimensionalities d_i of the subsystems, in this case the individual degrees of freedom:

$$D_\mathrm{s} = \prod_{i=1}^{m} d_i = d_1 \cdot ... \cdot d_m \tag{3.35}$$

The number m of degrees of freedom for an experimental system is usually limited to small values, e.g. 2 when utilising position and polarisation as external and internal degree of freedom. Increasing this number requires fundamental modifications to the experimental platform for each degree that is to be added, e.g. a frequency-dependent splitting (internal degree) or an additional spatial dimension (external degree). Furthermore, there are fundamental limits for certain degrees of freedom, e.g. the dimensionality of the position space.
The dimensionality D_m of a multi-particle system, on the other hand, also depends on the

number n of involved particles:

$$D_{\mathrm{m}} = \prod_{i=1}^{m} \prod_{j=1}^{n} d_{i,j} \tag{3.36}$$

The second index j for $d_{j,i}$ indicates that now the product incorporates multiplying the dimensionalities of each of the individual photons. As a consequence, already a relatively small number of photons leads to a high-dimensional Hilbert space and thus to a high computational complexity when solving related problems. Note that the particles in this case have to be in different input modes as for multiple particles in the same input mode there is no difference to just one particle in this mode [124].
A prominent experimental system that relies on multiple photons in different input modes and the associated complexity is boson sampling [54]. This model system assumes sampling from the output of a unitary which governs the evolution of n photons in different input modes. The output probability distribution is then given by matrix permanent, a quantity which is hard to compute classically. Boson sampling is therefore an example for an experiment that presumably cannot be simulated efficiently classically and could consequently be a possible platform for experimentally refuting the extended Church-Turing thesis and demonstrating fundamental advantages of quantum systems.
It has been proven that any finite-dimensional discrete unitary can be optically implemented [125]. More recently, improved designs for such universal multiport interferometers have been demonstrated [126].
A number of experiments have shown that the principle of boson sampling, i.e. the implementation of linear-optical network for photons occupying multiple spatially separated input modes, is in principle possible for photonic systems [56, 64, 127]. Consequently, boson sampling experiments have been conducted in integrated platforms [49, 50, 128, 67] with PDC sources, free-space beam splitter arrangements with quantum dot sources [53], fibre-based spatial multiplexing architectures with quantum dot sources [129] or fibre-based time-multiplexing setups with quantum dot sources [52]. Note that these are indeed proof-of-principle experiments in the sense that they lack the requirements for a quantum advantage in terms of number of photons, number of modes, losses, etc. [130, 131, 132].
It has been proposed to enhance the architecture of preceding time-multiplexing quantum walk experiments [9, 11] such that they enable the implementation of boson sampling [51]. The current status of the experiment as presented in this thesis exhibits all the features required for a proof-of-principle boson sampling experiment except for the possibility of realising an arbitrarily variable beam splitter unitary. Especially, PDC sources as used in our experiment have been shown to be compatible with boson sampling [133, 99] and schemes using the characteristics of PDC sources for advantages in boson sampling implementations have been proposed [99, 100, 134]. Concerning the beam splitter unitary, we are limited by the three possible switching states of our EOMs. We are, however, in contact with a manufacturer of EOMs in order to acquire devices exhibiting a high

flexibility in the range of voltages applied during a certain experimental run. Having such an apparatus at hand would not only be a big step towards the experimental implementation of a proof-of-principle boson sampling experiment, but also allow for realising a wide range of unitaries, enabling a versatile quantum simulator.

4 Experimental Setup

As pointed out previously, a complete quantum network incorporates state preparation, evolution and detection. This structure will also guide us through the presentation of the experimental setup in this section.
Ensuring purity and indistinguishability of the generated photons is a complex undertaking to which we devote an own chapter (chapter 5).
The investigations described in this thesis are conducted with two similar but different setups. Both incorporate the well-established time-multiplexing feed-back loop which provides the basis of numerous research works [9, 10, 11, 12, 73]. While all of these experiments rely on coherent input states, we draw on expertise in PDC source engineering [31] to merge a time-multiplexing setup based on a loop architecture with a matching PDC source.
The experiments described in this thesis that investigate topological phenomena are conducted with a setup operating according to the same principle as in the aforementioned publications, while the experiments relying on non-classical input states or controlled losses are measured with a setup that has been significantly extended as described in the following.
The fibre loop setup has been elaborated on previous works [22], where further helpful information e.g. on the operation of Pockels cell acting on the polarisation can be found, which is however not necessary for the understanding of the working principle. Combining the fibre loop with PDC input states, requires substantial modifications, especially concerning the synchronisation of 4 electro-optic modulators (EOMs) as well as adjusting the spacing of the input pulses to the time bins of the network. We will consequently focus our description on the extensions in comparison to the previous versions. The basic principle of time multiplexing underlying the setup will be briefly introduced in section 4.1. Since time multiplexing translates positions into time bins, the two terms can be used interchangeably in the following.
Figure 4.1 shows an overview of the setup highlighting the three main sections dedicated to different stages of the experiment: state preparation (red), evolution (blue) and detection (yellow).
In the following, we will take a closer look at these sections. Here, we will present the setup in a level of detail we deem necessary for its reproduction, even if certain readers might feel that it compromises the elegance of presentation.

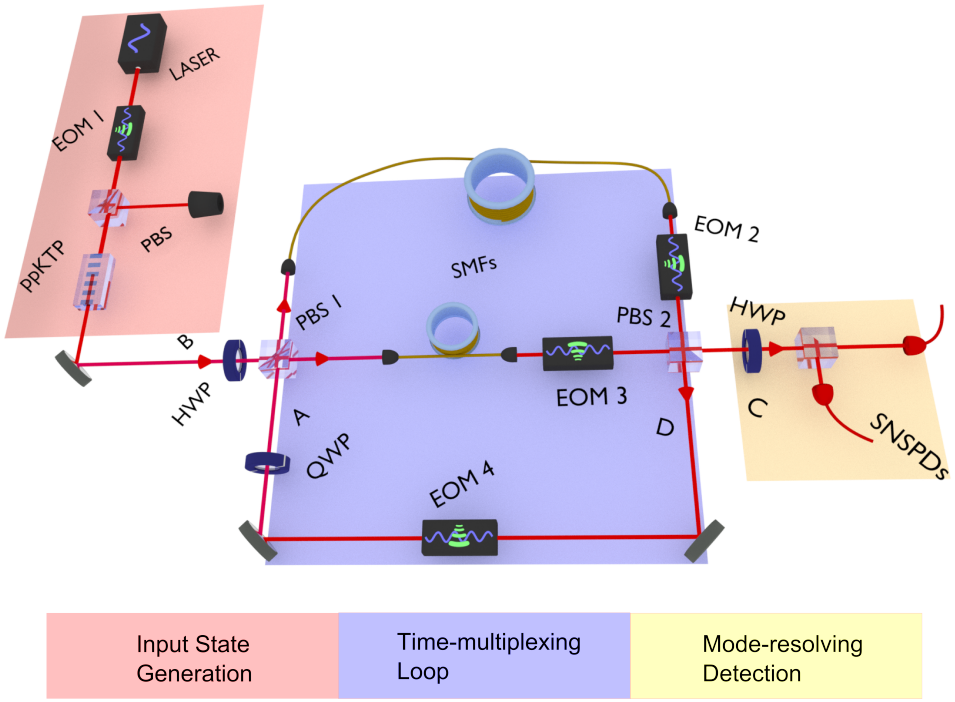

Figure 4.1: Sketch of the setup implemented for quantum walks with single photons. The state preparation section is highlighted in red, the evolution section in blue and the detection section in yellow.

4.1 Time Multiplexing

The basic principle of time multiplexing remains unchanged from what has been reported in previous works. It is illustrated in Figure 4.2: A polarising beam splitter (PBS 1) carries out a polarisation-dependent splitting, directing the light either to a long fibre (introducing the delay τ_H) or a short fibre (introducing the delay τ_V), introducing a relative time-delay between the two pulses $\Delta\tau_{\text{pos}} = \tau_H - \tau_V$ of 104.704 ns, called position spacing.
The two paths are merged again at a beam splitter (BS), so that now the outcome of the split-operation at PBS 1 can only be inferred from the time-signature of the pulses. At BS part of the light is directed to the detection and part routed to the feed-back loop, where it is sent back to PBS 1. Details on how the light is directed at the beam splitter BS can be found in section 4.3.
A coin operation can be carried out in the feedback arm, allowing for the cascaded application of coin and split operation according to (3.12). Note that the coin operation can either be conducted by a dynamic Pockels cell (EOM 4 in Figure 4.1) or static half- resp. quarter-wave plates (HWP/QWP).

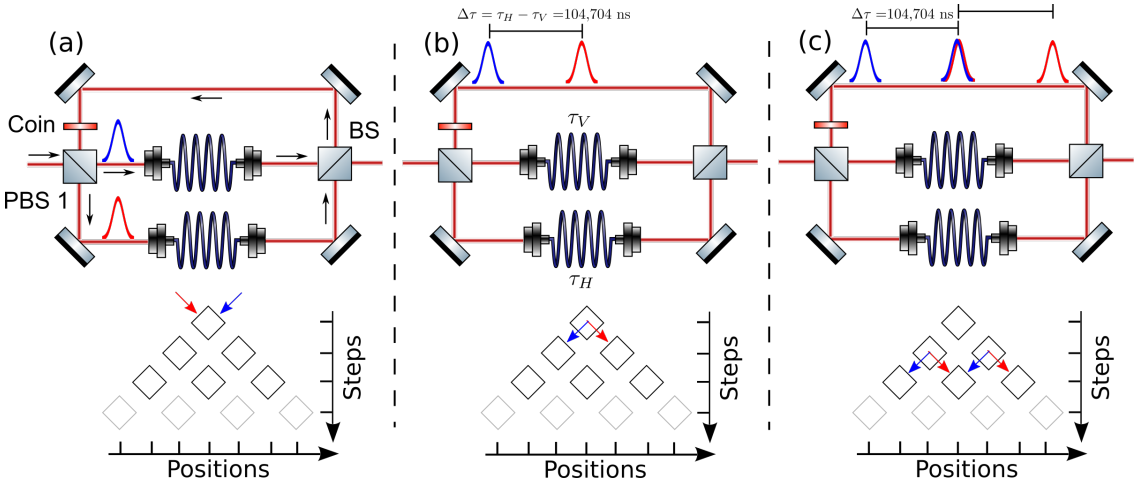

Figure 4.2: Illustration of how time-multiplexing is implemented in our setup. (a): Incident light undergoes a polarisation-dependent splitting at PBS 1. Horizontal components are represented by red pulses, vertical light by blue pulses. (b): In the two arms the pulses are delayed by τ_H resp. τ_V, introducing a delay between them of the position spacing $\Delta\tau_{\text{pos}} = \tau_H - \tau_V$ =104.704 ns. The two paths are merged again at a beam splitter BS, mapping the outcome of the initial split operation into the time-domain. The pulses are fed back to PBS 1. Before they are split again here, they can undergo a coin operation. (c): By repeating the splitting and delaying in time, we achieve the cascaded application of coin and step operation. As a result, the walker's wavefunction spreads with increasing step number over an increasing number of positions. This spreads lends itself to the pyramidal representation which is found below the sketches of the setup and will be used throughout this work.

Figure 4.3, (a) shows exemplarily the number of measured events per time bin for a time-multiplexed quantum walk in which a fixed proportion of the light is detected for each step. The blue shaded regions corresponds to the time bins where part of the walker's intensity is expected to arrive. We are looking at steps 3 and 4 in which the wave function is spreading out over 4 resp. 5 bins or positions. The red (black) bars mark the counts for horizontal (vertical) polarisation. From the number of counts in a certain time bin we can infer the relative probability with which the walker is found at a certain position within a certain step when normalising the number of counts in this step to one. We can represent the step-wise evolution of the probability distribution in a chessboard diagram as shown exemplarily in Figure 4.3, (b). Here, the x-axis corresponds to the position index and the y-axis to the step index with the relative probability being encoded in the colour. The representation in Figure 4.3, (a) is analogues to the intensity distribution shown in Figure 3.3, (d), while the evolution shown in Figure 4.3, (b) resembles the step-wise propagation along a pyramidal arrangement depicted in Figure 3.3, (c).

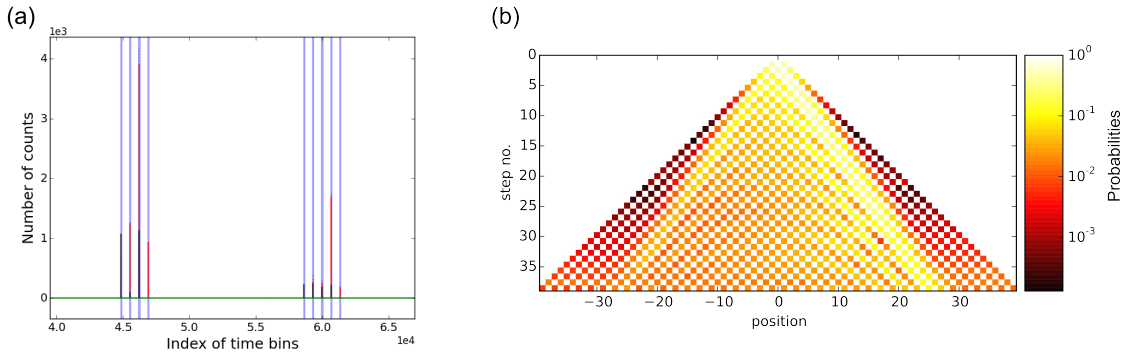

Figure 4.3: (a): Exemplary plot of the number of counts per time bin for step 3 and 4. The blue shaded regions correspond to the time bins where the walker is expected to arrive, the red (black) bars to the actual number of counts in horizontal resp. vertical polarisation. (b): Representation of the probability distribution in a chessboard diagram. The x-axis corresponds to the position within a step and the y-axis to the step index, while the relative probability is colour coded. Note that the two plots do not refer to experiments with the same settings.

4.2 State Preparation

In order to conduct a quantum walk with quantum particles (in this case photons) in multiple input modes, we have to prepare a time-multiplexed input state with PDC photons in at least two time bins. In our case, the PDC state is generated by pumping a crystal of periodically-poled Potassium Titanyl Phosphate (ppKTP). We will devote a whole chapter (chapter 5) to the question of how the purity and indistinguishability of these photons can be optimised, so that here we focus on the technical aspects of the state preparation.

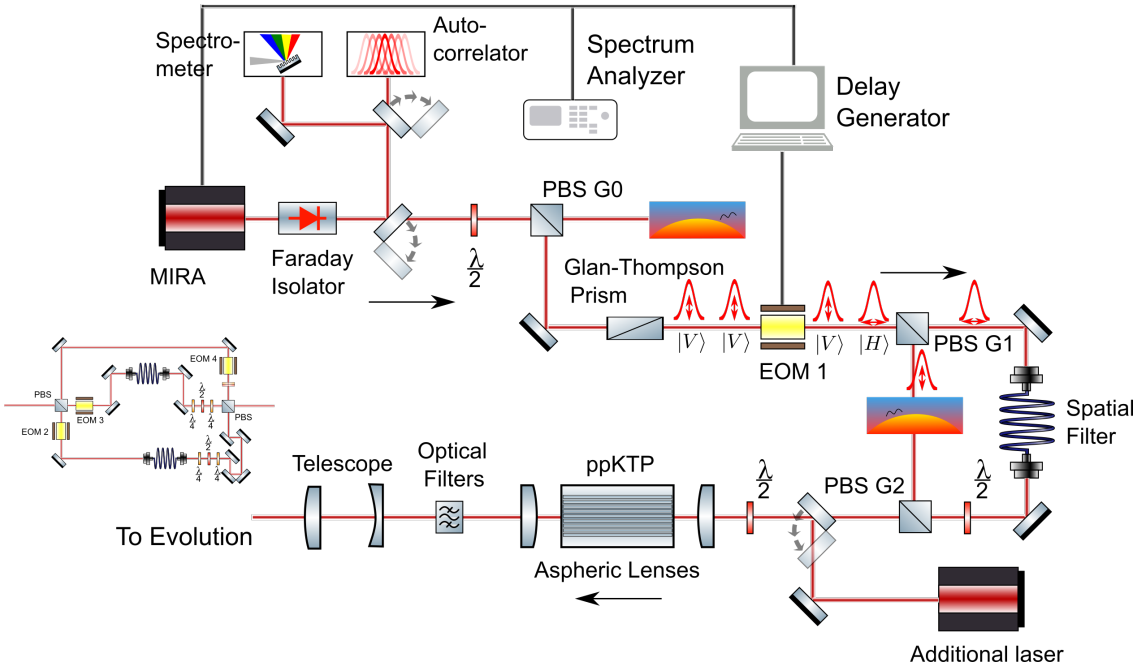

Figure 4.4: Schematic of the section of the setup dedicated to the preparation of the the initial states. Note that this sketch does not show the actual beam path as several mirrors have been omitted to achieve a clearer presentation. The EOM's operation, rotating $|V\rangle$ to $|H\rangle$, and the subsequent routing of the pulses at PBS G1 is crucial for the preparation of the time-multiplexed input state.

Figure 4.4 shows a schematic of the section of our setup that is implemented to generate appropriate initial states. In the following subsections we will explain its functioning in detail.

4.2.1 Time-multiplexed Pump

The pump laser is a Coherent MIRA 900D [135] operated in picosecond (ps) mode such that it outputs pulses with an autocorrelation length of $\tau_{\text{ac}} \approx 2.2$ ps. Since this value is affected by the setting of the Gires-Tournois interferometer (GTI) used to adjust chromatic dispersion inside the laser cavity, we check on a regular basis with an autocorrelator that it is approximately τ_{ac} and adjust it if necessary. A mirror on a magnetic mount (indicated as flip mirror in Figure 4.4) is harnessed to direct the light either to an autocorrelator resp. a spectrometer or to allow the light to proceed further into the setup. Furthermore, a Faraday isolator is placed behind the laser to prevent light from being reflected back into the laser cavity and thus disturbing its operation.
The repetition rate f_{rep} has a value of 76.402 MHz, which depends on the exact configuration of the cavity and especially changes when re-adapting the system from the femtosecond (fs) to the ps mode. This operation requires changing one of cavity's end

mirrors which significantly affects the cavity length and thus the repetition rate. As the synchronisation of source and fibre loop relies on f_{rep} to be accurate up to ≈ 1 kHz (see section 5.2), this quantity has to be checked with a spectrum analyser after each reconfiguration of the cavity. Note that such a reconfiguration is only necessary when the laser is used for other experiments requiring fs-pulses.
f_{rep} corresponds to a spacing of the laser pulses of τ_{rep} =13.088 ns. However, when synchronizing the spacing of laser pulses and the spacing of positions in the time-multiplexing setup, technical limitations on the pulse spacing arise in the evolution and in the detection stage: During the evolution a position-dependent coin requires different switching states of the electro-optical modulator (EOM, see section 4.3) in use for two neighbouring positions. Consequently, the technically feasible minimum spacing of EOM switchings imposes a lower bound of 50 ns on the spacing of two time-bins of the input state. Furthermore, being able to detect coincidences between two neighbouring positions requires the position spacing to be greater than the detector dead time for which we determined a upper bound of 100 ns. In order to reduce f_{rep} and therefore increase τ_{rep}, we again make use of an EOM (EOM 1 in Figure 4.4) with which we are able to pick every n-th pulse by rotating its polarisation from $|V\rangle$ to $|H\rangle$ such it is transmitted at the first polarising beam splitter (PBS G1), while the unpicked pulses are reflected here and directed to a beam dump. Picking every 8-th pulses results in a temporal spacing $\tau_{\text{pulse}} = 8 \cdot \tau_{\text{rep}}$ of 104.704 ns. This value consequently sets the temporal position spacing τ_{pos} as well. Section 4.3 will give a more detailed account on how the exact synchronisation of τ_{pulse} and τ_{pos} is achieved.
The quality of the picking operation depends on the extinction ratio between picked and unpicked time-bins. A good value here requires rotating the incident light's polarisation from $|V\rangle$ to $|H\rangle$ with the highest precision possible when a voltage is applied to the EOM and on the other hand preserving $|V\rangle$-polarisation precisely when applying no voltage. In order to achieve this, we place a Glan-Thompson prism acting as a polarisation filter in front of EOM 1. We then remove the Pockels cell inside EOM and check that we see good extinction at PBS G1. Having put the cell back in, the extinction is optimised again by adjusting its orientation.
By placing half-wave plates (HWP) in front of PBS 0, we can control which proportion of the initial power is directed into the setup at PBS G0 and which part continues along its previous path to go to other experiments. A second power-control-unit is implemented by placing a HWP in front of PBS G2, so that we can now control what percentage of the light inside the setup is actually used to pump the ppKTP crystal.

4.2.2 PDC Crystal

The ppKTP crystals harnessed to generate the PDC state exhibit waveguides with a width of 2,3 and 4 μm to increase the effective length and thus the brightness of the source. Another very important feature of the waveguided PDC process is that it allows to engineer its spectral properties (see section 5.4).
The waveguides are designed to be spatially mono-mode around 1550 nm, consequently the

quality of the incoupling of the pump into the waveguide should not affect any properties of the PDC process apart from output power. In practice, however, the incoupling might determine the degree to which we excite additional processes. In order to minimise spatial variations in the mode coupled into the waveguide, we thus send the pump light through a 10 cm long polarisation maintaining fibre and then couple the output from this fibre into the waveguide. By doing so, we translate variations in the spatial mode coming from the laser into variations of the power coupled into the chip. These changes in power can be easily monitored and do not influence the input states for the time-multiplexing setup in more hidden ways. We employ aspheric lenses with a focal length of 4.5 mm to couple light into and out of the waveguide. As the PDC process is polarisation-dependent, a HWP in front of the source is used to adjust the polarisation to maximal brightness.
After the PDC state has been generated in the ppKTP crystal (a detailed account on its properties is found in chapter 5), it has to be separated from the pump field. To do so, we use an AR-coated slab of silicon which exhibits a transmission of >97 % around 1550 nm and a Semrock FF01-1538/82-25 filter with a transmission of >96 % from 1550 nm to 1555 nm (summarised under "optical filters" in the sketch). In addition, dense wavelength division multiplexing (DWDM) filters centered around the wavelength of the PDC photons and exhibiting a full transmission range of 0.9 nm are inserted into the fibres leading to the detectors (see section 5.4.3 for the effect of these filters). When using a different waveguide or ppKTP crystal, another DWDM filter centred around the respective wavelength has to be chosen.
Again, a fully or partially-reflecting mirror on a magnetic mount can be inserted into the beam path in front of the sample in order to couple a different (e.g. alignment laser) or an additional laser (e.g. laser for seeding, see section 8.5) into the ppKTP crystal. Here as well, polarisation-filtering might be necessary. However, the corresponding components are omitted in the sketch as the principle is the same as described previously and the exact arrangement depends on the laser resp. the required accuracy of the polarisation.
Eventually, we employ a telescope consisting of a plano-concave and a plano-convex lens to maximise the overlap of the output field of the waveguide with the spatial mode of the fibres used to implement the time-multiplexing feedback loop. By doing so, waveguide-to-fibre coupling efficiencies of up to 75 % are achieved.

4.3 Evolution

The basic principle of the time-multiplexing feed-back loop remains unchanged from what has been reported in previous works (see section 4.1).
Two substantial modifications have been for the current implementation (see Figure 4.5) in regard to previous ones: To start with, the setup is now designed to operate at a wavelength around 1550 nm, while the previous implementation were constructed for a wavelength around 800 nm. The latter wavelength has the advantage of being compatible with the detection by silicon avalanche photodiodes (APDs), which is why it was originally

built this way. Furthermore, we require a lower voltages at this wavelength to introduce a certain phase retardation with the EOM, which is why it is used for the measurements of topological phenomena, which involve a relative phase retardation between two polarisation components in excess of $\pi/2$.

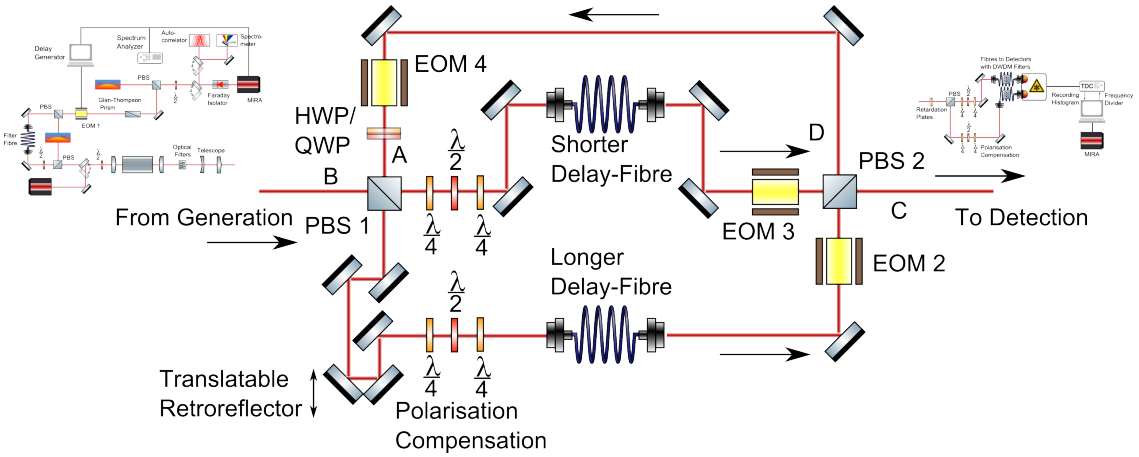

Figure 4.5: Sketch of the setup's section where the time-multiplexed evolution is conducted. It is precedent by the generation section and succeeded by the detection section, as it is indicated by the miniaturised versions of the corresponding sketches.

On the other hand, fibres (SMF 28) optimised for the telecom wavelength of 1550 nm introduce only losses of <0.18 dB/km, while fibres designed for a wavelength around 800 nm exhibit losses of ≈ 3 dB/km , which is prohibitively high for experiments with quantum input states. As a consequence, a setup operating with PDC input states has to be designed for a wavelength with very low losses, ideally the telecom wavelength where losses are minimal. Apart from attenuation in the fibres, on a roundtrip through the setup the light passes two PBS each introducing losses around 3 % and is subjected to losses of ≈ 10 % at the fibre incouplings. All in all, the roundtrip efficiency η_{RT} is between 80 % and 85 % depending on the exact combination of fibres.
The second crucial modification is the implementation of active in- and outcoupling which is carried out with two additional EOMs (EOM 2 and EOM 3 in Figure 4.5) in combination with PBS 2. With these EOMs we can deliberately switch the polarisation of the light in front of PBS 2 such that it is either transmitted or reflected. This operation decides whether the photons end up in port C or port D of PBS 2, directing them either into the feedback loop or to the detection unit. This active routing of the light allows us to get rid of the probabilistic in- and outcouplers that were used previously. With these we could otherwise only couple a small proportion of the light in and out of the setup or would have to tolerate high losses in each roundtrip. Without the active directing, losses would consequently be prohibitively high for the operation with PDC states.
Since the polarisation determines how light is directed at PBS 2, the polarisation rotation

due to birefrigence to which light travelling through the fibres is subjected might become problematic: Light that is supposed to stay in the feedback loop might be directed to the detection unit and vice versa. We use a polarisation compensation unit consisting of two quarter-wave plates (QWP) and a half-wave plate (HWP) in front of each fibre to minimise the intensity in the wrong port of PBS 2. This compensation unit allows for implementing an arbitrary SU(2) polarisation transformation [136]. However, the fibre's birefringence is susceptible to temperature changes, so that these might induce additional and uncontrolled losses.

4.3.1 Dynamic Switchings - Electronics

Further details on the operation of the delay generators and EOMs can be found in [22]. At this point it is important to know that the EOMs are fast enough to apply either no voltage $U = 0$ or a voltage of $\pm U$ for each of the time bins independent of the voltages applied to the neighbouring bins. As a result, they allow for the implementation of position- or time-bin-dependent operations acting on the polarisation. The focus of the following elaborations is on the extensions in regard to the preceding work, especially concerning the synchronisation of multiple delay generators and EOMs.
In addition to the pulse picking conducted by EOM 1 and the in- and outcoupling carried out by EOMs 2 and 3, EOM 4 is able to switch different coins for different positions. As all of these operations have to be carried out on the same pulses along their propagation through the setup, exact synchronisation of all four EOMs is crucial.

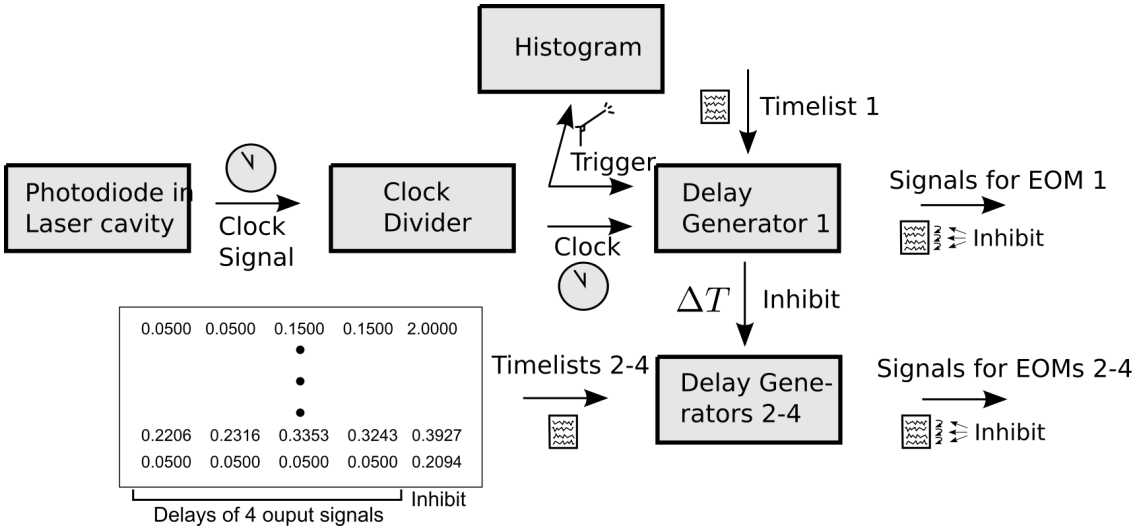

Figure 4.6: Illustration of the scheme implemented to synchronise laser pulses, the switchings of four EOMs and the histogram of photon arrival times. The structure of the time lists is illustrated in the lower left corner: They consist of lines in which the first four entries provide the delays of the individual switches, while the fifth entry gives the inhibit time determining when the delay generator starts processing a new line.

Figure 4.6 illustrates the scheme used for this purpose: It starts with a master clock signal provided by a photodiode in the cavity of the pump laser. This detector converts the optical output of the laser into an electrical signal that exhibits the same repetition rate f_{rep} as the laser pulses. The shape of the signal are individual peaks spaced by $1/f_{\mathrm{rep}}$. The frequency of the signal is divided from f_{rep} =76.4 MHz down to f_{exp} which assumes values (depending on exact experiment) in the range of several 10 kHZ to several 100 kHZ. This operation is actually carried out by two separate devices, since one of them does not accept the initial repetition rate, while the other does not provide the necessary constant offset between the pulses repeated with f_{rep} and those repeated with f_{exp}. We will see later why this criterium has to be fulfilled. As these two devices do not operate in a fundamentally different way, we represent them by one symbol for the clock divider in Figure 4.6.
The next step is conducted by delay generators which output the switching signals for the EOMs at exactly specified times. Each of the EOMs is timed by an individual delay generator, so that they are controlled by an ensemble of four delay generators that are connected by a common bus.
The switching times are fed to the delay generators via a timelists. One run through this list is triggered by the signal f_{exp}, which is thus called trigger. In addition, this signal also provides the start trigger for the recording of histograms of photon arrival times. The signal at f_{rep}, on the other hand, provides the clock for the delay generator and is thus dubbed clock signal.

Having a constant offset between the clock and the trigger signal is indispensable for having also a constant relative timing between laser pulses and EOM switchings. It can be explained by the fact that the timings of the laser pulses are translated into the electrical pulses of the clock signal, while the trigger times the EOM switchings. This requirement rules out using a clock generated by an additional function generator, as the offset of pulses in the two signals would not be constant in this case. An external clock is consequently only suitable for testing the generation of the electrical signals, in which case they do not have to synchronised with optical pulses generated by the pump laser. Another constraint regarding an external clock arises from the fact that the delay generators cannot reliably generate the electronic signals for clock frequencies exceeding 77 MHz. The problem is this case are errors such as missing electronic pulses in the output switching patterns that occur rather rarely and might thus be hard to spot when checking the patterns with an oscilloscope.
Details on how the time lists fed into the delay generators are processed, including common pitfalls and how to avoid them, can be found in appendix C.

4.3.2 Dynamic Switchings - Pockels Cells

The dynamic, i.e. position-dependent, operations on the walker's polarisation are conducted by applying a voltage of several kV to a Pockels cell made of Rubidium Titanyl Phosphate (RTP). Since a detailed account on its operation can be found in other works [22], we focus on new observations here.
The Pockels cells rotate the walker's polarisation according to (3.15) with the actual angle θ depending on the applied voltage. In this way, we are able to implement dynamic operations such as identity ($\theta = 0°$), a fair-splitting, Hadamard-like coin ($\theta = 45°$) or reflection ($\theta = 90°$).
The value U of the voltage applied to the Pockels cell is set manually at the power supply and is consequently fixed for a certain experimental run. The freedom for the coin operation consists in whether $+U$, $-U$ or no voltage at all is applied at a certain position. Consequently, one out of three possible switching states is expected to be assigned to each position during the walker's evolution.

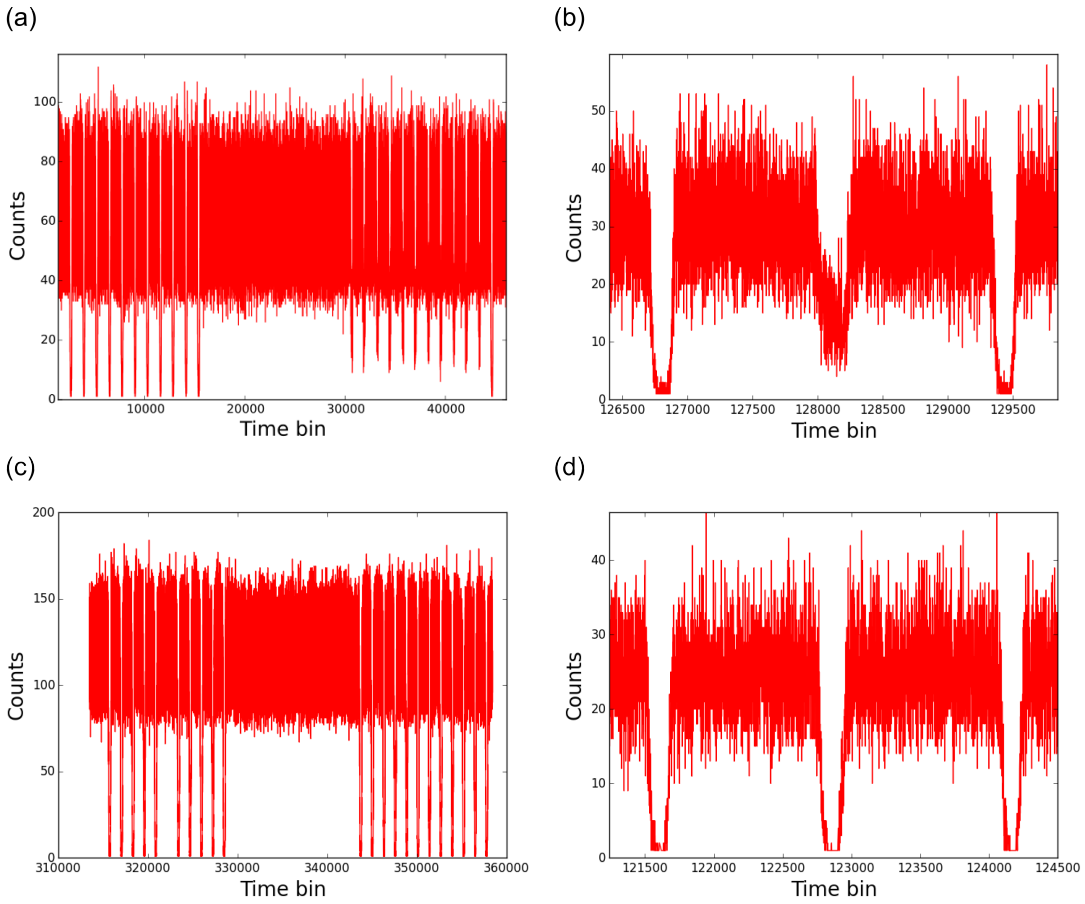

Figure 4.7: (a): Time-resolved counts for two sequences of switchings with spacings of around 100 ns (position separation) within one sequence and a spacing of around 2.2 µs (step separation) between the two sequences We clearly observe a degradation of the extinction from the first sequence to the second. (b): Time-resolved counts for three switching spaced by around 100 ns. In this case we even see a significant difference in extinction on the time-scale of the position separation. (c) and (d): Time-bin resolved counts for the same two sequences (except for one single switching in (c)) after refurbishing the Pockels cells to achieve better damping of Piezo-acoustic resonances.

In order to check whether a certain operation, in this case the reflection, is implemented reproducibly for all positions, we send a cw-laser into the setup and record the clicks in one of the ports of the PBS placed behind EOM 2 and EOM 3 (see Figure 4.5).
It turns out that we cannot expect the same behaviour for each individual switching. Figures 4.7, (a) and (b) illustrate this problem: For the times when a high voltage is applied to the crystals, the polarisation of the light should be rotated such that the number of counts drops to zero for perfect EOM operation and PBS extinction. In the shown measurements we observe extinctions of around 90%, which is not ideal, but not the main

problem at this point. More severe is the fact that the extinction is varying significantly between steps (Figure 4.7, (a)) or even between positions within a step (Figure 4.7, (b)). We verify with an oscilloscope that the electronic signals as well as the applied voltages are the same for all of the observed positions. Consequently, the cause of this behaviour has to be sought elsewhere.
Indeed, correspondence with the manufacturer reveals that the RTP Pockels cells exhibit Piezo-acoustic resonances to signals with frequencies of several 100 kHz. Since these resonances affect the spontaneous polarisation of the RTP crystal and thus its effect on the polarisation, it can be expected that this is the cause of the observed additional modulation of the extinction. A first test of the plausibility of this assumption is replacing one of the crystals, which have an aperture of 4 mm, by one with an aperture of 3 mm, as changing the dimensions of the crystal is also modifying its acoustic resonance frequencies. It turns out that the crystal with the smaller aperture does not exhibit the particularly problematic resonance resulting in the poor extinction seen in Figure 4.7, (b). Consequently, the Pockels cells were shipped back to the manufacturer and refurbished in order to allow for better damping of undesired resonances. As a result, we observe afterwards a much more homogeneous switching operation with negligible variations of the extinction (see Figures 4.7, (c) and (d).
Another effect we observe is that a switching sequence can result in a polarisation rotation for several seconds even after it has been switched off. We dub this phenomenon memory-effect as it links the effect of Pockels cell to voltages that have been applied previously. The extend of this effect depends on the duty cycle of the switching pattern as well as on the value of the voltage. By redesigning the switching patterns such that they exhibit a lower duty cycle, we can avoid the occurrence of this polarisation rotations with relaxation times of several seconds. Consequently, we did not carry out a closer examination of this phenomenon. It is, however, important to keep it in mind when applying switching patterns with high duty cycles and/or voltages.

4.4 Detection

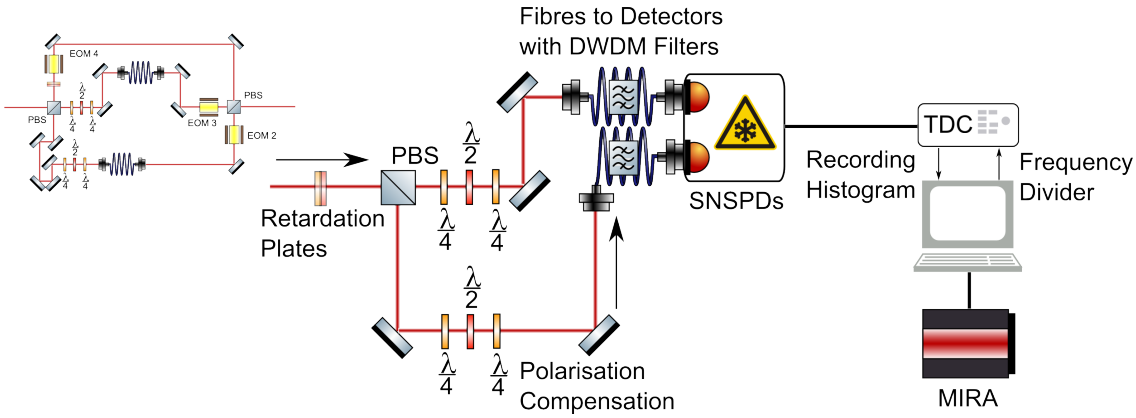

Figure 4.8: Schematic of the polarisation-resolved detection unit incorporating two fibre-coupled superconducting nanowire single-photon detectors (SNSPDs). This section of the setup is preceded by the evolution section as indicated by the miniaturised sketch.

The detection unit (see Figure 4.8) incorporates a PBS whose two ports lead to fibre-coupled superconducting nanowire single-photon detectors (SNSPDs), allowing for polarisation-resolved detection. Furthermore, we determined the dead time of the detectors to be below the position spacing in the walker's evolution of 100 ns, thus enabling the reliable read-out of the walker's distribution over the time-multiplexed positions.
The working principle of SNSPDs is based on a superconducting meandering wire to which a certain bias voltage is applied. Photons impinging on the wire lead to the breakdown of superconductance which results in a measurable voltage spike. Afterwards, the detectors are quenched to restore the superconducting state. The time required for this process is responsible for the dead time, while the bias voltage determines the detection efficiency, but also the amount of dark counts. In case detections events become so frequent that quenching no longer works sufficiently, the detectors latch and cannot be used until they are reset.
We characterise the detection efficiency to be between 90% and 97.5% depending on the exact detector. These values, however, only constitute an estimation since an accurate calibration measurement is out of the scope of what can be done without specialised equipment. In the following, we consequently assume an efficiency of 90%. Note that this number depends on the polarisation of the light impinging on the detectors, so that we use polarisation controllers consisting of a series of three fibre coils to optimise the detection efficiency.
At a bias voltage that allows for the aforementioned detection efficiency the dark count rate is between 500 and 1000 per second. This sounds like a high number at first, but we know at which times we expect the arrival of photons and thus only consider the corresponding time bins. Usually we choose time bins with a width of 6 ns which results

in around 10^{-5} dark counts per second for one time bin. Furthermore, we except the dark counts to be uncorrelated so that when detecting n-fold coincidences the probability that a coincidence is caused by dark counts scales with the dark count rate to the power of n.

4.4.1 Possible Measurement Times

Indeed, the main challenge concerning minimum required count rates is not caused by dark counts, but from the overall time needed to collect sufficient statistics for a certain count rate. Constrains on the measurement time mainly arise from drifts of the setup's characteristics. Temperature is the most significant cause of such drifts. Section 5.2 treats the effects of temperature on the temporal delay. Furthermore, the temperature also affects the polarisation rotation introduced by the fibres, possibly introducing a significant amount of additional loss. This loss does not necessarily have to be balanced, since the polarisation rotation in the two fibres does not have to show exactly the same temperature dependence. As a consequence unbalanced losses cannot only decrease count rates, but also HOM-dip visibilities (see sections 5.8 and 8.5.4). The problem can be countered by either an active polarisation control or in a passive way, i.e. conducting the experiment in a way that temperature changes are limited. Apart from building a temperature stabilisation for the fibre spools (see section 5.2.2), this means that measurements are confined to times with minimal temperature changes such as during the night and especially times when no people are in the lab. Thus, mitigating polarisation rotations is one of the factors limiting measurement times, others are dealt with in section 5.2.
We also have to bear in mind that the adsorption fridge cooling the detectors has to regenerate after a time of approximately 30 hours. However, this does not constitute a hard limit on the measurement times, since measurement runs can be continued after a regeneration cycle.

4.4.2 Achievable Rates

Since arbitrarily long measurements are neither feasible nor desirable, the rates of valid events should be as high as possible. Experiments with quantum states rely on the detection of n-photon coincidence events whose rates scale with the detection probabilities to the power of n. Consequently, achieving the highest possible detection efficiencies is crucial for the success of such experiments.
The collection efficiency of photons can be determined as ratio of coincidence to singles events, which is then called the Klyshko-efficiency η. In addition, the mean photon number $\bar{n}$ of the probabilistic PDC process and the rate f_{exp} with which new experimental runs are started influence the rate f_n of n-fold coincidences. In case the photons are subjected to m roundtrips through the setup with efficiencies η_{RT} before detection and/or are split

up to n_{bin} time bins, these quantities have to be accounted for as well:

$$f_n = f_{\mathrm{exp}} \cdot \bar{n}^n \cdot \eta^{2 \cdot n} \cdot \eta_{\mathrm{RT}}^{n \cdot m} \cdot \frac{1}{n_{\mathrm{bin}}} \tag{4.1}$$

Note that the above equation is valid for heralded n-fold coincidences, for which the herald is directed immediately to the detection unit, while the n signal photons undergo an m-step evolution. Consequently the Klyshko-efficiency η affects both signal and idler and is thus accounted for with a factor of 2 in the exponent. On the other hand, the roundtrip efficiency η_{RT} only affects the signal.
In our experimental setup, we measure Klyshko-efficiencies η between 20% and 30% depending on alignment and detectors used. This value incorporates the detector efficiencies η_{Detect} which we assume to be 90%, the transmission η_{Fibres} of the fibres leading to the detectors, including DWDM-filters and polarisation controllers, of 77% (87% transmission of filters multiplied with 89% transmission of the rest), the incoupling efficiency $\eta_{\mathrm{Detect-coupl}}$ into those fibres of 75% (including two PBSs on the path), the coupling efficiency $\eta_{\mathrm{Source-loop}}$ from the source into the loop fibres of 75%, the transmission η_{Filter} through the pump filters behind the ppKTP chip of 93% as well as the losses L_{chip} in the chip, which we estimate with a transmission measurement to be around 50%. All of the mentioned contributions add up multiplicatively, so that the overall Klyshko-efficiency η is given by the following formula:

$$\eta = \eta_{\mathrm{Detect}} \cdot \eta_{\mathrm{Fibres}} \cdot \eta_{\mathrm{Detect-coupl}} \cdot \eta_{\mathrm{Source-loop}} \cdot \eta_{\mathrm{Filter}} \cdot (1 - L_{\mathrm{chip}}/2) \tag{4.2}$$

With the given numbers we estimate η to be around 27%, which is in reasonably good agreement with measured values of around $25 - 30\%$, telling us that the assumed numbers are plausible and that there is no unknown major source of losses in our setup. Note, however, that Klyshko-efficiencies of around $25 - 30\%$ are only achieved if alignment and especially polarisation compensation for the loop fibres are optimal and have not been degraded due to temperature changes.
Knowing the Klyshko-efficiencies η and roundtrip efficiencies η_{RT}, we can estimate the measurement times needed to accumulate sufficient statistics for certain combinations of mean photon number $\bar{n}$, number n of photons to be detected and number of roundtrips m after which the photons are to be detected. Tables 4.1 and 4.2 give estimated necessary measurement times depending on mean photon number $\bar{n}$ and roundtrip number m for Klyshko efficiencies η of 20%, a repetition rate f_{exp} of 40 kHz, roundtrip efficiencies η_{RT} of 80% and desired number of 20 photons per bin. The number are determined for count rates f_n according to (4.1), thus assuming that the photons are distributed equally over $n_{\mathrm{bin}} = m + 1$ bins. This is usually not the case, but the attained numbers still serve as a reasonable estimate of measurement times, since the relative intensity per bin enters the equation as a linear term.

m	5	6	7	8	9	10	11
$\bar{n}$							
0.02	12.13	22.11	39.47	69.39	120.47	207.5	352.93
0.04	3.03	5.53	9.87	17.35	30.12	51.76	88.23
0.06	1.35	2.46	4.39	7.71	13.39	23.01	39.21
0.08	0.76	1.38	2.47	4.34	7.53	12.94	22.06
0.10	0.49	0.88	1.58	2.78	4.82	8.28	14.12
0.12	0.34	0.61	1.10	1.93	3.35	5.75	9.80
0.14	0.25	0.45	0.81	1.42	2.46	4.23	7.20
0.16	0.19	0.35	0.62	1.08	1.88	3.24	5.51
0.18	0.15	0.27	0.49	0.86	1.49	2.56	4.36

Table 4.1: Estimated Measurement times in hours depending on the roundtrip number m and the mean photon number $\bar{n}$ for a two-photon state, Klyshko efficiencies η of 20%, a repetition rate f_{rep} of 40 kHz, roundtrip efficiencies η_{RT} of 80% and desired number of 20 photons per bin.

m	5	6	7	8	9	10	11
$\bar{n}$							
0.02	46,259.29	105,408.54	-	-	-	-	-
0.04	5,782.41	13,176.07	29,410.87	64,623.49	-	-	-
0.06	1,713.31	3,904.02	8,714.33	19,147.70	41,553.17	89,274.38	-
0.08	722.80	1,647.01	3,676.36	8,077.94	17,530.24	37,662.63	80,247.08
0.10	370.07	843.27	1,882.30	4,135.90	8,975.48	19,283.27	41,086.51
0.12	214.16	488.00	1,089.29	2,393.46	5,194.15	11,159.30	23,776.91
0.14	134.87	307.31	685.97	1,507.25	3,270.95	7,027.43	14,973.22
0.16	90.35	205.88	459.54	1,009.74	2,191.28	4,707.83	10,030.89
0.18	63.46	144.59	322.75	709.17	1,539.01	3,306.46	7,045.01

Table 4.2: Estimated Measurement times in hours depending on the roundtrip number m and the mean photon number $\bar{n}$ for a three-photon state, Klyshko efficiencies η of 20%, a repetition rate f_{exp} of 40 kHz, roundtrip efficiencies η_{RT} of 80% and desired number of 20 photons per bin. Note that times clearly in excess of 100,000 h are simply denoted by "-" for readability.

The numerical simulations concerning the influence of the mean photon number on HOM-dip visibilities in section 5.7 show that ideally $\bar{n}$ should be around 10^{-3} as we calculate for value visibilities close to 1. On the other hand, we predict a visibility of around 0.85 for a mean photon number of 0.1. We thus have to find a mean photon number for which there is a good trade-off between HOM-dip visibility and measurement time.
Assuming a value around $\bar{n} = 0.1$ as a good compromise, we find that two-photon exper-

iments should exhibit reasonable measurement times for up to 10 steps (see table 4.1). Three-photon experiments (see table 4.2), however, seem to require prohibitively long measurement times unless conducted with high mean photon numbers. The problem here is that the count rates according to (4.1) incorporate the photon number n as an exponent for $\bar{n}$, η and η_{RT}. Achieving reasonable measurement times for a five-step experiment would require a Klyshko efficiency of 30% for $\bar{n} = 0.1$ and 40% for $\bar{n} = 0.05$. Since we measure satisfactory visibilities for mean photon numbers around 0.1 (see sections 5.9 and 5.10) and the experimentally observed Klyshko efficiencies can get close to 30%, conducting three-photon experiments with small step numbers is a realistic perspective.
In the above calculations, we assume a repetition rate f_{exp} of 40 kHz which corresponds to starting a new experiment every 25 μs. This time allows for roughly 10 roundtrips with a duration of 2.3 μs. In principle, the repetition could be increased by interlacing multiple experimental runs. In practice, however, the duty cycle of the EOM can possibly reach a value where the quality of the switchings suffers from a memory effect (see section 4.3.1). On the other hand, interlacing can only increase count rates by a linear factor, which means that the advantages for experiments involving more than two photons are limited. As the implementation of interlacing would need to be preceded by a thorough investigation of possible memory effects, it consequently constitutes an outlook of how to increase repetitions rates, but is beyond the scope of what is done in this thesis.

4.4.3 Comparison with Quantum Dot Source

How do the achievable rates for the PDC source compare with a quantum dot (QD) source? We do an estimation assuming a QD with parameters similar to the ones of a state-of-the-art source [96]: A resonantly excited Purcell-enhanced quantum dot-micropillar systems exhibits loss corrected collection efficiencies n_{QD} of 0.66 with the raw collection efficiency η_{raw} being 0.046 and HOM-dip visibilities V_{HOM} of 0.985 for photons generated quasi-deterministically at 897.5 nm. For this source we estimate count rates according to (4.1) with a mean photon number $\bar{n}$ of 1, i.e. assuming deterministic emission, a collection efficiency η of 0.05 and a loop efficiency η_{RT} of 0.45. The significantly lower loop efficiency of the QD is a consequence of its emission wavelength of 897.5 nm: The fibre losses which can be neglected for the PDC-source at 1540 nm now become relevant: These are specified with up to 5 dB/km, amounting to ≈ 2.5 dB additional loss for the used fibres of 480 m length. We also consider a third hypothetical QD-source at 1550 nm which exhibits a mean photon number $\bar{n}$ of 1, a collection efficiency η of 0.05 and a loop efficiency η_{Loop} remaining at 0.8. For the PDC we assume a mean photon number $\bar{n}$ of 0.05.
The resulting estimated measurement times for 20 events in each time-bin (assuming a homogeneous distribution) are shown in Figure 4.9. The numbers for PDC are in accordance with Table 4.2: Assuming reasonable measurement times of the order of magnitude of 10^1 h, we see that a PDC source should allow for a two-photon experiment with ca. 10 steps, while a three-photon experiment is hardly feasible with the given

parameters.
QD sources around 900 nm are only able to outperform PDC at 1550 nm for up to maximally five steps, as the low loop efficiencies lead to a very unfavourable scaling of count rates with step number. A hypothetical QD source at 1550 nm, on the other hand, profits from a high mean photon number as well as from high loop efficiencies, therefore allowing even for three-photon experiments with reasonable step numbers.
Considering the sources currently available, PDC sources seem in comparison to QD sources to be the better fit to our setup operating around 1550 nm.

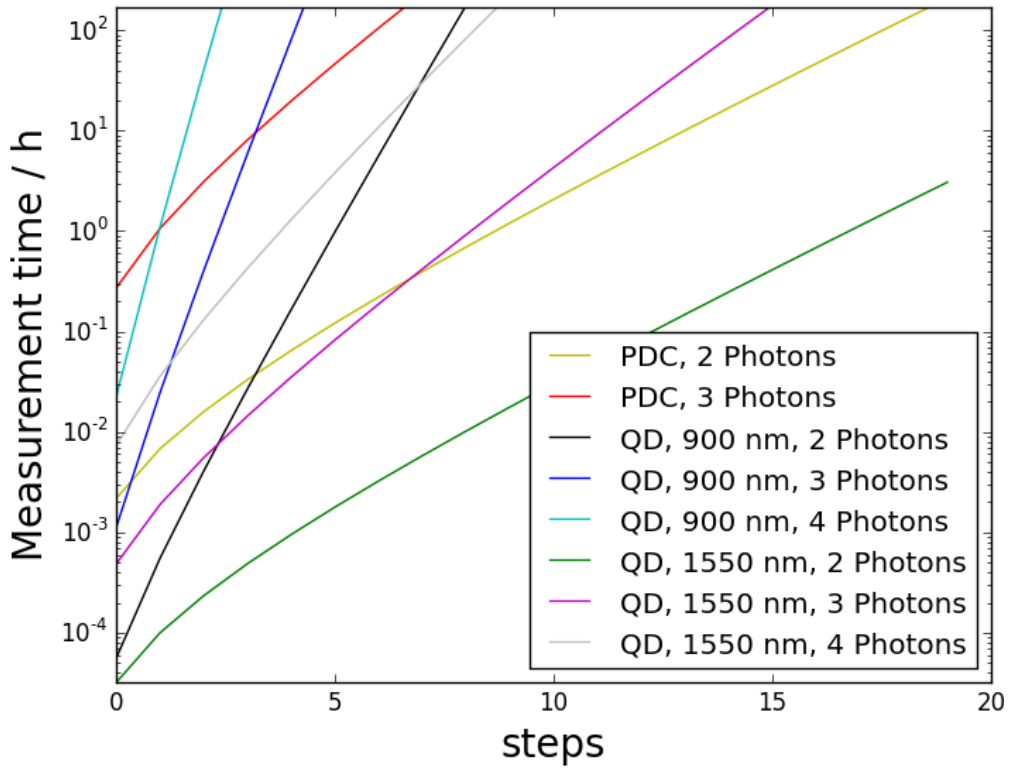

Figure 4.9: Estimated measurement times needed for recording 20 events in each time-bin depending on the step number for different sources and numbers of photons involved in the experiment (see legend).

4.4.4 Photon-number Resolution

The SNSPDs constitute binary "click"- or "bucket"-detectors, i.e. any pulse of light impinging on the detectors is registered either as one or no detection event, regardless of the number of photons in such a pulse. Consequently, the detectors themselves do not allow for photon-number resolution. As we saw in section 3.1, lacking photon-number resolution

reduces the purity of heralded PDC states and therefore also the visibility of HOM-dips between these PDC states.
However, "chopping" [137] up a state and sending it to multiple detection bins allows for obtaining a certain degree of photon-number resolution. This principle can be illustrated by a beam-splitter cascade (see Figure 4.10, (a)). With s being the number of stages of the beam splitter cascade, it will chop the initial state into 2^s bins. The corresponding principle of chopping the initial state can also be implemented via time-multiplexing as illustrated in Figure 4.10, (b).

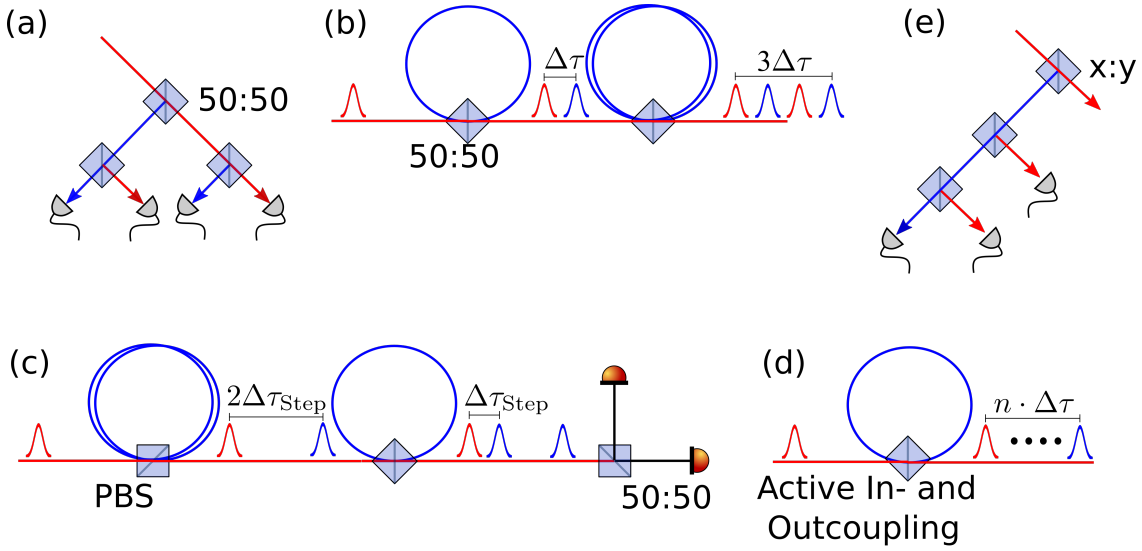

Figure 4.10: Illustrating different scenarios for chopping up an input state to achieve photon-number resolution: The principle is analog to a beam splitter cascade (a). (b) shows the translation of this principle into the time domain. (c): Schematic of the loopy actually built for use together with the quantum walk setup. (d) and (e): The principle of a multiplexing architecture using only one delay line illustrated in the time domain and with a beam splitter cascade.

For our experimental setup we built a fibre-based time-multiplexing unit (loopy) conducting a splitting into 4 time bins. In combination with the two detectors available we thus achieve a split into 8 bins, i.e. 4 time bins and 2 detector bins (Figure 4.10, (c)). Since the quantum walk evolution is also time-multiplexed (see section 4.3), we have to make sure that the time delays introduce by the loopy can be distinguished from those introduced in the evolution section. The active in- and outcoupling allows for analysing only a certain step at a time. Together with the delays of $\Delta\tau_{\mathrm{Step}}$ resp. $2\Delta\tau_{\mathrm{Step}}$ introduced in the loopy, this ensures that the delays introduced by the loopy can be separated from those introduced in evolution section. Furthermore, this design also avoids possible problems arising from dead times which might be problematic when interlacing the two types of delays.

From the fact that the polarisation-resolving detection unit exhibits two detector-bins we can also conclude that the setup provides a certain degree of photon-number resolution even without the loopy: When applying a mixing coin in front of the PBS, we have a 50 % chance that a two-photon contribution leads to a coincidence of the two detectors.
The quantum walk setup itself resembles a loopy and can indeed be used as one. In this context, the loop setup, i.e. either one of the fibres plus the feedback arm, is regarded as a delay line and the operation at PBS 2 decides after each roundtrip whether the light travels through this delay again or is routed to the detection unit (see Figure 4.10, (d)). In contrast to the cascaded architecture shown in Figure 4.10, (b), this design only subjects one of the two outputs of each splitting operation to additional splits (see Figure 4.10, (e)). The active in- and outcoupling can be used in this scenario to increase the dynamic range of the detectors [138].

4.4.5 Conclusion

In the previous sections we have seen how we can prepare a time-multiplexed input state occupying multiple time bins, implement dynamic and position-dependent coin operations resp. losses and resolve both polarisation modes as well as time bins during detection. The combination of approximative single-photon states with position-dependent coin operation and losses presents to our knowledge a novelty has not been realised before.
Exploiting the features of a input state exhibiting single photons in multiple modes for quantum interference requires, however, the purity and indistinguishability of these photons. Consequently, the next chapter will be devoted to the question how these properties can be ensured in our experimental setup.

5 Optimising HOM-Dip Visibility

In order to be able to speak of a fully-fledged quantum system (see section 3.5), we have to show the good approximation of perfectly indistinguishable and pure single particles in multiple input modes.
Ideally, time-multiplexed single-photon interference experiments would be conducted with a source that not only emits exactly one photon at a time, but also ensures that two photons emitted at different times are perfectly indistinguishable. In a real experiment, however, this ideal can only approached in a more or less good approximation. In principle, PDC sources can constitute a good approximation of a source of indistinguishable single photons [95].
In the following, we will discuss to what extent this is achieved in our experiment. Here, we employ the measurable visibility in a HOM-dip experiment as the standard for quantifying to what degree we can approximate two perfectly indistinguishable pure single photons generated at different points in time. This does not only depend on the crystal in which the PDC process takes place, but also on devices such as the pump laser and the time-multiplexing loop.
The discussion is structured as follows: Having already introduced HOM-dip experiments in section 3.3.2, we present in section 5.1 the more specific case of HOM-interference between photons generated at different points in time as implemented for our work.
Subsequently, we discuss experimental imperfections arising from the temporal delay (section 5.2) and the temporal shape (section 5.3) of the photons as well as from the spectral characteristics of the PDC process (section 5.4). Here, we start by relating spectral features to the phase-matching properties of the sample. We then compare the spectral characteristics obtained for Lithium-Niobate (subsection 5.4.1) and KTP (subsection 5.4.2). The two concrete samples investigated for compatibility with our experimental setup are presented in subsections 5.4.3 and 5.4.6.
Section 5.7 refers to issues related to the photon-number statistics of PDC sources, while the numerical framework allowing for quantifying their influence on HOM-dip visibilities is elaborated on in section 5.6 with the results being presented in section 5.7. This framework can also be used for simulating the effect of balanced as well as imbalanced losses as shown in section 5.8.
The observed visibilities as the ultimate measure of indistinguishability and purity in the various degrees of freedom are discussed in sections 5.9 and 5.10.
Eventually, we present a method for characterising the effect of the loop on visibilities, i.e. excluding influences from the source, by sending coherent states into the setup (section 5.11).

In the following we will discuss how the influence of the most relevant parameters can be quantified and controlled. To do so, we will look how the indistinguishability changes when variations occur in only one degree of freedom while the others are held constant. Thus, we will analyse what happens to the visibility according to (3.29) for imperfect overlap of ψ_1 and ψ_2 in a certain subspace.
From (3.28) we see that not only the indistinguishability but also the purity of the states plays a crucial role for HOM-dip visibilities. Consequently, our considerations will also involve the purity of the generated states, focusing on their spectral properties and photon-number statistics after one mode of the PDC state is traced out.

5.1 HOM-Dip Experiment between Different Time Bins

Usually, a HOM-dip experiment, as introduced in section 3.3.2, is thought of and illustrated as the interference of modes in the spatial domain. However, it can be implemented in arbitrary degrees of freedom as long as a beam splitter operation and mode-resolved detection can be implemented for them, e.g. in the frequency domain [139].
Refering to (3.24) and (3.25), the two input mode a and b can be replaced by horizontally resp. vertically polarised input modes h_i and v_i and the two output mode c and d by the horizontally resp. vertically polarised output modes h_o and v_o. The effect of a HWP at 45°, i.e. a so-called Hadamard-coin conducting a fair splitting, on the polarisation can then be written analogous to (3.24):

$$\begin{aligned} \hat{B}_{\mathrm{H/V}}: \quad & \hat{h}_o^\dagger = \frac{1}{\sqrt{2}}\left(\hat{h}_i^\dagger + \hat{v}_i^\dagger\right) \qquad \hat{v}_o^\dagger = \frac{1}{\sqrt{2}}\left(\hat{h}_i^\dagger - \hat{v}_i^\dagger\right) \\ \Leftrightarrow \quad & \hat{h}_i^\dagger = \frac{1}{\sqrt{2}}\left(\hat{h}_o^\dagger + \hat{v}_o^\dagger\right) \qquad \hat{v}_i^\dagger = \frac{1}{\sqrt{2}}\left(\hat{h}_o^\dagger - \hat{v}_o^\dagger\right) \end{aligned} \tag{5.1}$$

Consequently, (3.25) can be rephrased in terms of polarisation modes as well:

$$\hat{h}_i^\dagger \hat{v}_i^\dagger \left|0,0\right\rangle = \frac{1}{2}\left(\hat{h}_o^\dagger \hat{h}_o^\dagger + \hat{v}_o^\dagger \hat{h}_o^\dagger - \hat{h}_o^\dagger \hat{v}_o^\dagger - \hat{v}_o^\dagger \hat{v}_o^\dagger\right)\left|0,0\right\rangle \tag{5.2}$$

The PBS of the polarisation-resolved detection unit is then used to carry out a measurement resolving these modes. In case the horizontal and the vertical photon are indistinguishable in all other degrees of freedom, $\hat{h}_o$ and $\hat{v}_o^\dagger$ commute and the terms in the wave function leading to coincidences between the two polarisation modes vanish (compare 3.6).
A HOM-dip with polarisation modes also be implemented with the polarisation splitting $\hat{B}_{\mathrm{QWP}}$ conducted by a quarter-wave plate (QWP) at 45° which leads to the following

relations:

$$\begin{aligned} \hat{B}_{\mathrm{QWP}}: \quad \hat{h}_o^\dagger &= \frac{1}{\sqrt{4}}[(1+i)\hat{h}_i^\dagger + (1-i)\hat{v}_i^\dagger] \qquad \hat{v}_o^\dagger = \frac{1}{\sqrt{4}}[(1-i)\hat{h}_i^\dagger + (1+i)\hat{v}_i^\dagger] \\ \Leftrightarrow \quad \hat{h}_i^\dagger &= \frac{1}{\sqrt{4}}[(1-i)\hat{h}_o^\dagger + (1+i)\hat{v}_o^\dagger] \qquad \hat{v}_i^\dagger = \frac{1}{\sqrt{4}}[(1+i)\hat{h}_o^\dagger + (1-i)\hat{v}_o^\dagger] \end{aligned} \tag{5.3}$$

The above transformations result in the following state:

$$\begin{aligned} \hat{h}_i^\dagger \hat{v}_i^\dagger \left|0,0\right\rangle = \frac{1}{4}[&(1-i)(1+i)\hat{h}_o^\dagger \hat{h}_o^\dagger + (1+i)(1+i)\hat{v}_o^\dagger \hat{h}_o^\dagger + (1-i)(1-i)\hat{h}_o^\dagger \hat{v}_o^\dagger \\ &+ (1+i)(1-i)\hat{v}_o^\dagger \hat{v}_o^\dagger] \left|0,0\right\rangle = \frac{1}{2}[\hat{h}_o^\dagger \hat{h}_o^\dagger + i\hat{v}_o^\dagger \hat{h}_o^\dagger - i\hat{h}_o^\dagger \hat{v}_o^\dagger + \hat{v}_o^\dagger \hat{v}_o^\dagger] \left|0,0\right\rangle \end{aligned} \tag{5.4}$$

Again, the terms leading to coincidences vanish for indistinguishable photons, which shows the beam splitter operation in polarisation can carried out by a HWP as well as a QWP. Although the interference takes place between polarisation modes, the photons for which we want to ensure indistinguishability are initially in two different time-bins spaced by 104.7 ns, which corresponds to the position separation of the time-multiplexed quantum walk setup. Here, we want to observe HOM-interference for photons belonging to an input state occupying at least two time-bins.

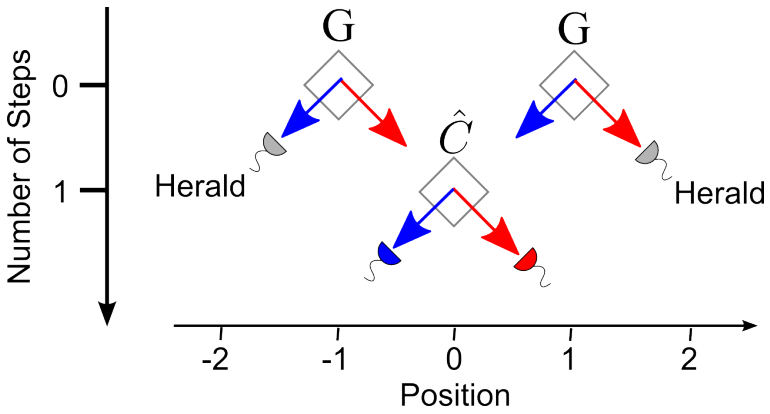

Figure 5.1: Illustration of how photons from PDC states generated (marked by G) in different time-bins are brought to interference passively (interference at coin $\hat{C}$). Horizontally and vertically polarised photons travel through fibres of different length so that eventually two of them overlap in time, while the other two serve as heralds.

Figure 5.1 illustrates the way two photons in different time-bins can be brought to interference passively: Two type-II PDC states are generated (marked with G) with a temporal spacing that is the position separation by pumping a KTP crystal at the

corresponding times (see section 4.2). Since horizontally polarised photons travel through the longer fibre and vertical light through the shorter fibre, the horizontal photon of the first pulse and the vertical photon of the second pulse will overlap in time after one roundtrip through the setup. The other two photons are temporally separated from these and serve as heralds to improve the signal-to-noise ratio (SNR). Note that this scheme does not require any EOM switchings.

5.2 Temporal Delay

While the difference in time needed to travel through the two fibres ensures approximate temporal overlap of photons generated in different time-bins, the fine tuning is done via a translation stage in one of the arms. This stage is operated with a step motor, so the delay can be calculated when knowing the number of steps translated and the translation per step. For the configuration used in our setup the delay is $3.472 \cdot 10^{-5}$ ps/step for a possible translation range of 3 800 000 steps.
Apart from this controlled temporal delay, fluctuations in the environment can introduce uncontrolled changes in the temporal delay. To what extent these affect the indistinguishability of two photons depends on both the time scale and the magnitude of theses changes. Assuming perfect indistinguishability in the other subspaces, the effect on the visibility can be quantified by analysing (3.29) for the temporal subspace:

$$V_{\mathrm{HOM}} = \left| \int T_1^*(t) T_2(t) dt \right|^2 \tag{5.5}$$

In this equation, T_1 and T_2 denote the temporal shape functions of the two photons.
In the experimental setup, uncontrolled changes of the temporal delay are mainly caused by two effects: fluctuations of the repetition rate of the pump laser and fluctuations of the time delay introduced by the fibres in which the photons are guided.

5.2.1 Fluctuations introduced by the Pump Laser

Figure 5.2 shows the repetition rate of the pump laser system (Coherent MIRA) over time. After the warm-up period the repetition does not change by more than 400 Hz (see Figure 5.2, (b)). This drift corresponds to a change in the pulse spacing of 0.0675 ps. This number adds up to $8 \cdot 0.0675$ ps $= 0.54$ ps when picking two pulses separated by 8 roundtrips through the laser cavity. As already mentioned in section 4.2.1, this pulse-picking is necessary to achieve synchronisation of the spacing of the laser pulses with the position spacing in the fibre network.
Assuming photons with a Gaussian shape and FWHM of 2.7 ps, the above temporal offset would lead to a visibility of 90% according to (5.5). This value, however, relates to the

drift in a period of more than 48 hours. To get a more realistic estimate of the effect of temporal drifts on the visibility, we have to look at the actual time of data acquisition. Assuming a maximum measurement time of 1000 s for a data point here, already a change of 100 Hz seems a conservative estimate, resulting in a temporal shift of 0.135 ps and a visibility of 99%. Consequently, we neglect the effects of a unstable pump laser repetition rate on the visibility in the following. Note that this assumption is only valid when the laser system is given enough time to warm up.

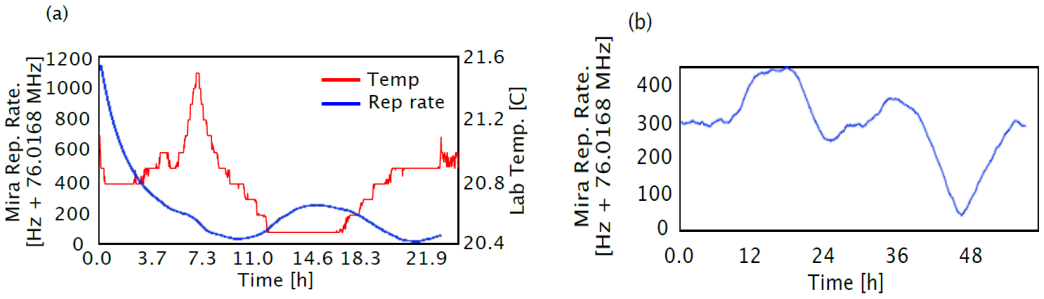

Figure 5.2: The repetion rate of the pump laser over time. (a) shows it together with the temperature for the time following the start-up of the laser system, including the 7 hour long warm-up period, while (b) shows it for an interval in which the laser has already been running for more than 24 hours.

5.2.2 Fluctuations introduced by the Fibres

The next effect we have to take into consideration are changes in the time the photons travel through the fibres. With a thermal expansion coefficient of fused silica of 0.51 μm/(K·m) [140] and a length difference of the two fibres of 20 m, even for a temperature change of 1 K, we calculate a change in the differential length of the fibres of 10.2 μm, corresponding to a time shift of 49.67 fs, which is negligibly small as can be seen when comparing it to the numbers estimated for the effect of the laser repetition rate.
The picture looks different when also taking into account the temperature-related refractive index change of the fibres. Considering a thermal coefficient of delay (TCD) of 53.9 ps/(km·K) for the fibres in use [141], we still only obtain a differential delay of 1 ps/K between the two fibres for their length difference of $\approx$ 20 m. Assuming, on the other hand, that the two fibres with a length of $\approx$ 400 m are coupled slightly differently to the surrounding environment and taking into account their complete length, we end up with a differential delay of 21.56 ps/(km·K). It is, however, hard to estimate the difference in temperature for the two fibres.
On the other hand, a measurement of the difference of the arrival times of light travelling through the two fibres (Figure 5.3, (a)) shows a drift of over 10 ps for the times averaged over 1000 s (red line) . This drift of the averaged arrival times is superimposed with

fluctuations of the individual measurements lasting 10 s of around ± 2-3 ps. The fast fluctuations are most likely a measurement artefact as we do not know of a physical process that would influence the arrival times on this time scale. Figure 5.3, (b) shows the temperature measured inside the lab over 80 hours. We see that oscillations of the temperature occur over hours, explaining the slow drift of the arrival times, but fast fluctuations of the temperature are not to be assumed. Note that Figures 5.3, (a) and (b) show disjunct measurement intervals.

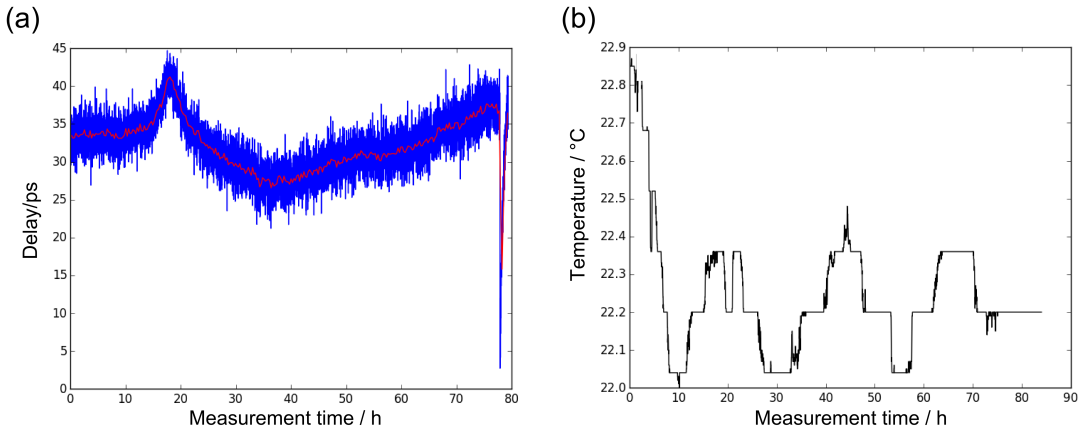

Figure 5.3: (a): The differential delay between the two fibres measured over roughly 80 h. The blue line gives the results of each 10 s measurement, while the read line corresponds to the average of 100 measurement points. The sharp peak towards the end is not a measurement artefact, but indeed the result of heating up one of the fibres with a hair-dryer. Note that the vertical axis is offset by around 104 ns, which is the difference in the delay introduced by the two fibres. (b): The temperature in the lab measured over 80 hours (not the same time interval as in (a)).

In order to verify that the changes in the arrival times are predominantly caused by effects of the temperature on the refractive index of the fibres, one of the fibres is heated up with a hair-dryer. The result is the sharp drop in the differential arrival times towards the end of the measurement time in Figure 5.3, (a).
The magnitude (>15 ps) alone of the arrival time drift makes it very problematic for the experimental setup, as it is significantly larger than the expected width of the HOM dip (around 4 ps). Consequently, it is difficult to find this point as it may drift out of the scanning range during a measurement.

(a)

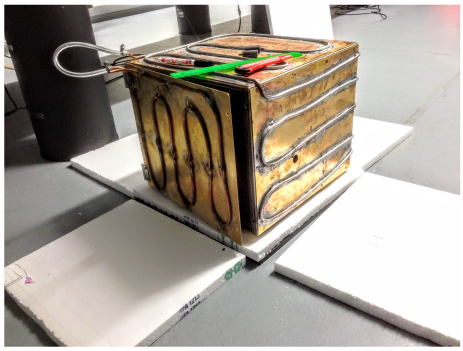

(b)

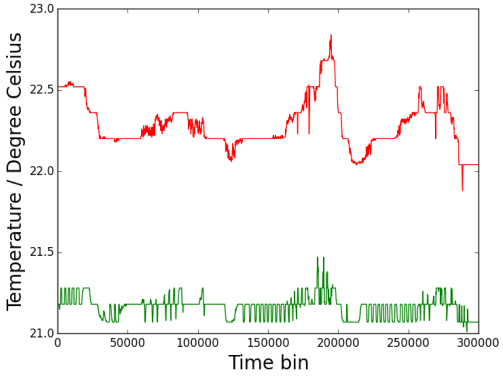

Figure 5.4: (a): Copper box with meandering copper tubes soldered to it and surrounded by a insulating layer of styrofoam which is installed to decouple the temperature of the delay-introducing fibres from the temperature inside the lab. Picture taken during the building process. The credit for processing the metal parts goes to the mechanical workshop at the university. (b): The measured temperature in the lab (red curve) resp. inside the box (green curve). We see that the magnitude of temperature changes is reduced by roughly an order of magnitude. Note that the data was taken using a chiller with a precision of $\pm 0.1°C$. The temperature changes were later reduced by another order of magnitude using a chiller with a precision of $\pm 0.01°C$

The solution to this problem is putting the fibres into a temperature-stabilised box (see Figure 5.4, (a)). We choose a design of a copper box with meandering copper tubes soldered to it and surrounded by a insulating layer of styrofoam. A thermoelectric chiller circulates water through the copper tubes whose temperature is controlled with a precision of $\pm 0.1°C$ for the first implementation, which is later upgraded to a chiller with a precision of $\pm 0.01°C$. This device makes sure that the thermal coupling between cooling water and box significantly exceeds the thermal coupling between box and laboratory. Thus, the temperature inside the box is virtually decoupled from the temperature in the lab (see Figure 5.4, (b)).

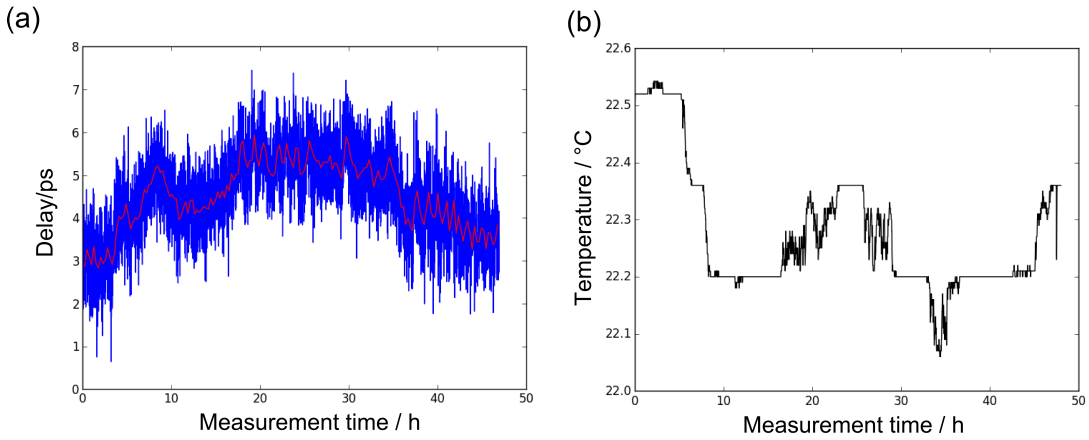

Figure 5.5: (a): The differential delay between the two fibres measured over roughly 50 hours after they have been placed in a temperature-stabilised box. The blue line gives the results of each 30 s measurement, while the read line corresponds to the average of 30 measurement points. Note that the vertical axis is offset by around 104 ns, which is the difference in the delay introduced by the two fibres. (b): The temperature in the lab measured in the same time interval.

Figure 5.5, (a) shows the difference in the arrival times after the fibres have been placed inside the box. In comparison to Figure 5.3, (b) the magnitude of the drift has been reduced by almost an order of magnitude. A drift of 1 ps might still be observed over 10 hours, which is significant when considering the effects on the visibility of a HOM-dip according to (5.5). Relevant, however, is the change within the measurement time of a data point for a HOM-Dip measurement. Consequently, we look at the average arrival time within intervals of 900 s (corresponding to averaging over 30 arrival time measurements of 30s) and find a maximum difference of 0.768 ps between two such intervals, related to a drop in the HOM-visibility to 80 %. The average difference between two intervals of 0.223 ps is, however, related to a visibility of 98 %.
Comparing Figure Figures 5.5, (a) and 5.5, (b), we see that above-the-average changes of the differential arrival times are still linked to drifts in the lab-temperature. This can be explained by the fact that the fibres may be decoupled from the rest of the lab, but other components such as the pump laser and opto-mechanics are not. The effect on the visibilities seems to be negligible as long as measurements are not taken during intervals with above-average temperature changes. The temperature can easily be monitored and these intervals be linked to either people working in the lab and/or the day-night-cycle (especially in warm weather). Synchronizing measurement times with intervals of little temperature change seems consequently to be the most feasible way of mitigating the effects of the temporal delay on HOM-dip visibilities.

5.3 Temporal Shape - Dispersion

Apart from a temporal delay between the two states, their indistinguishability can also be affected by a distortion of the temporal shapes, altering the overlap integral in (5.5). Here, the dispersion in two fibres introducing the temporal delay is the dominant effect. We assume the temporal pulse shape $T(z,t)$ depending on the distance z travelled through the fibre to be given by the following expression (normalising formula from [142] properly, so that the scalar product of the function with itself equals unity):

$$T(z,t) = \frac{\sqrt{\tau_0}}{\pi^{1/4}\sqrt{\tau_0^2 - i \cdot k_2 \cdot z}} e^{-\frac{t^2}{2(\tau_0^2 - i \cdot k_2 \cdot z)}} \tag{5.6}$$

In the above expression τ_0 is related to the temporal duration of the pulse with $2 \cdot \sqrt{2 \cdot ln(2)} \cdot \tau_0$ being the FWHM of the pulse's temporal shape, while k_2 is the group velocity dispersion (GVD) of the fibres. The GVD is linked to the dispersion parameter D by the following expression [142]:

$$|k_2| = |D| \frac{\lambda^2}{2\pi \cdot c} \tag{5.7}$$

For the SMF 28 fibres used in the experimental setup we assume a value of 18 ps/(nm · km) for D [143] and lengths of l_1=450 m and l_2=471.5 m, resulting in a length difference of 21.5 m. For a temporal duration of the two pulses of 2.71 ps, corresponding to a FWHM bandwidth of 1.3 nm for photons generated by a source with a length of 20 mm (see section 5.4.2), we obtain the graph shown in Figure 5.6, (a) for the HOM-dip visibility depending on the number n of positions that one photon is shifted by the fibre delay in regard to the other. In order to do so, we calculate the overlap of $T(z = n \cdot l_1)$ and $T(z = n \cdot l_2)$ according to (5.5). A photon is shifted one position relative to another when it takes either the long or the short fibre while the second photon goes through the other fibre. When two photons interfere after having been translated n positions relative to each other, this means that they were initially n positions spaced apart. Consequently, (5.5) can also be interpreted as showing the HOM-dip visibility depending on the initial spacing of two pulses. For initial spacings of less than 5 positions, we can thus assume the effect of the dispersion on the visibility to be negligible.
In contrast, a 8 mm ppKTP crystal as it is commonly used in our group exhibits a significantly more problematic scaling behaviour concerning the initial spacing (see Figure 5.6, (b)). Using a a pump with a FWHM bandwidth of 1 nm, the generated photons exhibit roughly 3 nm FWHM bandwidth at 1550 nm, corresponding to a duration of 1.2 ps for Gaussian pulses. Consequently, dispersion leads to a severe loss of visibility even for an initial spacing of less than 5 positions.
These results show why the scalability of network requires a longer source than commonly

used, even if this creates new challenges, especially concerning the homogeneity of the poling over the whole sample length.

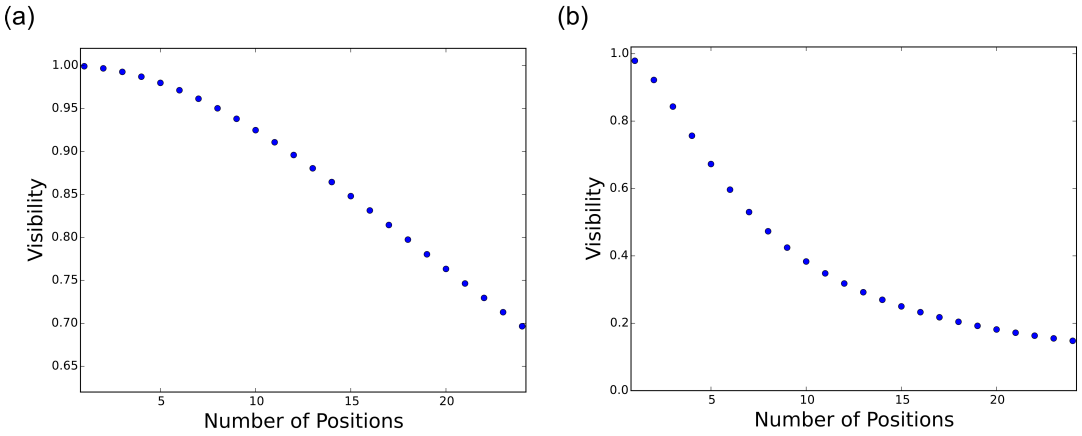

Figure 5.6: The visibility of a HOM-dip between two photons of which one has to be translated n positions relative to the other in a time-multiplexing fibre network in order to interfere it with the other. The photons are translated to different positions in respect to each other when one photon travels through the longer fibre while the other moves through the shorter fibre. Here, we assume a temporal duration τ_0 of the photons of 2.71 ps in (a), which corresponds to a 20 mm long crystal, resp. 1.2 ps in (b), corresponding to a 8 mm long crystal, a dispersion value D of 18 ps/(nm · km) and a length difference of the two fibres of 21.5 m. Note the different scaling of the y-axis for the two graphs.

5.4 Spectral Characteristics

In section 3.1, we introduced the joint spectral amplitude (JSA) reflecting the spectral properties of type-II PDC state. In the following, we will elaborate on how these affect the purities and thus HOM-dip visibilities for heralded PDC states.
As extensive treatments of this topic can be found for example in [144, 145], we will restrict ourselves to what is necessary in the context of this work.
Focusing on the purity and neglecting a possible distinguishability of the two states described by the term $Tr\left\{(\hat{\rho}_1 - \hat{\rho}_2)^2\right\}$, i.e. we assume that both states are described by the same density matrices for a not perfectly pure state, (3.28) simplifies to the following term:

$$V_{\mathrm{HOM}} = Tr\left\{\hat{\rho}_s\hat{\rho}_i\right\} = 1/2\left(Tr\left\{\hat{\rho}_s{}^2\right\} + Tr\left\{\hat{\rho}_i{}^2\right\}\right) \tag{5.8}$$

To evaluate this expression, we conduct a singular value decomposition of the JSA $f(\lambda_s, \lambda_i)$ and obtain its representation in the Schmidt-mode basis with the eigenvectors $\psi_k(\lambda_s)$ and

$\phi_k(\lambda_i)$ and the eigenvalues c_k [146]:

$$f(\lambda_s, \lambda_i) = \sum_k \sqrt{c_k}\psi_k(\lambda_s)\phi_k(\lambda_i) \tag{5.9}$$

Usually the Schmidt-modes ψ_k and ϕ_k are represented by Hermite-Gauss-modes.
In the Schmidt-mode basis, (3.28) assumes the following form with $K = 1/\sum_k c_k^2$ being the Schmidt-number:

$$V_{\mathrm{HOM}} = 1/2\left(Tr\left\{\hat{\rho_s}^2\right\} + Tr\left\{\hat{\rho_i}^2\right\}\right) = 1/2\left(\sum_k c_k^2 + \sum_k c_k^2\right) = 1/K \tag{5.10}$$

It follows that the Schmidt-number K is the crucial quantity when evaluating effects of the spectral purity on the HOM-dip visibility.
Consequently, the visibility is affected by the purity of the photons as well as by the distance of their density matrices (see (3.28)). We will illustrate with two examples how the PDC-process has to be engineered in order to achieve good visibilities.

5.4.1 PDC in LN sample

In the first example, we consider a type-II-PDC-process in a Lithium-Niobate(LN) crystal with a length L of 10 mm. Figure 5.7, (b) shows the numerically calculated phase-matching function $\Phi(\lambda_s, \lambda_i)$ of this system. Its width is determined by the length L of the crystal, while its angle is given by the dispersion properties of the material. The pump distribution $\alpha(\lambda_s, \lambda_i)$ in Figure 5.7, (a) corresponds to a pump wavelength of λ_p=775 nm with a spectral width $\Delta\lambda_p$=0.4 nm. With these parameters we calculate the JSA shown in Figure 5.7, (c) as the product of the phase-matching function and the pump distribution. We notice that the signal has a wavelength of λ_s=1539.77 nm and a width of $\Delta\lambda_p$=2.56 nm, while the idler exhibits a wavelength of λ_i=1560.33 nm and a width of $\Delta\lambda_i$=3.06 nm. Even if we assumed signal and idler to be perfectly pure, the overlap between their wave functions is approximately zero, so that a similar value can be assumed for the HOM-dip visibility according to (3.29). In other words, signal and idler are spectrally almost perfectly distinguishable due to their different wavelengths and thus we do not expect to see a HOM-dip between them.

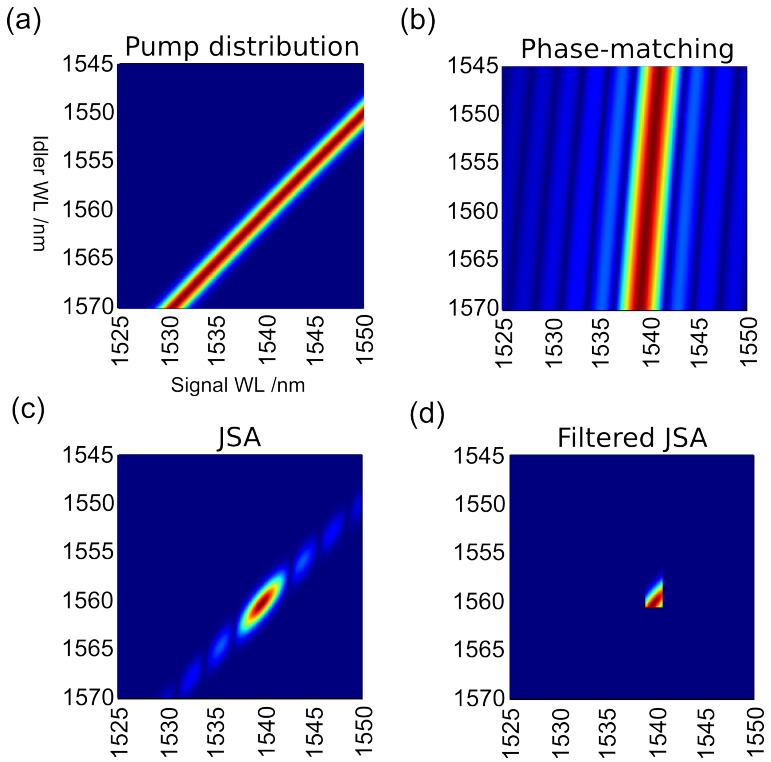

Figure 5.7: (a): The pump distribution with a central wavelength λ_p of 775 nm and a spectral width $\Delta\lambda_p$ of 0.4 nm. (b): Phase-matching function for a 10 cm long LN crystal. (c): The JSA obtained for the system by multiplying pump distribution and phase-matching function. Note that signal and idler are non-degenerate. (d): The JSA after filtering with a top-hat filter with a full transmission range of $\Delta\lambda_f$=0.9 nm. All the data shown is obtained numerically.

It is, however, still instructive to consider the purity of signal and idler. A Schmidt-decomposition of the JSA for the case shown above yields a Schmidt-number of 2.12, which would correspond to a HOM-dip visibility of 0.472 according to (5.10), when neglecting that the visibility is already lost almost completely due to non-degenerate signal and idler wavelengths.

While degeneracy of signal and idler can be easily achieved by selecting the appropriate pump wavelength (in this case λ_p=769.9 nm), increasing the spectral purity is more involved.

Figure 5.7, (d) shows the JSA after the introduction of a top-hat filter which transmits around a wavelength of λ_f=1539.8 nm with a full transmission range of $\Delta\lambda_f$=0.9 nm. Note that in the numerics we assume perfect square filters, for the actual profile of the filters see section 5.4.4.

Performing a Schmidt-decomposition of the filtered JSA, we obtain a filtered Schmidt-number K_f=1.14 which is linked to a visibility of 0.88. However, narrowband spectral

filtering comes at the cost of introducing significant losses, reducing the collection efficiency η. When conducting experiments with multiple single photons n, these additional losses quickly become prohibitive as count rates scale with η^n.

5.4.2 PDC in KTP sample

Spectrally engineering the PDC-process is thus favourable to spectral filtering [147, 148]. As already mentioned, the width of the phase-matching function is determined by the length of the crystal and its angle by the dispersion properties of the used material.
We are able to obtain smaller Schmidt-numbers and thus better visibilities by adapting the spectral bandwidth of the pump and the phase-matching function.
In sections 5.2 and 5.3 we saw that longer pulse durations increase the resilience of the indistinguishability towards fluctations in the temporal delay as well as towards dispersion. Longer pulses in the temporal domain correspond to narrower pulses in the spectral domain and would thus require longer samples, as can be seen from (3.4).
However, we have to consider for which length it is possible to homogeneously manufacture a periodically-poled crystal. In our case this means that we are limited to sample lengths of around 20 mm. For a sample of this length we expect from numerics a Schmidt-number of 1.54, which is already a significant improvement to the 10 mm, but still far from optimal.
Furthermore, we are also limited in the wavelengths of signal and idler as we want them to be close to the telecom wavelength of 1550 nm where propagation losses in fibres are minimal and well-developed technology is available. Consequently, we have to look for materials that exhibit dispersion properties leading to more desirable phase-matching angles.
In contrast to LN, Potassium Titanyl Phosphate (KTP) exhibits a positive phase-matching angle around 59° near the telecom wavelength [149]. This property allows for the implementation of a PDC-source with spectrally almost pure signal and idler [150, 31].
Figures 5.8 (a),(b) show numerics for the pump distribution and phase-matching function assuming a 20 mm long KTP crystal and a pump with a wavelength of λ_p=769.9 nm and a spectral width (FWHM) of $\Delta\lambda_p$=0.4 nm. The resulting numeric JSA is shown in Figure 5.8 (c) and looks already significantly more symmetric regarding a mirroring at the 45° line in the λ_s, λ_i-plot, which is indicative of a better HOM-dip visibility [31]. Indeed, a numerically conducted Schmidt-decomposition yields a Schmidt-number of 1.26 and a HOM-dip visibility of 0.79 before filtering.
Note that the spectral bandwidth of the laser can only be tuned in a very limited range around either 0.4 nm (ps-mode) or 1 nm (fs-mode) and can thus not be considered a free parameter for minimising the Schmidt-number.

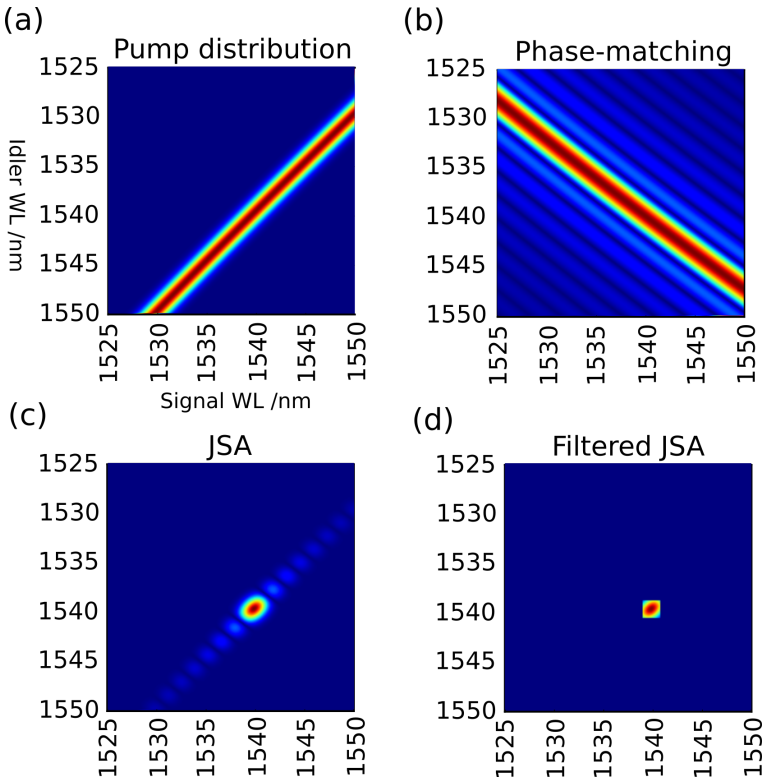

Figure 5.8: (a): The pump distribution with a wavelength λ_p of 769.9 nm and a spectral width $\Delta\lambda_p$ of 0.4 nm. (b): Phase-matching function for a 20 cm long KTP crystal. (c): The JSA exhibiting degeneracy of signal and idler and a high degree of symmetry when mirroring along the 45° axis. (d): The JSA after filtering with a top-hat filter with a full transmission range of $\Delta\lambda_f$=0.9 nm. All the data shown is obtained numerically.

On the other hand, filtering (see Figure 5.8 d) can further decrease the Schmidt-number down to 1.03 where the effect of spectral impurities become almost negligible with a HOM-dip visibility of 0.97. Although the JSA already exhibits a high degree of symmetry before filtering, the sidelobes of the sinc-function present in the unfiltered JSA are removed by the filters and the spectral purity is thereby further increased.
Last but not least, adjusting the pump wavelength results in almost perfect degeneracy of the signal at λ_s=1539.79 nm and the idler at λ_i=1539.78 nm. Also the values for the spectral width (FWHM) of $\Delta\lambda_s$= 1.253 nm and $\Delta\lambda_i$= 1.383 nm do not degrade the spectral overlap of signal and idler significantly.
As we can see from (3.6), the JSA does not only depend on the phase-matching function $\Phi(\lambda_s, \lambda_i)$, but also on the the pump distribution $\alpha(\lambda_s, \lambda_i)$. In appendix E we discuss the effect of a quadratic spectral phase on the pump light (so called chirp) and conclude its effect should be negligible.
For our experiment we have bought two periodically-poled KTP crystals for which we will

discuss in the following to what extend they fit to the assumptions made in the numerics.

5.4.3 PDC in Sample 2

All of the above discussions concern numerically simulated PDC-processes where the dispersion properties of the materials involved are taken from Sellmeier's equations that are fitted to empirical data. In addition, the simulation implicitly assumes homogeneous poling over the whole length of the sample. In practice, however, it turns out that homogeneous poling is difficult to achieve for poling length exceeding 20 mm.
The sample used for the experiment is a periodically-poled KTP crystals with a length of 25 mm. The concrete specimen discussed in this section is BCT 1402 B25 produced by ADVR. In order to determine the effective length of the poled region in the sample, we conduct a measurement of the second-harmonic-generation(SHG)-signal. SHG can be considered the inverse process to PDC where instead of one pump photon decaying to a signal and an idler photon, two pump photons are combined to one signal photon.

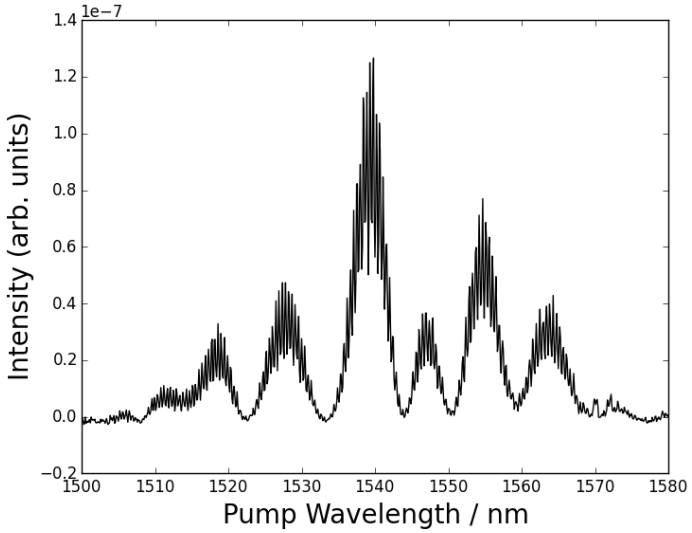

Figure 5.9: The SHG-spectrum measured for waveguide 3.3. The sidepeaks are more pronounced than would be expected for the sidelobes of a sinc-function, which is indicative of inhomogeneous poling. From the width of the central peak we can estimate an effective poling length of around 16 nm.

Figure 5.9 shows the SHG-spectrum measured for waveguide 3.3. From the width of the central peak of around 4.5 nm (FWHM) we can estimate an effective poling length of around 16 mm, which less than the expected 25 mm. We run the numerical simulations with the same parameters as in section 5.4.2 except for a poled length of 16 mm instead of 20 mm, the expected unfiltered HOM-dip visibility changes from 0.79 to 0.74 and the

expected filtered visibility from 0.97 to 0.95.
These considerations do, however, just account for the consequences of the effective poling length on the phase-matching bandwidth. The shape of the SHG-spectrum in Figure 5.9 indicates that this is probably not the full picture as it exhibit sidepeaks that are significantly more pronounced than would be expected for the sidelobes of a sinc-function. This phenomenon is probably linked to inhomogeneities in the poling period. It might be assumed that the extent to which it influences HOM-dip visibilites depends on how well these sidepeaks can be filtered out, but the current numerical framework does not quantify the effects of these inhomogeneities.
The actual joint-spectral-intensities (JSI) are mesasured for several waveguides on the sample with a fibre spectrometer [151]. Note that so far we have considered the joint-spectral-amplitudes, but since our way of measuring does not resolve phases, we are now limited to intensities.
A fibre spectrometer consists of spools of dispersive fibres that introduce temporal delays between different spectral components. We now record coincidences between signal and idler in a temporally resolved way. After calibration, a certain arrival time can be linked to a certain wavelength. Plotting the relative intensities of coincidence clicks depending on the signal and idler wavelengths λ_s and λ_i, we obtain plots (see Figure 5.10) for the measured JSIs similar to those for numerically calculated JSAs (Figure 5.7 and 5.8). Note that the absolute values for the wavelengths in Figure 5.10 are not necessarily accurate, as the fibre spectrometer has not been calibrated especially for the presented measurements. However, the SHG-measurement (see Figure 5.9) constitutes the more reliable source of the absolute values in this case, which are further corroborated by being in accordance with the specified center wavelength of the DWDM filter in use.

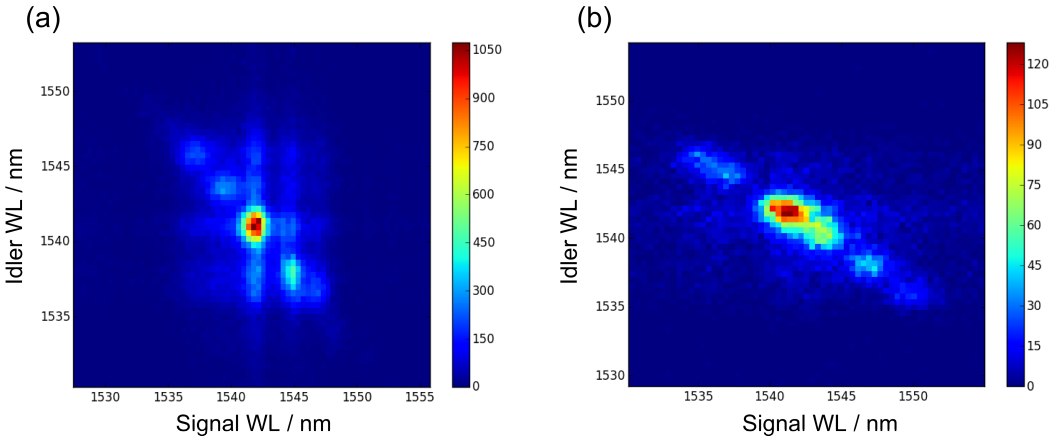

Figure 5.10: JSIs measured with a fibre spectrometer for waveguides 3.2 (a) and 3.3 (b). Note that the y-axis is inverted in respect to Figure 5.8.

The detectors used in measuring the JSIs exhibit a timing jitter of 300 ps, result in a broadening (FWHM) of 600 ps. Combining this number with an estimated delay intro-

duced by the fibre spools of 0.9 ns/nm, we obtain a spectral resolution of 0.67 nm.
Although the resolution of the obtained JSIs is limited, we can clearly discern a main peak and sidelobes with less intensity. In waveguide 3.2, the sidelobes seem to be asymmetric which is indicative of an inhomogeneous poling. Furthermore, the central peak in waveguide 3.3 does not seem to be clearly pronounced, but to have a second peak with less intensity beside it. This feature is as well a signature of inhomogeneous poling. By inserting dense wavelength division multiplexing(DWDM) filters with full transmission ranges of either 0.45 nm or 0.9 nm, we expect to get rid of the sidelobes as well as of the sidepeak in waveguide 3.3.
Another advantage of inserting these narrowband filters can be illustrated with Figure 5.11. Figure 5.11, (a) shows the marginal distributions for waveguide 3.3 before inserting DWDM filters for signal and idler that are obtained when tracing out either idler (resp. signal) for a certain signal (resp. idler) wavelength. The sharp drop in relative intensity at the sides is linked to a broadband filter placed in the beam path. In addition, we observe the presence of side peaks and a slight offset in wavelengths of the central peaks. At this point, it is important that the fibre spectrometer used has not been exactly calibrated, so the corresponding measurements are not a reliable way of verifying spectral overlap of signal and idler. Furthermore, the need to have a reliable measure for this overlap arises from the fact that it is depending on the frequency of the pump light, which might change depending on environment influences and the alignment of the pump laser.

5.4.4 Spectral Distinguishability

The DWDM filters placed in both signal and idler arm have a two-fold advantage: Apart from getting rid of sidepeaks, they also define a narrow wavelength range in which the two photons have to be. Consequently, the idea is to adjust the pump wavelength for ideal spectral indistinguishability of signal and idler by adjusting for maximum intensity transmitted through two filters with the same profile. In order to estimate how accurately filters ensure spectral overlap of signal and idler, we calculate the relative intensity passing through a filter as well as the overlap of the transmitted pulses. We assume filters with a central wavelength λ_c of 1539.8 nm that have full transmission in ranges of $\Delta\lambda_f/2 = 0.45$ nm, 0.9 nm and 1.9 nm, while the transmission $F(\lambda)$ at the edges of this range decreases

according to Gaussian profiles with a FWHM of $\Delta\lambda_f/8$:

$$F(\lambda) = \begin{cases} c \cdot \frac{1}{\sqrt{2\pi}\sigma} e^{-\frac{(\lambda_c - \Delta\lambda_f/4)^2}{2\sigma^2}} & \text{for} \quad \lambda < \lambda_c - \Delta\lambda_f/4 \\ 1 & \text{for} \quad \lambda_c - \Delta\lambda_f/4 \geq \lambda \leq \lambda_c + \Delta\lambda_f/4 \\ c \cdot \frac{1}{\sqrt{2\pi}\sigma} e^{-\frac{(\lambda_c + \Delta\lambda_f/4)^2}{2\sigma^2}} & \text{for} \quad \lambda > \lambda_c + \Delta\lambda_f/4 \end{cases} \tag{5.11}$$

$$\text{With } \sigma = \frac{\Delta\lambda_f/8}{2\sqrt{2\ln(2)}}$$

The constant c makes sure that $F(\lambda \pm \Delta\lambda_f/4)$ is 1, i.e. the filters have ideal transmission in this region and is given by $1/F(\pm\Delta\lambda_f/4)$. For $\Delta\lambda_f/2 = 0.45$ nm and $\Delta\lambda_f/2 = 0.9$ nm the resulting transmission profiles provide good approximations of the data measured for DWDM filters with a specified channel spacing of $\Delta\lambda_f$, while a DWDM filter with $\Delta\lambda_f/2 = 1.9$ nm is not commercially available. The black curve in Figures 5.11, (b), (c) and (d) show the value of $F(\lambda)$ depending on the wavelength.
The green curves $G(\lambda_1)$ in Figures 5.11, (b),(c) and (d) show the intensity transmitted through the filters depending on the central wavelength λ_1 of a pulse:

$$G(\lambda_1) = \int |F(\lambda)P(\lambda, \lambda_1, \Delta\lambda)|^2 d\lambda \tag{5.12}$$

In the above equation, $P(\lambda, \lambda_1, \Delta\lambda)$ describes the assumed Gaussian profile of the generated PDC photons. Here, λ_1 refers to the the central wavelength and $\Delta\lambda$ to the spectral width (FWHM). We assume values of $\lambda_1 = 1539.8$ nm and $\Delta\lambda = 1.3$ nm (see section 5.4.2).
The red curves show the visibility $\mathrm{Vis}(\lambda_1)$ according to (3.29) that is obtained when overlapping the pulse with a second pulse that is shifted in the opposite direction in regard to the central wavelength of the filter. Here, we write the wavelength λ_1 of the first pulse as $\lambda_1 = \lambda_c + \delta\lambda$ and the wavelength λ_2 of the second pulse as $\lambda_2 = \lambda_c - \delta\lambda$, which follows from energy conservation for small variations $\delta\lambda$ around $\lambda_c = 2\lambda_p$. Refering to (3.29) we calculate the visibility as the overlap of Gaussian profiles in the spectral domain:

$$\mathrm{Vis}(\lambda_1) = |1/G(\lambda_1) \int F(\lambda)P(\lambda, \lambda_c + \delta\lambda, \Delta\lambda)F(\lambda)P(\lambda, \lambda_c - \delta\lambda, \Delta\lambda)d\lambda|^2 \tag{5.13}$$

The factor $1/G(\lambda_1)$ renormalises the part that passes through the filter to one, since the symmetric losses do not affect the visibility as long as dark counts can be neglected (see section 5.8). Strictly speaking, this factor should be $1/(\sqrt{G(\lambda_1)} \cdot \sqrt{G(\lambda_2)})$, but the symmetry of both filters and pulse shapes allows us to use the simplified version.

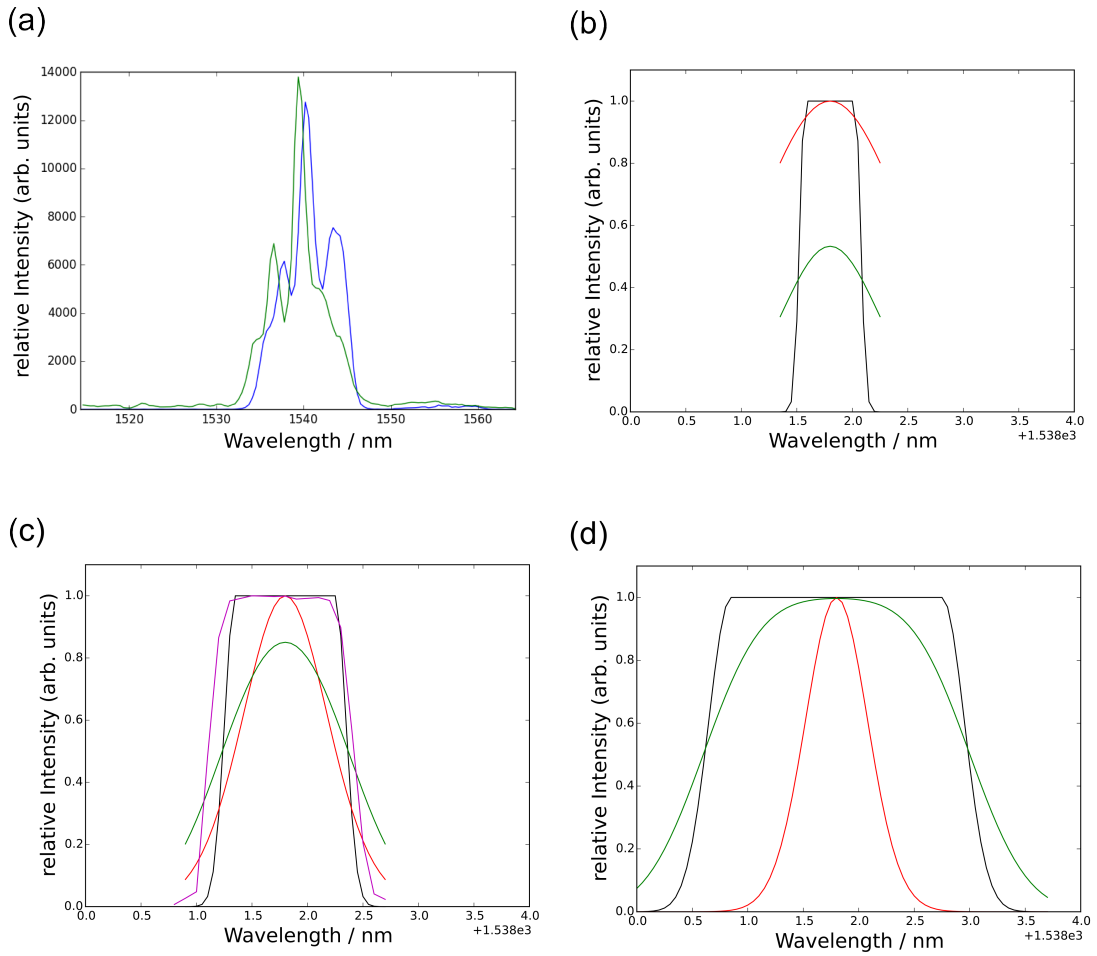

Figure 5.11: (a): The marginal distributions for signal and idler from waveguide 3.3 measured with a fibre spectrometer. (b),(c) and (d): The black curves show the transmission profile for filters with full-transmission bands $\Delta\lambda_f/2$ of 0.45 nm, 0.9 nm and 1.9 nm and a central wavelength of 1539.8 nm. Assuming pulses with a Gaussian shape in spectrum and a FWHM of 1.3 nm, we calculate the relative intensity passing through the filter depending on the central wavelength of the pulse (green curve) as well as the overlap (red curve) with a second pulse that is shifted in the opposite direction in regard to the central wavelength of the filter. The magenta curve in (c) corresponds to the measured transmission profile of a DWDM filter in use.

Comparing the transmitted intensity and the overlap for the three different filter widths, we see that the broadest filter (shown in (d)) allows all of the intensity to be transmitted, but on the other hand the intensity profile also exhibits a rather broad range where it remains close to one. This effect defies to a certain degree the purpose of ensuring spectral indistinguishability of signal and idler with the filter: there are wavelengths for which the visibility (red curve) has already dropped significantly, while the change in transmission is

so small that it might not be discernible in an experimental setting. When using the filter with the narrowest transmission curve (b), the transmitted intensity and the visibility show a very similar slope, which makes adjusting for optimal indistinguishability by looking at transmitted intensities relatively easy. However, the caveat here is that only around half of the intensity is transmitted through the filters, which adds a problematic amount of additional losses. The best compromise between accuracy and losses seems to be the filter with $\Delta\lambda_f/2 = 0.9$ nm (c), which exhibits a transmission of more than 80% and where the relation of the slopes of transmission and overlap should still allow for adjusting for more than 90% visibility.
At this point it has to be mentioned that the DWDM filters commercially available are highly standardised products for telecommunications applications. Consequently, we can expect the transmission profile of any two filters with the same specifications to be the same within the measurement accuracy (which has been verified in the context of this work). On the other hand, we are limited in our choice of filter characteristics to what is available on the market. Thus, only the filters with $\Delta\lambda_f/2 = 0.9$ nm and $\Delta\lambda_f/2 = 0.45$ nm are an option, out of which we choose filters with $\Delta\lambda_f/2 = 0.9$ nm and a central wavelength of 1539.8 nm for further use. The measured transmission profile for such a filter is given by the magenta curve in Figure 5.11, c. For the considerations following in this thesis, we will use values for the transmission efficiency of 80% and 90% for the spectral indistinguishability.

5.4.5 Spectral Purity

Having dealt with the indistinguishability assuming photons in a single Hermite-Gauss mode, another quantity relevant for the visibility are the spectral purities of signal and idler. Here, the numerics for the filtered PDC in KTP give us a Schmidt-number of $K = 1.03$ which is indicative of almost perfect purity. In order to experimentally verify this assumption, we conduct measurements of the unheralded $g^2(0)$-value. For an otherwise ideal PDC process, the $g^2(0)$-value is related to the Schmidt-number and thus the purity in the following way [152]:

$$g^2(0) = 1 + 1/K \tag{5.14}$$

As described in section 3.3.1, $g^2(0)$ can be measured with a Hanbury Brown-Twiss interferometer. Measuring the respective coincidence and single counts as well as the number of trigger events in the same time interval, we determine $g^2(0)$ according to (3.21).
The green and orange markers in Figure 5.12 show the experimentally determined values of $g^2(0)$ for the two modes of the PDC state generated in waveguide 3.3 depending on the mean photon number $\bar{n}$ of a photon pair. The green markers corresponds to the experimentally measured values for the reflective port of the PBS separating the two

modes of the PDC state, the orange markers to the transmissive port. Where we would ideally expected a flat line at a value of almost 2, we observe a decrease of the value for higher generation probabilities and a drop significantly below 2.
How can this be explained? The high values at low mean photon numbers $\bar{n}$ can be linked to a Type-0 PDC process, which is also called single-mode squeezed vacuum (SMSV). In such a process, both signal and idler have the same polarisation. Consequently, we have no longer photons from one but from two modes impinging on the probabilistic beam splitter of the Hanbury Brown-Twiss interferometer. This increases the coincidence probability and therefore also the g^2 value.
The deviation from the assumed asymptotic value of 2 on the other hand is modelled by incoherently adding Poissonian noise to the PDC state. In the experiment, Poissonian noise is e.g. originating from imperfect suppression of the pump.

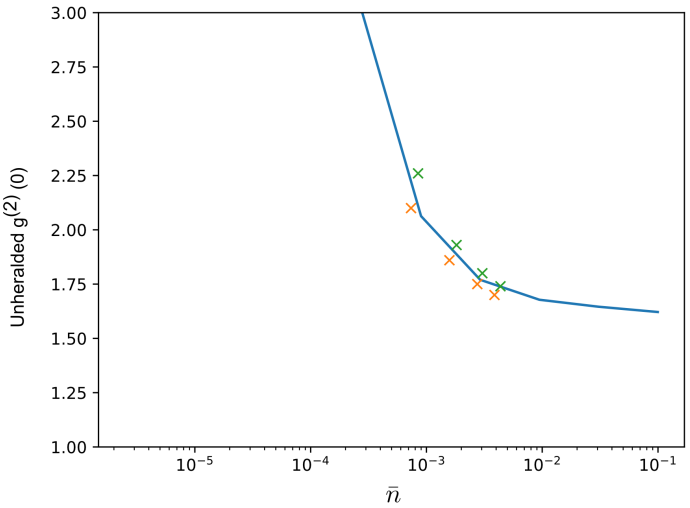

Figure 5.12: Estimated $g^2(0)$ values for SDPC-states depending on the mean photon number $\bar{n}$. The green markers corresponds to the experimentally measured values for the reflective port of the PBS separating the two modes of the PDC state, the orange markers to the transmissive port. The blue line represents the numerical values for a state incorporating Poissonian noise ($\alpha = \sqrt{0.25 \cdot \bar{n}}$) and SMSV ($r^* = \text{arcsinh}(\sqrt{1.5 \cdot 10^{-4} \cdot \bar{n}})$).

In order to numerically reproduce the measured values, we assume parameters of $\alpha = \sqrt{0.25 \cdot \bar{n}}$ for the Poissonian noise and $r^* = \sqrt{1.5 \cdot 10^{-4} \cdot \bar{n}}$ for the SMSV. The corresponding numerical values are given by the blue line Figure 5.12. A more detailed account on how Poissonian noise and SMSV are modelled can be found in section 5.6.
The influence of these processes on the measured $g^2(0)$ values severely impairs their informative values concerning the Schmidt number. Consequently, we will assume in the following a HOM-dip visibility related to the spectral purity of 0.95, which corresponds to

the numerically predicted value (see section 5.4.3). This hypothesis will be put to a test against measured HOM-dip visibilities in section 5.9.

5.4.6 PDC in Sample 2

A second ppKTP sample (BCT 1703 A30) is obtained at a latter stage of setting up the experiment. The specifications are similar to the sample used previously (BCT 1402 B25), again aiming for decorrelated type II PDC from roughly 775 nm to around 1550 nm. This time, however, the vendor specifies a poled length of $\geq$ 22 mm instead of 25 mm for the previous sample.
Furthermore, in contrast to the previous specimen, it is delivered without coatings on the endfaces, which are in this case applied in-house. Consequently, the reflectivites of the endfaces are initially high enough (ca. 7-8 %) to allow for measuring losses inside the waveguides using a Fabry-Perot method [153]. Here, we measure values of around 1-1.2 dB/cm with a few waveguides exhibiting significantly higher losses.
In order to evaluate the suitability of the spectral properties for our purposes, we conduct SHG measurements. It turns out that only around one third of the waveguides exhibits a measurable SHG signal in the range from 1530 -1570 nm. Out of these waveguides only one (WG 1.1) exhibits a spectrum that resembles a decent approximation of the expected sinc-shape (see Figure 5.13, (a)), others, for example WG 3.1 (see Figure 5.13, (b))), are more asymmetric and do not show the expected shape of the side lobes. As a result of these measurements, we decide to conduct further experiments with WG 1.1 and obtain the corresponding DWDM-filters.

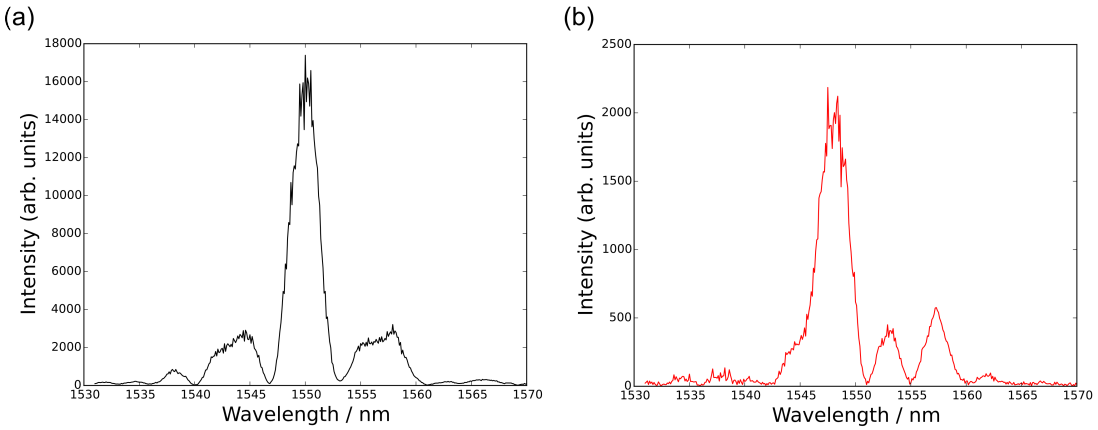

Figure 5.13: Wavelength-dependent SHG intensity in WG 1.1 (Subfigure (a)) resp. WG 3.1 (subfigure (b)). The spectrum of WG 1.1 resembles much more a sinc-function then the spectrum of WG 3.1 which is asymmetric and exhibits peaks where they are not expected. Here, the focus of our analysis is on the shape of the spectrum and not on the absolute intensities, so that these are not necessarily comparable.

In the first measurements conducted with DWDM filters exhibiting a central wavelength

of 1550.12 nm and a bandwidth $\Delta\lambda_f/2$ of 0.9 nm, it is not possible to simultaneous obtain Klyshko-efficiencies η and HOM-dip visibilities in a remotely acceptable range.
Measuring the wavelength-dependent transmission in the signal and the idler arm as well as the number of coincidences, we observe that the counts in the two arms peak at different wavelength, which is indicative of operating the source in a non-degenerate regime. Indeed, measuring again the SHG-signal of the sample as it is built-in into the assigned place of the setup (see section 4.2) indicates that the degeneracy point is to be expected at 1547nm. This discrepancy between the two measured SHG-signals shows that the validity of SHG measurements is better validated, e.g. by comparing the wavelengths set at the pump laser with those specified for a DWDM-filter, in case the result is supposed to be reliable.

5.5 Photon-Number Statistics

In section 3.1 we have seen that the PDC sources used in our experimental setup are not ideal single photon sources, but two mode squeezers with exponential photon number statistics. Doing experiments with one of the mode while not conducting photon-number-resolving measurements on the other will consequently lead to a reduction of the state's purity and thus of HOM-dip visibilities.
The photon-number characteristics also affect $g^{(2)}$-measurements: Conducting a measurement on one mode (signal) of the PDC state while not heralding on the other (idler) corresponds to tracing out the idler mode and results in super-poissonian photon number statistics. As a consequence, a $g^{(2)}$-measurement of an unheralded mode of a PDC state yields the same value as for thermal light, i.e. 2.
Furthermore, the unheralded $g^{(2)}$-value is affected by the frequency spectrum of the PDC process (see subsection 5.4.3).
Using bucket detectors also distorts the mean photon number $\bar{n}_{\text{detected}}$ detected in our experiment in relation to the real mean photon number $\bar{n}$. Our detectors record only one click even if more than one photon is present. However, the probability of detecting at least one of multiple photons is higher than the probability of detecting one photon, which is accounted for by a factor of $\frac{1-(1-\eta)^n}{1-\eta}$ in the expression for the detected mean photon number $\bar{n}_{\text{detected}}$:

$$\bar{n}_{\text{detected}} = \sum_{n=0}^{\infty} \frac{1-(1-\eta)^n}{1-\eta} \cdot (1-\lambda^2) \cdot \lambda^{2n} \tag{5.15}$$

The division by the factor $1-\eta$ is due to the fact that we are considering the mean photon number at the source and are thus normalising out the Klyshko-efficiencies η. Exactly because a measurement of η is distorted by multi-photon contributions, its value is determined for low mean photon numbers where their effect is still negligible.
Figures 5.16, (a) and (b) illustrate the photon-number distribution for two PDC states after tracing out one of the modes with mean photon numbers $\bar{n}$ of 0.1 resp. 0.5. Apart

from the fact that the vacuum component dominates in both cases, it can be observed that the weight of the multi-photon contributions is significantly increased for $\bar{n} = 0.5$ in comparison with $\bar{n} = 0.1$.
Figure 5.16, (c) shows the detected mean photon number $\bar{n}_{\text{detected}}$ depending on the real mean photon number $\bar{n}$ for different Klyshko-efficiencies η ranging from 0.1 (green curve) to 0.5 (red curve) in intervals of 0.1. For reference, the black curves represents an ideal detector giving the real mean photon number. Here, we see that the detected mean photon number $\bar{n}_{\text{detected}}$ corresponds almost exactly to the real mean photon number $\bar{n}$ for values up to around 0.1. For Klyshko-efficiencies η of around 0.3 (yellow curve) the measured numbers remain very close to the real numbers up to values of $\bar{n}$ of around 0.2. It is only for high mean photon numbers and especially high Klyshko-efficiencies that significant deviations of measured and real mean photon numbers occur.

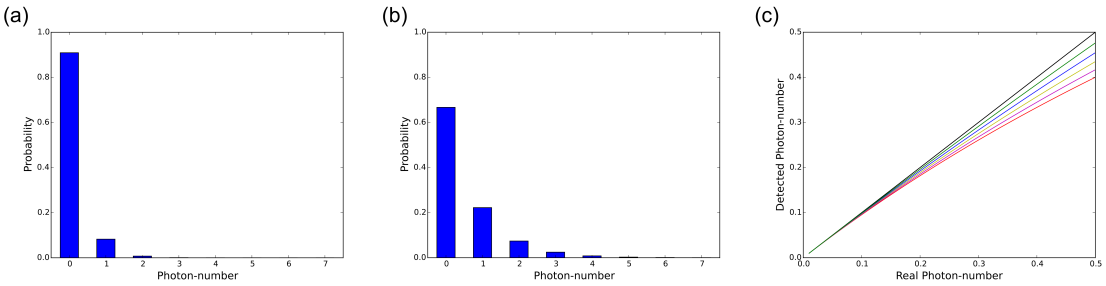

Figure 5.14: (a): The probabilities of the different photon-number components for a PDC state with a mean photon-number $\bar{n}$ of 0.1 after tracing out one mode. (b): The corresponding probabilities for a mean photon-number of 0.5. (c): The detected photon-number $\bar{n}_{\text{detected}}$ vs. the real photon-number $\bar{n}$ for Klyshko-efficiencies η ranging from 0.1 (green curve) to 0.5 (red curve) in intervals of 0.1. The black curve corresponds to an ideal detector measuring exactly $\bar{n}$.

5.6 Numerical Simulations in Framework QuTip

In order to quantify the impact of the mean photon number, simulations are implemented in the computational framework QuTip [154]. It contains a library with the definition of a number of states and operators that we complement with further definitions from textbooks (unless stated otherwise [155]). Apart from allowing to quantify the impact of the photon number, the numerically implemented framework will also be utilised for estimating the influence of noise in the form of single-mode squeezed vacuum and Poissonian noise. In addition, balanced as well as imbalanced losses can be simulated.
We start by defining the Hamiltoninan $\hat{H}_{\text{SPDC}}$ and the respective unitary $\hat{U}_{\text{SPDC}}$ according to (3.1) resp. (3.2) (see section 3.1) for a two-mode squeezed SPDC-state.
In section 5.4.5 we saw that there is evidence that the generated states are affected by Poissonian noise as well as by single-mode squeezed vacuum (SMSV). Consequently, we want to simulate their influence on the HOM-dip visibilities. Poissonian noise has the same

photon-number statistics as a coherent state $|\alpha\rangle$, described by applying the displacement operator $\hat{D}(\alpha)$ depending on the parameter α related to the noise strength to the vacuum:

$$|\alpha\rangle = \hat{D}(\alpha)\,|0\rangle = e^{\alpha\hat{a}^\dagger - \alpha^*\hat{a}}\,|0\rangle \tag{5.16}$$

Single-mode squeezed vacuum (SMSV) is similar to the two-mode squeezed state according to (3.2), except for the fact that this operation only occurs in a single mode:

$$|\psi_{\mathrm{SMSV}}\rangle = \hat{U}_{\mathrm{SMSV}}\,|0\rangle = e^{-i(r^*\cdot(\hat{a}^{\dagger\,2} - \hat{a}^2))}\,|0\rangle \tag{5.17}$$

We introduce a second squeezing parameter r^* here to allow the squeezing strength for the SMSV-state to be different from the one for the SPDC-state.
Having defined the input states, we now define the operations which act upon them. The unitary $\hat{U}_{\mathrm{BS}}(\theta)$ acts as a beam splitter transformation between the two modes 1 and 2 with a splitting ration tunable by θ:

$$\hat{U}_{\mathrm{BS}}(\theta) = e^{-i(i\cdot\hat{a}_1\hat{a}_2^\dagger - i\cdot\hat{a}_1^\dagger\hat{a}_2)\theta} \tag{5.18}$$

With this general definition of a beam splitter, we define the swap operation $\hat{U}_{\mathrm{swap}} = \hat{U}_{\mathrm{BS}}(\theta = \pi/2)$ as a beam splitter transformation with a θ of $\pi/2$ and the Hadamard operation $\hat{U}_{\mathrm{Had}} = \hat{U}_{\mathrm{BS}}(\theta = \pi/4)$ as a balanced beam splitter transformation for which θ is $\pi/4$. Setting θ to 0 results in a completely transmissive beam splitter $\hat{U}_{\mathrm{Trans}} = \hat{U}_{\mathrm{BS}}(\theta = 0)$ with no mixing.
Eventually, the final state is detected with non-photon-number-resolving bucket detectors which have the following operators for either measuring no click ($\hat{E}^{(no\ click)}$) or measuring a click-event ($\hat{E}^{(click)}$):

$$\hat{E}^{(no\ click)} = D(0)\sum_{m=0}^{\infty}(1-\eta)^m\,|m\rangle\,\langle m| \tag{5.19}$$

$$\hat{E}^{(click)} = \sum_{m=0}^{\infty}[1 - D(0)(1-\eta)^m]\,|m\rangle\,\langle m| \tag{5.20}$$

In the above formulas, $D(0)$ denotes the probability of having no dark counts, which is the complement of the probability $D(1)$ of having a dark count, η is the detection efficiency of the detectors and m the number of photons that do not lead to a click.

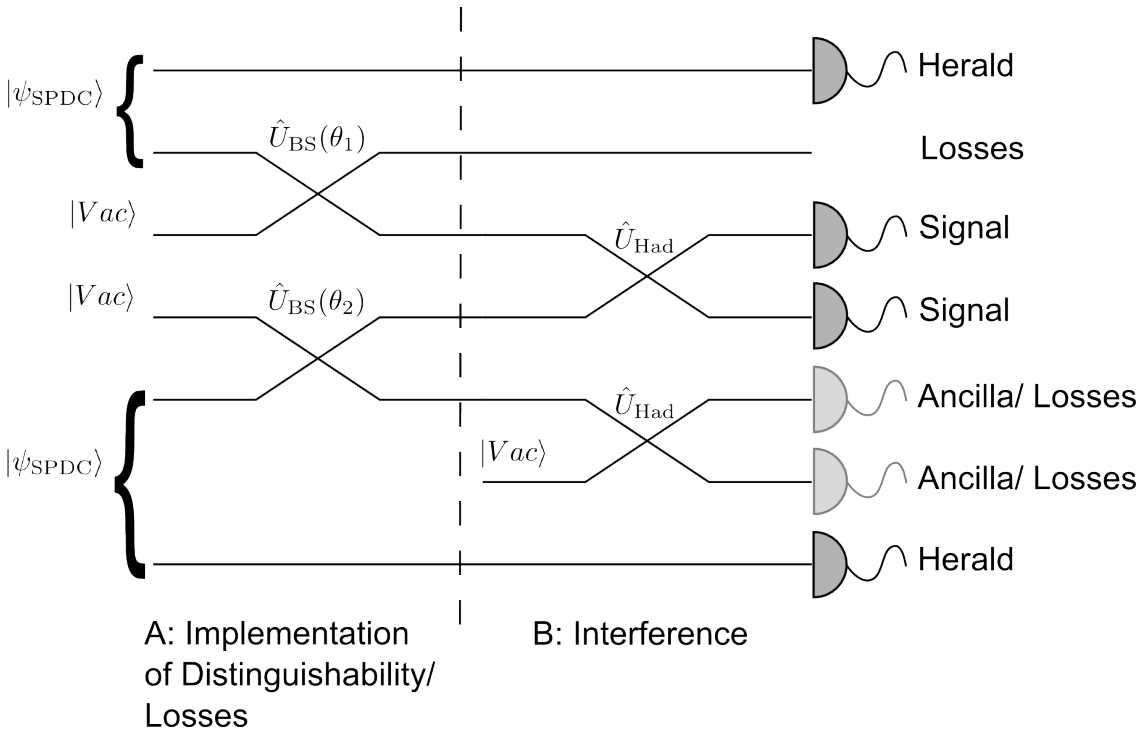

Figure 5.15: Schematic of the model implemented to simulate the HOM-dip visibilities: One photon of each of the two PDC states serves as a herald. The other photon first undergoes a beam splitter operation $\hat{U}_{\mathrm{BS}}(\theta_{1/2})$ with which either distinguishability or losses can be simulated depending on whether the second output mode is detected. The two PDC signal photons are interfered in a Hadamard operation $\hat{U}_{\mathrm{Had}}$. Eventually, fourfold detection events between two herald and two signal/ancilla modes are counted. Whether the ancilla mode is considered for fourfolds as well depends on whether they are meant to simulate distinguishability (in this case they are accounted for) or losses (in this case they are not accounted for). When simulating distinguishability, the ancilla mode is interfered with vacuum in a Hadamard operation $\hat{U}_{\mathrm{Had}}$

The HOM-dip is analysed for heralded PDC-states whose signal photons are brought to interference at a 50:50 beam splitter (equivalent to a Hadamard transformation $\hat{U}_{\mathrm{Had}}$). Figure 5.15 illustrates the scheme implemented for calculating HOM-dip visibilities. The two beam splitter transformations $\hat{U}(\theta_{1/2})_{\mathrm{BS}}$ taking place before the interference can be used to simulate either losses or distinguishability. In the first case, θ_1 is set to 0 (i.e. the upper photon stays in its original mode and does not interfere with the second one), while θ_2 is used to tune the distinguishability between the two PDC states and shifts part of the lower photon into an ancilla mode. This ancilla mode is sent to one input mode of a Hadamard beam splitter and vacuum to the other, which simulates the fact that photons in the ancilla mode can no longer interfere with photons from the other input state, but multi-photon contributions might still be split-up in the Hadamard operation.

The ancillary modes are a virtual construct to implemented to simulate distinguishability. In a real experiment, however, our click detectors will count distinguishable and indistinguishable photons alike, which means that we have to simulate the detection of the ancillary modes in the same bins as the modes from which they have been taken. Consequently, ancillary modes and the original modes are combined in QuTip again before the detection is simulated, however, only after the operation $\hat{U}_{\mathrm{Had}}$ leading to interference has been conducted.
In order to obtain a reference for complete distinguishability of the two input states, θ_2 is set to $\pi/2$, so that a swap operation $\hat{U}_{\mathrm{swap}}$ is conducted, making the two input states perfectly distinguishable. The visibility is then obtained by comparing the number of four-fold coincidences in the distinguishable case to the number of four-fold coincidences for indistinguishable photons. Since no interference takes place in the first case, it corresponds to $P_{\tau=\infty}$, while the second case represents $P_{\tau=0}$. Consequently, the visibility can be determined analogous to (3.26) by dividing the difference between the minimum number of fourfolds and the maximum number of fourfolds by the maximum.
Simulating losses corresponds to setting either one or both of the angles θ_1 and θ_2 to a non-zero value depending on whether balanced or unbalanced losses are to be accounted for. The difference to distinguishability simulations is that now we do not assume detection of the components transferred to ancilla modes, but trace these modes out.

5.7 Mean Photon Number

Having implemented this numerical framework, we can now study the influence of the mean photon number $\bar{n}$ on the HOM-dip visibility.
In order to do so, the squeezing parameter according to (3.1) for the simulated SPDC-state is set to $r = \mathrm{arcsinh}(\sqrt{\bar{n}})$ and the numerically assumed Klyshko-efficiency to 0.2. The orange line in Figure 5.16 shows the HOM-dip visibility depending on the mean photon number for a PDC-state that is neither subjected to Poissonian noise nor to single-mode squeezed vacuum (SMSV). In contrast, the red line in Figure 5.16 represents an input state that is influenced by both noise processes. Here, we assume a value of $\alpha = \sqrt{0.25 \cdot \bar{n}}$ for the Poissonian noise (see (5.16)) and $r^* = \mathrm{arcsinh}(\sqrt{1.5 \cdot 10^{-4} \cdot \bar{n}})$ for the SMSV (see (5.17)). These values are fitted to yield a good approximation of the measured results for the power-dependent $g^{(2)}$ (see section 5.4.5).

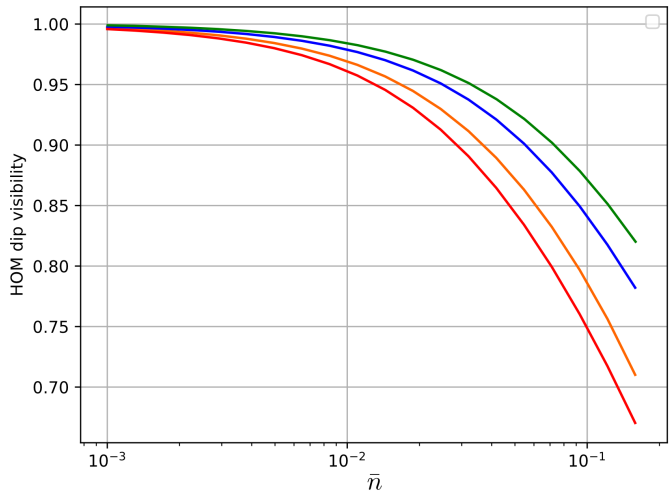

Figure 5.16: Estimated HOM-dip visibility for SDPC-states depending on the mean photon number $\bar{n}$. The orange line corresponds to a state for which we assume no additional noise processes, while the state represented by the red line is subjected to Poissonian noise and SMSV. For both curves we assume "click"-detectors. The blue (with added noise) and the green (no added noise) line are obtained assuming two-mode detectors offering some degree of photon-number resolution. The parameters assumed are $\alpha = \sqrt{0.25 \cdot \bar{n}}$ for the Poissonian noise and $r^* = \text{arcsinh}(\sqrt{1.5 \cdot 10^{-4} \cdot \bar{n}})$ for the SMSV. In both cases we assume a Klyshko-efficiency of 0.2

Figure 5.16 clearly shows the significant influence of the mean photon number $\bar{n}$ on the HOM-dip visibility. It is even magnified when assuming parameters leading to realistic $g^{(2)}$ values (blue and red curves in Figure 5.16).
The effect of $\bar{n}$ on the visibilities originates in the fact that we are using "click"- or bucket-detectors that do not offer photon-number resolution. Consequently, heralding on one mode of the PDC state corresponds to tracing out over the non-zero photon-number components, which reduces the purity of the state. This problem can be mitigated to some extent by splitting the herald up to two modes and post-selecting on those fourfold coincidences for which there are no coincidences between the two modes of one herald. In the following we will refer to such a detection scheme as two-mode detectors.
We model this experimental device numerically by implementing a two-mode detector for the heralds that allows for filtering out higher order photon-number contributions with a probability of $(1/2)^{m-1}$ where m is the number of photons arriving at the detector. We adapt expression (5.20) by assuming that the detection probability for higher photon

numbers is reduced accordingly:

$$\hat{E}^{(click)} = \sum_{m=0}^{1} [1 - D(0)(1-\eta)^m] \, |m\rangle \langle m| + \sum_{m=2}^{\infty} [1 - D(0)(1 - \frac{\eta}{2^{m-1}})^m] \, |m\rangle \langle m| \quad (5.21)$$

The data obtained when modelling two-mode detectors is represented by the blue (added noise) and the green (no added noise) curve in Figure 5.16. It can be observed that even this limited degree of photon-number resolution leads to a significant increase of visibilities.

5.8 Losses

The HOM-dip visibility of an ideal single-photon source in an ideal noise-free system is loss-independent, as losses cannot lead to spurious coincidences in these conditions. The situation becomes different when considering SPDC-input-states and realistic amounts of noise. Thus, we will discuss in the following the effect of the input states and balanced as well as unbalanced losses.
To model the effect of losses, both input states are subjected to a beam splitter operation before they interfere (see section 5.7). The input modes of this operations are the respective states and vacuum, the output modes are the ones that are brought to interference plus two ancillary modes that are traced out.
In this framework, balanced loss corresponds to setting the beam splitter angles θ_1 and θ_2 to the same value $\theta = \arccos(\sqrt{1-L})$ with L being the loss parameter assumed for the intensities.

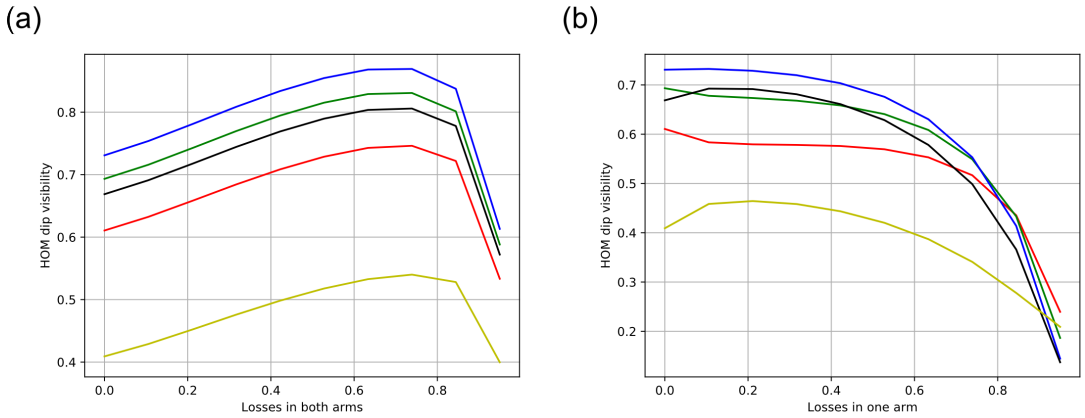

Figure 5.17: (a): The visibility depending on the loss parameter L for balanced losses with different beam splitter transformations $\hat{U}_{\mathrm{BS}}(\beta)$ in the interference (β=$\pi/5$ (red), $\pi/4.5$ (green), $\pi/4$ (blue), $\pi/3.5$ (black) and $\pi/3$ (yellow). (b): The visibility depending on losses in just one input mode ($\theta_1 = \arccos(\sqrt{1-L})$, θ_2=0). The colour coding for the different beam splitting ratios is the same as in subfigure (a). For both figures we assume a mean photon number $\bar{n}$ of 0.1 and a Klyshko-efficiency of 0.2. Furthermore, Poissonian noise with $\alpha = \sqrt{0.25 \cdot \bar{n}}$, SMSV with $r^* \operatorname{arcsinh}(= \sqrt{1.5 \cdot 10^{-4} \cdot \bar{n}})$ is added to the PDC state (corresponding to the blue and red curve in Figure 5.16). Note the different scaling of the y-axis for (a) and (b).

Figure 5.17, (a) shows the visibility depending on the loss parameter for balanced losses with different beam splitter transformations $\hat{U}_{\mathrm{BS}}(\beta)$ in the interference. Comparing the curves for different beam splitter transformations $\hat{U}_{\mathrm{BS}}(\beta)$ in the interference, we see that a 50:50 beam splitter ($\beta = \pi/4$, blue curve) allows for the best visibilities. Furthermore, the plots show that balanced losses actually increase visibilities as long as dark counts can be neglected. This is not surprising when considering that attenuating a heralded PDC state decreases the relative weight of contributions from higher photon numbers. It is only when losses bring the PDC counts close to the dark count level that visibilities drop rapidly, which happens for $L > 0.8$.
The plots of the visibilities for losses only in one input mode ($\theta_1 = \arccos(\sqrt{1-L})$, θ_2=0) show a different picture (see Figure 5.17, (b)): Depending on whether the unbalanced losses are offsetting or increasing an imbalance in the beam splitting ratio, losses in one arm of up to $L \approx 0.1$ lead to either a slight increase ($\beta = \pi/3$, yellow curve and $\beta = \pi/3.5$, black curve) or a decrease of the visibility ($\beta = \pi/4$, blue curve; $\beta = \pi/4.5$, green curve and $\beta = \pi/5$, red curve). Losses in one arm of $L > 0.1$ result in a significantly decreasing visibility with increasing losses well before dark counts become dominant.
Note that all of the numerical simulations have been conducted assuming "click"- or bucket-detectors without any photon-number resolution.
How do these findings relate to experimental parameters? This question is particularly interesting as effects of unbalanced losses accumulating with an increasing number of round trips through a fibre network might lead to visibilities that are decreasing with the

number of round trips. For the given implementation of the fibre network, we measure additional relative losses of up to $L_{\mathrm{exp}} = 0.08$ for the worst configuration in comparison to the best one. Note that these values give the differential losses for different paths through the setup and do not account for imbalanced losses related to an inhomogeneous switching operation of the EOM for different time bins. Concerning a time-multiplexed input state where the two input modes are initially spaced m positions apart from each other, the resulting total differential losses $1 - L_{\mathrm{exp,total}} = (1 - L_{\mathrm{exp}})^m$ scale exponentially with m. Still, we expect an initial spacing of $m = 8$, which corresponds to differential losses of around 0.5, to be possible without the visibility dropping by more than an absolute value of 0.05. Again these numbers do not account for a possible effect of the EOM switchings.

5.9 Measured Visibilities - Results and Conclusion for Sample 1

We saw that visibilities are sensitive to a range of parameters which can affect purity or indistinguishability. In the following we will estimate their combined effect.
According to (3.30), the different degrees of distinguishability introduced in the individual subspaces add up multiplicatively. We have identified sources of distinguishability in the temporal (estimated visibility: $\mathrm{Vis}_{\mathrm{temp}} = 0.98$) and in the spectral subspace (estimated visibility: $\mathrm{Vis}_{\mathrm{spectral}} = 0.95$). Regarding the temporal domain we have looked at fluctuations of the delay as well as broadening due to dispersion (estimated visibility: $\mathrm{Vis}_{\mathrm{disp}} = 0.99$). In the spectral domain we assume at this point that both states exhibit only a single Hermite-Gauss-mode that are, however, at a slightly different central wavelength.
These consideration still involve pure states. On the other hand, we saw that multimodedness in the Schmidt- as well as the Fock-basis introduces mixedness which also decreases visibilities. For the Schmidt-modes, we assume a numerically expected reduction of the HOM-dip visibilities to $\mathrm{Vis}_{\mathrm{Schmidt}} = 0.90$. The purity in the Fock-basis, on the other hand, depends significantly on the mean photon number as a free parameter (see section 5.6.)
Multiplying the visibilities for temporal and the spectral domain we end up with a reduction of the overall visibility to $\mathrm{Vis} = 0.83$, still assuming perfect purity in the Fock space:

$$\mathrm{Vis} = \mathrm{Vis}_{\mathrm{temp}} \cdot \mathrm{Vis}_{\mathrm{spectral}} \cdot \mathrm{Vis}_{\mathrm{disp}} \cdot \mathrm{Vis}_{\mathrm{Schmidt}} = 0.98 \cdot 0.95 \cdot 0.99 \cdot 0.90 = 0.83 \quad (5.22)$$

In the following, we will probe this domain experimentally by measuring HOM-dip visibilities for different mean photon numbers $\bar{n}$. Bearing in mind that there is a difference between the detected mean photon number $\bar{n}_{\mathrm{detected}}$ and real mean photon number $\bar{n}$ (see section 5.7) for higher pump powers, we retrieve the real values from the measured ones for $\bar{n}_{\mathrm{detected}} > 0.1$, while we assume that the error is negligible for smaller photon numbers.
In order to measure HOM-dips between photons generated in different time bins (see section 5.1), we introduce distinguishability between the interfering modes by varying the

delay for one of the interferometer arms via a retroreflector on a translation stage. We then record the number of fourfold coincidences (two heralds and two interfering photons) depending on this delay. Figure 5.18, (a) shows exemplarily the HOM-dip measured for a mean photon-number $\bar{n}$ of 0.03 in sample BCT 1402 B25. We fit an inverse Gaussian profiles to the data from which we obtain the number of counts for the baseline C_b, the amplitude of the dip C_a and its FWHM. The visibilities Vis are obtained by dividing the amplitude by the number of baseline counts, i.e. Vis $= C_\mathrm{a}/C_\mathrm{b}$, which is in accordance with (3.26).

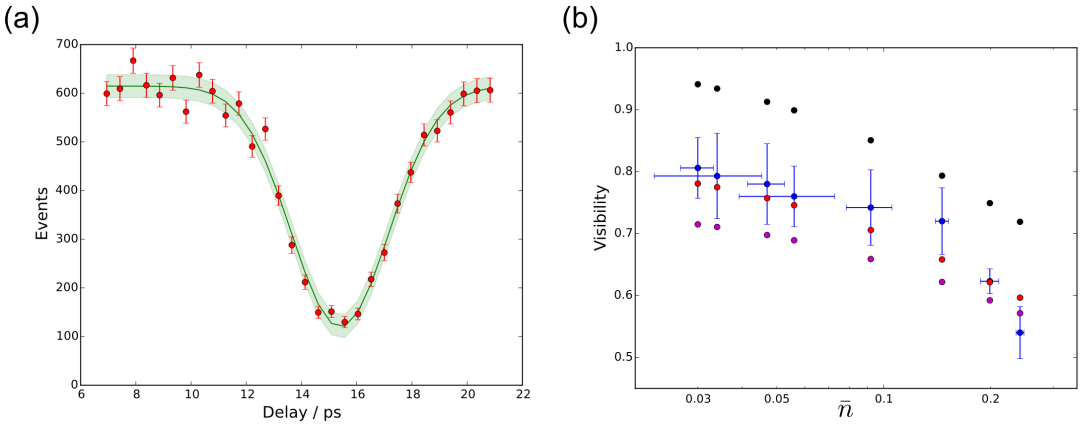

Figure 5.18: (a): HOM-dip measured for a mean photon number $\bar{n}$ of 0.03. The red dots give the number of counts for different delays. Their error bars are determined as Poissonian errors. The green line represents a least square fit for the number of counts. Its error (mean square deviation) is indicated by the green shaded region. (b): The visibilities depending on the mean photon number $\bar{n}$. The black dots correspond to a numerical simulation taking into account effects in the Fock space, but ignoring the other subspaces. Here, we assume Poissonian noise with $\alpha = \sqrt{0.25 \cdot \bar{n}}$, SMSV with $r^* = \mathrm{arcsinh}(\sqrt{1.5 \cdot 10^{-4} \cdot \bar{n}})$ and a Klyshko-efficiency of 0.2 (see section 5.6). The blue dots stand for the experimentally obtained values with the error bars on the visibility calculated by propagating the errors for the baseline and amplitude and the error bars on the mean photon number given by the range of $\bar{n}$ within a measurement interval which largely depends on the fluctuations of the lab temperature during this time. The red dots represent numerical values corrected by a factor of 0.83 as an estimate for the reduction of visibility originating from other subspaces. The magenta dots show the numerical values with a correction factor of 0.75 reflecting the Schmidt-number extracted from the $g^{(2)}$-measurements.

The errorbars of each data point in the plot are calculated as the square root of the number of counts under the assumption of a Poissonian error. With the visibility Vis given by $C_\mathrm{a}/C_\mathrm{b}$, its error ΔVis is evaluated with Gaussian error propagation according to

the following expression:

$$\Delta\mathrm{Vis} = \left[\left(\frac{1}{C_\mathrm{b}}\Delta C_\mathrm{a}\right)^2 + \left(\frac{1}{C_\mathrm{b}^2}C_\mathrm{a}\Delta C_\mathrm{b}\right)^2\right]^{1/2} \tag{5.23}$$

The errors ΔC_a and ΔC_b of the amplitude and of the baseline are computed as the mean square deviation of the fit from the data points. In Figure 5.18, (a) this quantity is depicted as the green shaded region around the fit function given by the green line.
For the sample BCT 1402 B25, we experimentally measure HOM-dip visibilities for mean photon-numbers $\bar{n}$ ranging from 0.03 to 0.242 (see blue symbols in Figure 5.18, (b)). In addition to the error of the visibility the data points exhibit error bars reflecting the range of $\bar{n}$ recorded within a measurement interval. This uncertainty originates from changes in the power coupled into the sample during the corresponding time span.
We compare the experimentally determined values with numerical ones calculated under different assumptions: The black dots are computed via QuTip (see section 5.6) for a PDC state combined with Poissonian noise ($\alpha = \sqrt{0.25 \cdot \bar{n}}$) and SMSV ($r^* = \mathrm{arcsinh}(\sqrt{1.5 \cdot 10^{-4} \cdot \bar{n}})$). Consequently, it reflects effects on the visibility originating from the Fock space, but ignores other subspaces.
These are taken into account by multiplying the visibility with the estimated correction factor of 0.83 explained earlier in this section (indicated by red dots). Assuming the measured $g^{(2)}$ values to correctly reflect the Schmidt-number of the PDC process, we obtain a correction factor of 0.75 only reflecting the Schmidt-basis and ignoring all other effects (e.g. temporal delay or spectral distinguishability). The values for this correction factor are given by the magenta dots. Since they are significantly below the measured data, we have strong evidence that the measured $g^{(2)}$ values do not allow to derive the Schmidt-number. Conducting an estimation with the correction factor of 0.83, on the other hand, leads to values that agree with the experiment for most of the data points when taking the error bars into account. The observed and the numerically determined visibilities seems to show a different scaling behaviour with increasing photon-numbers, suggesting that effects so far unaccounted for play a role here. It is, however, possible to explain the observed visibilities in the regions of $\bar{n}$ where experiments utilising the fibre network are likely to be conducted (see chapter 8). Note that multiplying the numerically obtained values with a correction factor is not an exact method, but only an approximation, as (3.30) has been derived assuming pure states. However, our SPDC states are no longer perfectly pure after heralding due to multi-modedness in the Fock- and Schmidt-basis. The comparison with experimental data shows that our approximation still seems to a good estimate. An exact computation of the visibilities involving all relevant degree of freedom is not possible in our numerical framework, as the dimensionality of the required Hilbert space is beyond what the software can handle.
The temporal width of the HOM-dip also allows us to estimate the spectral width of the

PDC photons: The inverse Gaussian profile fitted to the dip shown in Figure 5.16, (a) exhibits a FWHM width of 4.2 ps, which yields a temporal duration of 2.97 ps (FWHM) after deconvolution for the individual photons. Assuming for them a TBWP of 0.44, corresponding to Gaussian pulses, we obtain for their spectral bandwidth (FWHM) a value of 1.17 nm. This number compares to numeric values of 1.253 nm (signal) resp. 1.383 nm (idler) for a 20 mm long sample, on the one hand, and, on the other hand, to a value of $\approx$ 1 nm for the full transmission window of the DWDM filters in use. Since we expect the filters to define the bandwidth relevant for the HOM-interference, this is not a surprising result, but it shows at least that the HOM-dip is not significantly broadened by changes of the temporal delay during the measurement time.

5.10 Conclusion and Results for Sample 2

HOM-dip visibilities are probed experimentally for sample BCT 1703 A30 as well. Here, we use two different types of filters: The first one is a freespace filter with a central wavelength of 1550 nm and a FWHM bandwidth of 2 nm that can be angle-tuned to lower wavelengths. The second configuration involves fibre-coupled DWDM filters whose transmission profile is very similar to the filters presented in section 5.4.4 in terms of shape and full transmission range ($\Delta\lambda_f/2 = 0.9$ nm), but are now centered around 1546.1 nm resp. 1546.9 nm.
The freespace filters exhibit a broader spectral bandwidth and also a higher transmission (almost unity) at the center wavelength. Consequently, we observe in this case higher Klyshko-efficiencies of around 35 %. The HOM-dip visibilities obtained in this case are given by the blue markers in Figure 5.19, (a).
The experimental visibilities are again compared with numerical values: The black markers correspond to the results of the numerical simulations accounting for the effects of mean photon-number $\bar{n}$ and noise. They are implemented as described in section 5.6 and analogue to those for sample BCT 1402 B25 (see section 5.9). In contrast to the previous section, we assume an increased amount of Poissonian noise with $\alpha = \sqrt{0.5 \cdot \bar{n}}$ to account for even lower measured $g^{(2)}$-values. The red and the magenta markers give numerical visibilities corrected for additional effects as described in section 5.9 with the purity in the spectral domain estimated to allow for 0.95 (red markers) resp. 0.75 (magenta markers). In both cases (2 nm freespace filter shwon in Figure 5.19, (a) and DWDM filter shown in Figure 5.19, (b)) the data represented by the red dots seems to be a better estimate, even though there is a increased discrepancy to the measured data for higher mean photon-numbers, again hinting that effects so far not included play a role here.
The application of DWDM filters reduces Klyshko-efficiencies down to 26-28 %, but on the other hand improves visibilities considerably in the relevant region (grey-shaded areas) of mean photon-numbers $\bar{n}$ around 0.1 (see Figure 5.19, (b)).

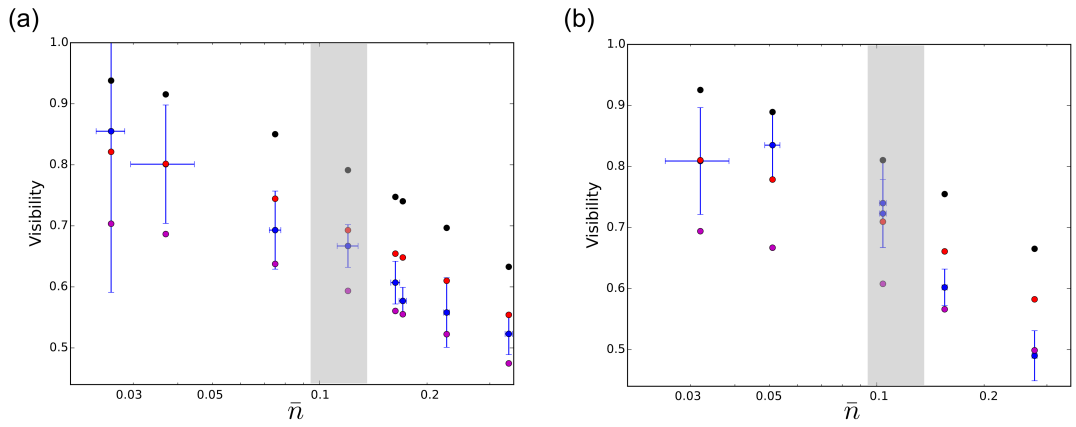

Figure 5.19: The visibility depending on the mean photon-number $\bar{n}$ for source BCT 1703 A30 with a 2 nm freespace filter (a) resp. DWDM filters (b). The blue markers correspond to the measured values, while the black markers show the numerical data only considering the Fock space. The red markers correspond to a correction assuming a purity in the spectral domain of 0.95, resulting in an overall correction factor of 0.88 when incorporating additional effects, as quantified in the previous section. A presumed spectral purity of 0.75 leads to the values represented by the magenta markers, even when ignoring all other possible effects. The grey-shaded area marks the region of mean photon numbers most relevant for experiments.

$g^{(2)}$-measurements again turn out to be inconclusive as we measure values between 1.48 and 1.51 for the configuration with the 2 nm freespace filter resp. 1.65 and 1.75 for the configuration with the DWDM filters. If these measurements were accurate the spectral purities would be around 0.5 for the freespace filter and 0.75 for the DWDM filter. Neglecting all other effects possibly reducing visibilities, a purity of 0.75 would lead to the values represented by the magenta markers in Figures 5.19, (a) and (b), which are significantly below the experimentally measured values. A spectral purity of 0.95 as estimated according to the numerical simulation of the PDC process (see section 5.4.2), on the other hand, results in the data represented by the red dots and seems to give a more reasonable estimation of the measured visibilities. It is worth to mention that the purity of the filtered process only decreases from 0.97 to 0.95 when assuming a sample length of 16 mm instead of 25 mm, which shows that it is resilient to at least this type of imperfections in sample fabrication. Again, we have to note that the numerical approximation shows larger deviations from the measured data for higher mean photon numbers.
Also the joint intensity distribution for the arrival times of signal and idler measured for waveguide 1.1 in the sample under investigation (see Figure 5.20) can give some hints on the spectral purity of the PDC process. It looks like a reasonable good approximation of a decorrelated process exhibiting a circular intensity distribution, although the FWHM of the marginal distributions of signal and idler have a ratio of 1.23.

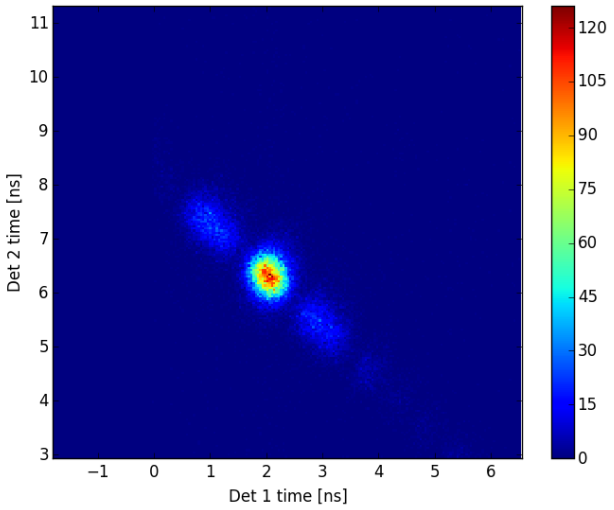

Figure 5.20: Joint intensity distribution for the arrival times of signal and idler measured for waveguide 1.1 in the sample under investigation

The Gaussian profile fitted to the dip exhibits a FWHM of 4.75 ps, corresponding to a temporal duration of the individual pulses of 3.35 ps, which can be linked to spectral bandwidth of 1.05 nm. This value is similar to the bandwidth of 1.17 nm measured for BCT 1402 B25 and is mainly determined by the transmission profile of the DWDM filters. With the 2 nm freespace filter, on the other hand, we observe FWHM values for the dips of around 3.8 ps, corresponding to a temporal duration of the pulses of 2.7 ps. From this we can deduce a spectral bandwidth (FWHM) of 1.31 nm, which is in good agreement with the numerically expected values for the PDC process. In addition, this result provides evidence for the validity of the values assumed in section 5.4.4 for estimating the spectral transmission profile of the filters.
Furthermore, we conduct measurements allowing to assess the effect of dispersion on visibilities. From numerical calculations, we expect it to be negligible (see section 5.3). This assumption is verified experimentally by measuring a visibility of 0.56 ± 0.059 for an initial spacing of the photons of one position and a visibility of 0.55 ± 0.052 for an initial spacing of two positions. Both measurements are conducted with the same mean photon-number $\bar{n}$ of 0.19 ± 0.005.

5.11 Testing Loop with seeded PDC

The factors influencing HOM-dip visibility that have been discussed originate from characteristics of the interferometer loop that is used to make the input states interfere (sections 5.2 and 5.3) as well as from characteristics of the source (see sections 5.4, 5.4.1, 5.4.2, 5.4.3

and E). In order to be able to investigate influences of the loop independently from effects originating from the source, we make use of difference frequency generation (DFG).
By sending an additional seed field into the crystal, DFG between the pump and the seed frequency dominates over the SPDC which is seeded by the vacuum. The output of the DFG process will be pulsed coherent light that can be used to probe to HOM-dip visibilities [156].
In such a setting, we will effectively measure the interference of phase-randomised coherent states, so that the possible visibilities are limited to 50 %. However, these will be less sensitive to the mean photon-number than those obtained with PDC input states. The numerical simulations represented in Figure 5.21 show that for coherent states the visibilities are virtually insensitive to the mean photon-number as long as dark counts and detector saturation (present in the case with Klyshko-efficiency 1) can be neglected. In addition, using a cw-laser ("Nettest Tunics") as the seed allows for a DFG field that exhibits virtually only one Schmidt-mode for its spectral decomposition. Consequently, investigating HOM-dip visibilities with coherent states generated by DFG rules out effects related to photon-number and spectrum. We will make extensive use of this possibility in section 8.5.

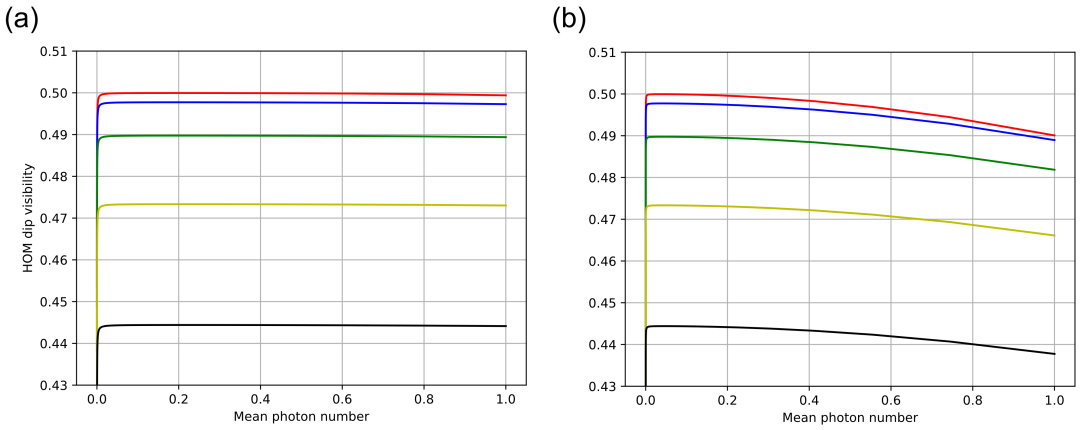

Figure 5.21: The visibility of the HOM-dip between phase-randomised coherent states depending on the mean photon number for a Klyshko-efficiency of 0.2 (a) resp. 1 (b). The different curves correspond to different values L of the parameter quantifying imbalanced losses with the intensity in one mode being $1 - L$ when the intensity in the other mode is 1: Red corresponds to $L = 0$, blue to $L = 0.125$, green to $L = 0.25$, yellow to $L = 0.375$ and black to $L = 0.5$. For very low mean photon number visibilities are affected by noise counts.

A brief description of how to implement a setup allowing for the investigation of visibilities with seeded PDC can be found in appendix F.

6 Experiments with Coherent States Part 1: Investigating Topological Phenomena

After all describing the effort undertaken to make multiple single photons sent into the network pure and indistinguishable, it is worth to remember that the evolution of single photons starting at just one initial position can be simulated with coherent states (see appendix A for more details). While such a setting does neither allow for observing HOM-interference between photons nor suffices for the approaches to quantum computation mentioned in chapter 3, quantum walks starting at a single position still allow for the investigation of the non-classical propagation and interference behaviour of the walker according to the first two axioms of quantum mechanics (see section 3.5). In the following, we will present the investigation of topological phenomena as an example of the simulation capabilities of quantum walks with coherent states. Here, it's the symmetry properties of the evolution unitary $\hat{U}$ that give rise to phenomena such as distinct topological phases or topologically protected edge states.

6.1 Introduction

The discovery of the quantum Hall effect [157] was accompanied by great excitement, as it turned out that the Hall conductivity in a 2-dimensional electron gas at low temperatures and the presence of a strong magnetic field is quantized to integer multiples of $\frac{e^2}{h}$. Most remarkably, the conductivity is independent of the density of mobile electrons. The quantum Hall effect is considered to be a consequence of Gauge invariance [158]. Furthermore, the phenomenon can be explained with the help of the Chern number [159, 160], sheding light on its topological aspects.
More recently, the quantum spin Hall effect allowed for the experimental realisation of topological insulators in HgTe quantum wells (not to be confused with H.G. Wells) [161]. The quantum spin Hall phase relevant here is associated with a Z_2 invariant [162], which is analogous to the Chern number classification of quantum Hall effect.
In addition, it is assumed that topological phenomena can be harnessed for quantum computing [163].
All this sparks the interest in the search of feasible model systems. Current approaches include ensembles of ultracold bosonic atoms [164, 165, 166, 167] allowing for measuring the Chern number as well as photonic model systems [168, 169, 170, 171] in which e.g. topologically protected bound states can be observed. Other possible ways include solid-state systems [172, 173], superconducting circuits [174], mechanical oscillators [175] and

microwave networks [176, 177, 178].
In photonic systems, topological phenomena can be accessed by implementing a split-step quantum walk on a 1D optical lattice [46, 47, 75].
Here, we present the implementation of three different schemes that allow for accessing the topological properties of split-step quantum walks.
The first one is based on the measurement of scattered reflection amplitudes and also enables the observation of localised edge states [179, 75].
In the second scheme we realise a bulk-boundary setting with decoupling which makes not only edge states accessible but also the eigenvalues associated to the walk operator [180, 48, 76].
As a third scheme we implement a supersymmetric single-step quantum walk in which we observe a topological midgap state with anomalous polarisation [105]. Here, in contrast to the other two experiments, we do not rely on a split-step quantum walk for accessing topological phenomena.

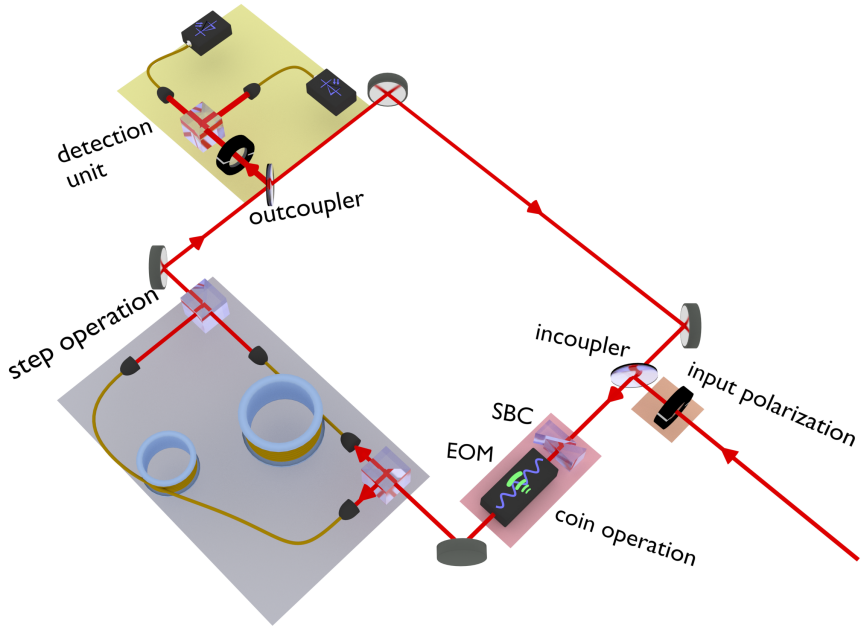

Figure 6.1: Schematic of the setup used for the investigation of topological phenomena: As the new setup it is based on time-multiplexing by splitting light to two fibres of different length and feeding the output of this operation back to the input. In contrast to the new setup, light is coupled in and out probabilistically. Furthermore, the coin operation is carried out by a Soleil-Babinet compensator (SBC) which gives us more freedom in setting the coin angle in comparison to a single HWP or QWP. Figure from [76].

These experiments are implemented with the conventional architecture of the time-multiplexing quantum walk setup [73] (see Figure 6.1), i.e. a setup operated with coherent

input states and without deterministic in- and outcoupling. In contrast to the new setup, it is designed for wavelengths around 800 nm, which is less favourable in terms of losses than 1550 nm, but on the other hand allows for switching greater angles with the EOMs. This is a necessary condition for the experiments described in the following, since they require EOM angles of up to $3/4\pi$. For the experiment measuring the eigenvalues, we upgraded the fibre couplings, thus improving coupling efficiencies from $\approx 38\%$ to $\approx 50\%$ and consequently increasing significantly the number of possible steps. The supersymmetric single-step quantum walk experiment, conducted subsequently, also benefits from these improvements.

6.2 Split-step Quantum Walk and Topological Invariants

The first two experiments presented in the following are based on a split-step protocol [169] with an evolution unitary of the following form:

$$\hat{U} = \hat{S}_{+}^{\mathrm{H}} \cdot \hat{C}(\theta_2) \cdot \hat{S}_{-}^{\mathrm{V}} \cdot \hat{C}(\theta_1) \tag{6.1}$$

Here, the walker undergoes the coin operation $\hat{C}(\theta_1)$ corresponding to a polarisation rotation by the angle θ_1, which is followed by the conditional shift operation $\hat{S}_{-}^{\mathrm{V}}$ acting on the walker's vertical polarisation components. Subsequently, the polarisation is rotated by the angle θ_2 in the coin operation $\hat{C}(\theta_2)$ and the walker's horizontal polarisation components are translated in the conditional shift operation $\hat{S}_{+}^{\mathrm{H}}$. The conditional shift operators are defined in the following way:

$$\begin{aligned} \hat{S}_{+}^{\mathrm{H}} &= \sum_x |x+2, H\rangle\langle x, H| + |x, V\rangle\langle x, V| \\ \hat{S}_{-}^{\mathrm{V}} &= \sum_x |x, H\rangle\langle x, H| + |x-2, V\rangle\langle x, V| \end{aligned} \tag{6.2}$$

Lengthy but straightforward calculations lead to the following equivalence (see appendix G):

$$\hat{U} = \hat{S}_{+}^{\mathrm{H}} \cdot \hat{C}(\theta_2) \cdot \hat{S}_{-}^{\mathrm{V}} \cdot \hat{C}(\theta_1) = \hat{S} \cdot \hat{C}(\theta_2) \cdot \hat{S} \cdot \hat{C}(\theta_1) \tag{6.3}$$

With $\hat{S}$ being defined as follows:

$$\hat{S} = \sum_x |x+1, H\rangle\langle x, H| + |x-1, V\rangle\langle x, V| \tag{6.4}$$

Expression (6.3) is important, as it shows that the step operation conducted by our experimental setup according to (6.2) is compatible with the common definition of the split-step unitary according to (6.1).
A quantum walk in the split-step protocol belongs to the symmetry class BDI [181] and consequently exhibits particle-hole, time-reversal as well as chiral symmetry, which are defined in the following way with γ, η and τ being the respective symmetry operators [76]:

$$\begin{aligned}
\textbf{chiral symmetry:} \quad & \gamma\hat{U}\gamma^\dagger = U^\dagger \quad \text{with} \quad \gamma \text{ unitary} \\
\textbf{particle-hole symmetry:} \quad & \eta\hat{U}\eta^\dagger = U \quad \text{with} \quad \eta \text{ anti-unitary} \\
\textbf{time-reversal symmetry:} \quad & \tau\hat{U}\tau^\dagger = U^\dagger \quad \text{with} \quad \tau \text{ anti-unitary}
\end{aligned} \tag{6.5}$$

Furthermore, translational symmetry results in a band structure, as can be seen by determining the effective Hamiltonian H_{eff} with eigenvalues ε that is associated to the walk unitary $\hat{U}$ [181]:

$$\hat{U} \equiv ie^{-iH_{\text{eff}}} \tag{6.6}$$

The quantum walk exhibits relevant quasienergy gaps at $\varepsilon = 0$ and $\varepsilon = \pi$ in which topologically protected states may be present [182].

6.3 Scattering Approach

In the following, we outline a method of experimentally accessing topology in one-dimensional quantum walks using a scattering approach according to [179]. The results of these experiments are published in [75].
According to [179] the corresponding topological invariants are given by simple function, e.g. trace, determinant or Pfaffian, of the reflection blocks of the scattering matrix at these quasienergies. The concrete correspondence between the reflection elements and the topological invariant is determined by the symmetry class of a particular setting. The example studied here belongs to the BDI symmetry class with the symmetries defined above [181]. Consequently, the eigenvalues of the reflection blocks are ± 1 and the topological

invariants are given by the traces of the reflection matrices $r(\varepsilon)$ for $\varepsilon = 0$ and $\varepsilon = \pi$:

$$(Q_0, Q_\pi) = 1/2[Tr\, r(0), Tr\, r(\pi)] \tag{6.7}$$

The reflection blocks of the scattering matrix for a one-dimensional quantum walk are also one-dimensional, consequently the above expression simplifies to equating the topological invariants with scalar reflection amplitudes $r(0)$ and $r(\pi)$:

$$(Q_0, Q_\pi) = 1/2[r(0), r(\pi)] \tag{6.8}$$

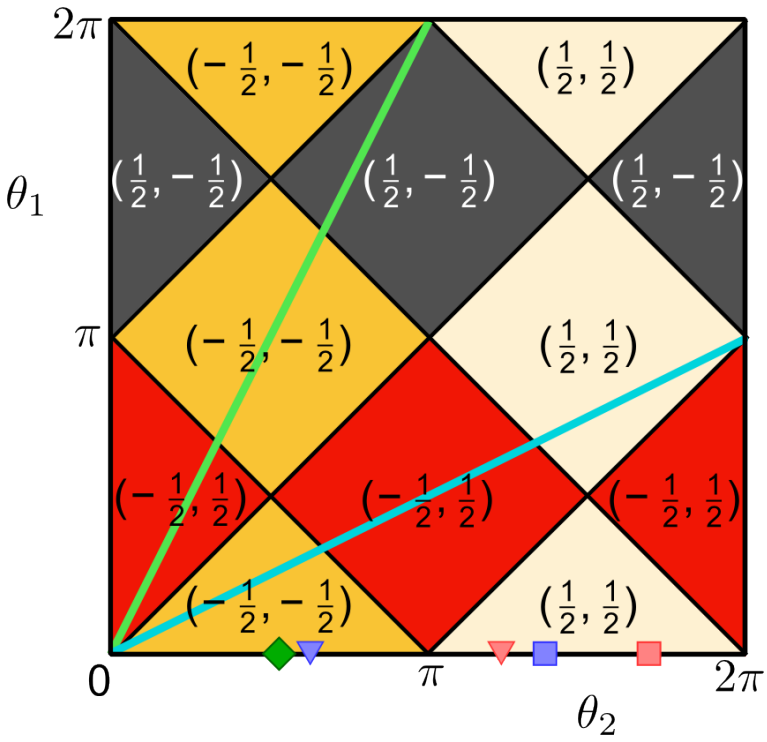

Figure 6.2: The value of the invariant $Q(0) \times Q(\pi)$ depending on the coin angles θ_1 and θ_2 for the case of an application of a split-step protocol in the scattering region. The parameters of the experimentally realised systems are given by the coloured markers and lines (explained in section 6.5). Figure from [75].

Figure 6.2 illustrates that the tuple (Q_0, Q_π) constitutes a topological invariant. It shows the value of this number depending on the coin angles θ_1 and θ_2. We see that (Q_0, Q_π) is robust to variations of the two coin angles as long as these stay within a certain topological

sector.

6.4 Experimental Implementation of the Scattering Approach

In order to see how we can experimentally access (Q_0, Q_π), we take a closer look at the lead-sample scattering system (see Figure 6.3).

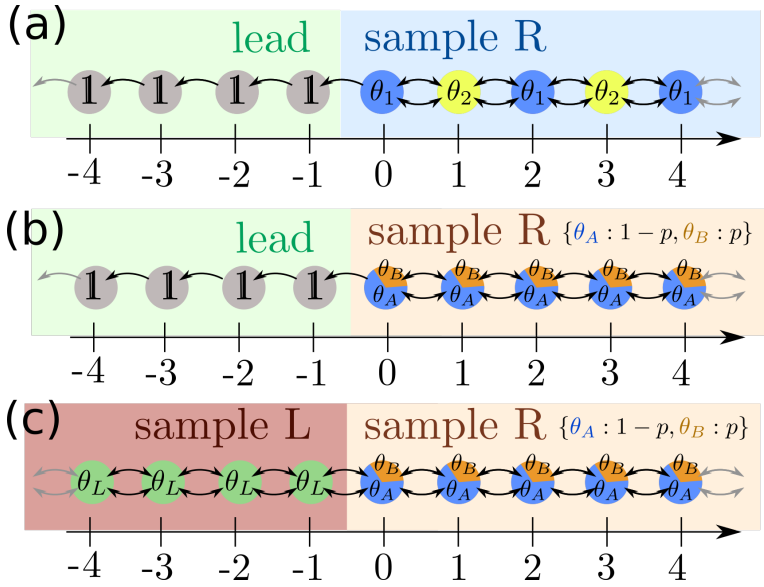

Figure 6.3: (a): Illustration of the graph configuration in the scattering setting: The left region of the graph constitutes the lead where the applied coin is the identity operation ($Id = \hat{C}(0°)$). The lead is also the region in which we conduct the phase-sensitive measurements. The scattering takes place in the right region (sample) where $\hat{C}(\theta_1)$ and $\hat{C}(\theta_2)$ are applied in an alternating way. This setting is used for the scans along the topological phase diagram shown in Figure 6.2. (b): Setting used for testing the robustness of the topological invariant. Here, one of the coins in the sample is the identity, while the other is either $\hat{C}(\theta_A)$ with probability p or $\hat{C}(\theta_B)$ with probability $p-1$. (c): Setting in which we interface two samples: In the left sample we apply $\hat{C}(\theta_L)$ or the identity. In the right sample the non-identity coin is either $\hat{C}(\theta_A)$ or $\hat{C}(\theta_B)$ with corresponding probabilities p and $p-1$. Figure from [75].

The sample is the region on the right where we apply either $\hat{C}(\theta_1)$ or $\hat{C}(\theta_2)$. The exact values of θ_1 and θ_2 as well as the sequence of their application depends on the concrete setting that is to be investigated. From here the light is scattered into the lead on the left where the identity operation is applied on all positions.
In order to obtain (Q_0, Q_π), we have to determine r_j which is the reflection amplitude at position -1, i.e. at the border between lead and sample, after the j-times application of

the unitary $\hat{U}$ on a state in horizontal polarisation initially localised at position 0:

$$r_j = \langle -1, V | \hat{U}^j | 0, H \rangle \tag{6.9}$$

With r_j the energy-dependent reflection matrix element can be written as the discrete Fourier transform of the reflection amplitudes:

$$r(\varepsilon) = \sum_{j=1}^{j\to\infty} e^{ij\varepsilon} r_j \tag{6.10}$$

For the eigenenergies $\varepsilon = 0$ and $\varepsilon = \pi$ present in our system this corresponds to either the sum or the alternating sum of the individual reflection amplitudes r_j.

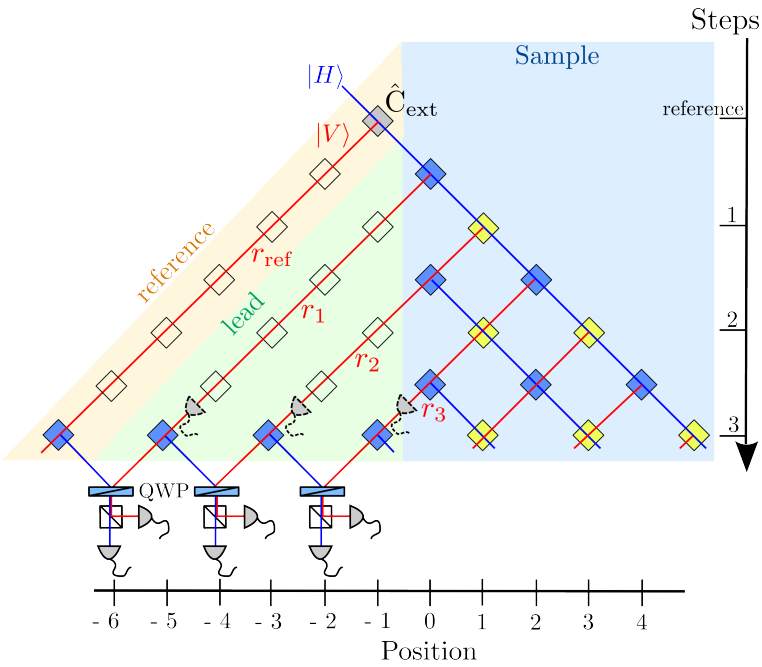

Figure 6.4: Illustration of the scheme implemented for measuring r_j including phase. The detector symbols in dashed lines indicate the positions where we measure the intensities, while the detector symbols drawn in solid lines mark the measurements for the read-out of the phases. The blue and yellow diamonds represent the application of the two different coins for the split-step scheme. Figure from [75].

Figure 6.4 shows the scheme implemented for determining r_j. The quantum walk evolves in the sample on the right side. From there intensity is scattered into the lead on the left.

Here, we find the r_j corresponding to different steps j on different positions of the read-out step, where we measure their intensities. Since the r_j constitute amplitudes, we also need to extract their phases. We extract the phase of r_1 by interfering it with a reference that is split-off with by the application of $\hat{C}_{\text{ext}}$ before the start of the split-step quantum walk. The phase of the subsequent r_j are then read-out by interfering one component of r_j with a component of r_{j-1}. This interference takes place in the step following the measurement of the intensities and requires a mixing coin, which is in this case a QWP at 45°.

6.5 Results for the Scattering Approach

6.5.1 Topological Phase Transitions

In a first experiment we want to verify that we can indeed access the topological invariants (Q_0, Q_π) as theoretically expected (see Figure 6.2). Consequently, we scan the values of θ_1 and θ_2 along the green line and along the turquoise line in Figure 6.2. These lines are given by the fact that in our experimental implementation one of the angles needs to have twice the value of the other: One angle (e.g. θ_1) is set statically with a Soleil-Babinet Compensator (SBC). An EOM then dynamically switches to either the identity in the lead by reversing the static polarisation rotation (i.e. rotating by $-\theta_1$) or to $\theta_2 = 2\theta_1$ by applying a certain voltage with either a positive or a negative sign. The corresponding sequence of coins is shown in Figure 6.3 (a).

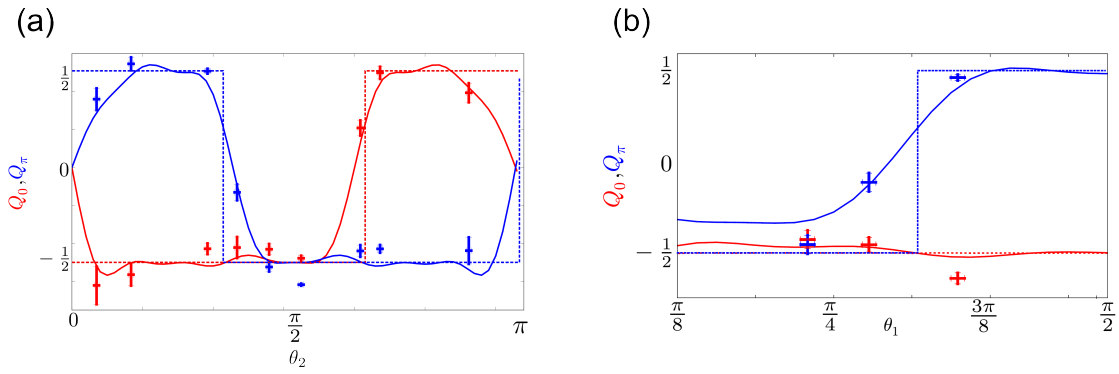

Figure 6.5: (a): The experimentally obtained and the simulated values of the topological invariant Q_0 (red circles resp. solid line) as well as the theoretical values for an infinite number of steps (dashed red line). The respective quantities for Q_π are marked in blue. The displayed data corresponds to a scan along the green line in Figure 6.2. The error bars are obtained via Monte-Carlo scans. (b): The topological invariants Q_0 and Q_π for a scan along the turquoise line in Figure 6.2. Figure from [75].

The results of this scan are shown in Figures 6.5 (a) and (b): The experimentally obtained and the simulated values of Q_0 for five steps, i.e. 10 roundtrips, are marked by the red

circles resp. the solid line, the expected theoretical values for an infinite number of steps by the dashed line. The corresponding quantities for Q_π are marked in blue. We observe that both experiment and numerics clearly exhibit the expected transition from -1/2 to + 1/2 resp. 1/2 to - 1/2 for scans along the green line (Figure 6.5 (a)) and along the turquoise line (Figure 6.5 (b)). Due to the finite size effects, i.e. the limited number of steps, however, it is not as sharp as it would be for a system with an infinite number of steps.
The error bars for this as well as for the other figures are obtained via Monte-Carlo scans for which we assume inaccuracies of 3% for the coupling efficiencies and of 1% for the SBC and EOM angle. We produce a 1000 samples with parameters randomly chosen within these ranges and take the resulting standard deviations for the error bars.

6.5.2 Robustness against Disorder

We expect topological invariants to be robust against disorder which leaves the system in the same topological sector. In order to experimentally observe this feature, we look at two different cases: In case one we pick two coins with angles $\theta_A = 1.68\pi$ and $\theta_B = 1.36\pi$ that correspond to the blue and the red square in Figure 6.2. In case two, the the two coins with $\theta_A = 0.63\pi$ and $\theta_B = 1.26\pi$ are represented by the blue and the red triangle. In case one the two coins belong to the same topological sector, while they are in different topological sectors in the second case. The arrangement of the coins is shown in Figure 6.3 (b). As the three possible switching states of the EOM are needed for implementing the identity as well as $\hat{C}(\theta_A)$ and $\hat{C}(\theta_B)$, the second coin in the sample region is chosen to be the identity as well. This choice of coins still allows to have them in either one or two topological sectors.
In our experimental setting, we apply $\hat{C}(\theta_B)$ with a probability p and $\hat{C}(\theta_A)$ with the probability $1 - p$. We scan p in 8 discrete steps ranging from 0 to 1 with $p = 0{,}1$ corresponding to minimum disorder and $p = 0.5$ to maximum disorder. For each of the 8 data points we produce 50 samples in which we choose randomly according to the respective probabilities at each side whether we apply θ_A or θ_B.

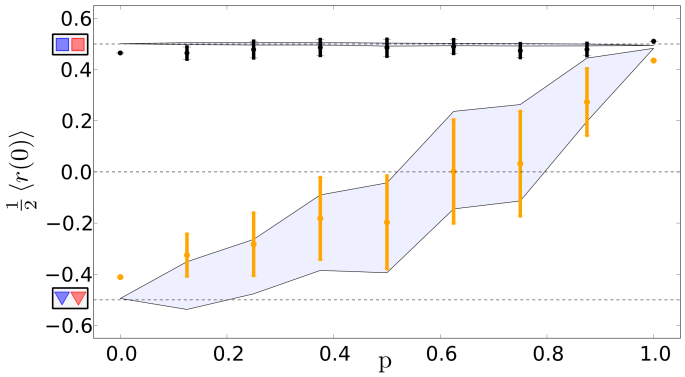

Figure 6.6: The average reflection matrix element $1/2\langle r(0)\rangle$ over the probability p with which $\hat{C}(\theta_B)$ is applied. The yellow markers correspond to case two where $\hat{C}(\theta_A)$ and $\hat{C}(\theta_B)$ belong to different topological sectors (triangles in Figure 6.2), while black markers refer to case one in which the two coins are located in the same topological sector (squares in Figure 6.2). The error bars on the experimental data are given by the standard deviation over the 50 measured patterns. The range of the standard deviation of the numerical simulations is indicated by the grey shaded region. Figure from [75].

We measure the average reflection matrix element $1/2\langle r(0)\rangle$ for both cases (see Figure 6.6): Case two exhibits a clear transition from -1/2 to + 1/2 as p increases. Furthermore, we observe significant fluctuations between the 50 individual samples for a certain probability value as indicated by the error bars on the yellow markers, which are obtained as the standard deviation of the individual values. For case one, on the other hand, we measure very similar values of $1/2\langle r(0)\rangle$ for all values of p and also the fluctuations between the individual samples (indicated by black error bars) are more than an order of magnitude smaller. We consequently see that case one exhibits the expected robustness against disorder, while it is not observed for case two.

6.5.3 Emergence of Edge States

Eventually, we experimentally study the emergence of edge states which are theoretically predicted to appear at the boundary of two topologically different bulks due to bulk-boundary correspondence [183]. The sequence of applied coins is depicted in Figure 6.3, (c): On the left side of the graph we no longer implement the lead, but another sample (sample L) in which the identity on even sites and $\hat{C}(\theta_L)$ on uneven sites with $\theta_L = 3/2\theta = 0.52\pi$ (green diamond in Figure 6.2) are applied in alternation. On the right side of the graph the identity on even sites is alternated with either $\hat{C}(\theta_A)$ or $\hat{C}(\theta_B)$ on uneven sites with $\theta_A = \theta = 1.68\pi$ and $\theta_B = 2\theta \; mod \; 2\pi = 1.36\pi$ (blue and red square in Figure 6.2). Note that the identity in this scheme is only applied on even sites that would only be occupied in steps with even numbers. These steps do not need to be actually carried out, but can be accounted for implicitly, allowing to implement twice the number of steps in split-step quantum walk for a given number of round trips. As a consequence of this and the

omission of the read-out procedure at the end, we are no longer limited to 5 steps as for the measurement of the reflection matrices, but can now investigate 13 steps.
Again, we scan the probability p and thus the strength of the disorder by measuring 50 randomly generated patterns for each value of p. In addition, we look at a reference system where the coins in the two halves of the graph are $\hat{C}(\theta_A)$ and $\hat{C}(\theta_B)$ and consequently are in the same topological sector.
We expect the edge states to be localised at the boundary and thus quantify the degree of localisation with the probability P_{Loc} to find the walker on the six innermost positions, i.e. in the interval [-3,3]:

$$P_{\text{Loc}} = \sum_{i=-3}^{3} P_i \tag{6.11}$$

The degree of localisation at the boundary after 13 steps is shown in Figure 6.7, (a): We observe values of P_{Loc} of at least ≈ 0.8 for all values of p. Even when considering the error bars, the localisation is significantly stronger than in the reference system. The error bars are obtained as the standard deviation over the 50 individual patterns for the disordered systems and by Monte-Carlo scans for the configurations without disorder, i.e. those with $p = 0$ and $p = 1$ and the reference system. Furthermore, the localisation is robust to disorder as the ordered instances ($p = 0{,}1$) exhibit localisation values that do not significantly differ from the most disordered case ($p = 0.5$). The similar degrees of localisation for $p = 0$ and $p = 0.5$ resp. the large difference to the reference system are also reflected by the intensity plots (Figures 6.7 (b)-(d): While the wavefunction remains localised at the boundary in (b) and (c), it clearly spreads out in (d). The fact that the localisation is also present in the ordered configurations rules out that it is caused by Anderson localisation [74].

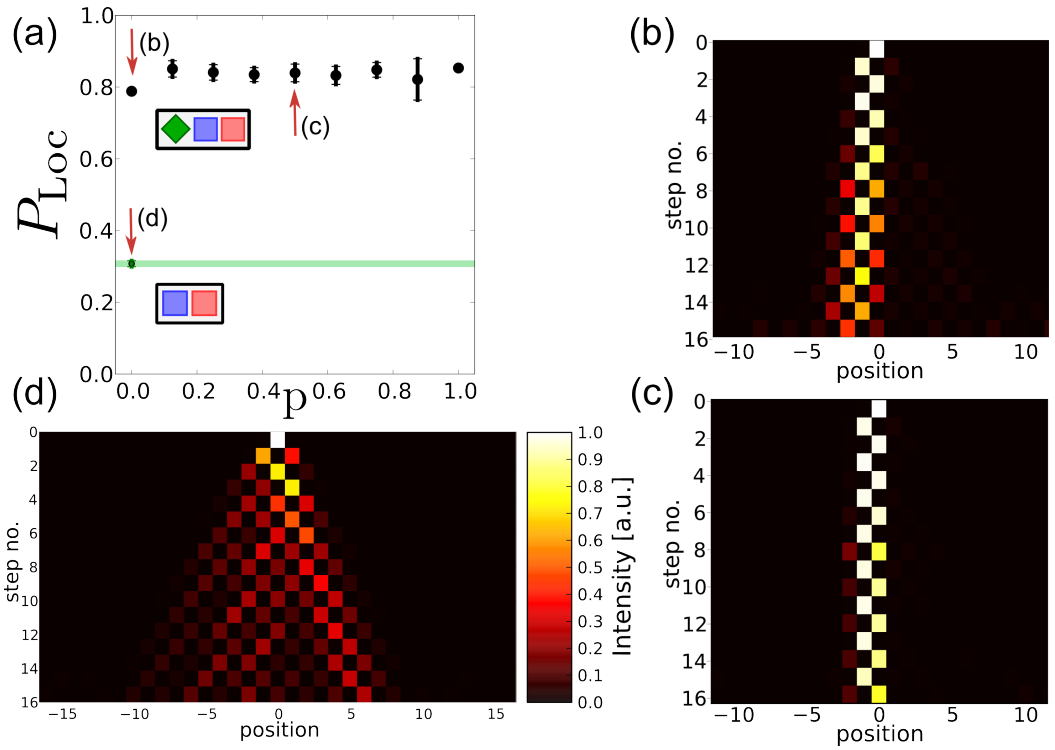

Figure 6.7: (a): The degree of localisation at the boundary P_{Loc} after 13 steps of the walker for different values of p. The value for the reference system is marked by the green shaded region. The error bars for the disordered systems are given as the standard deviation over the 50 individual patterns, while they are obtained using Monte-Carlo scans for the reference system and the ordered instances. (b),(c) and (d): The step-wise evolution of the walker's distribution of intensity over positions. The corresponding configurations are marked in subfigure (a). Figure from [75].

6.6 Measuring Eigenvalues of Edge States

The previously described scattering approach allows for accessing topological invariants via reflection matrices. Furthermore, we can observe edge states localised at bulk-boundaries. However, the eigenvalues associated with the walk operator remain outside of the reach of this method. In case of disorder, only determining the explicit eigenvalues of a localised state allows for distinguishing whether this localisation is due to Anderson localisation [74] or topological protection [184], [185].
In order to extend the range of experimentally accessible topological properties to these eigenvalues, we implement a split-step quantum walk with decoupling that allows for measuring eigenvalues via a phase reference method. The results of the experiments described in the following are published in [76].
We restrict our treatment of the theoretical aspects of this experiment to a necessary

minimum, since more detailed accounts can be found in the corresponding publications by our theory partners [180, 186, 48].
In contrast to the scheme presented previously, the topological invariants with which we classify different configurations of the walk are no longer reflection amplitudes, but symmetry indices (see Figure 6.9, (a)).

6.6.1 Decoupling

The important difference to the bulk-boundary setting implemented previously for observing edge states (see section 6.5.3, illustrated in Figure 6.3) is the decoupling: By switching a reflection coin we split the graph in two halves with negligible transition amplitude between them. In such a setting exponentially localised eigenstates are predicted at the interface for non-trivial topological phases by bulk-boundary correspondence [180, 48].
In the region to right of the decoupling we can describe the split-step quantum walk with chiral, particle-hole and time-reversal symmetry as in section 6.2.

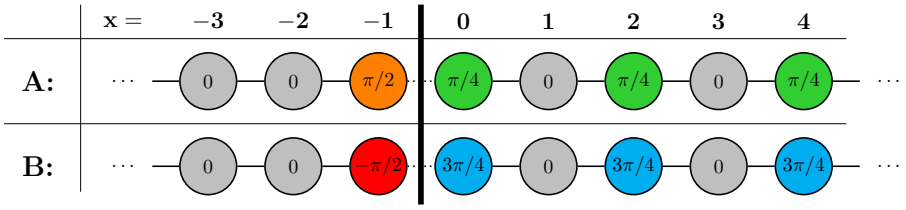

Figure 6.8: Schematic picture of the coin angle set-up for the walk (6.3) in our two settings. The coin angles at $x = -1$ decouple the walk between $x = -1$ and $x = 0$. Figure modified from [76].

In order to observe the emergence of edge states corresponding to different eigenvalues, we consider two settings for the values of the coin. In both of them, the quantum walks exhibit a non-trivial symmetry index and are decoupled between the positions -1 and 0 (see Figure 6.8):

Setting A:

$$\theta_2 = \pi/4 \qquad \text{and} \qquad \theta_1(x) = \begin{cases} \pi/2 & x = -1 \\ 0 & \text{else} \end{cases} \tag{6.12}$$

Setting B:

$$\theta_2 = 3\pi/4 \qquad \text{and} \qquad \theta_1(x) = \begin{cases} -\pi/2 & x = -1 \\ 0 & \text{else} \end{cases} \tag{6.13}$$

The decoupling coin $\theta_1(x)$ is defined such that it decouples the walk on the even sub-lattice.

Since we are only interested in the edge states of the decoupled walk located in the right half, we do not need to specify the left half chain, leaving it available for the routing of a phase-reference.
The symmetry indices for both settings are in the (non-trivial) -1 sector (see Figure 6.9, (a)), consequently we expect the emergence of edge states, as . It depends on the specific decoupling in the two settings whether the eigenfunctions correspond to eigenvalue +1 or -1. In our case, setting **A** is associated with the eigenvalue -1 and setting **B** with eigenvalue +1.

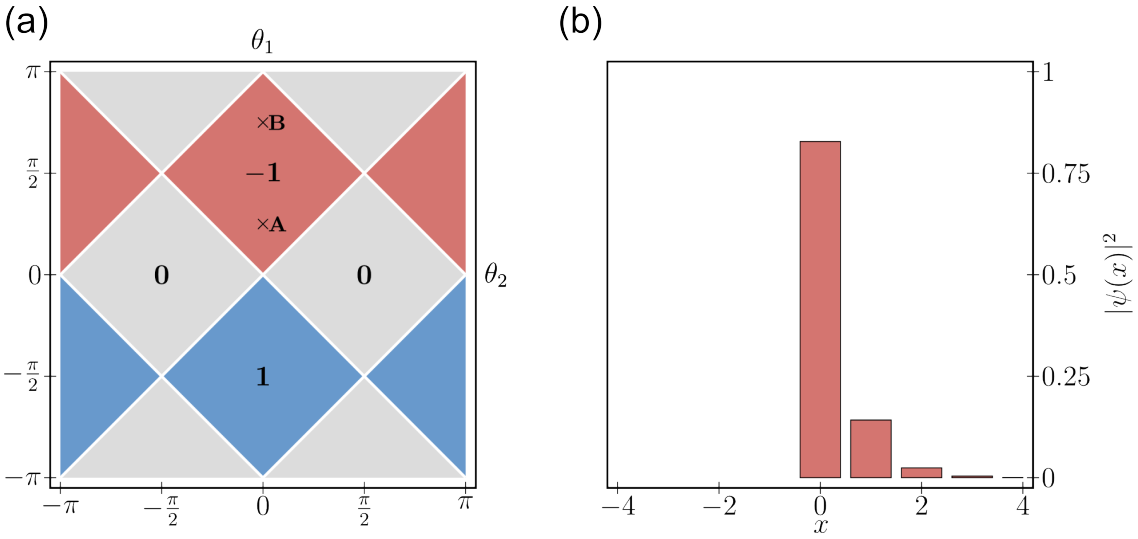

Figure 6.9: (a): Parameter plane for the split-step walk (6.3) with regions of constant symmetry index (left). The crosses mark the parameters for our two settings (**A**/**B**).
(b): Intensity distribution $|\psi(x)|^2$ of the corresponding eigenfunction (right). The distribution is the same for both settings. Figure from [76].

The eigenfunctions $\varphi_R(2x)$ of $\hat{U}$ (see (6.3)) located in the right half are given by the following expression with the normalisation factor $c = \left((1+\sqrt{2})(1-\sin(\theta_2)\right)^{-\frac{1}{2}}$ (see also Figure 6.9, (b)):

$$\varphi_R(2x) = \begin{cases} 0 & x < 0 \\ c(1-\sqrt{2})^x \begin{pmatrix} i\cos(\theta_2) \\ 1-\sin(\theta_2) \end{pmatrix} & x \geq 0, \end{cases} \tag{6.14}$$

6.6.2 Eigenstate Distillation

The exponentially localised edge states according to (6.14) cannot be excited directly with an input state restricted to one position, but only be approximated. In order to do so, we start with an input state at position 0 (see Figure 6.10) that exhibits some overlap with

the localised eigenstate. As the walker's wave function evolves with an increasing number of steps, the components that do not overlap with the eigenstate propagate away from the boundary, so that the edge state is approximated with increasing quality on the positions near the boundary. Consequently, we focus our investigation to the three inner positions and renormalise the intensity here to 1. The quality of the approximation is quantified via the similarity which can attain values between 0 (no overlap of intensities) and 1 (perfect overlap of intensities):

$$d = \left| \sum_x \sqrt{P_{H,x}^{(\text{theo})} \cdot P_{H,x}^{(\text{exp})}} + \sum_x \sqrt{P_{V,x}^{(\text{theo})} \cdot P_{V,x}^{(\text{exp})}} \right| \tag{6.15}$$

In the above expression, we sum up the square roots of the products of the theoretically expected probabilities $P^{(\text{theo})}$ and the experimentally obtained probabilities $P^{(\text{exp})}$ for positions x ranging from 0 to 3 and both polarisations H and V.

6.6.3 Phase-Reference Method

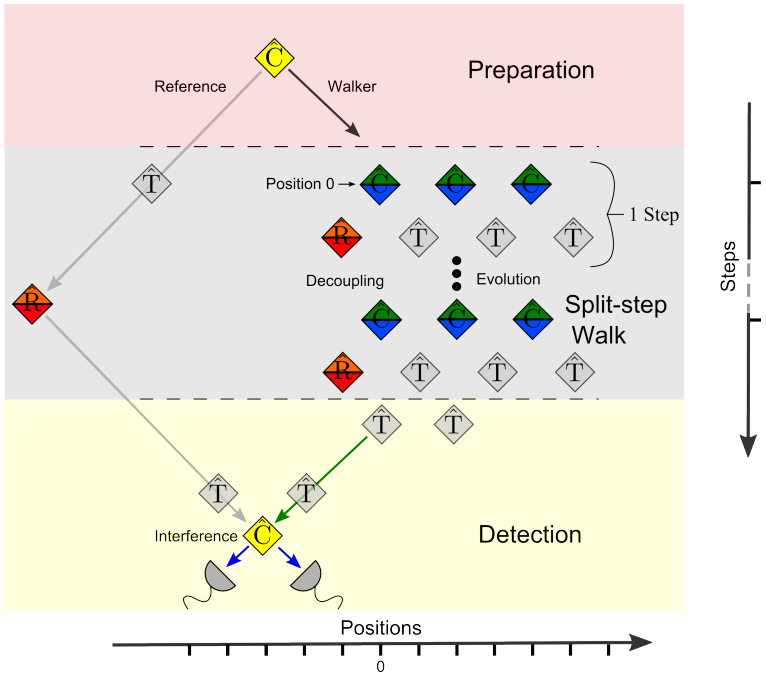

Figure 6.10: Illustration of the implementation of the phase-reference method: An initial coin operation $\hat{C}$ splits the light into two components, one of which will constitute the phase-reference, the other one the walker. The walker undergoes the split-step walk with decoupling, while the reference is routed via transmission ($\hat{T}$) and reflection operations ($\hat{R}$). Eventually, the reference is brought to interference with a certain mode of the walker having evolved according to the split-step protocol. Figure from [76].

The implementation of the decoupling scheme frees the left side of the graph for routing of a phase-reference that can be harnessed to obtain the phase of the individual position and polarisation modes of the walker. The phase-reference method is illustrated in Figure 6.10: We use an external coin to split the initial pulse into one component that is the walker and one that constitutes the phase-reference.
The walker undergoes the split-step quantum on the right half chain where one step corresponds to two round trips, one in which we apply the walk coin and one in which the identity as well as the reflective coin realising the decoupling is applied. Note that the steps with uneven positions cannot be conducted implicitly, as we need to decouple the walk between positions 0 and -1 by switching a reflective coin. After either 6, 7 or 8 steps of the quantum walk evolution, we no longer apply the quantum walk unitary, but separate a certain mode from the others and direct it such that it will interfere with the phase-reference.
This phase-reference is routed on the left half-chain. The routing is carried out by a

sequence of transmissions and one reflection that ensures that the reference stays separated from the right half-chain and losses as little intensity as possible.
The read-out component and the reference are interfered at a mixing coin (in this case the balanced Hadamard coin $\hat{C}_{\mathrm{Had}}$)).This operation is described by the following equation with I_{w} and I_{r} denoting the intensities of the walker resp. the reference and α_{w} resp. α_{r} their phases:

$$|\Phi\rangle = \hat{C}_{\mathrm{Had}} \begin{pmatrix} e^{i\alpha_{\mathrm{w}}}\sqrt{I_{\mathrm{w}}} \\ e^{i\alpha_{\mathrm{r}}}\sqrt{I_{\mathrm{r}}} \end{pmatrix} = \frac{1}{\sqrt{2}} \begin{pmatrix} 1 & 1 \\ 1 & -1 \end{pmatrix} \begin{pmatrix} e^{i\alpha_{\mathrm{w}}}\sqrt{I_{\mathrm{w}}} \\ e^{i\alpha_{\mathrm{r}}}\sqrt{I_{\mathrm{r}}} \end{pmatrix} \tag{6.16}$$

Polarisation-resolved detection consequently yields the following intensities I_{H} and I_{V} for the horizontal and the vertical mode:

$$\begin{aligned} I_{\mathrm{H}} &= \frac{1}{2}(I_{\mathrm{w}} + I_{\mathrm{r}} - 2\sqrt{I_{\mathrm{w}}} \cdot \sqrt{I_{\mathrm{r}}} \sin(\alpha_{\mathrm{r}} - \alpha_{\mathrm{w}}))) \\ I_{\mathrm{V}} &= \frac{1}{2}(I_{\mathrm{w}} + I_{\mathrm{r}} + 2\sqrt{I_{\mathrm{w}}} \cdot \sqrt{I_{\mathrm{r}}} \sin(\alpha_{\mathrm{r}} - \alpha_{\mathrm{w}}))) \end{aligned} \tag{6.17}$$

With theses quantities we can determine the phase difference between the reference and a certain component of the walker:

$$M := \sin(\alpha_{\mathrm{r}} - \alpha_{\mathrm{w}}) = \frac{I_{\mathrm{V}} - I_{\mathrm{H}}}{2\sqrt{I_{\mathrm{w}}} \cdot \sqrt{I_{\mathrm{r}}}} \tag{6.18}$$

The M-parameter given by the above expression is not an injective function, but still allows for the clear distinction of cases with eigenvalue 1 and those with eigenvalue -1.
In our experiment, we monitor the step-wise evolution of the M-parameter for a certain component. Here, we expect from step to step a change of the walker's phase by $\Delta\alpha_{\mathrm{w}} = \pi$ for setting **A** with eigenvalue -1 and by $\Delta\alpha_{\mathrm{w}} = 0$ or integer multiples of 2π for setting **B** with eigenvalue +1. On the other hand, the phase α_{r} of the reference is assumed to be constant with changing step numbers, so that the step-wise evolution of the M-parameter is expected to reveal the eigenvalue of the walk unitary.
The read-out is conducted in steps 6 to 8 for the two polarisation modes at each of the three positions on the right closest to the boundary. Also considering that we are investigating two different settings, we end up with 36 data sets that have to be taken.

6.6.4 Evolution of the Wave Function

Figures 6.11 (a) and (b) show the measured intensities of the walker for an evolution in a scheme similar to the one sketched in Figure 6.10: The split-step QW takes place over 6 steps (12 round trips) on the right side of the graph, while the reference is routed on

the left side of the graph. Afterwards, a certain mode of the walker's wave function (in this example the vertical mode (a) resp. the horizontal mode at positions 0 (b), marked by a green arrow) is brought to interference with the reference (marked by a grey arrow). This read-out is shown in more detail in Figures 6.11 (c) and (d), where we can see how both are directed to the position where a mixing coin (marked in yellow) is applied. The intensity in the two modes marked by the detector symbols is recorded to extract the M-parameter according to (6.18).
In addition, Figures 6.11, (a) and (b) also serve to illustrate the distillation of the localised eigenstates, as we can observe how the components not overlapping with the eigenstate are propagating away from the boundary, while those that do overlap stay.

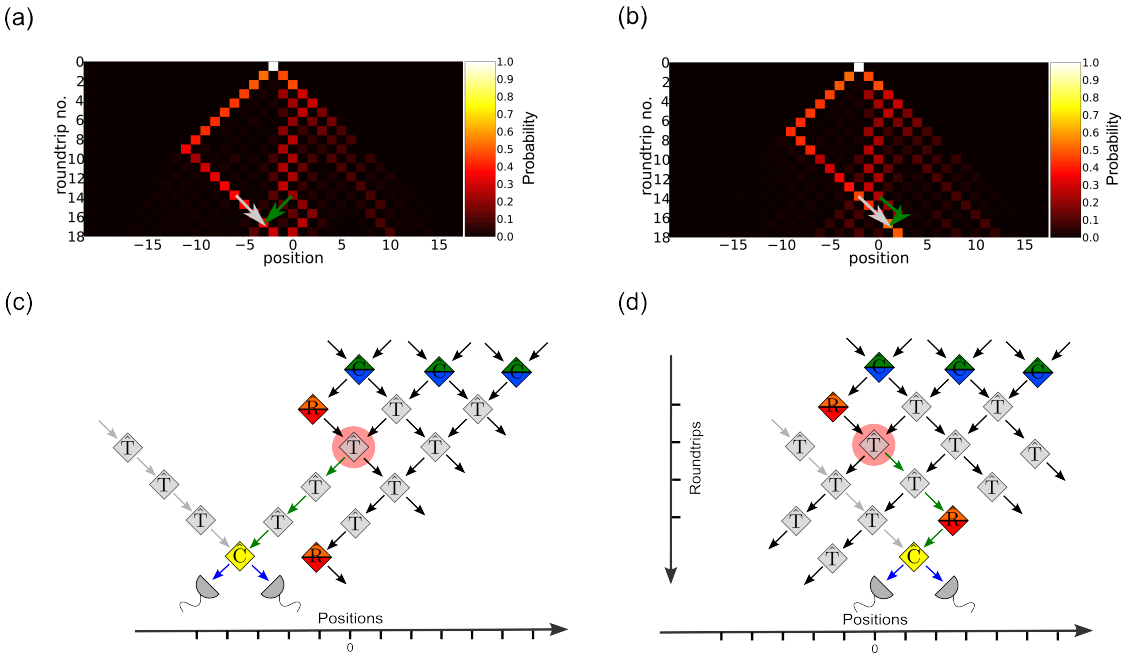

Figure 6.11: (a) and (b): The walker's intensity distribution for an split-step QW evolution over 6 steps (12 round trips) and subsequent read-out of the vertical (a) resp. the horizontal mode (b) at position 0. Subfigures (c) (vertical polarisation) and (d) (horizontal polarisation) show the read-out in more detail: The position marked in red is routed (marked by green arrow) to the position marked in yellow where it interferes with the reference (marked by white arrow). The position of the interference is such that it allows for separating the read-out mode from the others and for having the read-out in the same step for both polarisations. In addition, reflection operations can be used for preventing that light from other positions reaches the modes where the outcome of the interference is detected. Figure from [76].

Figure 6.12 shows the probability distribution in step 8 (i.e. round trip 17) of the split-step QW. The phase-reference is represented by the large horizontal bar at position -2, the eigenstate is expected at positions 0-4, which are the three occupied positions closest to

the boundary. The intensity at positions around 10 are the modes not overlapping with the eigenstate which are propagating away from the boundary.

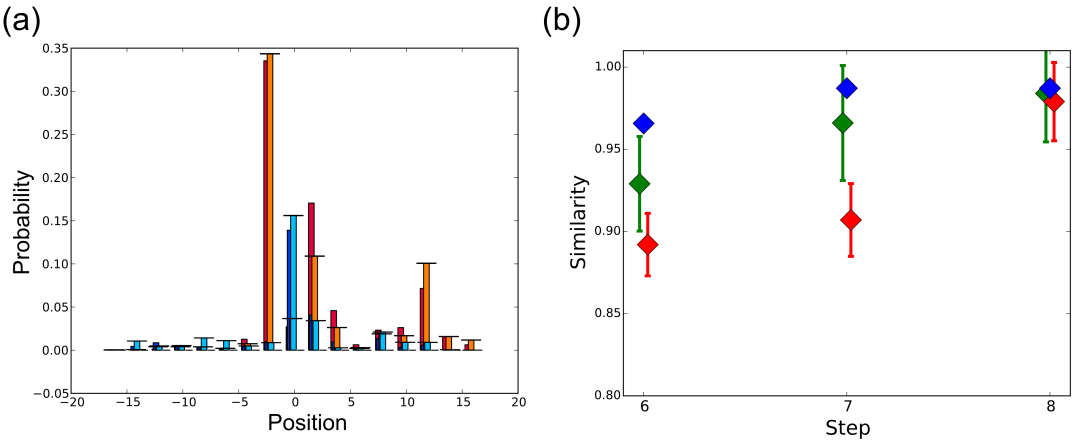

Figure 6.12: (a): Probability distribution in step 8 (round trip 17) of the split-step QW. Orange resp. light blue bars represent the measured intensities in horizontal resp. vertical polarisation, while the numerically obtained values correspond to dark blue resp. red bars. **(b):** The similarities in respect to the ideal eigenstate for steps 6-8: The values for the numerically calculated states are given by the blue symbols, the values for experimentally obtained intensities by the green (eigenvalue +1) resp. red markers (eigenvalue -1). Note that all markers correspond to integer step numbers, although they might be slightly shifted on the horizontal axis for better readability. The error bars for the similarity are determined in Monte-Carlo scans assuming uncertainties of the coupling efficiency of 2% and an error of the coin angle of 2°. Figure from [76].

The overlap of the measured intensities with those of the theoretically expected eigenstate is quantified according to (6.15). The blue symbols Figure 6.12 (b) show the evolution of the similarities from step 6 to 8 for a numerically computed state accounting for the finite step number, but no other experimental imperfections. Note that these similarities are the same for both eigenvalues. The green (resp. red) symbols on the other hand correspond to the measured intensities for the case with eigenvalue +1 resp. for the case with eigenvalue -1. These similarities are lower than those for the numerically values, which indicates that they are affected by experimental imperfections in addition to the limited step numbers. Note that the similarities are slightly worse for the eigenvalue -1 case, as it requires higher voltages of the EOM, thereby increasing experimental imperfections due to acoustic resonances (see section 4.3.2). With values of at least $\approx 90\%$ they, however, still reflect a good experimental approximation of the ideal eigenstates. The error of the experimental values are obtained in Monte-Carlo simulation where we generate a 1000 different random settings assuming an error of the coupling efficiency of 2% and an error of the coin angle of 2°. The same applies for the error bars on the rest of the data shown in this section. The errors resulting from the Pockels cell's operation are, on the other

hand, hard to quantify in an error model as they affect individual switchings in a way that is hard to predict.

6.6.5 Experimental Eigenvalues

Having verified a good experimental approximation of the ideal eigenfunctions, we investigate the eigenvalues by monitoring the step-wise evolution of the M-parameter.
Figures 6.13 (a) and (b) show the evolution of the M-parameter at position 0 for horizontally (a) as well as vertically polarised light (b) from step 6 to step 8. In setting **A** (orange symbols) the M-parameter clearly exhibits a sign flip in its step-wise evolution, while it remains around -1 in setting **B** (blue symbols).

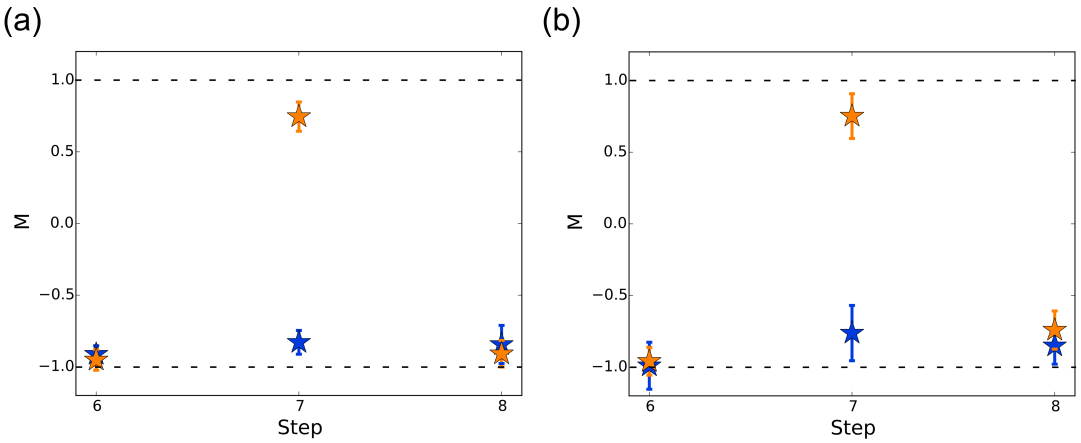

Figure 6.13: Evolution of the M-parameter from step 6 to step 8 for both horizontal light (a) and vertical light (b) at position 0. The orange markers correspond to setting **A**, where a sign flip is clearly visible, while it is absent for setting **B** (blue markers). The error bars are obtained in Monte-Carlo scans with the same parameters as for Figure 6.12. Figure from [76].

The same qualitative behaviour is observed for position 1 (see Figure 6.14). However, the limits of this method become visible for vertical polarisation in step 8, where the exponential amplitude scaling does not leave sufficient intensity for a reliable read-out.

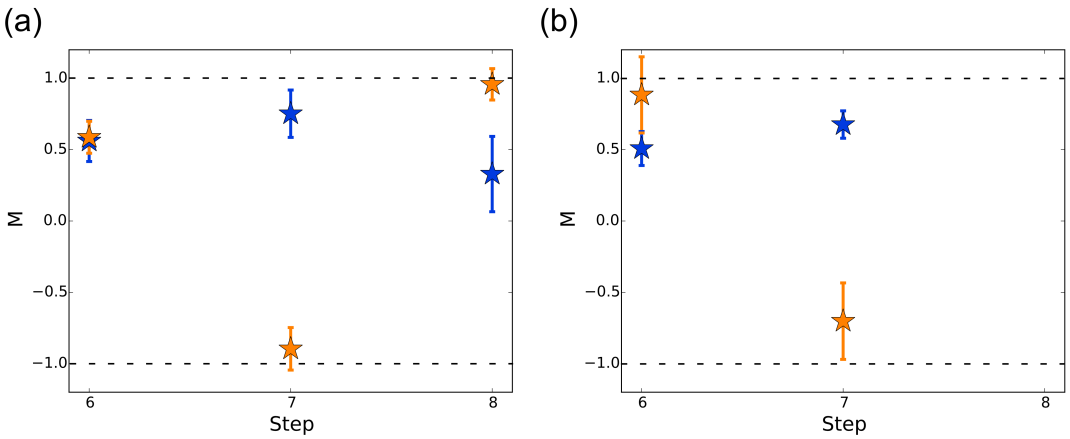

Figure 6.14: Evolution of the M-parameter at position 1, the other parameters are the same as in Figure 6.13. Note that the read-out for vertical polarisation in step 8 is no longer possible due to low intensities. Figure from [76].

In conclusion, we have achieved in our experimental system a good approximation of the theoretically expected eigenstate. By accessing the eigenvalues of the walk operator, we extend the range of experimentally accessible signatures of topological properties.

6.7 Supersymmetric Polarisation Anomaly

Eventually, we explore a system where we again alternately apply two different coins, but analyse it as a single-step quantum walk system. This time the analysis focuses on the k-space representation. Here, we find that chiral symmetry together with a unitary version of supersymmetry gives rise to anomalously polarised midgap states. The results have been published in [105], for which the theoretical background has provided by our theory collaborator.

6.7.1 Midgap States with Anomalous Polarisation

The midgap states can be observed when interfacing two topologically distinct systems. Figure 6.15, (a) shows the sequence of coins applied for such a configuration. The red and blue boxes mark unit cells. Here, the order of polarisation rotation angles θ_1 and θ_2 is exchanged for each cell in regard to the neighbouring one. The polarisation of the localised midgap states trapped by the interface is illustrated in Figure 6.15, (b).

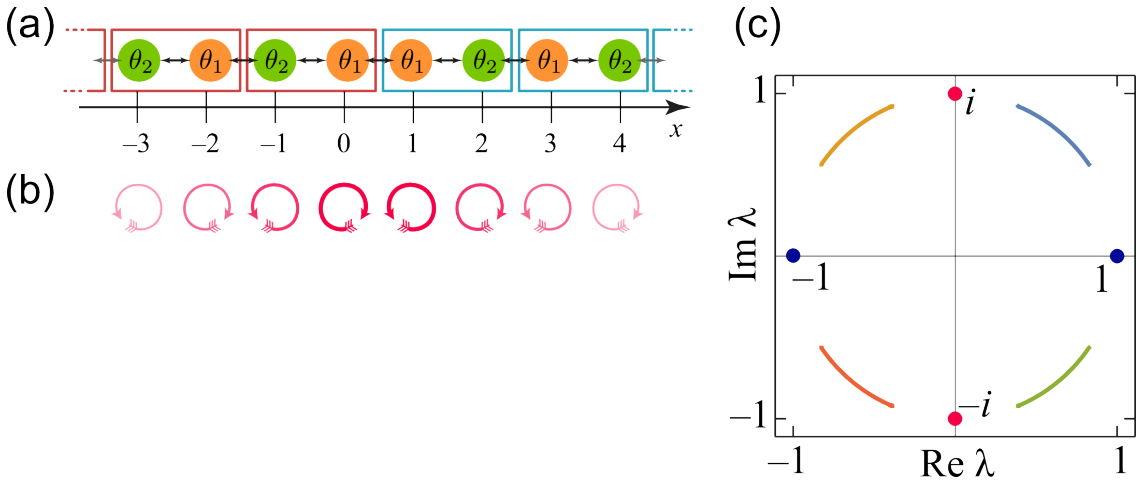

Figure 6.15: (a): Coin sequence applied for interfacing two topologically distinct systems. The positions of polarisation rotation angles θ_1 and θ_2 are exchanged for neighbouring cells. (b): The polarisation of the localised midgap states for each position. (c): The quasi-energy band structure for $\lambda(k) = e^{-i\varepsilon(k)}$ which exhibits four symmetric band. The shown values correspond to $\theta_1 = 1$ and $\theta_2 = 0.2$. The experimentally realised midgap states are at $\lambda = \pm i$ (marked by red dots). Figure modified from [105].

The periodic system consisting of the two-site unit cells is analysed with Floquet-Bloch theory [46, 47], yielding the following eigenvalue equation for the walker's wavefunction $\psi(k)$ with the quasienergy bands $\lambda(k) = e^{-i\varepsilon(k)}$:

$$u(k)\psi(k) = \lambda(k)\psi(k) \tag{6.19}$$

Here, $u(k)$ denotes the walk operator in k-space:

$$u(k) = \begin{pmatrix} 0 & \sigma_x f_{-k} \sigma_x \hat{C}(\theta_2) \\ f_k \hat{C}(\theta_1) & 0 \end{pmatrix} \tag{6.20}$$

In the above equation σ_x stands for the Pauli matrix and the matrix f_k is defined as follows:

$$f(k) = \begin{pmatrix} 1 & 0 \\ 0 & e^{ik} \end{pmatrix} \tag{6.21}$$

Four symmetric bands $\lambda_1(k) = \lambda_2^*(k) = -\lambda_3(k) = -\lambda_4^*(k)$ can be deduced from the eigenvalue equation (see Figure 6.15, (c)). We find gaps between the bands at $\lambda = \pm 1$ and $\lambda = \pm i$. The experimentally realised midgap states with circular polarisation are at

$\lambda = \pm i$ (marked by red dot). In order to derive their origin, we conduct a basis change to the symmetric basis:

$$\begin{aligned} |H'\rangle &= \cos(\varphi/2)\,|H\rangle + i\sin(\varphi/2)\,|V\rangle \\ |V'\rangle &= \cos(\varphi/2)\,|V\rangle + i\sin(\varphi/2)\,|H\rangle \end{aligned} \tag{6.22}$$

In this basis, the walk operator from (6.20) obtains the following form:

$$u^{'}(k) = \begin{pmatrix} 0 & \hat{C}(\varphi_1/2)\sigma_x f_{-k}\sigma_x \hat{C}(\varphi_2/2) \\ \hat{C}(\varphi_2/2) f_k \hat{C}(\varphi_1/2) & 0 \end{pmatrix} \tag{6.23}$$

We find two symmetries for $u^{'}(k)$, namely $u^{'\dagger}(k) = \sigma_y u^{'}(k)\sigma_y$ and $u^{'}(k) = -\Sigma_z u^{'}(k)\Sigma_z$ with σ_y being the Pauli matrix operating on the polarization degrees of freedom and Σ_z the Pauli matrix acting on two positions in the unit cell.
Consequently, we find the following relation connecting the eigenvalues λ and σ_y:

$$0 = \psi^{\dagger}(\sigma_y u^{'} - u^{'\dagger}\sigma_y)\psi = (\lambda - \lambda^{-1})\psi^{\dagger}\sigma_y\psi \tag{6.24}$$

Unless $\lambda = \pm 1$, the condition requires the expectation values $\langle\sigma_y\rangle$ to be 0 which means that the circular parts of the states average out over a unit cell in the H'/V' basis.
In addition, σ_y and Σ_z are related to λ according to the following condition:

$$0 = \psi^{\dagger}(\Sigma_z\sigma_y u^{'} + u^{'\dagger}\Sigma_z\sigma_y)\psi = (\lambda + \lambda^{-1})\psi^{\dagger}\Sigma_z\sigma_y\psi \tag{6.25}$$

From the above expression we can derive the condition $\langle\Sigma_z\sigma_y\rangle = 0$ unless $\lambda = \pm i$ which signifies that the circular parts of the states do not average out over a unit cell. Consequently, only states with vanishing circular components, i.e. linearly polarised states, can fulfil (6.24) and (6.25) simultaneously, unless $\lambda = \pm 1, \pm i$. This condition distinguishes anomalously polarised midgap states with $\lambda = \pm 1, \pm i$ which we experimentally access for $\lambda = \pm i$ as described in the following.
Note that the symmetry properties exhibited by the unitary $u(k)$ are analogous to those of a supersymmetric Hamiltonian which is why we speak of a supersymmetric polarisation anomaly in this chapter.

6.7.2 Experimental Investigation of Midgap States

We experimentally realise both the bulk and the interface configuration. In the bulk configuration coins with rotation angles $\theta_1 = 1.29\pi$ and $\theta_2 = 0.17\pi$ are applied alternately in the same sequence on the whole graph. In contrast, the interface configuration incorporates a

change in the order of the coins between sites $x = 0$ and $x = 1$. The walker is expected to exhibit different degrees of trapping at this interface depending on its initial polarisation. Figures 6.16 (a)-(d) show chessboard diagrams of the walker's intensity distribution for the interface configuration ((a) and (b)) as well as the bulk configuration ((c) and (d)). Furthermore, horizontal input polarisation ($|H\rangle$) is investigated with results shown in Figures 6.16, (a) and (c), while the results for the input polarisation $\hat{C}_{\mathrm{QWP}}(137°)\,|H\rangle$ are given in Figures 6.16, (b) and (d). Already here we can see that the trapping depends on both the graph configuration and the initial polarisation.
This dependency is investigated in a more systematic way as shown in Figure 6.16, (e): Depending on the polarisation rotation angle α for the initial state we obtain varying probabilities of finding the walker at position 0. The orange resp. green markers give the experimental values after 13 steps for the interface resp. the bulk configuration, while the solid resp. dashed lines give numerically calculated values for 13 resp. 100 steps. We see that the interface configuration exhibits a significantly higher degree of trapping independent of the initial polarisation. For the interface configuration the trapping is highest for linear input polarisation and lowest for circular polarised light, while for the bulk configuration the intensity at position 0 peaks for an input polarisation given by $\hat{C}_{\mathrm{QWP}}(45°)\,|H\rangle$ and shows little dependency on α for values greater than 100°. Note that the relatively high probability to find the walker at position 0 for $\alpha = 45°$ seems to be a result of the relatively small measured step number, as it is expected to be significantly lower for 100 steps.

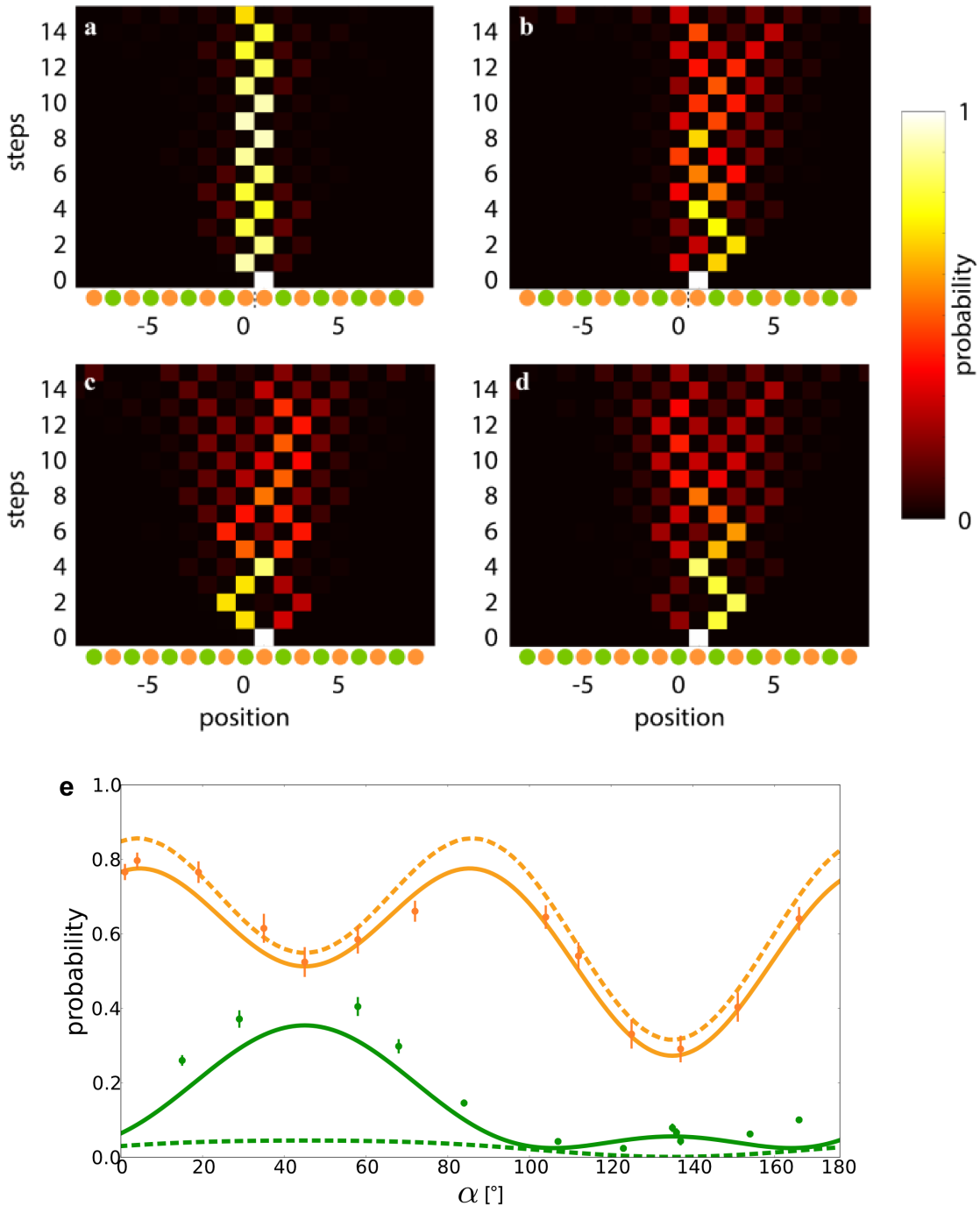

Figure 6.16: (a)-(d): Chessboard diagrams for the walker's evolution for both the interface configuration ((a) and (b)) as well as the bulk configuration ((c) and (d)). (a) and (c) correspond to horizontal ($|H\rangle$) input polarisation, (b) and (d) to $\hat{C}_{\mathrm{QWP}}(137°)\,|H\rangle$. The impact of the initial polarisation on the trapping, i.e. the intensity at position 0 after 13 steps, is shown in (e): The orange markers (experimental data) resp. curves (numerical data) correspond to the interface configuration, the green markers and curves to the bulk configuration. The solid lines give the numerical values for 13 steps, the dashed lines for 100 steps. Figure from [105].

The polarisation dependence of the excitability of the midgap state results from the system's symmetry properties. In contrast to the input states, symmetry constrains imply horizontal polarisation for the bulk states and circular polarisation alternating from site to site (see Figure 6.15, b) for the interface states [105]. We perform a state tomography after the walker's evolution over 17 steps in order to measure its full polarisation state for the interface configuration. This is done by conducting measurements in the horizontal-vertical, diagonal-anti-diagonal and right- and left-handed circular basis, thus allowing for determining the Stokes parameters S_i and the corresponding density matrices $\rho = 1/2 \sum_{i=0}^{3} S_i \sigma_i$. The measured density matrices are shown in Figure 6.17. Note that these are presented in the symmetric basis as defined by (6.22).

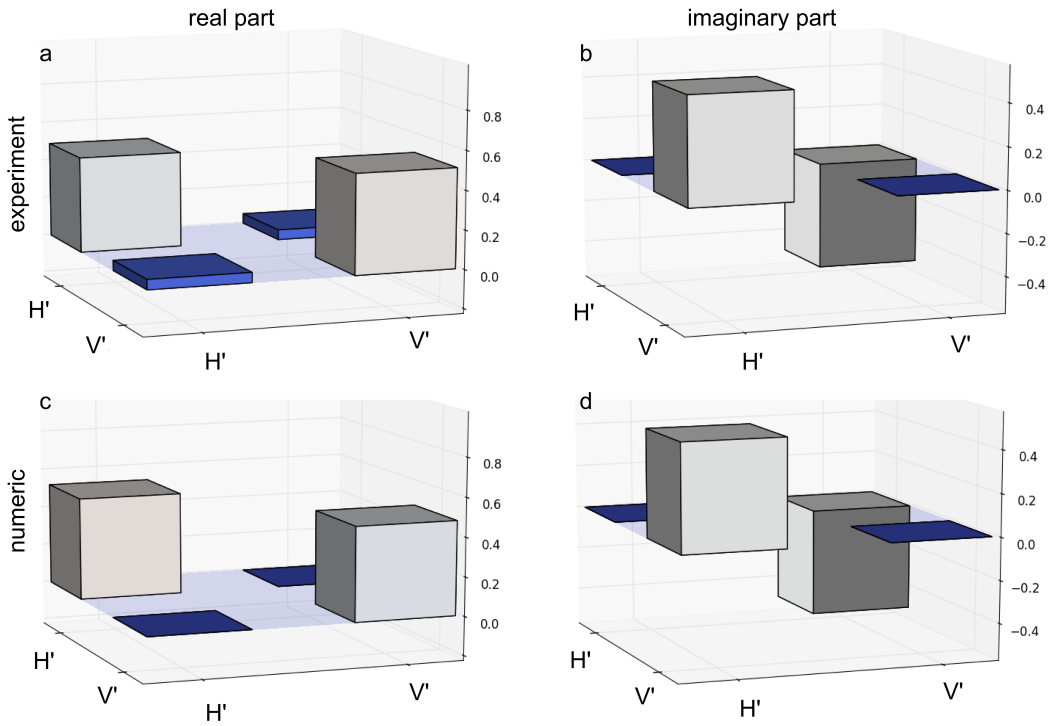

Figure 6.17: The density matrices for the trapped midgap state at position $x = 0$ after an evolution over 17 steps in the interface configuration. The experimental results for the real and imaginary part are shown in (a) and (b), the numerical predictions in (c) and (d). The H'H' and the V'V' component for the real part exhibit almost equal amplitudes, while the V'H' and the H'V' component for the imaginary part exhibit a phase shift of $\pi/2$. Consequently, the observed density matrices are indicative of right-handed circular polarisation. The shown data corresponds to horizontal input polarisation. Figure from [105].

The measured as well as the numerically obtained density matrices show that the

trapped midgap states for horizontal input polarisation exhibit right-handed circular polarisation with the experimental polarisation state being $(0.70 \pm 0.03)\,|H'\rangle + (0.71 \pm 0.02)e^{(0.47\pm0.02)i\pi}\,|V'\rangle$ and the numerically state given by $0.72\,|H'\rangle + 0.69e^{0.50i\pi}\,|V'\rangle$. These result agree with the expected right-handed circular polarisation $1/\sqrt{2}(|H'\rangle + i\,|V'\rangle)$ on even sites and thus verify the anomalous expectation values.

6.8 Conclusion: Accessibility of Topological Properties

We have seen that the presence of chiral, particle-hole as well as time-reversal symmetry in split-step quantum walks leads to the emergence of topological invariants. It depends on the concrete experimental setting how these invariants manifest themselves.
The scattering approach translates them into measurable reflection amplitudes and a bulk-boundary setting interfacing two samples with different topological properties leads to the emergence of localised edge states which are robust against disorder. The presence of these states in the absence of disorder is strong evidence that they are indeed a topological phenomenon and not the result of Anderson localisation.
The decoupling approach and the phase-reference method extend the range of accessible properties to the eigenvalues of edge states, providing even stronger evidence for their topological origin.
The third scheme demonstrates that a split-step quantum walk is not necessarily required for the emergence of topologically protected states. Here, chiral symmetry in combination with an unitary version of supersymmetry leads to the emergence of midgape states with anomalous polarisation.
So far our experiments have been conducted with coherent input states. Investigating the effect of topological properties on networks of multiple quantum particles, i.e. multiple single photons in our case, is a very interesting outlook, as it has been suggested that noise-robust quantum information processing can achieved via topological protection [187, 188, 189, 163].

7 Experiments with Coherent States Part 2: Investigating Measurement-induced Effects

In chapter 3.5 we discussed to what extent a quantum mechanical evolution according to the four axioms [102] can be simulated with classical, i.e. coherent states. Here, we show that the implications of the third axiom, i.e. projective measurements can be simulated with coherent states as well.
In order to do so, we investigate the difference of the recurrence as our figure of merit in two different measurement schemes.
On the experimental side, we harness the possibility of deterministic outcoupling with EOMs 2 and 3 to implement inhomogeneous losses, dubbed sinks.
The results have been published in [77].

7.1 Recurrence

7.1.1 Reset and Continual Scheme

The term recurrence corresponds to the return of a dynamical system to its initial state or very close to it. First studies of this property were conducted for classical random walks [190]. Referring to the author of this work, the probability of the walker to return to the origin in the limit of an infinite number of steps is also called Polya-number. Later studies were extended to quantum walks [191, 192].
The recurrence probability as a function of the step number can be defined in two different ways: Either depending on the probabilities that the walker has returned to the origin at all in a certain step or depending on the probabilities that the walker has returned for the first time in a certain step. In the first case, it is possible to measure the return probability for a certain step and then start a new experimental run, i.e. we reset the walker to its initial conditions and let it evolve again. Consequently, this definition of the return probability belongs to what we call the reset scheme.
The second case, on the other hand, requires having a certain knowledge of the walker's position for all steps prior to the one for which the return probability is to be determined. In an experimental setting this involves measuring whether the walker is at the origin and continuing the experiment afterwards. Thus this definition of the return probability corresponds to what we dub the continual scheme.
In the reset scheme, the return probability $\mathcal{P}_r(T)$ after T steps is determined in independent trials in each of the preceding steps t. A trial in a certain step t yields the probability $p(0,t)$ to find the walker at position 0 in this particular step. Since these are independent,

the probability that we do not find the walker at the origin in any of the steps is given by the product $\prod_{t=1}^{T}(1-p(0,t))$. The return probability $\mathcal{P}_r(T)$ for the reset scheme is then the probability of the complementary event and given by the following formula:

$$\mathcal{P}_r(T) = 1 - \prod_{t=1}^{T}(1-p(0,t)) \tag{7.1}$$

In the continual scheme, on the other hand, the probabilities $q(t)$ of a first time return in step t are mutually exclusive. Consequently, the return probability $\mathcal{P}_c(T)$ for the continual scheme after T steps is given by the sum over the probabilities of all previous steps:

$$\mathcal{P}_c(T) = \sum_{t=1}^{T} q(0,t), \tag{7.2}$$

For an unbiased classical random walk on a line or in a plane both $\mathcal{P}_r(T)$ and $\mathcal{P}_c(T)$ reach 1 for infinite step numbers T, i.e. both schemes are recurrent.
However, reset and continual scheme lead to qualitatively different results when considering a quantum walk described by a wavefunction $|\psi(t)\rangle$ and a unitary [191, 192].

7.1.2 Walker's Evolution with Projective Measurements

In the reset scheme the evolution of the wavefunction $|\psi(t)_r\rangle$ is obtained by the t-times application of the unitary $\hat{U}$:

$$|\psi(t)_r\rangle = \hat{U}^t|\psi(0)\rangle \tag{7.3}$$

The probability $p(0,t)$ to find the walker at the origin is then given by the following expression, which assumes an unperturbed evolution over t steps:

$$p(0,t)_r = |\langle 0|\psi(t)_r\rangle|^2. \tag{7.4}$$

In the continual regime we have to account for the fact that here the recurrence probabilities for a certain step t involve knowledge of the walker's state in previous steps. More precisely, only photons that have reached the origin for the first time are accounted for. This corresponds to projecting the walker's state to the complement of the position-0-subspace,

which is mathematically described by the projection operator $\hat{M_0}^{\perp}$:

$$\hat{M_0}^{\perp} = \hat{\mathbb{1}} - |0\rangle\langle 0| \tag{7.5}$$

In case the photon has not been detected in any of the $t-1$ previous steps, the state of the walker in step t is given by the wavefunction $|\psi(t)_c\rangle$:

$$|\psi_c(t)\rangle = \frac{1}{\sqrt{s_{t-1}}} \hat{U}\,(\hat{M_0}^{\perp}\,\hat{U})^{t-1}|\psi(0)\rangle \tag{7.6}$$

The term $\sqrt{s_{t-1}}$ in the above expression denotes the survival probability until step t, i.e. the probability that the walker has not reached the origin until this step:

$$s_{t-1} = \left\|(\hat{M_0}^{\perp}\,\hat{U})^{t-1}|\psi(0)\rangle\right\|^2. \tag{7.7}$$

The expression for the recurrence probability $p(0,t)_c$ in the continual scheme is analogous to (7.4), i.e. $p(0,t)_c = |\langle 0|\psi(t)_c\rangle|^2$. The first return probability $q(t)$ needed to determine $\mathcal{P}_c(T)$ is obtained by multiplying $p(0,t)_c$ with the survival probability s_{t-1}:

$$q(0,t) = \left|\langle 0|\hat{U}\,(\hat{M_0}^{\perp}\,\hat{U})^{t-1}|\psi(0)\rangle\right|^2 = s_{t-1}\; p_c(0,t). \tag{7.8}$$

The multiplication with the survival probability is due to the fact that proper normalisation of the wavefunction after a projection requires dividing by the survival probability but the "non-survival"-events are not counted in the first return probability $q(t)$. Consequently, we have to reverse the normalisation again by multiplying with the survival probability.
As already mentioned, we expect qualitatively different results for the Polya-number in the reset scheme $P_r = \lim_{T\to\infty} P_r(T)$ and the Polya-number in the continual scheme $P_c = \lim_{T\to\infty} P_c(T)$: The former one attains a value of 1 and thus reflects a recurrent regime, while the latter one is assumed to be $2/\pi$ and is thus indicative of a transient regime [192].

7.2 Experimental Implementation

Since we want to show that an evolution according to the third axiom can be obtained with coherent states, the walker in this experiment is an attenuated laser pulse.
In order to experimentally investigate the different recurrence probabilities for the two schemes, we have to implement a projection according to (7.5). We achieve this by making use of the active in- and outcoupling with EOMs 2 and 3 which allow to send the light at individual positions either to the detection unit or back into the feedback-loop. Figure

7.1 illustrates the evolution in the two cases with a beam splitter cascade: In the reset scheme (a) the walker evolves in an unperturbed way until the final detection, while it is projected to the complement of the position-0-subspace in intermediate steps of the continual scheme.

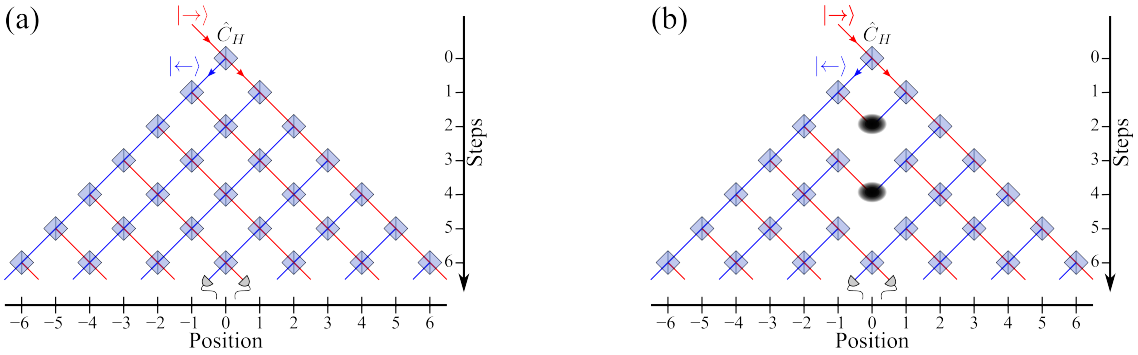

Figure 7.1: Illustration of the implementation of both the reset scheme (a) and the continual scheme (b). In the reset scheme we measure the probability to find the walker at the origin after an unperturbed evolution. In contrast, the continual scheme contains projections $\hat{M}_0^{\perp}$ to the complement of the position-0-subspace in intermediate steps. This is achieved by implementing losses for position 0, dubbed sinks, which are indicated by the black dots. Figure from [77].

In the experiment, these projections are implemented by switching the light at position zero out of the setup for all steps preceding the one in which $q(0,t)$ is measured. For brevity's sake we call these operations sinks in the following. Their implementation is made possible by the switching speed of the EOM which allows to address individual positions of the walk. Note that due to imperfect extinction of the EOM switchings and PBS 2 not all of the light is switched out of the setup and we account for this residual transmission of the sinks in the numerics and error bars.
Figures 7.2 (a) and (b) show the measured intensity distribution in step 30 for the two regimes. The effect of the sinks is clearly visible as missing intensity around the origin in Subfigure (b). It is also prominently manifested in the chessboard diagrams of the evolution over 36 steps (Figures (c) and (d), where the region around the middle is significantly darker in the right Figure.

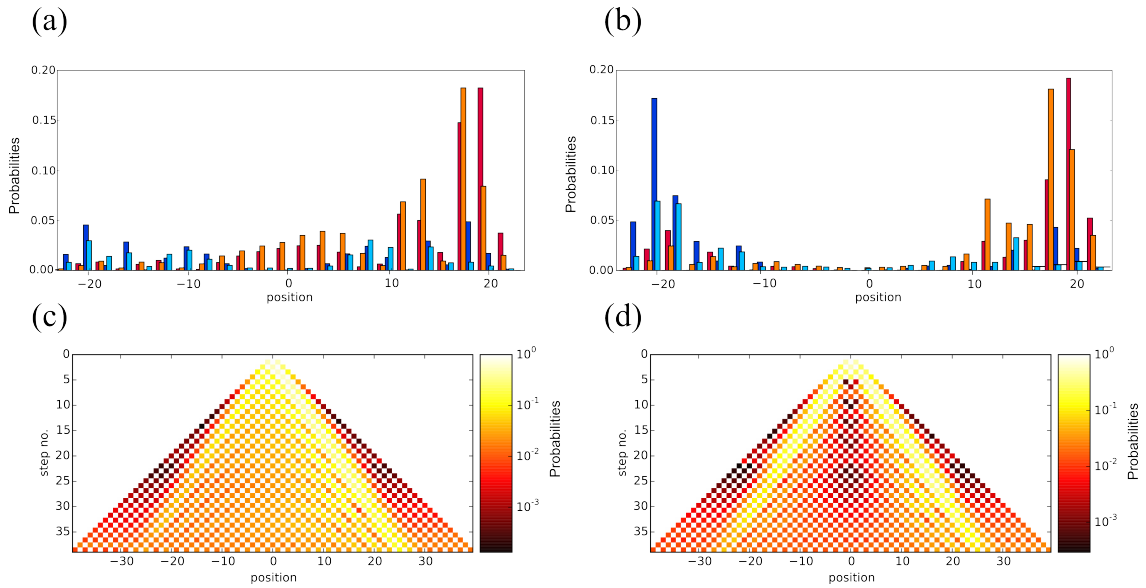

Figure 7.2: (a) and (b): Bar chart representation of the intensity distribution in step 30 for both the reset (right) and the continual regime (left). Orange (red) bars correspond to the experimental (numerical) values for horizontal polarisation and light (dark) blue bars to the experimental (numerical) values for vertical light. (c) and (d): Chessboard diagram of the evolution over 36 steps for the reset (right) and the continual regime (left). Figure from [77].

From the measured intensity distributions we extract the step-wise evolution of the recurrence probabilities $P_r(T)$ and $P_c(T)$ according to (7.1) resp. (7.2). The results are shown in Figure 7.3. The quantitative and qualitative difference between the two regimes is clearly visible: The recurrence probability in the reset scheme (red dots resp. orange line for the numerical values) keeps increasing monotonously for all of the measured steps and is predicted to reach 1 in the asymptotic limit. In contrast, the continual scheme results in a recurrence probability (blue dots resp. green line for the numerical values) that quickly attains a value close to $2/\pi$ and remains constant within the experimental error for all subsequent steps. As the quantitative difference between the two schemes is clearly larger than the error bars, the transition between them induced by projective measurements is experimentally verified.

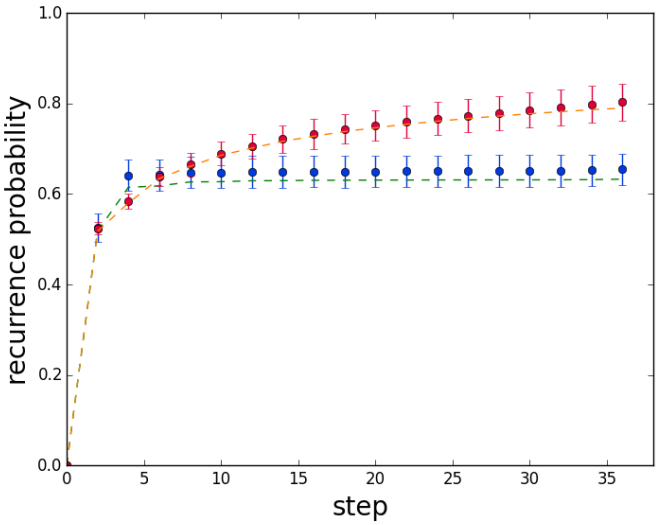

Figure 7.3: The evolution of the recurrence probability over 36 steps for both the reset (red dots for measured values and orange line for numerical prediction) and the continual scheme (blue dots for measured values and green line for numerical prediction). The error bars are obtained by numerically simulating deviations from the best fit of ± 1 for coupling efficiencies, $\pm 0.15\%$ for the coin angle and possible residual sink transmission of 1%. Figure from [77].

In conclusion, these results show that an evolution according to the third axiom of quantum mechanics (projective measurements) can be simulated with coherent, i.e. classical, states. As an outlook, the absorptive sinks could be used to simulate the annihilation of an electron and a positron following Hardy's experiment devised to test local hidden variable models [193]. Other possible application could lie in the investigation of interaction-free measurements [194].

8 Time-multiplexed HOM-Dip

In section 3.3.2 we saw that HOM-interference crucially depends on the purity of the input states. In an experimental setting purity is lost when the state's multi-mode structure cannot be resolved during detection and is consequently traced out. A prominent example of a degree of freedom where undesired multi-modedness can occur are the frequency modes of a PDC state. In this regard, a possible solution consists in ensuring single-modedness, e.g. via source engineering [147, 148]. An opposite approach would be to guarantee purity by conducting mode-resolving measurements. As this would require detectors that are able to distinguish different modes, such an approach is challenging in terms of implementation. Considering time-frequency modes in the Schmidt-basis, a possible device is a quantum pulse gate [195, 196]. Another approach suggested consists in quantum beat interference [197].
On the other hand, multi-modedness cannot only be considered a source of undesired reduction of purity, but also provides a higher-dimensional basis for information encoding. Consequently, it seems desirable to deliberately synthesize and read-out the mode structure of quantum states.
Even though photons are thought of as indivisible particles, they can nevertheless be delocalised over multiple modes in a certain degree of freedom, e.g. positions or time bins. In the following we introduce a scheme in which we deliberately split photons up into multiple time bins and then make them interfere [198]. We can think of the resulting experiment as a time-multiplexed beam splitter (illustrated in Figure 8.1): It interferes the two subsystems A and B, each constituted by one of the interfering photons.
By splitting these photons up in time, we imprint an additional mode structure on them. As indicated by the flipped envelop for subsystem A, the eventual interference is sensitive to the phase between the time bins, so that we can speak of the coherent control of quantum interference. The term coherent control (see [199] for a review) is commonly used for tailoring the outcome of chemical reactions by controlling the interference of competing reaction path ways. In this sense, we can think of our experimental results as being the consequence of the interference of multiple paths leading to the same detection event.

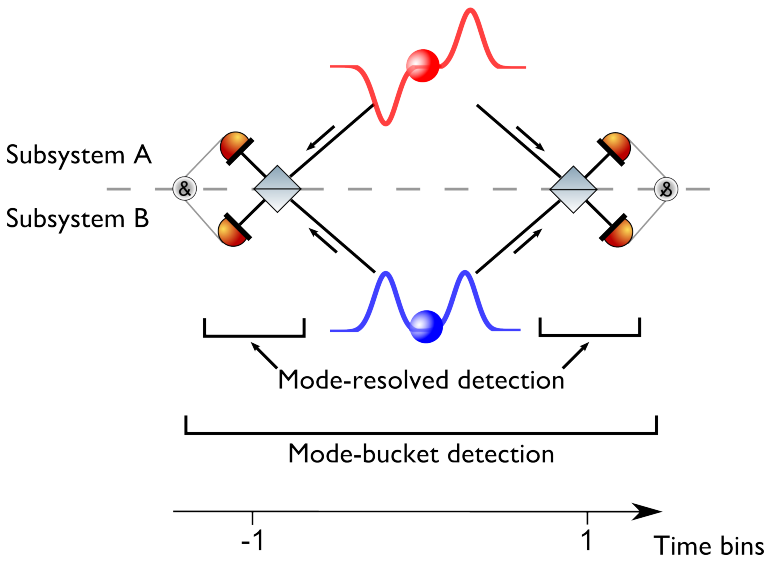

Figure 8.1: Illustration of a time-multiplexed beam splitter: Two photons constituting the subsystems A and B are split-up in time and brought to interference at multiple positions (modes or bins) in time. The flipped envelop for subsystem A indicates that the coherence between the individual time bins plays role. Coincidence detection can be conducted in either a mode-resolving or a mode-bucket scheme. In the first case only coincidences at a certain position are counted, while in the latter scenario coincidences spread across the two time bins are accounted for as well. The colour coding is consistent with the convention used throughout this work, i.e. red corresponds to horizontal light and blue to vertical light, as photons from subsystem A impinge with horizontal polarisation on the PBS where the final interference takes place, while those from subsystem B exhibit vertical polarisation.

The outcome of the interference is read-out in a coincidence measurement. Here, coincidences can either be detected in a mode-resolving detection scheme, where they are only registered when they happen between modes associated to the same time bin or in a mode-bucket detection scheme, where they are also counted when they occur between modes belonging to different time bins. We will refer to coincidences in a mode-bin resolving detection scheme also as coincidences under strict conditions and to coincidences in a mode-bucket detection scheme as coincidences under loose conditions. In the mode- or time-bucket detection scheme, we loose all information on which photon paths have contributed to a certain coincidence event, which is analogue to the different possible paths that can lead to a certain state in a chemical reaction.
In the following, we will see how shaping the mode structure of the subsystems leads to qualitatively different outcomes of HOM-interference experiments (see section 8.1). In addition, we investigate visibilities when the two subsystems are temporally shifted relative to each other in section 8.2.
Section 8.3 is devoted to studying the case in which each photon is split up into three time bins.

Subsequently, we discuss the numerical modelling of the time-multiplexed HOM-dip experiment in section 8.4.
Section 8.5 is then devoted to investigating with coherent states how the time-multiplexing network affects visibilities.
Splitting up photons into multiple time bins can under certain conditions increase the detrimental effect of higher photon-number components, which is analysed in section 8.6.
An experimental investigation of imperfections is discussed in section 8.7.
Eventually, we draw a conclusion in section 8.8.

8.1 Probing Parity

One of the most striking differences between time-bin resolved and time-bucket detection becomes apparent when examining interference depending on the parity of the subsystems, which reflects the relative phase between the time bins. This is illustrated in Figure 8.1, where subsystem B exhibits a relative phase of zero between the bins (indicated by the two blue envelops having the same sign), while there is a relative phase of π between the two time bins in subsystem A (indicated by the flipped red envelop). Consequently, the envelop of B does not change when inverting the signs of the time bins, i.e. the system is of even parity. On the other hand,the envelop of A changes its sign under inversion, i.e. the system is of odd parity.
In our experiment we can prepare these states by sending two photons with either orthogonal or parallel polarisation into the time-multiplexing network. Referring to Figure 8.1, the two subsystems A and B are represented by a photon in horizontal and a photon in vertical polarisation. By applying a HWP operation $\hat{C}_{\mathrm{HWP}}$ according to (3.16) for the final interference, the two polarisation modes interfere in the same way as two spatial modes at a probabilistic beam splitter (see section 5.1).
The protocol implemented for the state preparation is illustrated in Figure 8.2: We generate two photon pairs (operation marked by G) out of which one photon acts as a herald and the other is sent into the network. Here, the photons are split up by coin operations $\hat{C}_{\mathrm{QWP}}$ conducted by quarter-wave plates at 45°. Subsequently, the EOM switches reflection (denoted by $\hat{R}$) resp. transmission operations (marked by $\hat{T}$) in order to direct the four resulting modes such that they interfere again. Depending on the polarisation of the photons sent into the network, we obtain different interfering states.
Figure 8.2 also serves to illustrate how the two detection schemes can be realised experimentally: For time-bin resolving detection only coincidences between horizontal and vertical light at a certain position are counted, while for time-bucket detectors coincidences between a horizontal and a vertical mode are registered also when these modes belong to different positions.

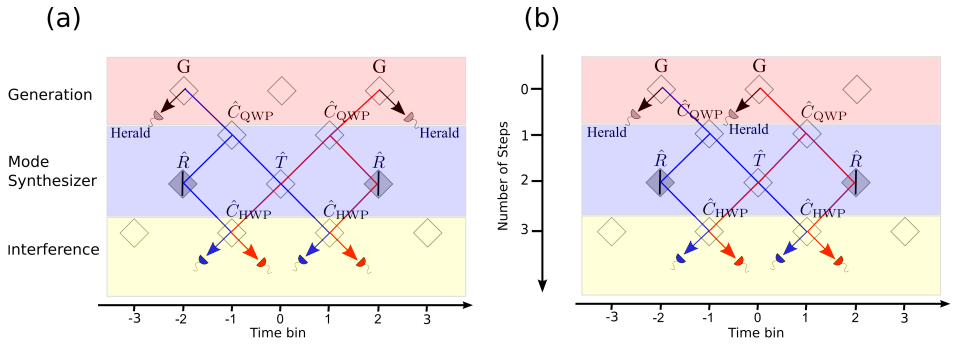

$$\hat{C}_{\mathrm{QWP}}(45°) = \frac{1}{\sqrt{2}}\begin{pmatrix} 1 & -i \\ -i & 1 \end{pmatrix} \quad \hat{C}_{\mathrm{HWP}}(\theta) = \frac{1}{\sqrt{2}}\begin{pmatrix} \cos(\theta) & \sin(\theta) \\ \sin(\theta) & -\cos(\theta) \end{pmatrix} \quad \hat{R} = \frac{1}{\sqrt{2}}\begin{pmatrix} 0 & -i \\ -i & 0 \end{pmatrix} \quad \text{G : Generation of PDC state}$$

$\frac{-1}{\sqrt{2}}\left(\hat{a}^\dagger_{-1,H} - \hat{a}^\dagger_{1,H}\right)|0\rangle_A$ Odd
$\frac{1}{\sqrt{2}}\left(\hat{b}^\dagger_{-1,V} - \hat{b}^\dagger_{1,V}\right)|0\rangle_B$ Odd
Same Parity

$\frac{-1}{\sqrt{2}}\left(\hat{a}^\dagger_{-1,H} - \hat{a}^\dagger_{1,H}\right)|0\rangle_A$ Odd
$\frac{-i}{\sqrt{2}}\left(\hat{b}^\dagger_{-1,V} + \hat{b}^\dagger_{1,V}\right)|0\rangle_B$ Even
Different Parity

Figure 8.2: Illustration of the protocols for the preparation of the interfering states. (a): By sending two photons with orthogonal polarisation into the setup, we prepare an interfering state which exhibits the same parity in the two subsystems. (b): Photons initially having the same polarisation result in a state with two subsystems of different parity. In both cases the photons are split up by the operation $\hat{C}_{\mathrm{QWP}}$, routed by the operations $\hat{R}$ and $\hat{T}$ implemented with the EOM and finally brought to interference by the coin $\hat{C}_{\mathrm{HWP}}$. Red resp. blue arrows mark the propagation of photons from subsystem A resp. subsystem B, while red (blue) detector symbols correspond to the detection of horizontal (vertical) light. Time-bin resolving detection counts coincidences between a horizontal and a vertical mode at the same position, while time-bucket detection also accounts for coincidences that occur between a horizontal and a vertical mode of different positions. Regarding the creation operators $\hat{a}^\dagger$ for subsystem A resp. $\hat{b}^\dagger$ for subsystem B, the first index denotes the time bin and the second one the polarisation.

When selecting the signal, i.e. the horizontal polarisation mode, of one photon-pair and the idler, i.e. the vertical polarisation mode, of the other, we obtain the following state state $|E\rangle$ before the final interference (see Figure 8.2, (a)):

$$|E\rangle = \frac{1}{\sqrt{4}}\left(-\hat{a}^\dagger_{-1,H}\hat{b}^\dagger_{-1,V} - \hat{a}^\dagger_{1,H}\hat{b}^\dagger_{1,V} + \hat{a}^\dagger_{-1,H}\hat{b}^\dagger_{1,V} + \hat{a}^\dagger_{1,H}\hat{b}^\dagger_{-1,V}\right)|0\rangle_A \otimes |0\rangle_B \tag{8.1}$$

Note that here we assume an ideal single-photon state and neglect higher photon-number contributions, whose influence is investigated numerically in section 8.6. Considering subsystems A and B separately, this state can be written in the following way:

$$|E\rangle = \frac{-1}{\sqrt{2}}\left(\hat{a}^\dagger_{-1,H} - \hat{a}^\dagger_{1,H}\right)|0\rangle_A \otimes \frac{1}{\sqrt{2}}\left(\hat{b}^\dagger_{-1,V} - \hat{b}^\dagger_{1,V}\right)|0\rangle_B \tag{8.2}$$

Note that the two subsystems A and B are assumed to be indistinguishable at the bottom of the HOM-dip. The above nomenclature is thus only appropriate when the experimental system is configured such that the delay makes the two subsystems distinguishable.
On the other hand, sending two signal photons, i.e. horizontally polarised photons, into the setup results in the state $|O\rangle$ before interference (see Figure 8.2, b):

$$|O\rangle = \frac{1}{\sqrt{4}}\left(i\hat{a}^\dagger_{-1,H}\hat{b}^\dagger_{-1,V} - i\hat{a}^\dagger_{1,H}\hat{b}^\dagger_{1,V} + i\hat{a}^\dagger_{-1,H}\hat{b}^\dagger_{1,V} - i\hat{a}^\dagger_{1,H}\hat{b}^\dagger_{-1,V}\right)|0\rangle_A \otimes |0\rangle_B \tag{8.3}$$

Again, we can write the state in a way that allows to discern the two subsystems:

$$|O\rangle = \frac{1}{\sqrt{2}}\left(-\hat{a}^\dagger_{-1,H} + \hat{a}^\dagger_{1,H}\right)|0\rangle_A \otimes \frac{-i}{\sqrt{2}}\left(\hat{b}^\dagger_{-1,V} + \hat{b}^\dagger_{1,V}\right)|0\rangle_B \tag{8.4}$$

Comparing the parity of the individual subsystems for the two cases as given by expressions (8.2) and (8.4), we notice that in the first case, i.e. for photons input with orthogonal polarisation, both subsystem exhibit an odd parity, while in the second case, i.e. for photons with parallel polarisation, subsystem A exhibits odd parity, while subsystem B is of even parity. Here, the term parity refers to the behaviour of the state when the signs of the indices of the time bins are flipped: For even parity the state remains unchanged, while its sign is inverted for odd parity.
In appendix B, we compare the coincidence probabilities for $|E\rangle$ and $|O\rangle$ after the application of the interference coin $\hat{C}_{\mathrm{HWP}}$ for either perfect distinguishability or perfect indistinguishability of the two subsystems. From these considerations we can deduce the corresponding HOM-dip visibilities. We find that $|E\rangle$ exhibits full visibility in both detection schemes, while $|O\rangle$ gives full visibility only for time-bin resolving (tbr) detection. For a time-bucket (tb) detection scheme, on the other hand, we do not expect any HOM-dip. Consequently, we find that a time-bin resolving detection scheme is insensitive to the parity of the subsystems. In contrast, a time-bucket detection scheme leads to full visibility in case both subsystems have the same parity and no visibility in case the two subsystems have different parities.
This behaviour is reminiscent of the interference properties of orthogonal sets of modes, e.g. Schmidt-modes. Indeed for $|O\rangle$, even when assuming indistinguishability of subsystems A and B, the scalar product, i.e. the overlap, of their states $|X\rangle$ in position space is 0:

$$|\langle X_{O,A}|X_{O,B}\rangle| = |\frac{1}{2}(-\langle x=-1| + \langle x=1|)\cdot(-i|x=-1\rangle - i|x=1\rangle)| = 0 \tag{8.5}$$

As the position state $|X\rangle$ does not only reflect the time bins the photons are in, but also the phases between them, terms can cancel each other out. This is analogue to the overlap integral of orthogonal Hermite-Gaussian modes where negative and positive contributions

cancel each other out as well.
On the other hand, we obtain an overlap of 1 and thus full visibility for $|E\rangle$:

$$|\langle X_{E,A}|X_{E,B}\rangle| = |\frac{1}{2}(-\langle x=-1| + \langle x=1|)\cdot(|x=-1\rangle - |x=1\rangle)| = 1 \tag{8.6}$$

Bearing these consideration in mind, we turn our attention to the experimental results. Figure 8.3 shows the experimentally obtained HOM-dips for the states $|E\rangle$ and $|O\rangle$ for both detection schemes. The error analysis is conducted in an analogue way to the scheme explained in section 5.9.

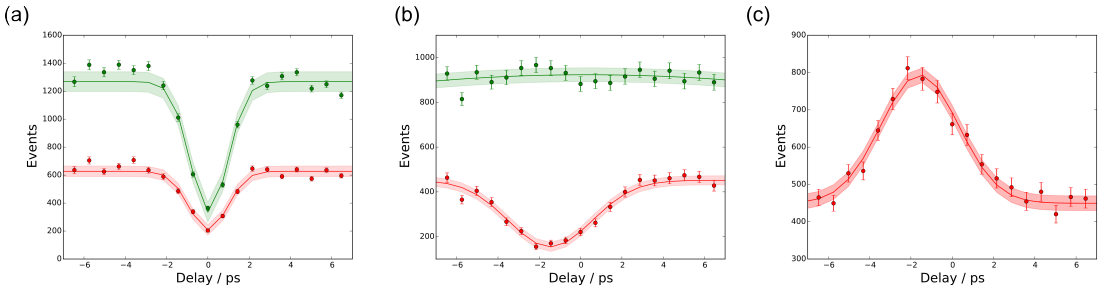

Figure 8.3: (a): Coincidence counts depending on the relative delay between the two interferometer arms for the state $|E\rangle$. Red markers correspond to time-bin resolving detection, green markers to time-bucket detection. Since time-bucket detection comprises the combinations accounted for by time-bin resolving detection plus additional ones, we see twice the number of counts here. (b): Coincidence counts as in the left figure, but for the state $|O\rangle$. Note that for $|E\rangle$ the photons are initially spaced two positions apart, for $|O\rangle$ only one position apart (see Figure 8.2). $|E\rangle$ is thus subjected to two times the delay introduced by the stage, $|O\rangle$ only to one time the delay. Consequently, the dip for the latter case exhibits twice the width of the other one. (c): The difference of the counts in the two detection schemes. Here, we find a peak that offsets the dip in the time-bin resolving detection scheme. The dots with error bars for Poissonian errors correspond to the measured counts. The line gives the values of the Gaussian fit function for which the error (shaded region) is computed as the mean square deviation of the fit from the data points.

In each measurement run we pick three additional pairs at positions which ensure that these pairs do not interfere with the measurement of the time-multiplexed HOM-dip. Signal and idler of two of these pairs are brought to interference passively (illustrated in Figure 5.1 in section 5.1), i.e. without directing them with any EOM-switchings, and thus provide a reference for the expected visibilities of a heralded HOM-dip. The third pair is simply split up and used to extract Klyshko-efficiencies as the ratio of coincidences and singles for a case in which the coincidences are not subjected to HOM-interference. These efficiencies are then used to normalise the fourfold coincidences recorded for the HOM-dips.
As expected, the state $|E\rangle$ leads within experimental errors to the same visibilities for both

detection schemes (0.669 ± 0.072 for time-bin resolving detection and 0.737 ± 0.069 for time-bucket detection, see Figure 8.3, (a)). This reflects the fact that the overlap according to (8.6) is insensitive to the detection scheme. The visibilities for the time-multiplexed HOM-dip compare with a value of 0.749 ± 0.03 for the reference. All three visibilities are measured for a mean photon number $\bar{n} = 0.1 \pm 0.016$.
In contrast, the time-bin resolving detection scheme leads for $|O\rangle$ to a visibility of 0.659 ± 0.054, while we cannot extract a dip from the data recorded for the time-bucket detection scheme (see Figure 8.3, (b)). Looking at the difference of the counts in the two detection schemes, we indeed find a peak that offsets the dip in the time-bin resolving detection scheme (see Figure 8.3, (c)). This phenomenon is counter-intuitive is so far as the photons in this case pass the interference coin in different time bins and thus never physically encounter each other. The visibility of the reference is 0.726 ± 0.017 for $|O\rangle$ and $\bar{n} = 0.115 \pm 0.012$.

8.2 Probing Relative Translation

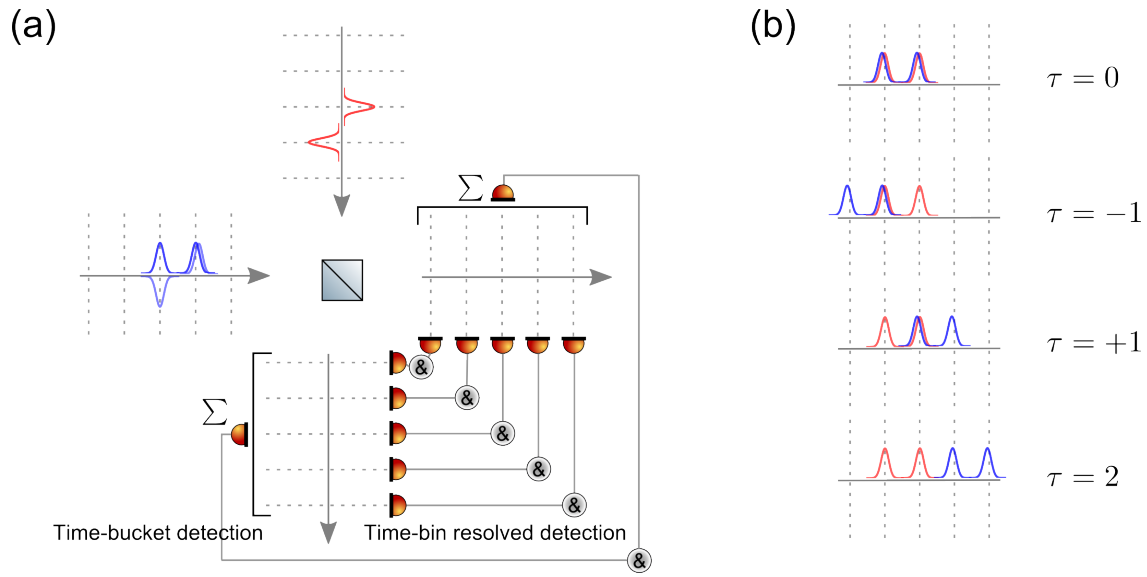

Figure 8.4: (a): Illustration of how two input photons (marked in red resp. blue colour) in different time bins and polarisation are interfered at a time-multiplexed beam splitter (indicated by multiple time bins for the input and output ports). For the output state coincidences (indicated by "&"-symbol) can be detected in either a time-bin resolved way or for the sum over all time-bins, which can be called time-bucket detection. In case of time-bucket detection, visibilities are influenced by the parities of the interfering states. In our setting, the subsystem marked in red is always of odd parity, while the subsystem marked in blue can exhibit either even or odd parity. (b): Illustration of how the time-bins belonging to each of the photons are shifted in relation to each other depending on the value of τ.

In addition to the parity, visibilities depend upon the relative translation of the time bins. We introduce the parameter τ which quantifies how much the time-bins belonging to one of the photons are shifted in respect to those of the other photon (see Figure 8.4, (b)). When splitting a photon into two time-bins, $\tau = 0$ corresponds to complete overlap of the time-bins of the two photons, $\tau = \pm 1$ to an overlap of 2 out of 4 bins and $\tau = 2$ to no overlap.

This scheme can be thought of as a discretised version of conventional HOM-dip experiments [28, 200, 201, 202]. In order to understand how the mode structure in time affects the interference, we describe the experiment as a series of beam splitters in time that each interferes two input modes. In our experimental setting, these two modes are horizontal and vertical polarisation which are brought to interference by a HWP in front of the detection unit.

For the interference of a signal and an idler photon, i.e. one photon initially in horizontal

polarisation and one initially in vertical polarisation, we saw that the two subsystems of the interfering states are expected to exhibit the same parity. As a consequence, the visibilities for time-bin resolving and time-bucket detection are assumed to be the same in case their time-bins completely overlap, i.e. $\tau = 0$. On the other hand, shifts between the bins of the two pulses by $\tau = \pm 1$ are expected to yield full visibility in case the time-bins are resolved, but significantly reduced visibilities in case the time-bins are not resolved. For no overlap, i.e. $\tau = 2$, a dip is not predicted in any detection scheme. Note that in the following we will examine the effect of varying τ for the state $|E\rangle$ alone as a difference to the state $|O\rangle$ is only expected in case two time-bins overlap, i.e. $\tau = 0$, which has already been investigate in the previous section.
Figure 8.5 provides a schematic of the pulse routing for the four different cases $\tau = 0$, $\tau = -1$, $\tau = +1$ and $\tau = 2$.

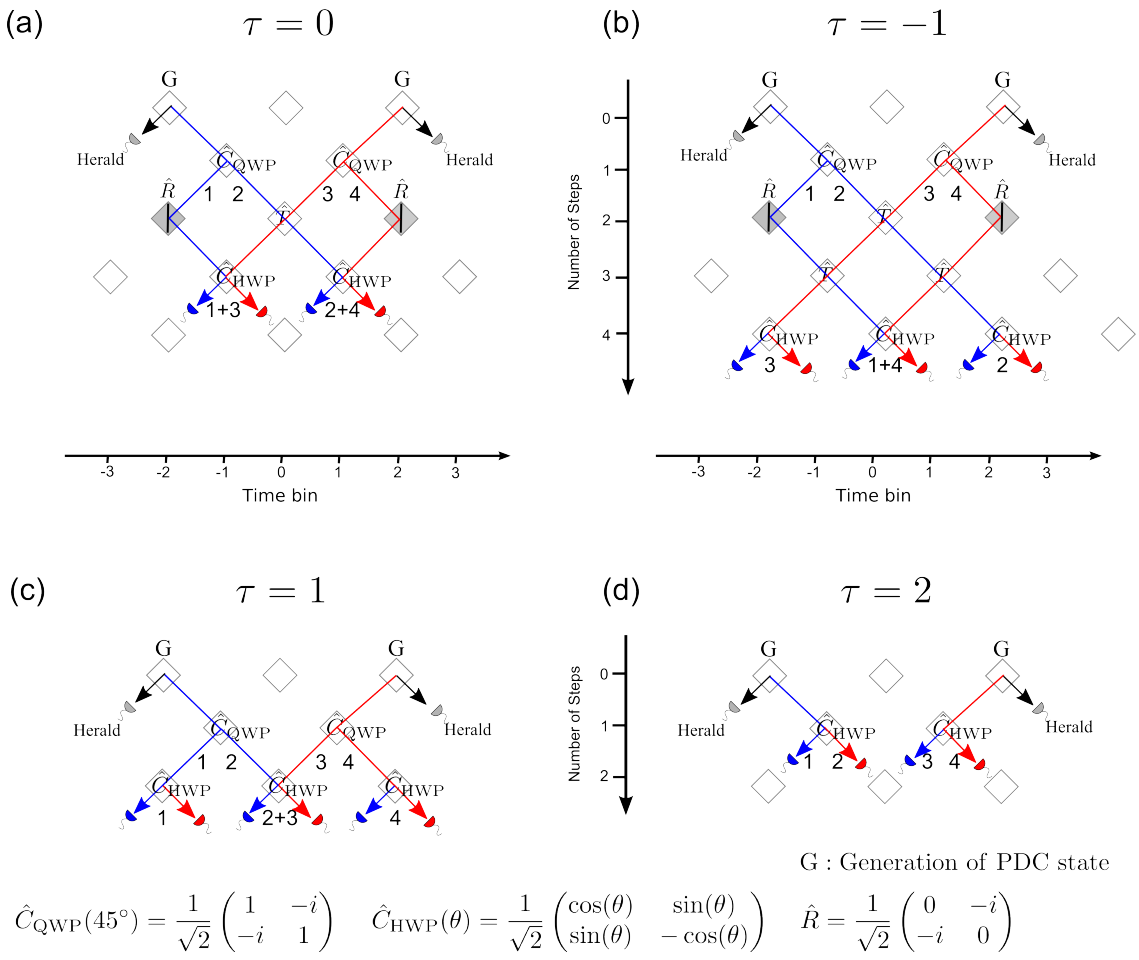

Figure 8.5: Schematic of the switchings for the cases $\tau = 0$ (a), $\tau = -1$ (b), $\tau = +1$ (c) and $\tau = 2$ (d). Red resp. blue arrows mark the propagation of photons from subsystem A resp. subsystem B, while red (blue) detector symbols correspond to the detection of horizontal (vertical) light. In each of the cases, two photons are split up into modes 1-4, which are then overlapped again to varying degrees before the final interference takes place. Time-bin resolving detection counts coincidences between a horizontal and a vertical mode for the same time bin, while time-bucket detection also accounts for coincidences that occur between a horizontal and a vertical mode for different time bins.

We see that implementing different values of τ involves different numbers of steps, e.g. just one step for $\tau = 2$ but 4 steps for $\tau = -1$, resulting in varying count rates for the same mean photon number $\bar{n}$. Due to limitations in the measurement time (see section 4.4.1), the value of $\bar{n}$ that still allows to obtain sufficient click statistics is thus different for the individual cases, resulting in varying visibilities of the reference HOM-dip. In order to achieve comparability between measurement conducted with different mean photon numbers, we consequently calculate visibilities relative to the reference, i.e. the ratio of a

certain visibility and the visibility of the reference.
As will be elaborated on in section 8.7, the detrimental influence of higher photon-number contributions on visibilities becomes more severe for cases with partial overlap, i.e. $\tau = -1$ and $\tau = +1$, where spurious coincidences can also be detected for time bins where ideally only a single photon is expected to arrive. This effect can be counteracted by only considering coincidences for the time bin where two photons are supposed to interfere, in this case time bin 0. Consequently, we consider in following for the cases $\tau = -1$ and $\tau = +1$ the visibilities determined for time bin 0 as these are less susceptible to spurious higher photon-number contributions.

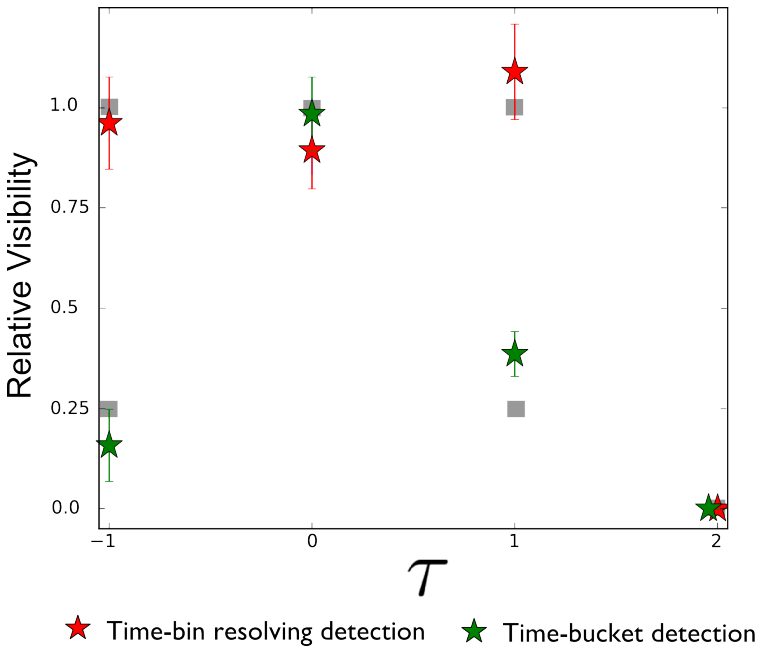

Figure 8.6: Relative visibilities depending on τ calculated as the ratio of the visibilities for a time-multiplexed HOM-dip and the visibility of the reference HOM-dip. Red markers correspond to a time-bin resolving detection scheme and green markers to a time-bucket detection scheme. The grey markers indicate the numerically expected relative visibilites of 1 for full overlap and/or a time-bin resolving detection scheme, 0.25 for partial overlap and time-bucket detection and 0 for no overlap. Error bars are determined according to (5.23).

Figure 8.6 shows the relative visibilities for time-bin resolving (green markers) as well as time-bucket detection scheme (red markers).
We observe that time-bin resolving detection preserves visibilities when translating the two subsystems relative to each other so that they only partially overlap, while visibilities drop significantly for time-bucket detection. In case there is no overlap at all, i.e. $\tau = 2$, none of the detection schemes is able to detect a HOM-dip. The grey markers give the numerically expected visibilities which yield a value of 1 for a time-bin resolving detection

or $\tau = 0$, 0.25 for a time-bucket detection scheme and $\tau = \pm 1$ as well as 0 for $\tau = 2$.
In section 8.4 we will take a closer look at how the numerical values for the visibilities are determined.

8.3 Higher Numbers of Time Bins

The time-multiplexed HOM-dip experiment exhibits scalability in the number of synthesized modes. In the following, we will demonstrate a proof-of-principle experiment for this scalability by splitting each of the two photons up into three modes and interfering them afterwards.
While we are limited to either full or no overlap when changing the phase between two time bins, a higher dimensional mode structure in time also allows for partial overlap. Furthermore, we can pick different subsets of two out of the three modes that then again show either full or no overlap.
The experimental results are shown along with numerically obtained values in Figure 8.7.

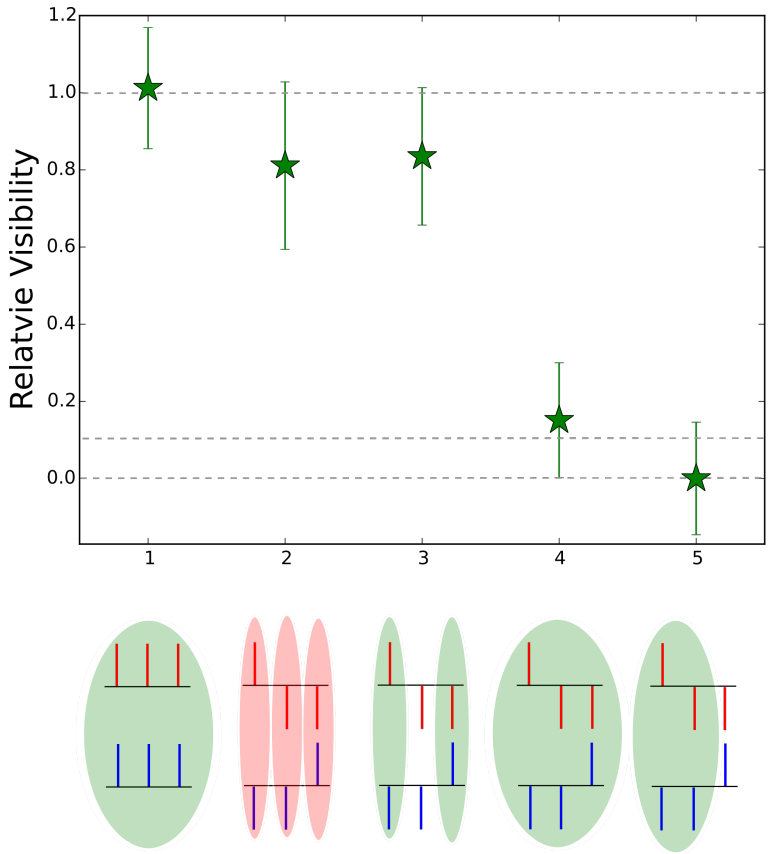

Figure 8.7: Relative visibilities for three bin scenarios with different relative phases and time bins taken into consideration (marked in red). The dashed grey lines gives the theoretically expected visibilities for either full, partial or no overlap.

With a relative phase of zero between all three bins (scenario 1) we observe a relative visibility close to 1 even when tracing out over the time bins in a time-bucket detection scheme. In scenarios 2-5 the relative phases are such that the contributions of two out of the three time bins cancel each other out, so that we expect a relative visibilities of 1/9 (see (8.8)) when accounting for all three time bins in a time-bucket detection scheme (scenario 4). In contrast to a system with two time bins we do now, however, have the possibility to pick two out of three time bins for the time-bucket detection. In scenario 3, both of them exhibit a phase of π between the two subsystems and thus add up constructively, yielding full visibility. On the other hand, in scenario 5 the two subsystems have a relative phase of zero for one of the time bins and a relative phase of π for the other, such that they add up destructively and we see no visibility in either experiment or numerics. Mode-resolving detection (scenario 2), i.e. analysing each of the three time bins separately, yields as expected full visibility.
In this regard, the scalability of our architecture allows to increase the number of time

bins in a straightforward way while retaining full control over phases and polarisation.

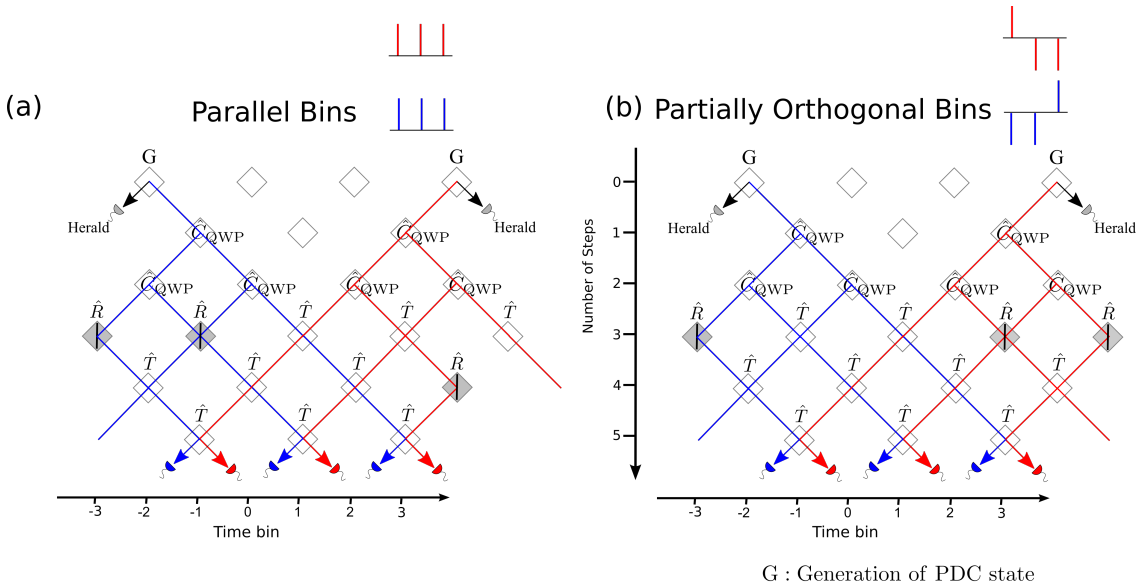

Figure 8.8: (a): Switching pattern to implement the two subsystems with parallel bins i.e. a relative phase of 0 between all of them. (b): Switching pattern to implement the two subsystems with partially orthogonal bins i.e. some exhibit a relative phase of π between them.

Figure 8.8 shows the switching patterns implemented for splitting the subsystem up into three bins. Each of the photons is subjected three times to the coin operation $\hat{C}_{\mathrm{QWP}}(45°)$ which is spreading it out over 4 time bins. Three of these are brought to interference, while the fourth ones are not recorded. Routing these bins to a position where they both interfere would require a significant number of additional steps.
Realising the pattern shown in Figure 8.8, (a) results in the following interfering state in which all bins exhibit a relative phase of 0:

$$|P\rangle = \frac{1}{\sqrt{3}}\left(\hat{a}^\dagger_{-1,H} + \hat{a}^\dagger_{1,H} + \hat{a}^\dagger_{3,H}\right)|0\rangle_A \otimes \frac{1}{\sqrt{3}}\left(\hat{b}^\dagger_{-1,V} + \hat{b}^\dagger_{1,V} + \hat{b}^\dagger_{3,V}\right)|0\rangle_B \tag{8.7}$$

In contrast, the pattern depicted in Figure 8.8, (b) implements a state that also exhibits relative phases of π between individual bins:

$$|O\rangle = \frac{1}{\sqrt{3}}\left(-\hat{a}^\dagger_{-1,H} - \hat{a}^\dagger_{1,H} + \hat{a}^\dagger_{3,H}\right)|0\rangle_A \otimes \frac{1}{\sqrt{3}}\left(\hat{b}^\dagger_{-1,V} - \hat{b}^\dagger_{1,V} - \hat{b}^\dagger_{3,V}\right)|0\rangle_B \tag{8.8}$$

Comparing the overlaps of the states$|X\rangle$ in position space, we find $|\langle X_{P,A}|X_{P,B}\rangle| = 1$ and $|\langle X_{O,A}|X_{O,B}\rangle| = 1/9$.

8.4 Simulating Time-multiplexed HOM-Dip with QuTip

In order to get estimates for the influence of possible experimental imperfections such as higher photon-number contributions, losses or dark counts, we implement a numerical simulation of the system in QuTip. Figure 8.9 shows a schematic of the operations implemented in QuTip to simulate the time-multiplexed HOM-dip.

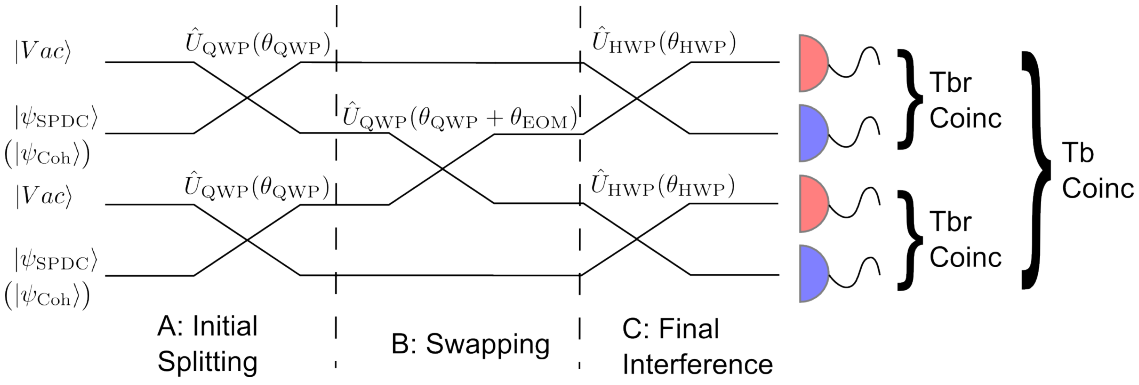

Figure 8.9: Schematic of the operations implemented in QuTip in order to simulate the DHOM measurement for the $\tau = 0$ case. The simulations are conducted for either PDC or coherent states as the input. Note that we use ancillary modes to mimic distinguishability that are omitted in this sketch for clarity. The same applies to the herald modes.

We start with two input states that are either PDC or coherent states. As will be elaborated on in section 8.5, the latter states can be used to investigate effects of the loop on visibilities independent of source characteristics such as the mean photon number.
The input states undergo the beam splitter operation $\hat{U}_{\mathrm{QWP}}(\theta_{\mathrm{QWP}} = \pi/4)$, implementing the required splitting of the photons. Subsequently two of the four output modes are swapped such that they can interfere with an output mode of the other input state. This swapping is conducted by the unitary $\hat{U}_{\mathrm{QWP}}(\theta_{\mathrm{QWP}} + \theta_{\mathrm{EOM}})$ which leads to a perfect transfer for $\theta_{\mathrm{EOM}} = \pi/4$ and no swap for $\theta_{\mathrm{EOM}} = -\pi/4$. The actual interference then takes place with the operation $\hat{U}_{\mathrm{HWP}}(\theta_{\mathrm{HWP}} = \pi/4)$.
The final detection counts coincidences between the two modes marked in blue and red for either the two top or the two bottom modes under time-bin resolved (tbr) coincidence conditions or for all four modes under time-bucket (tb) coincidence conditions. Visibilities are then evaluated by introducing distinguishability in a way similar to the scheme described in section 5.6. Since our system now has a higher number of modes, we have to implement two ancillary modes for each of the two mode pairs can produce strict coincidences.

For the coin and EOM operations we are assuming unitaries of the following form:

$$\hat{U}_{\mathrm{QWP}}(\theta) = e^{-i\theta(\hat{a}\hat{a}^\dagger + \hat{a}^\dagger\hat{a})} \tag{8.9}$$

For the QWP inside the feedback loop we set θ to $\pi/4$. The coin outside the loop is fixed to a phase of $\pi/4$ and modelled by a slightly different unitary, since it is not a QWP but a HWP:

$$\hat{U}_{\mathrm{HWP}}(\pi/4) = e^{\pi/4\cdot(-i)\cdot(i\hat{a}\hat{a}^\dagger - i\hat{a}^\dagger\hat{a})} \tag{8.10}$$

As we have seen in section 5.1, we could as well implement this coin with a QWP. Due to availability, however, we use a HWP and thus account for it in the numerics to rule out unforeseen consequences.

8.5 Time-multiplexed HOM-Dip with Coherent Light

In order to examine effects on the visibilities originating from the light's propagation a through time-multiplexing network independent from source properties such as spectral characteristics and mean photon number, we investigate time-multiplexed HOM-dips for coherent input states (compare with 5.11).

8.5.1 Mean Photon Number

First, we verify numerically that coherent input states allow in good approximation for measuring visibilities independent of the mean photon number $\bar{n}$. Herefore, we consider the $\tau = 0$ case (shown in Figure 8.10,a) under strict coincidence conditions. Even for a mean photon number of 1, visibilities of above 0.49 are predicted for low values of imbalanced loss, while the mean photon number in the experimental runs with coherent states is around 0.3. Consequently, we assume that visibilities measured with coherent states are not affected by the mean photon number. Note that in order to handle the computational complexity of the numerical simulation, the implemented Fock space is limited to 5 dimensions for the numerical runs involving coherent states.
The high resilience of visibilities towards the increasing the mean photon number is reminiscent of the result presented in section 5.11.

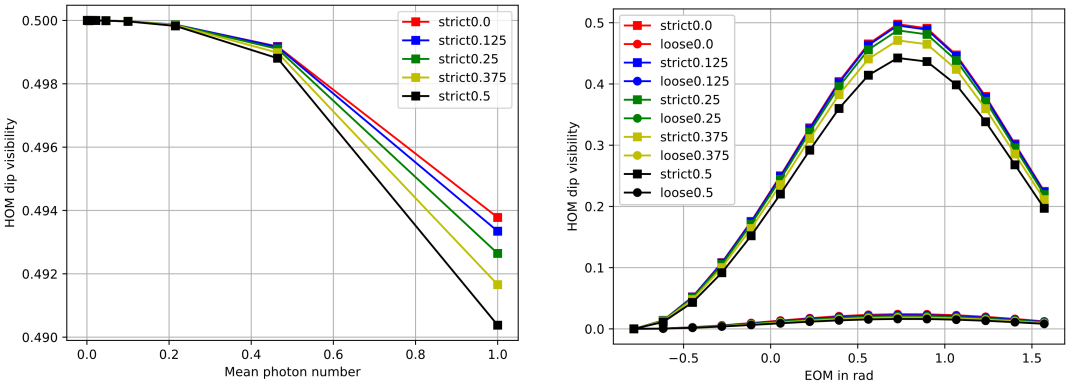

Figure 8.10: (a): Numerically simulated visibilities depending on the mean photon number for coherent input states in the $\tau = 0$ case for different values of loss on one input mode. (b): Numerically simulated visibilities depending on the beam splitter angle of the EOM operation in radiant for different values of loss on one input mode. Squares represent coincidences under strict conditions, circles coincidences under loose conditions. For coherent input states these are close to zero.

8.5.2 EOM Beam Splitter Angle

Experimental imperfections that can possibly affect the visibility of time-multiplexed HOM-dips include inaccurate settings of the static (HWPs and QWPs) as well as of the dynamic coins (EOM-switchings), imbalanced losses and phases acquired by parts of the state during evolution.
Ideally, a perfect swap operation between a mode of the upper input state and a mode of the lower input is conducted in the second stage of the scheme (section B in Figure 8.9). Concerning the physical implementation in the setup, this corresponds to offsetting the coin operation of the QWP exactly with the switching operation of the EOM. In the numerical implementation, however, a perfect swap operation requires the sum of the beam splitter angle of the QWP operation and the beam splitter angle of the EOM switching to be $\pi/2$. Assuming the QWP angle to be $\pi/4$, we simulate the effect of deviations of the EOM switching from its ideal angle which is $\pi/4$ as well.
Figure 8.10, (b) shows the resulting visibilities over the EOM beam splitter angle for different amounts of imbalanced loss (see the next subsection for how imbalanced losses are implemented). We see that the slope of the visibility around the maximum is low enough to allow for small experimental imperfections in the EOM switching without drastic effects on the visibility. In addition, we see that visibilities under loose conditions are close to zero for coherent input states.

8.5.3 QWP Beam Splitter Angle

Concerning the static QWP, we consider a deviation of its angle from the ideal value of $\pi/4$. Figure 8.11, (a) shows the numerically calculated HOM-dip visibility depending on the EOM angle in radiant for different angles for the static QWP. We see that an imperfect angle setting of the QWP shifts the EOM beam splitter angle for which we expect optimal visibility. Furthermore, the plot shows that we do not expect small deviations of the QWP angle from $\pi/4$ to have a significant impact on the visibility.

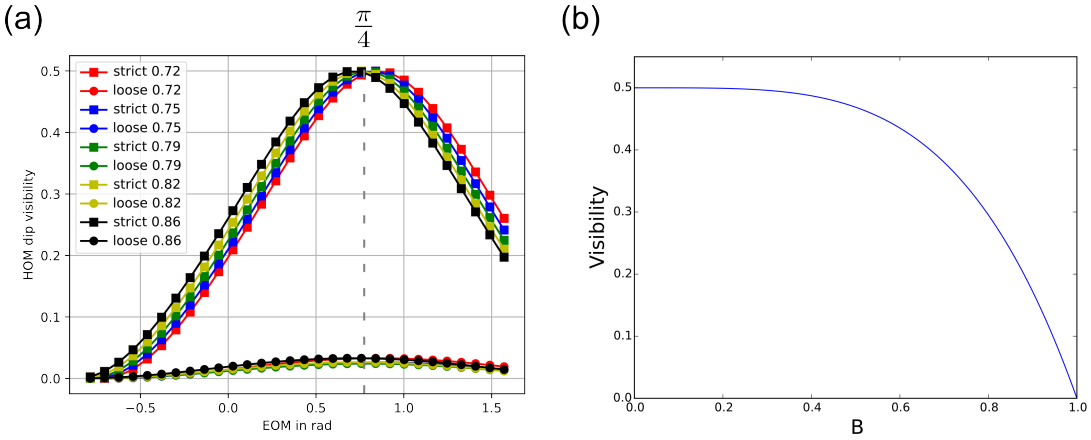

Figure 8.11: (a): Numerically calculated HOM-dip visibility depending on the EOM angle in radiant for different angles (also in radiant) of the static QWP. Again, visibilities under loose coincidence conditions are very low. The grey dashed line marks an EOM angle corresponding to $\pi/4$. (b): Expected visibility for a coherent input state depending on the balancedness parameter B.

8.5.4 Imbalanced Losses

When evaluating imbalanced losses, we have to consider that there are four different input ports for the two final time-multiplexed beam splitter operations $U_{\mathrm{HWP}}(\theta_{\mathrm{HWP}})$ (section C in Figure 8.9). In the case in which one of the initial input states is subjected to higher losses than the other (section A in Figure 8.9), for example due to an inhomogeneous picking operation by the EOM for different positions (see section 4.3.2), two out of the four modes eventually interfering in section C will have less intensity than the other two. In the experiment, these imbalances could as well originate from imbalanced losses for different paths. The origin of the different intensities is, however, not important, it only matters that there is an interference of unequal inputs.
The case under investigation, i.e. imbalanced inputs at both interference positions, should exhibit a higher susceptibility to imbalanced losses than other possible cases, e.g. when only one out of four input modes of the final interference is subjected to losses. We investigate the most imbalanced case numerically by implementing a tunable beam splitter operation

to an ancillary mode that is then traced out for one mode of the initial input state in section A. All of the graphs shown for imbalanced losses in Figure 8.10 are computed in this way.
If we numerically simulate, on the other hand, imbalanced losses introduced after the interference, i.e. in the detection, we do not observe any degradation of the visibility depending on the amount of loss.
In addition, the imbalanced losses can be modelled as an imbalance of the beam splitter at which the photons finally interfere [198]. Here, a beam splitter unitary $\hat{U}_{\mathrm{BS}}$ of the following form is assumed:

$$\hat{U}_{\mathrm{BS}} = \begin{pmatrix} u & v \\ -v^* & u^* \end{pmatrix} \tag{8.11}$$

The balancedness parameter B is then defined as $B = |u|^2 - |v|^2$, which leads to the following expression for the visibility in the strict case [198]:

$$\mathrm{Vis} = \mathrm{Vis}_{\mathrm{ref}} \cdot \frac{1 - B^2}{1 + B^2} \tag{8.12}$$

Here, $\mathrm{Vis}_{\mathrm{ref}}$ denotes the visibility assuming a value of $B = 0$ for an ideal 50:50 beam splitter, which is $\mathrm{Vis}_{\mathrm{ref}} = 0.5$ for coherent input states. Figure 8.11, (b) shows the expected visibility for such a state as a function of the balancedness parameter B. We see that the effects on the visibility are rather small for a balancedness parameter of up to 0.5. Furthermore, the results are in qualitative agreement with the numerical simulations implemented in QuTip (see Figure 8.10, (b)).

8.6 Effects of Partial Overlap

Having numerically investigated potential effects on the visibilities arising from imperfections of the time-multiplexing network, we now turn our attention to how splitting up photons into multiple time bins might enhance experimental imperfections originating from the source.
For the discussions in section 8.1 we assumed ideal single-photon sources. The heralded PDC states used in our experiment, however, exhibit exponential photon-number statistics. Assuming an ideal source the visibility for a time-multiplexed HOM-dip experiment with $\tau = \pm 1$ is not expected to differ from a HOM-dip experiment without additional splitting up of the photons (see section 5.9) when considering a time-bin resolving detection scheme. In this case, only coincidences between the two polarisation modes for a certain time bin are counted and for a perfect single photon source these cannot occur unless two modes overlap at this certain time bin, in which case they also perform a HOM-dip.

This assumption, however, only holds for perfect single photon sources as otherwise higher photon-number contributions can lead to coincidences between two polarisation modes also for time bins where in the ideal case only one photon is expected to arrive.
Again, we investigate this effect numerically with QuTip. Here, we consider two heralded PDC states which are split into four modes by a Hadamard-like coin. In a time-multiplexed HOM-dip experiment with $\tau = \pm 1$, two out of these four modes will overlap and interfere at another Hadamard-like coin, while the other two will simply be split-up by this coin. The results for time-bin resolved detection are given by the red markers in Figure 8.12.

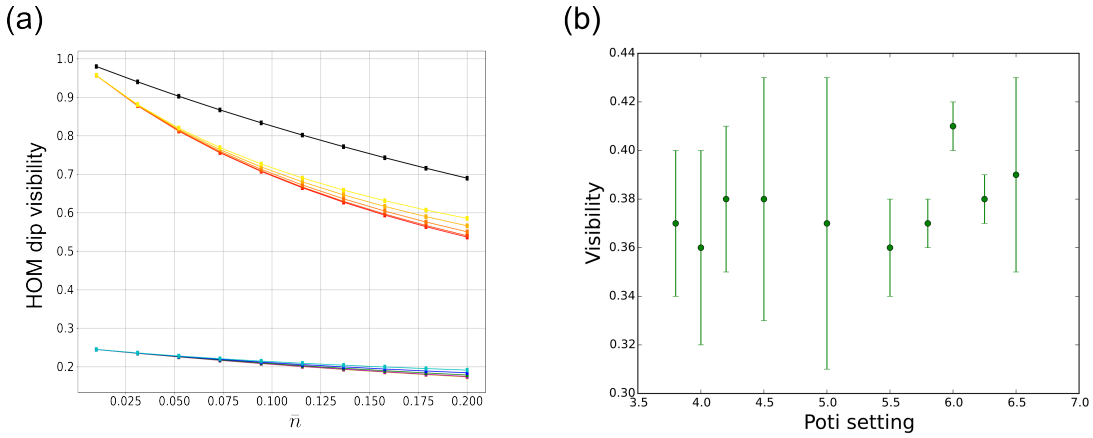

Figure 8.12: (a): Numerically expected visibilities depending on the mean photon number $\bar{n}$ for the $\tau = \pm 1$ case: The red curve corresponds to time-bin resolving detection. From the red to the yellow curve the phase on one of the input photons is gradually increased from $0°/360° \cdot 2\pi$ to $40°/360° \cdot 2\pi$. On the other hand, the purple curve gives visibilities for time-bucket detection. Again, the phase on one of the input photons is gradually increased from $0°/360° \cdot 2\pi$ (purple curve) to $40°/360° \cdot 2\pi$ (turquoise curve). The black curve represents a reference HOM-dip without additional splitting of the photons. We assume contributions from Poissonian noise ($\alpha = \sqrt{0.25 \cdot \bar{n}}$) and single-mode squeezed vacuum ($r^* = \sqrt{1.5 \cdot 10^{-4} \cdot \bar{n}}$) as well as a Klyshko-efficiency η of 0.3. (b): Experimentally obtained HOM-dip visibilities depending on the Poti setting for the EOM. Scanning the EOM voltage corresponds to varying the EOM angle in the numerics. The error bars are determined according to (5.23) as explained in section 5.9. The rather low absolute values are due to the fact that they were recorded during the optimisation process and e.g. before fixing the problems with Piezo-acoustic resonances in the Pockels cells (see section 4.3.2).

They are compared with the results of a reference experiment in which two heralded PDC states are interfered without splitting them up beforehands (see black markers in Figure 8.12). The parameters assumed for Poissonian noise ($\alpha = \sqrt{0.25 \cdot \bar{n}}$) and single-mode squeezed vacuum ($r^* = \sqrt{1.5 \cdot 10^{-4} \cdot \bar{n}}$) are the same as in section 5.6.
The comparison between the two cases shows clearly that we expect a significant degradation of visibilities as soon as higher photon number contributions are no longer negligible,

e.g. an absolute reduction by around 13 % for a mean photon number $\bar{n} = 0.1$. Just considering effect originating from the photon number distribution, this degradation should be the same for the $\tau = +1$ and $\tau = -1$ case.
In addition, we numerically calculate HOM-dip visibilities for time-bucket detection, which are given by the purple curve in Figure 8.12. We observe a value of ≈ 0.25 for low mean photon numbers $\bar{n}$. This what one would expect from the combinatorial argument that the two photons end up in the same time bin and thus interfere there with a 25 % chance when subjected to a 50:50 splitting.
We also investigate the effect of a phase on one of the input photons. To this purpose, we assume a phase that is increased in increments of $10°/360° \cdot 2\pi$ from $0°/360° \cdot 2\pi$ to $40°/360° \cdot 2\pi$. A phase of $40°/360° \cdot 2\pi$ corresponds to the yellow (time-bin resolved detection) resp. the turquoise curve (time-bucket detection). It turns out that at least the numerics predict a slightly advantageous effect of a phase between input photons on the visibilities. In an experiment, this phase originates mainly from the relative phase of the pump pulses and is thus hard to control. Consequently, the most relevant aspect of this numerical finding is that at least we do not expect a significantly detrimental effect of a phase between the input photons.

8.7 Experimental Investigation of Imperfections

Since the effect of the mean photon-number on a time-multiplexed HOM-dip-experiment with coherent input states should be negligible, we expect to obtain a visibility of roughly 0.5. Indeed, passively routing coherent states from two different time-bins to an interference position with a scheme as described in section 5.1 yields a visibility of 0.46 ± 0.01. However, when splitting up the pulses and then merging them again as mandated for a time-multiplexed HOM-dip (see sections 8.1 and 8.2), we observe drops in the visibility to values as low as 0.35 ± 0.03 even for the $\tau = 0$ case.
A big difference between passive routing and the time-multiplexed HOM-dip scheme is the fact that the latter involves switchings of the EOMs for both the coin and active in- and outcoupling. Insufficient quality of these switchings could lead to unequal intensity for the path brought to interference. This effect can either be quantified via imbalanced losses implemented in the numerical simulations with QuTip (see section 5.8) or via the balancedness parameter as described in section 8.5.4. Both methods yield similar results and predict that imbalanced losses greater than 50% are required to explain a drop in visibility of 0.1 as observed in the experiment, i.e. one of the input ports of the interference beam splitter has only half the intensity of the other. Such imbalances can indeed occur when the Pockels cells exhibit unwanted acoustic resonances (see section 4.3.1). After fixing the problem, however, we no longer observe imbalanced losses of this extent.
Another parameter that changes between these two cases is the initial spacing of the pulses, which is two positions for a time-multiplexed HOM-dip with the state $|E\rangle$ and one position for the state $|O\rangle$ or in case of passive interference. Consequently, the reduction

in visibility could in principle be caused by dispersion in the fibres delaying the pulses. However, our experimental findings confirm the numerical prediction found in section 5.3, as passive routing of pulses spaced either 1 or 2 positions apart leads to the same visibilities, when considering the experimental error: By measuring passive interference between two coherent inputs spaced one and two initial positions apart, we verify that the effect of dispersion is negligible as we measure a visibility of 0.45 ± 0.03 for a spacing of one position and 0.46 ± 0.03 for two positions.
In order to investigate whether visibilities are reduced by an improper setting of the voltage applied to the EOM, we scan the voltage applied to the EOM switching between coin, transmission and reflection operation for voltages ranging from 3.8 to 6.5 on the control dial where 0 corresponds to an applied voltage of 0 kV and 10 to 2.2 kV. (see Figure 8.12, (b)). These settings correspond to EOM angles between approximately 0.6 and 1.0 in radiant, so that the negligible variation in visibilities observed experimentally might be caused by the fact that all of the EOM angles form part of the plateau predicted by the numerics (see Figure 8.11). It can be concluded that tuning the voltage applied to the EOM does not allow to significantly increase visibilities.
Detuning the angle of the static coin in the loop by $\pm 2^\circ$ results in both cases in a drop of the experimental visibility of roughly around 0.02. This change of visibility is within the experimental error bars and indeed the numerics do not predict a significant influence of the static coin in the plateau region.
In conclusion, we have thus verified that experimentally obtained visibilities are resilient towards imbalanced losses (after damping resonances), inaccuracies the initial spacing as well slightly inaccurate dynamic resp. static coin operations.

8.8 Conclusion for Time-multiplexed HOM-dip

The concept of time-multiplexed HOM-dips harnesses the capability of our time-multiplexing network to spread photons over multiple time bins in order to synthesize an additional mode structure for these photons. Time-multiplexed coincidence detection then allows for either resolving or tracing out this new degree of freedom. When tracing out the time bins, the HOM-interference becomes sensitive to the phase relation of these bins. By dynamically reconfiguring the network, we can easily engineer the relative translation of the time bins as well as their relative phases and thus exert coherent control over quantum interference.
In an experiment, we probe the interplay between characteristics of the state, i.e. phases and translation, and the detection scheme. When detecting coincidences in a mode-resolved way, phases relative to other modes as well as a translation do not affect visibilities. In this case they are only degraded by the degrees of freedom that our detection cannot resolve, e.g. Schmidt-modes or photon number.
In contrast to the aforementioned degrees of freedom, we can decide whether the modes synthesized in time are resolved in a measurement. When deliberately tracing them out,

we experimentally observe the significance of phase and translation: Concerning the phase, we can either measure full or no visibility when spreading each photon over two bins. When scaling the spread up to three bins per photon, we observe also partial visibility as well as a dependency on the concrete selection of bins considered. The translation, quantified by the parameter τ, can be tuned in discrete step from full overlap over partial overlap to no overlap.
The time-multiplexed HOM-dip experiment serves as a benchmark for the performance of both the PDC source preparing the quantum states as well as the time-multiplexing network with which they are manipulated. Preparing the time-multiplexed states with a dynamically reconfigurable fibre network introduces additional experimental challenges in comparison to passive routing of the pulses: When not counteracted, Piezo-acoustic resonances in the Pockels cells can bring imbalanced losses to a regime where they significantly degrade visibilities. In addition, the detrimental effect of higher photon-number contributions is increased in case the interfering states only partially overlap. On the other hand, we find that visibilities show a sufficient resilience towards inaccuracies of static and dynamic coins, initial spacing of the photons as well as imbalanced losses to assume that these parameters do not significantly affect the results.
At the time of the writing of this thesis, the results are being prepared for publication.

9 Conclusion and Outlook

The aim of our work was the implementation of a network comprising single-photon input states, a reconfigurable unitary evolution and the complete read-out of external as well as internal modes. On the other hand, we saw that a wide range of effects can be investigated by measuring the results of the coherent propagation of laser light. We thus first look at these experiments in section 9.1 before we turn our attention in 9.2 to experiments that indeed require quantum states of light (e.g. squeezed states).

9.1 Experiments with Coherent Quantum Walks

Considering the unitary governing the state's evolution, certain quantum walk protocols exhibit symmetries that give rise to topological phenomena (see sections 6.1 and 6.2). In the context of this thesis we have presented three different approaches:
In the first one we measure scattered amplitudes that are directly linked to topological invariants, namely reflection matrix elements. The high degree of reconfigurability regarding the coin angle in the setup allowed for scans across the topological phase diagram as well as for probing the effect of disorder on both reflection matrix elements and edge states emerging at topological boundaries (see sections 6.3, 6.4 and 6.5).
While there is good reason to assume that the localised states observed in the scheme referred to above are indeed topologically protected edge states, formally showing this would require the measurement of the eigenvalues corresponding to these eigenstates. The decoupled split-step quantum walk with a phase-reference as presented in section 6.6 allows for experimentally accessing the eigenvalues of the walk operator by probing its effect in relation to a reference.
Eventually, we investigate midgap states characterised by their anomalous polarisation (see section 6.7).
The implementation of deterministic in- and outcoupling allows to extend the simulation capabilities of the setup to projective measurements. In an experiment relying on this ability, we observe a measurement-induced change in the recurrence probability of the walker (see chapter 7).
The possibility to implement projective measurements via sinks offers an intriguing outlook for future experiments: Regarding quantum coherence as a signature of the non-classicality of a Markovian statistics [203], the sinks enable an experimental scheme in which we quantify non-classicality as function of the evolution's ability to generate and detect coherences (CGD).
In the experiment, the CGD depends on the coin angle while the non-classicality is quan-

tified via the Kolmogorov distance [204] between an unperturbed evolution over a certain number n of steps and an evolution with a decohering measurement at an intermediate step number $n/2$. This decohering measurement can be mimicked in our setup via the sinks with which we outcouple all but one remaining mode in step $n/2$. We successively collect data with all possible modes in step $n/2$ being the remaining mode in one distinct run. By summing up the data of the individual runs afterwards, we obtain the same statistics as for an evolution over n steps that has been decohered in step $n/2$.
The corresponding data has already been collected and at the time of the writing of this thesis the paper is being prepared together with our theory partners.
This example illustrates how the sinks could be harnessed to examine open system dynamics, which are relevant e.g. for the study of biological systems [41]. The high degree of reconfigurability in our setup allows us to easily implement disordered patterns of sinks that would likely be required for such extensions of the simulating capabilities.
Complementing position-dependent losses via sinks with position-dependent gain could be a way to implement a system exhibiting parity-time symmetry [205, 206].

9.2 Experiments with Quantum States

While the experiments mentioned above are usually described by the evolution of a wavefunction governed by a unitary, i.e. according to the axioms of quantum mechanics, they could equally well be understood as the spread of the amplitude of an electric field, i.e. by referring to a classical picture. In an experimental setting this means that coherent light and single photons lead to the same results. The reason is the equivalence of the evolution of single photons and the evolution of coherent light for an initial state occupying only one position (see appendix A).
One the other hand, we saw that a optical network with universal capabilities in quantum computation and simulation requires single-photon input states. So where are the limitations of coherent states? Only when considering quantum walks with several walkers starting at multiple positions the differences between the two types of states become apparent in a coincidence resolving detection scheme. It is consequently via Hong-Ou-Mandel-interference that the quantum properties of states are experimentally revealed.
A crucial challenge in setting up the experimental platform thus consists in ensuring the indistinguishability resp. the purity of the input modes. The three degrees of freedom requiring most of our attention are found in the temporal domain (sections 5.2 and 5.3), the frequency space (section 5.4) and the photon-number statistics (section 5.7).
Concerning the temporal characteristics, the most important measures consist in using a ps source to limit dispersion and minimising fluctuations in the temporal delay via temperature stabilisation.
In order to achieve purity in the spectral domain, we harness an engineered source for which a spectral decomposition yields a Schmidt-number close to one.
Eventually, we investigate the effect of higher photon-number contributions numerically

as well as experimentally. We limit their detrimental effects by implementing two-mode detection and pumping as weakly as possible.
As a consequence, we experimentally observe HOM-dip visibilities of around 80 % in case of passive routing, which is in accordance with numerical results.
We synthesize an additional mode structure for the PDC states by spreading their interference over multiple time bins in a time-multiplexed HOM-dip experiment. In such a scheme we can engineer the phase relation as well as the relative translation of these modes. The sensitivity to aforementioned parameters depends on whether coincidence detection is implemented such that it resolves the mode structure in a time-bin resolving detection scheme or such that the modes are traced out in a time-bucket detection scheme. We consequently obtain a high degree of control in synthesizing and reading-out the mode structure of single photons, offering an intriguing insight into the interplay of coherence and quantum interference.
We have shown a proof-of-principle experiment for the scalability of the network by extending the splitting of the photons to three time bins. Here, we find multiple ways of combining the bins leading to qualitatively different results.
Time-multiplexed HOM-interference also serves as a benchmark for the effects of active routing via EOM switchings on visibilities, showing that the active network does not lead to a significant degradation in this aspect.
As already mentioned, manipulating a time-multiplexed input state in a fibre network provides a possible platform for the implementation of boson sampling [51], especially Gaussian boson sampling [99, 100]. The state-of-the-art efficiencies do, however, not allow for more than proof-of-principle experiments.
In the previous section we have discussed possible applications of sinks together with classical input states. In combination with single photons we could implement experiments realising fundamental tests of quantumness such as the Hardy experiment [193, 207], interaction-free measurements [194] or tests of the Leggett-Garg inequality [208].
In principle, the setup exhibits the necessary ingredients for the implementation of a controlled-not gate [209, 88] and thus for linear optics quantum computing [4].
Having a reconfigurable network interfering quantum states available, an interesting prospect consists in studying the behaviour of quantum particles on a dynamical graph, e.g. a percolation graph [210]. Here, a concrete idea is using percolation as an entanglement witness [211].
In summary, we have implemented a system in which highly pure and indistinguishable photons can be fed into multiple space-like separated modes of a reconfigurable and scalable network and be detected resolving the mode structure in their internal as well as external degree of freedom.

Bibliography

[1] Richard P. Feynman. Simulating physics with computers. *International Journal of Theoretical Physics*, 21(6-7):467–488, June 1982. ISSN 0020-7748, 1572-9575. doi:10.1007/BF02650179. URL http://link.springer.com/10.1007/BF02650179.

[2] P. Shor. Polynomial-Time Algorithms for Prime Factorization and Discrete Logarithms on a Quantum Computer. *SIAM Journal on Computing*, 26(5):1484–1509, October 1997. ISSN 0097-5397. doi:10.1137/S0097539795293172. URL http://epubs.siam.org/doi/abs/10.1137/S0097539795293172.

[3] Lov K. Grover. A fast quantum mechanical algorithm for database search. *arXiv:quant-ph/9605043*, May 1996. URL http://arxiv.org/abs/quant-ph/9605043. arXiv: quant-ph/9605043.

[4] E. Knill, R. Laflamme, and G. J. Milburn. A scheme for efficient quantum computation with linear optics. *Nature*, 409(6816):46–52, January 2001. ISSN 1476-4687. doi:10.1038/35051009. URL https://www.nature.com/articles/35051009.

[5] Andrew M. Childs. Universal Computation by Quantum Walk. *Physical Review Letters*, 102(18):180501, May 2009. doi:10.1103/PhysRevLett.102.180501. URL https://link.aps.org/doi/10.1103/PhysRevLett.102.180501.

[6] Andrew M. Childs, David Gosset, and Zak Webb. Universal Computation by Multiparticle Quantum Walk. *Science*, 339(6121):791–794, February 2013. ISSN 0036-8075, 1095-9203. doi:10.1126/science.1229957. URL http://science.sciencemag.org/content/339/6121/791.

[7] Alán Aspuru-Guzik and Philip Walther. Photonic quantum simulators. *Nature Physics*, 8(4):285–291, April 2012. ISSN 1745-2481. doi:10.1038/nphys2253. URL https://www.nature.com/articles/nphys2253.

[8] Y. Aharonov, L. Davidovich, and N. Zagury. Quantum random walks. *Physical Review A*, 48(2):1687–1690, August 1993. doi:10.1103/PhysRevA.48.1687. URL https://link.aps.org/doi/10.1103/PhysRevA.48.1687.

[9] A. Schreiber, K. N. Cassemiro, V. Potoček, A. Gábris, P. J. Mosley, E. Andersson, I. Jex, and Ch. Silberhorn. Photons Walking the Line: A Quantum Walk with Adjustable Coin Operations. *Physical Review Letters*, 104(5):050502, February 2010.

doi:10.1103/PhysRevLett.104.050502. URL http://link.aps.org/doi/10.1103/PhysRevLett.104.050502.

[10] A. Schreiber, K. N. Cassemiro, V. Potoček, A. Gábris, I. Jex, and Ch. Silberhorn. Decoherence and Disorder in Quantum Walks: From Ballistic Spread to Localization. *Physical Review Letters*, 106(18):180403, May 2011. doi:10.1103/PhysRevLett.106.180403. URL http://link.aps.org/doi/10.1103/PhysRevLett.106.180403.

[11] Andreas Schreiber, Aurél Gábris, Peter P. Rohde, Kaisa Laiho, Martin Štefaňák, Václav Potoček, Craig Hamilton, Igor Jex, and Christine Silberhorn. A 2d Quantum Walk Simulation of Two-Particle Dynamics. *Science*, 336(6077):55–58, June 2012. ISSN 0036-8075, 1095-9203. doi:10.1126/science.1218448. URL http://www.sciencemag.org/content/336/6077/55.

[12] Fabian Elster, Sonja Barkhofen, Thomas Nitsche, Jaroslav Novotný, Aurél Gábris, Igor Jex, and Christine Silberhorn. Quantum walk coherences on a dynamical percolation graph. *Scientific Reports*, 5:13495, August 2015. ISSN 2045-2322. doi:10.1038/srep13495. URL http://www.nature.com/doifinder/10.1038/srep13495.

[13] Alan Migdall, Sergey V. Polyakov, Jingyun Fan, and Joshua C. Bienfang, editors. *Single-photon generation and detection: physics and applications*. Number 45 in Experimental methods in the physical sciences. Elsevier/Acad. Press, Amsterdam, 2013. ISBN 978-0-12-387696-6 978-0-12-387695-9. OCLC: 910935055.

[14] S. M. Barnett and P. M. Radmore. *Methods in theoretical quantum optics*. Number 15 in Oxford series in optical and imaging sciences. Clarendon Press ; Oxford University Press, Oxford : New York, 1997. ISBN 978-0-19-856362-4.

[15] Jack F. Douglas. Aspects and applications of the random walk: G. H. Weiss, North-Holland, New York, 1994. *Journal of Statistical Physics*, 79(1-2):497–500, April 1995. ISSN 0022-4715, 1572-9613. doi:10.1007/BF02179402. URL http://link.springer.com/10.1007/BF02179402.

[16] L. Bachelier. Théorie de la spéculation. *Annales scientifiques de l'École normale supérieure*, 17:21–86, 1900. ISSN 0012-9593, 1873-2151. doi:10.24033/asens.476. URL http://www.numdam.org/item?id=ASENS_1900_3_17__21_0.

[17] Johannes Voit. *The Statistical Mechanics of Financial Markets*. Theoretical and Mathematical Physics. Springer-Verlag, Berlin Heidelberg, 2 edition, 2003. ISBN 978-3-662-05125-2. URL https://www.springer.com/de/book/9783662051252.

[18] Robert Brown. On the particles contained in the pollen of plants; and on the general existence of active molecules in organic and inorganic bodies. *The Philosophical Magazine*, 4(21):161–173, September 1828. ISSN 1941-5850, 1941-5869.

doi:10.1080/14786442808674769. URL https://www.tandfonline.com/doi/full/10.1080/14786442808674769.

[19] Francis Galton. Natural Inheritance. *Science*, ns-13(322):266–267, April 1889. ISSN 0036-8075, 1095-9203. doi:10.1126/science.ns-13.322.266. URL http://www.sciencemag.org/cgi/doi/10.1126/science.ns-13.322.266.

[20] George L. Gerstein and Benoit Mandelbrot. Random Walk Models for the Spike Activity of a Single Neuron. *Biophysical Journal*, 4(1):41–68, January 1964. ISSN 00063495. doi:10.1016/S0006-3495(64)86768-0. URL https://linkinghub.elsevier.com/retrieve/pii/S0006349564867680.

[21] Andreas Schreiber. *Quantum walks in time*. Number Band 3 in FAU studies mathematics & physics. FAU University Press, Erlangen, 2014. ISBN 978-3-944057-15-6.

[22] Thomas Nitsche. Experimental simulation of time-multiplexed photonic quantum walks, 2014.

[23] Frederick W. Strauch. Connecting the discrete- and continuous-time quantum walks. *Physical Review A*, 74(3):030301, September 2006. doi:10.1103/PhysRevA.74.030301. URL https://link.aps.org/doi/10.1103/PhysRevA.74.030301.

[24] Andrew M. Childs. On the Relationship Between Continuous- and Discrete-Time Quantum Walk. *Communications in Mathematical Physics*, 294(2):581–603, March 2010. ISSN 1432-0916. doi:10.1007/s00220-009-0930-1. URL https://doi.org/10.1007/s00220-009-0930-1.

[25] Jan Sperling, Syamsundar De, Thomas Nitsche, Johannes Tiedau, Sonja Barkhofen, Benjamin Brecht, and Christine Silberhorn. Wave-particle duality revisited: Neither wave nor particle. *arXiv:1907.09836 [quant-ph]*, July 2019. URL http://arxiv.org/abs/1907.09836. arXiv: 1907.09836.

[26] R. Hanbury Brown and R. Q. Twiss. Correlation between Photons in two Coherent Beams of Light. *Nature*, 177(4497):27–29, January 1956. ISSN 1476-4687. doi:10.1038/177027a0. URL https://www.nature.com/articles/177027a0.

[27] Hans-Albert Bachor and Timothy C. Ralph. *A guide to experiments in quantum optics*. Physics textbook. Wiley-VCH, Weinheim, 2., rev. and enl. ed edition, 2004. ISBN 978-3-527-61923-8 978-3-527-40393-6. OCLC: 249363074.

[28] C. K. Hong, Z. Y. Ou, and L. Mandel. Measurement of subpicosecond time intervals between two photons by interference. *Physical Review Letters*, 59(18):2044–2046, November 1987. doi:10.1103/PhysRevLett.59.2044. URL https://link.aps.org/doi/10.1103/PhysRevLett.59.2044.

[29] T. B. Pittman, B. C. Jacobs, and J. D. Franson. Heralding single photons from pulsed parametric down-conversion. *Optics Communications*, 246(4):545–550, February 2005. ISSN 0030-4018. doi:10.1016/j.optcom.2004.11.027. URL http://www.sciencedirect.com/science/article/pii/S0030401804011551.

[30] P. J. Mosley, J. S. Lundeen, B. J. Smith, and I. A. Walmsley. Conditional preparation of single photons using parametric downconversion: a recipe for purity. *New Journal of Physics*, 10(9):093011, 2008. ISSN 1367-2630. doi:10.1088/1367-2630/10/9/093011. URL http://stacks.iop.org/1367-2630/10/i=9/a=093011.

[31] Georg Harder, Vahid Ansari, Benjamin Brecht, Thomas Dirmeier, Christoph Marquardt, and Christine Silberhorn. An optimized photon pair source for quantum circuits. *Optics Express*, 21(12):13975–13985, June 2013. ISSN 1094-4087. doi:10.1364/OE.21.013975. URL https://www.osapublishing.org/oe/abstract.cfm?uri=oe-21-12-13975.

[32] Christopher J. Chunnilall, Ivo Pietro Degiovanni, Stefan Kück, Ingmar Müller, and Alastair G. Sinclair. Metrology of single-photon sources and detectors: a review. *Optical Engineering*, 53(8):081910, July 2014. ISSN 0091-3286, 1560-2303. doi:10.1117/1.OE.53.8.081910. URL https://www.spiedigitallibrary.org/journals/Optical-Engineering/volume-53/issue-8/081910/Metrology-of-single-photon-sources-and-detectors-a-review/10.1117/1.OE.53.8.081910.short.

[33] Peter J. Mosley, Jeff S. Lundeen, Brian J. Smith, Piotr Wasylczyk, Alfred B. U'Ren, Christine Silberhorn, and Ian A. Walmsley. Heralded Generation of Ultrafast Single Photons in Pure Quantum States. *Physical Review Letters*, 100(13):133601, April 2008. doi:10.1103/PhysRevLett.100.133601. URL https://link.aps.org/doi/10.1103/PhysRevLett.100.133601.

[34] Jinhyoung Lee, M. S. Kim, and Časlav Brukner. Operationally Invariant Measure of the Distance between Quantum States by Complementary Measurements. *Physical Review Letters*, 91(8):087902, August 2003. doi:10.1103/PhysRevLett.91.087902. URL https://link.aps.org/doi/10.1103/PhysRevLett.91.087902.

[35] Masanao Ozawa. Entanglement measures and the Hilbert–Schmidt distance. *Physics Letters A*, 268(3):158–160, April 2000. ISSN 0375-9601. doi:10.1016/S0375-9601(00)00171-7. URL http://www.sciencedirect.com/science/article/pii/S0375960100001717.

[36] Neil B. Lovett, Sally Cooper, Matthew Everitt, Matthew Trevers, and Viv Kendon. Universal quantum computation using the discrete-time quantum walk. *Physical Review A*, 81(4):042330, April 2010. doi:10.1103/PhysRevA.81.042330. URL https://link.aps.org/doi/10.1103/PhysRevA.81.042330.

[37] Neil Shenvi, Julia Kempe, and K. Birgitta Whaley. Quantum random-walk search algorithm. *Physical Review A*, 67(5):052307, May 2003. doi:10.1103/PhysRevA.67.052307. URL https://link.aps.org/doi/10.1103/PhysRevA.67.052307.

[38] Andris Ambainis. Quantum Walk Algorithm for Element Distinctness. *SIAM Journal on Computing*, 37(1):210–239, January 2007. ISSN 0097-5397, 1095-7111. doi:10.1137/S0097539705447311. URL http://epubs.siam.org/doi/10.1137/S0097539705447311.

[39] Frederick W. Strauch. Relativistic quantum walks. *Physical Review A*, 73(5):054302, May 2006. doi:10.1103/PhysRevA.73.054302. URL https://link.aps.org/doi/10.1103/PhysRevA.73.054302.

[40] Gregory S. Engel, Tessa R. Calhoun, Elizabeth L. Read, Tae-Kyu Ahn, Tomáš Mančal, Yuan-Chung Cheng, Robert E. Blankenship, and Graham R. Fleming. Evidence for wavelike energy transfer through quantum coherence in photosynthetic systems. *Nature*, 446(7137):782–786, April 2007. ISSN 1476-4687. doi:10.1038/nature05678. URL https://www.nature.com/articles/nature05678.

[41] Masoud Mohseni, Patrick Rebentrost, Seth Lloyd, and Alán Aspuru-Guzik. Environment-assisted quantum walks in photosynthetic energy transfer. *The Journal of Chemical Physics*, 129(17):174106, November 2008. ISSN 0021-9606. doi:10.1063/1.3002335. URL https://aip.scitation.org/doi/10.1063/1.3002335.

[42] M. B. Plenio and S. F. Huelga. Dephasing-assisted transport: quantum networks and biomolecules. *New Journal of Physics*, 10(11):113019, 2008. ISSN 1367-2630. doi:10.1088/1367-2630/10/11/113019. URL http://stacks.iop.org/1367-2630/10/i=11/a=113019.

[43] Andre Ahlbrecht, Andrea Alberti, Dieter Meschede, Volkher B. Scholz, Albert H. Werner, and Reinhard F. Werner. Molecular binding in interacting quantum walks. *New Journal of Physics*, 14(7):073050, 2012. ISSN 1367-2630. doi:10.1088/1367-2630/14/7/073050. URL http://stacks.iop.org/1367-2630/14/i=7/a=073050.

[44] D. Witthaut. Quantum walks and quantum simulations with Bloch-oscillating spinor atoms. *Physical Review A*, 82(3):033602, September 2010. doi:10.1103/PhysRevA.82.033602. URL https://link.aps.org/doi/10.1103/PhysRevA.82.033602.

[45] Chang-Woo Lee, Paweł Kurzyński, and Hyunchul Nha. Quantum walk as a simulator of nonlinear dynamics: Nonlinear Dirac equation and solitons. *Physical Review A*, 92(5):052336, November 2015. doi:10.1103/PhysRevA.92.052336. URL https://link.aps.org/doi/10.1103/PhysRevA.92.052336.

[46] Takuya Kitagawa, Mark S. Rudner, Erez Berg, and Eugene Demler. Exploring topological phases with quantum walks. *Physical Review A*, 82(3):033429, September 2010. doi:10.1103/PhysRevA.82.033429. URL `https://link.aps.org/doi/10.1103/PhysRevA.82.033429`.

[47] J. K. Asbóth. Symmetries, topological phases, and bound states in the one-dimensional quantum walk. *Physical Review B*, 86(19):195414, November 2012. doi:10.1103/PhysRevB.86.195414. URL `https://link.aps.org/doi/10.1103/PhysRevB.86.195414`.

[48] C. Cedzich, T. Geib, F. A. Grünbaum, C. Stahl, L. Velázquez, A. H. Werner, and R. F. Werner. The Topological Classification of One-Dimensional Symmetric Quantum Walks. *Annales Henri Poincaré*, 19(2):325–383, February 2018. ISSN 1424-0637, 1424-0661. doi:10.1007/s00023-017-0630-x. URL `https://link.springer.com/article/10.1007/s00023-017-0630-x`.

[49] Matthew A. Broome, Alessandro Fedrizzi, Saleh Rahimi-Keshari, Justin Dove, Scott Aaronson, Timothy C. Ralph, and Andrew G. White. Photonic Boson Sampling in a Tunable Circuit. *Science*, 339(6121):794–798, February 2013. ISSN 0036-8075, 1095-9203. doi:10.1126/science.1231440. URL `http://science.sciencemag.org/content/339/6121/794`.

[50] Justin B. Spring, Benjamin J. Metcalf, Peter C. Humphreys, W. Steven Kolthammer, Xian-Min Jin, Marco Barbieri, Animesh Datta, Nicholas Thomas-Peter, Nathan K. Langford, Dmytro Kundys, James C. Gates, Brian J. Smith, Peter G. R. Smith, and Ian A. Walmsley. Boson Sampling on a Photonic Chip. *Science*, 339(6121):798–801, February 2013. ISSN 0036-8075, 1095-9203. doi:10.1126/science.1231692. URL `http://science.sciencemag.org/content/339/6121/798`.

[51] Keith R. Motes, Alexei Gilchrist, Jonathan P. Dowling, and Peter P. Rohde. Scalable Boson Sampling with Time-Bin Encoding Using a Loop-Based Architecture. *Physical Review Letters*, 113(12):120501, September 2014. doi:10.1103/PhysRevLett.113.120501. URL `https://link.aps.org/doi/10.1103/PhysRevLett.113.120501`.

[52] Yu He, X. Ding, Z.-E. Su, H.-L. Huang, J. Qin, C. Wang, S. Unsleber, C. Chen, H. Wang, Y.-M. He, X.-L. Wang, W.-J. Zhang, S.-J. Chen, C. Schneider, M. Kamp, L.-X. You, Z. Wang, S. Höfling, Chao-Yang Lu, and Jian-Wei Pan. Time-Bin-Encoded Boson Sampling with a Single-Photon Device. *Physical Review Letters*, 118(19):190501, May 2017. doi:10.1103/PhysRevLett.118.190501. URL `https://link.aps.org/doi/10.1103/PhysRevLett.118.190501`.

[53] Hui Wang, Yu He, Yu-Huai Li, Zu-En Su, Bo Li, He-Liang Huang, Xing Ding, Ming-Cheng Chen, Chang Liu, Jian Qin, Jin-Peng Li, Yu-Ming He, Christian

Schneider, Martin Kamp, Cheng-Zhi Peng, Sven Höfling, Chao-Yang Lu, and Jian-Wei Pan. High-efficiency multiphoton boson sampling. *Nature Photonics*, 11(6): 361–365, June 2017. ISSN 1749-4885. doi:10.1038/nphoton.2017.63. URL http://www.nature.com/nphoton/journal/v11/n6/full/nphoton.2017.63.html.

[54] Scott Aaronson and Alex Arkhipov. The Computational Complexity of Linear Optics. In *Proceedings of the Forty-third Annual ACM Symposium on Theory of Computing*, STOC '11, pages 333–342, New York, NY, USA, 2011. ACM. ISBN 978-1-4503-0691-1. doi:10.1145/1993636.1993682. URL http://doi.acm.org/10.1145/1993636.1993682.

[55] Hagai Perets, Yoav Lahini, Francesca Pozzi, Marc Sorel, Roberto Morandotti, and Yaron Silberberg. Realization of Quantum Walks with Negligible Decoherence in Waveguide Lattices. *Physical Review Letters*, 100(17):1–4, May 2008. doi:10.1103/PhysRevLett.100.170506. URL http://link.aps.org/doi/10.1103/PhysRevLett.100.170506.

[56] Alberto Peruzzo, Mirko Lobino, Jonathan C. F. Matthews, Nobuyuki Matsuda, Alberto Politi, Konstantinos Poulios, Xiao-Qi Zhou, Yoav Lahini, Nur Ismail, Kerstin Wörhoff, Yaron Bromberg, Yaron Silberberg, Mark G. Thompson, and Jeremy L. OBrien. Quantum Walks of Correlated Photons. *Science*, 329(5998):1500–1503, September 2010. ISSN 0036-8075, 1095-9203. doi:10.1126/science.1193515. URL http://science.sciencemag.org/content/329/5998/1500.

[57] R. Kruse, F. Katzschmann, A. Christ, A. Schreiber, S. Wilhelm, K. Laiho, A. Gábris, C. S. Hamilton, I. Jex, and C Silberhorn. Spatio-spectral characteristics of parametric down-conversion in waveguide arrays. *New Journal of Physics*, 15(8):083046, 2013. ISSN 1367-2630. doi:10.1088/1367-2630/15/8/083046. URL http://stacks.iop.org/1367-2630/15/i=8/a=083046.

[58] J. D. A. Meinecke, K. Poulios, A. Politi, J. C. F. Matthews, A. Peruzzo, N. Ismail, K. Wörhoff, J. L. O'Brien, and M. G. Thompson. Coherent time evolution and boundary conditions of two-photon quantum walks in waveguide arrays. *Physical Review A*, 88(1):012308, July 2013. doi:10.1103/PhysRevA.88.012308. URL http://link.aps.org/doi/10.1103/PhysRevA.88.012308.

[59] H. Schmitz, R. Matjeschk, Ch. Schneider, J. Glueckert, M. Enderlein, T. Huber, and T. Schaetz. Quantum Walk of a Trapped Ion in Phase Space. *Physical Review Letters*, 103(9):090504, August 2009. doi:10.1103/PhysRevLett.103.090504. URL https://link.aps.org/doi/10.1103/PhysRevLett.103.090504.

[60] F. Zähringer, G. Kirchmair, R. Gerritsma, E. Solano, R. Blatt, and C. F. Roos. Realization of a Quantum Walk with One and Two Trapped Ions. *Physical Review Letters*, 104(10):100503, March 2010. doi:10.1103/PhysRevLett.104.100503. URL https://link.aps.org/doi/10.1103/PhysRevLett.104.100503.

[61] Michal Karski, Leonid Förster, Jai-Min Choi, Andreas Steffen, Wolfgang Alt, Dieter Meschede, and Artur Widera. Quantum Walk in Position Space with Single Optically Trapped Atoms. *Science*, 325(5937):174–177, July 2009. ISSN 0036-8075, 1095-9203. doi:10.1126/science.1174436. URL http://science.sciencemag.org/content/325/5937/174.

[62] Maximilian Genske, Wolfgang Alt, Andreas Steffen, Albert H. Werner, Reinhard F. Werner, Dieter Meschede, and Andrea Alberti. Electric Quantum Walks with Individual Atoms. *Physical Review Letters*, 110(19):190601, May 2013. doi:10.1103/PhysRevLett.110.190601. URL https://link.aps.org/doi/10.1103/PhysRevLett.110.190601.

[63] C. A. Ryan, M. Laforest, J. C. Boileau, and R. Laflamme. Experimental implementation of a discrete-time quantum random walk on an NMR quantum-information processor. *Physical Review A*, 72(6):062317, December 2005. doi:10.1103/PhysRevA.72.062317. URL https://link.aps.org/doi/10.1103/PhysRevA.72.062317.

[64] J. O. Owens, M. A. Broome, D. N. Biggerstaff, M. E. Goggin, A. Fedrizzi, T. Linjordet, M. Ams, G. D. Marshall, J. Twamley, M. J. Withford, and A. G. White. Two-photon quantum walks in an elliptical direct-write waveguide array. *New Journal of Physics*, 13(7):075003, July 2011. ISSN 1367-2630. doi:10.1088/1367-2630/13/7/075003. URL http://iopscience.iop.org/1367-2630/13/7/075003.

[65] Linda Sansoni, Fabio Sciarrino, Giuseppe Vallone, Paolo Mataloni, Andrea Crespi, Roberta Ramponi, and Roberto Osellame. Two-Particle Bosonic-Fermionic Quantum Walk via Integrated Photonics. *Physical Review Letters*, 108(1):010502, January 2012. doi:10.1103/PhysRevLett.108.010502. URL http://link.aps.org/doi/10.1103/PhysRevLett.108.010502.

[66] Andrea Crespi, Roberto Osellame, Roberta Ramponi, Vittorio Giovannetti, Rosario Fazio, Linda Sansoni, Francesco De Nicola, Fabio Sciarrino, and Paolo Mataloni. Anderson localization of entangled photons in an integrated quantum walk. *Nature Photonics*, 7(4):322–328, April 2013. ISSN 1749-4885. doi:10.1038/nphoton.2013.26. URL http://www.nature.com/nphoton/journal/v7/n4/abs/nphoton.2013.26.html.

[67] Jacques Carolan, Chris Harrold, Chris Sparrow, Enrique Martín-López, Nicholas J. Russell, Joshua W. Silverstone, Peter J. Shadbolt, Nobuyuki Matsuda, Manabu Oguma, Mikitaka Itoh, Graham D. Marshall, Mark G. Thompson, Jonathan C. F. Matthews, Toshikazu Hashimoto, Jeremy L. O'Brien, and Anthony Laing. Universal Linear Optics. *Science*, 349(6249):711–716, August 2015. ISSN 0036-8075, 1095-9203. doi:10.1126/science.aab3642. URL http://arxiv.org/abs/1505.01182. arXiv: 1505.01182.

[68] M. A. Broome, A. Fedrizzi, B. P. Lanyon, I. Kassal, A. Aspuru-Guzik, and A. G. White. Discrete Single-Photon Quantum Walks with Tunable Decoherence. *Physical Review Letters*, 104(15):153602, April 2010. doi:10.1103/PhysRevLett.104.153602. URL http://link.aps.org/doi/10.1103/PhysRevLett.104.153602.

[69] Peng Xue, Hao Qin, Bao Tang, and Barry C. Sanders. Observation of quasiperiodic dynamics in a one-dimensional quantum walk of single photons in space. *New Journal of Physics*, 16(5):053009, 2014. ISSN 1367-2630. doi:10.1088/1367-2630/16/5/053009. URL http://stacks.iop.org/1367-2630/16/i=5/a=053009.

[70] Peng Xue, Rong Zhang, Zhihao Bian, Xiang Zhan, Hao Qin, and Barry C. Sanders. Localized state in a two-dimensional quantum walk on a disordered lattice. *Physical Review A*, 92(4):042316, October 2015. doi:10.1103/PhysRevA.92.042316. URL https://link.aps.org/doi/10.1103/PhysRevA.92.042316.

[71] Alois Regensburger, Christoph Bersch, Benjamin Hinrichs, Georgy Onishchukov, Andreas Schreiber, Christine Silberhorn, and Ulf Peschel. Photon Propagation in a Discrete Fiber Network: An Interplay of Coherence and Losses. *Physical Review Letters*, 107(23):233902, December 2011. doi:10.1103/PhysRevLett.107.233902. URL http://link.aps.org/doi/10.1103/PhysRevLett.107.233902.

[72] J. Boutari, A. Feizpour, S. Barz, C. Di Franco, M. S. Kim, W. S. Kolthammer, and I. A. Walmsley. Large scale quantum walks by means of optical fiber cavities. *Journal of Optics*, 18(9):094007, 2016. ISSN 2040-8986. doi:10.1088/2040-8978/18/9/094007. URL http://stacks.iop.org/2040-8986/18/i=9/a=094007.

[73] Thomas Nitsche, Fabian Elster, Jaroslav Novotný, Aurél Gábris, Igor Jex, Sonja Barkhofen, and Christine Silberhorn. Quantum walks with dynamical control: graph engineering, initial state preparation and state transfer. *New Journal of Physics*, 18(6):063017, 2016. ISSN 1367-2630. doi:10.1088/1367-2630/18/6/063017. URL http://stacks.iop.org/1367-2630/18/i=6/a=063017.

[74] P. W. Anderson. Absence of Diffusion in Certain Random Lattices. *Physical Review*, 109(5):1492–1505, March 1958. doi:10.1103/PhysRev.109.1492. URL https://link.aps.org/doi/10.1103/PhysRev.109.1492.

[75] Sonja Barkhofen, Thomas Nitsche, Fabian Elster, Lennart Lorz, Aurél Gábris, Igor Jex, and Christine Silberhorn. Measuring topological invariants in disordered discrete-time quantum walks. *Physical Review A*, 96(3):033846, September 2017. doi:10.1103/PhysRevA.96.033846. URL https://link.aps.org/doi/10.1103/PhysRevA.96.033846.

[76] Thomas Nitsche, Tobias Geib, Christoph Stahl, Lennart Lorz, Christopher Cedzich, Sonja Barkhofen, Reinhard F Werner, and Christine Silberhorn. Eigenvalue measurement of topologically protected edge states in split-step quantum walks. *New*

Journal of Physics, 21(4):043031, April 2019. ISSN 1367-2630. doi:10.1088/1367-2630/ab12fa. URL http://stacks.iop.org/1367-2630/21/i=4/a=043031?key=crossref.66b39a0a5dff47a4d251ec1892d7e3d1.

[77] Thomas Nitsche, Sonja Barkhofen, Regina Kruse, Linda Sansoni, Martin Štefaňák, Aurél Gábris, Václav Potoček, Tamás Kiss, Igor Jex, and Christine Silberhorn. Probing measurement-induced effects in quantum walks via recurrence. *Science Advances*, 4(6):eaar6444, June 2018. ISSN 2375-2548. doi:10.1126/sciadv.aar6444. URL http://advances.sciencemag.org/content/4/6/eaar6444.

[78] B. Brecht, Dileep V. Reddy, C. Silberhorn, and M. G. Raymer. Photon Temporal Modes: A Complete Framework for Quantum Information Science. *Physical Review X*, 5(4):041017, October 2015. doi:10.1103/PhysRevX.5.041017. URL https://link.aps.org/doi/10.1103/PhysRevX.5.041017.

[79] Joseph M. Lukens and Pavel Lougovski. Frequency-encoded photonic qubits for scalable quantum information processing. *Optica*, 4(1):8–16, January 2017. ISSN 2334-2536. doi:10.1364/OPTICA.4.000008. URL https://www.osapublishing.org/optica/abstract.cfm?uri=optica-4-1-8.

[80] Vahid Ansari, John M. Donohue, Benjamin Brecht, and Christine Silberhorn. Tailoring nonlinear processes for quantum optics with pulsed temporal-mode encodings. *Optica*, 5(5):534–550, May 2018. ISSN 2334-2536. doi:10.1364/OPTICA.5.000534. URL https://www.osapublishing.org/optica/abstract.cfm?uri=optica-5-5-534.

[81] Pei Zhang, Xi-Feng Ren, Xu-Bo Zou, Bi-Heng Liu, Yun-Feng Huang, and Guang-Can Guo. Demonstration of one-dimensional quantum random walks using orbital angular momentum of photons. *Physical Review A*, 75(5):052310, May 2007. doi:10.1103/PhysRevA.75.052310. URL https://link.aps.org/doi/10.1103/PhysRevA.75.052310.

[82] Sandeep K. Goyal, Filippus S. Roux, Andrew Forbes, and Thomas Konrad. Implementing Quantum Walks Using Orbital Angular Momentum of Classical Light. *Physical Review Letters*, 110(26):263602, June 2013. doi:10.1103/PhysRevLett.110.263602. URL https://link.aps.org/doi/10.1103/PhysRevLett.110.263602.

[83] Filippo Cardano, Francesco Massa, Hammam Qassim, Ebrahim Karimi, Sergei Slussarenko, Domenico Paparo, Corrado de Lisio, Fabio Sciarrino, Enrico Santamato, Robert W. Boyd, and Lorenzo Marrucci. Quantum walks and wavepacket dynamics on a lattice with twisted photons. *Science Advances*, 1(2):e1500087, March 2015. ISSN 2375-2548. doi:10.1126/sciadv.1500087. URL http://advances.sciencemag.org/content/1/2/e1500087.

[84] Bereneice Sephton, Angela Dudley, Gianluca Ruffato, Filippo Romanato, Lorenzo Marrucci, Miles Padgett, Sandeep Goyal, Filippus Roux, Thomas Konrad, and

Andrew Forbes. A versatile quantum walk resonator with bright classical light. *PLOS ONE*, 14(4):e0214891, April 2019. ISSN 1932-6203. doi:10.1371/journal.pone.0214891. URL http://dx.plos.org/10.1371/journal.pone.0214891.

[85] C. M. Chandrashekar. Implementing the one-dimensional quantum (Hadamard) walk using a Bose-Einstein condensate. *Physical Review A*, 74(3):032307, September 2006. doi:10.1103/PhysRevA.74.032307. URL https://link.aps.org/doi/10.1103/PhysRevA.74.032307.

[86] Andrea Alberti and Sandro Wimberger. Quantum walk of a Bose-Einstein condensate in the Brillouin zone. *Physical Review A*, 96(2):023620, August 2017. doi:10.1103/PhysRevA.96.023620. URL https://link.aps.org/doi/10.1103/PhysRevA.96.023620.

[87] Kia Manouchehri and Jingbo Wang. *Physical Implementation of Quantum Walks*. Springer Berlin Heidelberg, Berlin, Heidelberg, 2014. ISBN 978-3-642-36013-8 978-3-642-36014-5. doi:10.1007/978-3-642-36014-5. URL http://link.springer.com/10.1007/978-3-642-36014-5.

[88] J. L. O'Brien, G. J. Pryde, A. G. White, T. C. Ralph, and D. Branning. Demonstration of an all-optical quantum controlled-NOT gate. *Nature*, 426(6964):264–267, November 2003. ISSN 1476-4687. doi:10.1038/nature02054. URL https://www.nature.com/articles/nature02054.

[89] Kae Nemoto and W. J. Munro. Nearly Deterministic Linear Optical Controlled-NOT Gate. *Physical Review Letters*, 93(25):250502, December 2004. doi:10.1103/PhysRevLett.93.250502. URL https://link.aps.org/doi/10.1103/PhysRevLett.93.250502.

[90] Berthold-Georg Englert, Christian Kurtsiefer, and Harald Weinfurter. Universal unitary gate for single-photon two-qubit states. *Physical Review A*, 63(3):032303, February 2001. doi:10.1103/PhysRevA.63.032303. URL https://link.aps.org/doi/10.1103/PhysRevA.63.032303.

[91] Marco Fiorentino and Franco N. C. Wong. Deterministic Controlled-NOT Gate For Single-Photon Two-Qubit Quantum Logic. *Physical Review Letters*, 93(7):070502, August 2004. doi:10.1103/PhysRevLett.93.070502. URL https://link.aps.org/doi/10.1103/PhysRevLett.93.070502.

[92] Jan Benhelm, Gerhard Kirchmair, Christian F. Roos, and Rainer Blatt. Towards fault-tolerant quantum computing with trapped ions. *Nature Physics*, 4(6):463–466, June 2008. ISSN 1745-2481. doi:10.1038/nphys961. URL https://www.nature.com/articles/nphys961.

[93] J. Beugnon, M. P. A. Jones, J. Dingjan, B. Darquié, G. Messin, A. Browaeys, and P. Grangier. Quantum interference between two single photons emitted by independently trapped atoms. *Nature*, 440(7085):779, April 2006. ISSN 1476-4687. doi:10.1038/nature04628. URL https://www.nature.com/articles/nature04628.

[94] Stephan Ritter, Christian Nölleke, Carolin Hahn, Andreas Reiserer, Andreas Neuzner, Manuel Uphoff, Martin Mücke, Eden Figueroa, Joerg Bochmann, and Gerhard Rempe. An elementary quantum network of single atoms in optical cavities. *Nature*, 484(7393):195–200, April 2012. ISSN 1476-4687. doi:10.1038/nature11023. URL https://www.nature.com/articles/nature11023.

[95] C. K. Hong and L. Mandel. Experimental realization of a localized one-photon state. *Physical Review Letters*, 56(1):58–60, January 1986. doi:10.1103/PhysRevLett.56.58. URL https://link.aps.org/doi/10.1103/PhysRevLett.56.58.

[96] Xing Ding, Yu He, Z.-C. Duan, Niels Gregersen, M.-C. Chen, S. Unsleber, S. Maier, Christian Schneider, Martin Kamp, Sven Höfling, Chao-Yang Lu, and Jian-Wei Pan. On-Demand Single Photons with High Extraction Efficiency and Near-Unity Indistinguishability from a Resonantly Driven Quantum Dot in a Micropillar. *Physical Review Letters*, 116(2):020401, January 2016. doi:10.1103/PhysRevLett.116.020401. URL http://link.aps.org/doi/10.1103/PhysRevLett.116.020401.

[97] A. Schlehahn, A. Thoma, P. Munnelly, M. Kamp, S. Höfling, T. Heindel, C. Schneider, and S. Reitzenstein. An electrically driven cavity-enhanced source of indistinguishable photons with 61% overall efficiency. *APL Photonics*, 1(1):011301, April 2016. ISSN 2378-0967. doi:10.1063/1.4939831. URL http://scitation.aip.org/content/aip/journal/app/1/1/10.1063/1.4939831.

[98] Peter Lodahl, Sahand Mahmoodian, and Søren Stobbe. Interfacing single photons and single quantum dots with photonic nanostructures. *Reviews of Modern Physics*, 87(2):347–400, May 2015. doi:10.1103/RevModPhys.87.347. URL https://link.aps.org/doi/10.1103/RevModPhys.87.347.

[99] A. P. Lund, A. Laing, S. Rahimi-Keshari, T. Rudolph, J. L. O'Brien, and T. C. Ralph. Boson Sampling from a Gaussian State. *Physical Review Letters*, 113(10), September 2014. ISSN 0031-9007, 1079-7114. doi:10.1103/PhysRevLett.113.100502. URL https://link.aps.org/doi/10.1103/PhysRevLett.113.100502.

[100] Craig S. Hamilton, Regina Kruse, Linda Sansoni, Sonja Barkhofen, Christine Silberhorn, and Igor Jex. Gaussian Boson Sampling. *Physical Review Letters*, 119(17):170501, October 2017. doi:10.1103/PhysRevLett.119.170501. URL https://link.aps.org/doi/10.1103/PhysRevLett.119.170501.

[101] Giacomo Corrielli, Andrea Crespi, Riccardo Geremia, Roberta Ramponi, Linda Sansoni, Andrea Santinelli, Paolo Mataloni, Fabio Sciarrino, and Roberto Osellame.

Rotated waveplates in integrated waveguide optics. *Nature Communications*, 5:4249, June 2014. ISSN 2041-1723. doi:10.1038/ncomms5249. URL https://www.nature.com/articles/ncomms5249.

[102] Michael A. Nielsen and Isaac L. Chuang. *Quantum Computation and Quantum Information: 10th Anniversary Edition*. Cambridge University Press, New York, NY, USA, 10th edition, 2011. ISBN 978-1-107-00217-3.

[103] D. Bouwmeester, I. Marzoli, G. Karman, W. Schleich, and J. Woerdman. Optical Galton board. *Physical Review A*, 61(1):1–9, December 1999. doi:10.1103/PhysRevA.61.013410. URL http://link.aps.org/doi/10.1103/PhysRevA.61.013410.

[104] Filippo Cardano, Alessio D'Errico, Alexandre Dauphin, Maria Maffei, Bruno Piccirillo, Corrado de Lisio, Giulio De Filippis, Vittorio Cataudella, Enrico Santamato, Lorenzo Marrucci, Maciej Lewenstein, and Pietro Massignan. Detection of Zak phases and topological invariants in a chiral quantum walk of twisted photons. *Nature Communications*, 8:15516, June 2017. ISSN 2041-1723. doi:10.1038/ncomms15516. URL https://www.nature.com/articles/ncomms15516.

[105] Sonja Barkhofen, Lennart Lorz, Thomas Nitsche, Christine Silberhorn, and Henning Schomerus. Supersymmetric Polarization Anomaly in Photonic Discrete-Time Quantum Walks. *Physical Review Letters*, 121(26):260501, December 2018. doi:10.1103/PhysRevLett.121.260501. URL https://link.aps.org/doi/10.1103/PhysRevLett.121.260501.

[106] Barry C. Sanders. Entangled coherent states. *Physical Review A*, 45(9):6811–6815, May 1992. doi:10.1103/PhysRevA.45.6811. URL https://link.aps.org/doi/10.1103/PhysRevA.45.6811.

[107] Alexander Streltsov, Gerardo Adesso, and Martin B. Plenio. Colloquium: Quantum coherence as a resource. *Reviews of Modern Physics*, 89(4):041003, October 2017. doi:10.1103/RevModPhys.89.041003. URL https://link.aps.org/doi/10.1103/RevModPhys.89.041003.

[108] E. Schrödinger. Discussion of Probability Relations between Separated Systems. *Mathematical Proceedings of the Cambridge Philosophical Society*, 31(4):555–563, October 1935. ISSN 1469-8064, 0305-0041. doi:10.1017/S0305004100013554. URL https://www.cambridge.org/core/journals/mathematical-proceedings-of-the-cambridge-philosophical-society/article/discussion-of-probability-relations-between-separated-systems/C1C71E1AA5BA56EBE6588AAACB9A222D.

[109] A. Einstein, B. Podolsky, and N. Rosen. Can Quantum-Mechanical Description of Physical Reality Be Considered Complete? *Physical Review*, 47(10):777–780, May

1935. doi:10.1103/PhysRev.47.777. URL https://link.aps.org/doi/10.1103/PhysRev.47.777.

[110] Stuart J. Freedman and John F. Clauser. Experimental Test of Local Hidden-Variable Theories. *Physical Review Letters*, 28(14):938–941, April 1972. doi:10.1103/PhysRevLett.28.938. URL https://link.aps.org/doi/10.1103/PhysRevLett.28.938.

[111] Alain Aspect, Philippe Grangier, and Gérard Roger. Experimental Tests of Realistic Local Theories via Bell's Theorem. *Physical Review Letters*, 47(7):460–463, August 1981. doi:10.1103/PhysRevLett.47.460. URL https://link.aps.org/doi/10.1103/PhysRevLett.47.460.

[112] Simon Gröblacher, Tomasz Paterek, Rainer Kaltenbaek, Časlav Brukner, Marek Żukowski, Markus Aspelmeyer, and Anton Zeilinger. An experimental test of non-local realism. *Nature*, 446(7138):871–875, April 2007. ISSN 1476-4687. doi:10.1038/nature05677. URL https://www.nature.com/articles/nature05677.

[113] Lynden K. Shalm, Evan Meyer-Scott, Bradley G. Christensen, Peter Bierhorst, Michael A. Wayne, Martin J. Stevens, Thomas Gerrits, Scott Glancy, Deny R. Hamel, Michael S. Allman, Kevin J. Coakley, Shellee D. Dyer, Carson Hodge, Adriana E. Lita, Varun B. Verma, Camilla Lambrocco, Edward Tortorici, Alan L. Migdall, Yanbao Zhang, Daniel R. Kumor, William H. Farr, Francesco Marsili, Matthew D. Shaw, Jeffrey A. Stern, Carlos Abellán, Waldimar Amaya, Valerio Pruneri, Thomas Jennewein, Morgan W. Mitchell, Paul G. Kwiat, Joshua C. Bienfang, Richard P. Mirin, Emanuel Knill, and Sae Woo Nam. Strong Loophole-Free Test of Local Realism. *Physical Review Letters*, 115(25):250402, December 2015. doi:10.1103/PhysRevLett.115.250402. URL https://link.aps.org/doi/10.1103/PhysRevLett.115.250402.

[114] Robert J. C. Spreeuw. A Classical Analogy of Entanglement. *Foundations of Physics*, 28(3):361–374, March 1998. ISSN 1572-9516. doi:10.1023/A:1018703709245. URL https://doi.org/10.1023/A:1018703709245.

[115] Ebrahim Karimi and Robert W. Boyd. Classical entanglement? *Science*, 350(6265): 1172–1173, December 2015. ISSN 0036-8075, 1095-9203. doi:10.1126/science.aad7174. URL http://science.sciencemag.org/content/350/6265/1172.

[116] Nicolas Brunner, Nicolas Gisin, and Valerio Scarani. Entanglement and non-locality are different resources. *New Journal of Physics*, 7(1):88, 2005. ISSN 1367-2630. doi:10.1088/1367-2630/7/1/088. URL http://stacks.iop.org/1367-2630/7/i=1/a=088.

[117] A. N. de Oliveira, S. P. Walborn, and C. H. Monken. Implementing the Deutsch algorithm with polarization and transverse spatial modes. *Journal of Optics B:*

Quantum and Semiclassical Optics, 7(9):288, 2005. ISSN 1464-4266. doi:10.1088/1464-4266/7/9/009. URL http://stacks.iop.org/1464-4266/7/i=9/a=009.

[118] C. V. S. Borges, M. Hor-Meyll, J. A. O. Huguenin, and A. Z. Khoury. Bell-like inequality for the spin-orbit separability of a laser beam. *Physical Review A*, 82(3):033833, September 2010. doi:10.1103/PhysRevA.82.033833. URL https://link.aps.org/doi/10.1103/PhysRevA.82.033833.

[119] Falk Töppel, Andrea Aiello, Christoph Marquardt, Elisabeth Giacobino, and Gerd Leuchs. Classical entanglement in polarization metrology. *New Journal of Physics*, 16(7):073019, 2014. ISSN 1367-2630. doi:10.1088/1367-2630/16/7/073019. URL http://stacks.iop.org/1367-2630/16/i=7/a=073019.

[120] S. J. van Enk. Single-particle entanglement. *Physical Review A*, 72(6):064306, December 2005. doi:10.1103/PhysRevA.72.064306. URL https://link.aps.org/doi/10.1103/PhysRevA.72.064306.

[121] Pieter Kok, W. J. Munro, Kae Nemoto, T. C. Ralph, Jonathan P. Dowling, and G. J. Milburn. Linear optical quantum computing with photonic qubits. *Reviews of Modern Physics*, 79(1):135–174, January 2007. doi:10.1103/RevModPhys.79.135. URL https://link.aps.org/doi/10.1103/RevModPhys.79.135.

[122] Jeremy L. O'Brien, Akira Furusawa, and Jelena Vučković. Photonic quantum technologies. *Nature Photonics*, 3(12):687–695, December 2009. ISSN 1749-4893. doi:10.1038/nphoton.2009.229. URL https://www.nature.com/articles/nphoton.2009.229.

[123] Jian-Wei Pan, Zeng-Bing Chen, Chao-Yang Lu, Harald Weinfurter, Anton Zeilinger, and Marek Żukowski. Multiphoton entanglement and interferometry. *Reviews of Modern Physics*, 84(2):777–838, May 2012. doi:10.1103/RevModPhys.84.777. URL https://link.aps.org/doi/10.1103/RevModPhys.84.777.

[124] Harry Paul and Igor Jex. *Introduction to Quantum Optics: From Light Quanta to Quantum Teleportation*. Cambridge University Press, Cambridge, 2004. ISBN 978-0-511-61675-4. doi:10.1017/CBO9780511616754. URL http://ebooks.cambridge.org/ref/id/CBO9780511616754.

[125] Michael Reck, Anton Zeilinger, Herbert J. Bernstein, and Philip Bertani. Experimental realization of any discrete unitary operator. *Physical Review Letters*, 73(1):58–61, July 1994. doi:10.1103/PhysRevLett.73.58. URL https://link.aps.org/doi/10.1103/PhysRevLett.73.58.

[126] William R. Clements, Peter C. Humphreys, Benjamin J. Metcalf, W. Steven Kolthammer, and Ian A. Walmsley. Optimal design for universal multiport interferometers. *Optica*, 3(12):1460–1465, December 2016. ISSN 2334-2536.

doi:10.1364/OPTICA.3.001460. URL https://www.osapublishing.org/optica/abstract.cfm?uri=optica-3-12-1460.

[127] Nicolò Spagnolo, Chiara Vitelli, Marco Bentivegna, Daniel J. Brod, Andrea Crespi, Fulvio Flamini, Sandro Giacomini, Giorgio Milani, Roberta Ramponi, Paolo Mataloni, Roberto Osellame, Ernesto F. Galvão, and Fabio Sciarrino. Experimental validation of photonic boson sampling. *Nature Photonics*, 8(8):615–620, August 2014. ISSN 1749-4893. doi:10.1038/nphoton.2014.135. URL https://www.nature.com/articles/nphoton.2014.135.

[128] Max Tillmann, Borivoje Dakić, René Heilmann, Stefan Nolte, Alexander Szameit, and Philip Walther. Experimental boson sampling. *Nature Photonics*, 7(7):540–544, July 2013. ISSN 1749-4893. doi:10.1038/nphoton.2013.102. URL https://www.nature.com/articles/nphoton.2013.102.

[129] J. C. Loredo, M. A. Broome, P. Hilaire, O. Gazzano, I. Sagnes, A. Lemaitre, M. P. Almeida, P. Senellart, and A. G. White. Boson Sampling with Single-Photon Fock States from a Bright Solid-State Source. *Physical Review Letters*, 118(13):130503, March 2017. doi:10.1103/PhysRevLett.118.130503. URL https://link.aps.org/doi/10.1103/PhysRevLett.118.130503.

[130] Ludovico Latmiral, Nicolò Spagnolo, and Fabio Sciarrino. Towards quantum supremacy with lossy scattershot boson sampling. *New Journal of Physics*, 18 (11):113008, 2016. ISSN 1367-2630. doi:10.1088/1367-2630/18/11/113008. URL http://stacks.iop.org/1367-2630/18/i=11/a=113008.

[131] Alex Neville, Chris Sparrow, Raphaël Clifford, Eric Johnston, Patrick M. Birchall, Ashley Montanaro, and Anthony Laing. Classical boson sampling algorithms with superior performance to near-term experiments. *Nature Physics*, 13(12):1153–1157, October 2017. ISSN 1745-2473, 1745-2481. doi:10.1038/nphys4270. URL http://www.nature.com/doifinder/10.1038/nphys4270.

[132] J. J. Renema, A. Menssen, W. R. Clements, G. Triginer, W. S. Kolthammer, and I. A. Walmsley. Efficient Classical Algorithm for Boson Sampling with Partially Distinguishable Photons. *Physical Review Letters*, 120(22):220502, May 2018. doi:10.1103/PhysRevLett.120.220502. URL https://link.aps.org/doi/10.1103/PhysRevLett.120.220502.

[133] Keith R. Motes, Jonathan P. Dowling, and Peter P. Rohde. Spontaneous parametric down-conversion photon sources are scalable in the asymptotic limit for boson sampling. *Physical Review A*, 88(6):063822, December 2013. doi:10.1103/PhysRevA.88.063822. URL https://link.aps.org/doi/10.1103/PhysRevA.88.063822.

[134] Sonja Barkhofen, Tim J. Bartley, Linda Sansoni, Regina Kruse, Craig S. Hamilton, Igor Jex, and Christine Silberhorn. Driven Boson Sampling. *Physical Review Letters*, 118(2):020502, January 2017. doi:10.1103/PhysRevLett.118.020502. URL https://link.aps.org/doi/10.1103/PhysRevLett.118.020502.

[135] Mira 900d data sheet, 2002. URL https://edge.coherent.com/assets/pdf/Mira-Optima-900-D-Data-Sheet.pdf.

[136] R. Simon and N. Mukunda. Minimal three-component SU(2) gadget for polarization optics. *Physics Letters A*, 143(4):165–169, January 1990. ISSN 0375-9601. doi:10.1016/0375-9601(90)90732-4. URL http://www.sciencedirect.com/science/article/pii/0375960190907324.

[137] H. Paul, P. Törmä, T. Kiss, and I. Jex. Photon Chopping: New Way to Measure the Quantum State of Light. *Physical Review Letters*, 76(14):2464–2467, April 1996. doi:10.1103/PhysRevLett.76.2464. URL https://link.aps.org/doi/10.1103/PhysRevLett.76.2464.

[138] Johannes Tiedau, Evan Meyer-Scott, Thomas Nitsche, Sonja Barkhofen, Tim J. Bartley, and Christine Silberhorn. A high dynamic range optical detector for measuring single photons and bright light. *Optics Express*, 27(1):1–15, January 2019. ISSN 1094-4087. doi:10.1364/OE.27.000001. URL https://www.osapublishing.org/oe/abstract.cfm?uri=oe-27-1-1.

[139] M. G. Raymer, S. J. van Enk, C. J. McKinstrie, and H. J. McGuinness. Interference of two photons of different color. *Optics Communications*, 283(5):747–752, March 2010. ISSN 0030-4018. doi:10.1016/j.optcom.2009.10.057. URL http://www.sciencedirect.com/science/article/pii/S0030401809010499.

[140] Properties of fused silica, August 2018. URL https://www.heraeus.com/en/hqs/fused_silica_quartz_knowledge_base/properties/properties.aspx.

[141] M Bousonville, M K Bock, M Felber, T Ladwig, T Lamb, H Schlarb, S Schulz, and C Sydlo. New Phase Stable Optical Fiber. *Proceedings of BIW 2012*, pages 101–103, 2012.

[142] Thomas Schneider. *Nonlinear Optics in Telecommunications*. Springer Berlin Heidelberg, Berlin, Heidelberg, 2004. ISBN 978-3-662-08996-5. URL http://nbn-resolving.de/urn:nbn:de:1111-201302031731. OCLC: 863945121.

[143] Corning® SMF-28® Ultra Optical Fiber Product Information. URL https://www.corning.com/media/worldwide/coc/documents/Fiber/SMF-28%20Ultra.pdf.

[144] Peter P. Rohde, Wolfgang Mauerer, and Christine Silberhorn. Spectral structure and decompositions of optical states, and their applications. *New Journal of Physics*,

9(4):91–91, April 2007. ISSN 1367-2630. doi:10.1088/1367-2630/9/4/091. URL https://doi.org/10.1088%2F1367-2630%2F9%2F4%2F091.

[145] Andreas Christ. *Theory of ultrafast waveguided parametric down-conversion : From fundamentals to applications*. PhD thesis, 2013.

[146] C. K. Law, I. A. Walmsley, and J. H. Eberly. Continuous Frequency Entanglement: Effective Finite Hilbert Space and Entropy Control. *Physical Review Letters*, 84(23): 5304–5307, June 2000. doi:10.1103/PhysRevLett.84.5304. URL https://link.aps.org/doi/10.1103/PhysRevLett.84.5304.

[147] W. P. Grice, A. B. U'Ren, and I. A. Walmsley. Eliminating frequency and space-time correlations in multiphoton states. *Physical Review A*, 64(6):063815, November 2001. doi:10.1103/PhysRevA.64.063815. URL https://link.aps.org/doi/10.1103/PhysRevA.64.063815.

[148] Alfred U'Ren, Christine Silberhorn, Reinhard Erdmann, Konrad Banaszek, Warren P. Grice, Ian Walmsley, and Michael Raymer. Generation of Pure-State Single-Photon Wavepackets by Conditional Preparation Based on Spontaneous Parametric Downconversion. *Laser Physics*, 15, December 2005.

[149] Andreas Eckstein. *Mastering quantum light pulses with nonlinear waveguide interactions*. PhD thesis, Naturwissenschaftliche Fakultät der Friedrich-Alexander-Universität Erlangen-Nürnberg, 2012.

[150] Andreas Eckstein, Andreas Christ, Peter J. Mosley, and Christine Silberhorn. Highly Efficient Single-Pass Source of Pulsed Single-Mode Twin Beams of Light. *Physical Review Letters*, 106(1):013603, January 2011. doi:10.1103/PhysRevLett.106.013603. URL https://link.aps.org/doi/10.1103/PhysRevLett.106.013603.

[151] Malte Avenhaus, Andreas Eckstein, Peter J. Mosley, and Christine Silberhorn. Fiber-assisted single-photon spectrograph. *Optics Letters*, 34(18):2873–2875, September 2009. ISSN 1539-4794. doi:10.1364/OL.34.002873. URL https://www.osapublishing.org/ol/abstract.cfm?uri=ol-34-18-2873.

[152] Andreas Christ, Kaisa Laiho, Andreas Eckstein, Katiúscia N. Cassemiro, and Christine Silberhorn. Probing multimode squeezing with correlation functions. *New Journal of Physics*, 13(3):033027, 2011. ISSN 1367-2630. doi:10.1088/1367-2630/13/3/033027. URL http://stacks.iop.org/1367-2630/13/i=3/a=033027.

[153] R. Regener and W. Sohler. Loss in low-finesse Ti:LiNbO3 optical waveguide resonators. *Applied Physics B Photophysics and Laser Chemistry*, 36(3):143–147, March 1985. ISSN 0721-7269, 1432-0649. doi:10.1007/BF00691779. URL http://link.springer.com/10.1007/BF00691779.

[154] J.R. Johansson, P.D. Nation, and Franco Nori. QuTiP: An open-source Python framework for the dynamics of open quantum systems. *Computer Physics Communications*, 183(8):1760–1772, August 2012. ISSN 00104655. doi:10.1016/j.cpc.2012.02.021. URL http://linkinghub.elsevier.com/retrieve/pii/S0010465512000835.

[155] Pieter Kok and Brendon W. Lovett. Introduction to Optical Quantum Information Processing by Pieter Kok, April 2010. URL /core/books/introduction-to-optical-quantum-information-processing/4CE9A569CAE92B026B2BA041506B9F4B.

[156] N. Bruno, A. Martin, and R. T. Thew. Generation of tunable wavelength coherent states and heralded single photons for quantum optics applications. *Optics Communications*, 327:17–21, September 2014. ISSN 0030-4018. doi:10.1016/j.optcom.2014.02.025. URL http://www.sciencedirect.com/science/article/pii/S0030401814001576.

[157] K. v. Klitzing, G. Dorda, and M. Pepper. New Method for High-Accuracy Determination of the Fine-Structure Constant Based on Quantized Hall Resistance. *Physical Review Letters*, 45(6):494–497, August 1980. doi:10.1103/PhysRevLett.45.494. URL https://link.aps.org/doi/10.1103/PhysRevLett.45.494.

[158] R. B. Laughlin. Quantized Hall conductivity in two dimensions. *Physical Review B*, 23(10):5632–5633, May 1981. doi:10.1103/PhysRevB.23.5632. URL https://link.aps.org/doi/10.1103/PhysRevB.23.5632.

[159] Joseph E. Avron, Daniel Osadchy, and Ruedi Seiler. A Topological Look at the Quantum Hall Effect. *Physics Today*, 56(8):38–42, August 2003. ISSN 0031-9228. doi:10.1063/1.1611351. URL https://physicstoday.scitation.org/doi/10.1063/1.1611351.

[160] D. J. Thouless. Electrons in disordered systems and the theory of localization. *Physics Reports*, 13(3):93–142, October 1974. ISSN 0370-1573. doi:10.1016/0370-1573(74)90029-5. URL http://www.sciencedirect.com/science/article/pii/0370157374900295.

[161] Markus König, Steffen Wiedmann, Christoph Brüne, Andreas Roth, Hartmut Buhmann, Laurens W. Molenkamp, Xiao-Liang Qi, and Shou-Cheng Zhang. Quantum Spin Hall Insulator State in HgTe Quantum Wells. *Science*, 318(5851):766–770, November 2007. ISSN 0036-8075, 1095-9203. doi:10.1126/science.1148047. URL http://science.sciencemag.org/content/318/5851/766.

[162] C. L. Kane and E. J. Mele. Topological Order and the Quantum Spin Hall Effect. *Physical Review Letters*, 95(14):146802, September 2005. doi:10.1103/PhysRevLett.95.146802. URL https://link.aps.org/doi/10.1103/PhysRevLett.95.146802.

[163] Chetan Nayak, Steven H. Simon, Ady Stern, Michael Freedman, and Sankar Das Sarma. Non-Abelian anyons and topological quantum computation. *Reviews of Modern Physics*, 80(3):1083–1159, September 2008. doi:10.1103/RevModPhys.80.1083. URL https://link.aps.org/doi/10.1103/RevModPhys.80.1083.

[164] M. Aidelsburger, M. Lohse, C. Schweizer, M. Atala, J. T. Barreiro, S. Nascimbène, N. R. Cooper, I. Bloch, and N. Goldman. Measuring the Chern number of Hofstadter bands with ultracold bosonic atoms. *Nature Physics*, 11(2):162–166, February 2015. ISSN 1745-2473. doi:10.1038/nphys3171. URL http://www.nature.com/nphys/journal/v11/n2/abs/nphys3171.html.

[165] M. Mancini, G. Pagano, G. Cappellini, L. Livi, M. Rider, J. Catani, C. Sias, P. Zoller, M. Inguscio, M. Dalmonte, and L. Fallani. Observation of chiral edge states with neutral fermions in synthetic Hall ribbons. *Science*, 349(6255):1510–1513, September 2015. ISSN 0036-8075, 1095-9203. doi:10.1126/science.aaa8736. URL http://science.sciencemag.org/content/349/6255/1510.

[166] B. K. Stuhl, H.-I. Lu, L. M. Aycock, D. Genkina, and I. B. Spielman. Visualizing edge states with an atomic Bose gas in the quantum Hall regime. *Science*, 349(6255):1514–1518, September 2015. ISSN 0036-8075, 1095-9203. doi:10.1126/science.aaa8515. URL http://science.sciencemag.org/content/349/6255/1514.

[167] Thorsten Groh, Stefan Brakhane, Wolfgang Alt, Dieter Meschede, Janos K. Asbóth, and Andrea Alberti. Robustness of topologically protected edge states in quantum walk experiments with neutral atoms. *Physical Review A*, 94(1):013620, July 2016. doi:10.1103/PhysRevA.94.013620. URL https://link.aps.org/doi/10.1103/PhysRevA.94.013620.

[168] Mohammad Hafezi, Eugene A. Demler, Mikhail D. Lukin, and Jacob M. Taylor. Robust optical delay lines with topological protection. *Nature Physics*, 7(11):907–912, November 2011. ISSN 1745-2481. doi:10.1038/nphys2063. URL https://www.nature.com/articles/nphys2063.

[169] Takuya Kitagawa, Matthew A. Broome, Alessandro Fedrizzi, Mark S. Rudner, Erez Berg, Ivan Kassal, Alán Aspuru-Guzik, Eugene Demler, and Andrew G. White. Observation of topologically protected bound states in photonic quantum walks. *Nature Communications*, 3:882, June 2012. ISSN 2041-1723. doi:10.1038/ncomms1872. URL https://www.nature.com/articles/ncomms1872.

[170] Mikael C. Rechtsman, Julia M. Zeuner, Yonatan Plotnik, Yaakov Lumer, Daniel Podolsky, Felix Dreisow, Stefan Nolte, Mordechai Segev, and Alexander Szameit. Photonic Floquet topological insulators. *Nature*, 496(7444):196–200, April 2013. ISSN 1476-4687. doi:10.1038/nature12066. URL https://www.nature.com/articles/nature12066.

[171] Tomoki Ozawa, Hannah M. Price, Alberto Amo, Nathan Goldman, Mohammad Hafezi, Ling Lu, Mikael C. Rechtsman, David Schuster, Jonathan Simon, Oded Zilberberg, and Iacopo Carusotto. Topological photonics. *Reviews of Modern Physics*, 91(1):015006, March 2019. ISSN 0034-6861, 1539-0756. doi:10.1103/RevModPhys.91.015006. URL https://link.aps.org/doi/10.1103/RevModPhys.91.015006.

[172] Jun Xiong, Satya K. Kushwaha, Tian Liang, Jason W. Krizan, Max Hirschberger, Wudi Wang, R. J. Cava, and N. P. Ong. Evidence for the chiral anomaly in the Dirac semimetal Na3bi. *Science*, 350(6259):413–416, October 2015. ISSN 0036-8075, 1095-9203. doi:10.1126/science.aac6089. URL http://science.sciencemag.org/content/350/6259/413.

[173] Johannes Gooth, Anna C. Niemann, Tobias Meng, Adolfo G. Grushin, Karl Landsteiner, Bernd Gotsmann, Fabian Menges, Marcus Schmidt, Chandra Shekhar, Vicky Süß, Ruben Hühne, Bernd Rellinghaus, Claudia Felser, Binghai Yan, and Kornelius Nielsch. Experimental signatures of the mixed axial–gravitational anomaly in the Weyl semimetal NbP. *Nature*, 547(7663):324–327, July 2017. ISSN 1476-4687. doi:10.1038/nature23005. URL https://www.nature.com/articles/nature23005.

[174] E. Flurin, V. V. Ramasesh, S. Hacohen-Gourgy, L. S. Martin, N. Y. Yao, and I. Siddiqi. Observing Topological Invariants Using Quantum Walks in Superconducting Circuits. *Physical Review X*, 7(3):031023, August 2017. doi:10.1103/PhysRevX.7.031023. URL https://link.aps.org/doi/10.1103/PhysRevX.7.031023.

[175] Roman Süsstrunk and Sebastian D. Huber. Observation of phononic helical edge states in a mechanical topological insulator. *Science*, 349(6243):47–50, July 2015. ISSN 0036-8075, 1095-9203. doi:10.1126/science.aab0239. URL http://science.sciencemag.org/content/349/6243/47.

[176] Zheng Wang, Yidong Chong, J. D. Joannopoulos, and Marin Soljačić. Observation of unidirectional backscattering-immune topological electromagnetic states. *Nature*, 461(7265):772–775, October 2009. ISSN 1476-4687. doi:10.1038/nature08293. URL https://www.nature.com/articles/nature08293.

[177] Wenchao Hu, Jason C. Pillay, Kan Wu, Michael Pasek, Perry Ping Shum, and Y. D. Chong. Measurement of a Topological Edge Invariant in a Microwave Network. *Physical Review X*, 5(1):011012, February 2015. doi:10.1103/PhysRevX.5.011012. URL https://link.aps.org/doi/10.1103/PhysRevX.5.011012.

[178] Charles Poli, Matthieu Bellec, Ulrich Kuhl, Fabrice Mortessagne, and Henning Schomerus. Selective enhancement of topologically induced interface states in a dielectric resonator chain. *Nature Communications*, 6:6710, April 2015. ISSN 2041-1723. doi:10.1038/ncomms7710. URL https://www.nature.com/articles/ncomms7710.

[179] B. Tarasinski, J. K. Asbóth, and J. P. Dahlhaus. Scattering theory of topological phases in discrete-time quantum walks. *Physical Review A*, 89(4):042327, April 2014. doi:10.1103/PhysRevA.89.042327. URL https://link.aps.org/doi/10.1103/PhysRevA.89.042327.

[180] C. Cedzich, F. A. Grünbaum, C. Stahl, L. Velázquez, A. H. Werner, and R. F. Werner. Bulk-edge correspondence of one-dimensional quantum walks. *Journal of Physics A: Mathematical and Theoretical*, 49(21):21LT01, May 2016. ISSN 1751-8113, 1751-8121. doi:10.1088/1751-8113/49/21/21LT01. URL http://arxiv.org/abs/1502.02592. arXiv: 1502.02592.

[181] János K. Asbóth and Hideaki Obuse. Bulk-boundary correspondence for chiral symmetric quantum walks. *Physical Review B*, 88(12):121406, September 2013. doi:10.1103/PhysRevB.88.121406. URL https://link.aps.org/doi/10.1103/PhysRevB.88.121406.

[182] Liang Jiang, Takuya Kitagawa, Jason Alicea, A. R. Akhmerov, David Pekker, Gil Refael, J. Ignacio Cirac, Eugene Demler, Mikhail D. Lukin, and Peter Zoller. Majorana Fermions in Equilibrium and in Driven Cold-Atom Quantum Wires. *Physical Review Letters*, 106(22):220402, June 2011. doi:10.1103/PhysRevLett.106.220402. URL https://link.aps.org/doi/10.1103/PhysRevLett.106.220402.

[183] M. Z. Hasan and C. L. Kane. Colloquium: Topological insulators. *Reviews of Modern Physics*, 82(4):3045–3067, November 2010. doi:10.1103/RevModPhys.82.3045. URL https://link.aps.org/doi/10.1103/RevModPhys.82.3045.

[184] Hideaki Obuse and Norio Kawakami. Topological phases and delocalization of quantum walks in random environments. *Physical Review B*, 84(19):195139, November 2011. doi:10.1103/PhysRevB.84.195139. URL https://link.aps.org/doi/10.1103/PhysRevB.84.195139.

[185] Tibor Rakovszky and Janos K. Asboth. Localization, delocalization, and topological phase transitions in the one-dimensional split-step quantum walk. *Physical Review A*, 92(5):052311, November 2015. doi:10.1103/PhysRevA.92.052311. URL https://link.aps.org/doi/10.1103/PhysRevA.92.052311.

[186] C. Cedzich, T. Geib, C. Stahl, L. Velázquez, A. H. Werner, and R. F. Werner. Complete homotopy invariants for translation invariant symmetric quantum walks on a chain. *Quantum*, 2:95, September 2018. ISSN 2521-327X. doi:10.22331/q-2018-09-24-95. URL https://quantum-journal.org/papers/q-2018-09-24-95/.

[187] R. Walter Ogburn and John Preskill. Topological Quantum Computation. In Colin P. Williams, editor, *Quantum Computing and Quantum Communications*, Lecture Notes in Computer Science, pages 341–356. Springer Berlin Heidelberg, 1999. ISBN 978-3-540-49208-5.

[188] Michael Freedman, Alexei Kitaev, Michael Larsen, and Zhenghan Wang. Topological quantum computation. *Bulletin of the American Mathematical Society*, 40(1):31–38, 2003. ISSN 0273-0979, 1088-9485. doi:10.1090/S0273-0979-02-00964-3. URL https://www.ams.org/home/page/.

[189] Paolo Zanardi and Seth Lloyd. Topological Protection and Quantum Noiseless Subsystems. *Physical Review Letters*, 90(6):067902, February 2003. doi:10.1103/PhysRevLett.90.067902. URL https://link.aps.org/doi/10.1103/PhysRevLett.90.067902.

[190] G. Pólya. Über eine Aufgabe der Wahrscheinlichkeitsrechnung betreffend die Irrfahrt im Straßennetz. *Mathematische Annalen*, 84:149–160, 1921. ISSN 0025-5831; 1432-1807/e. URL https://eudml.org/doc/158886.

[191] M. Štefaňák, I. Jex, and T. Kiss. Recurrence and Polya Number of Quantum Walks. *Physical Review Letters*, 100(2):020501, January 2008. doi:10.1103/PhysRevLett.100.020501. URL https://link.aps.org/doi/10.1103/PhysRevLett.100.020501.

[192] F. A. Grünbaum, L. Velázquez, A. H. Werner, and R. F. Werner. Recurrence for Discrete Time Unitary Evolutions. *Communications in Mathematical Physics*, 320(2):543–569, January 2013. ISSN 0010-3616, 1432-0916. doi:10.1007/s00220-012-1645-2. URL http://link.springer.com/article/10.1007/s00220-012-1645-2.

[193] Lucien Hardy. Quantum mechanics, local realistic theories, and Lorentz-invariant realistic theories. *Physical Review Letters*, 68(20):2981–2984, May 1992. doi:10.1103/PhysRevLett.68.2981. URL https://link.aps.org/doi/10.1103/PhysRevLett.68.2981.

[194] Avshalom C. Elitzur and Lev Vaidman. Quantum mechanical interaction-free measurements. *Foundations of Physics*, 23(7):987–997, July 1993. ISSN 1572-9516. doi:10.1007/BF00736012. URL https://doi.org/10.1007/BF00736012.

[195] Andreas Eckstein, Benjamin Brecht, and Christine Silberhorn. A quantum pulse gate based on spectrally engineered sum frequency generation. *Optics Express*, 19(15):13770–13778, July 2011. ISSN 1094-4087. doi:10.1364/OE.19.013770. URL https://www.osapublishing.org/oe/abstract.cfm?uri=oe-19-15-13770.

[196] Benjamin Brecht, Andreas Eckstein, Raimund Ricken, Viktor Quiring, Hubertus Suche, Linda Sansoni, and Christine Silberhorn. Demonstration of coherent time-frequency Schmidt mode selection using dispersion-engineered frequency conversion. *Physical Review A*, 90(3):030302, September 2014. doi:10.1103/PhysRevA.90.030302. URL https://link.aps.org/doi/10.1103/PhysRevA.90.030302.

[197] Vincenzo Tamma and Simon Laibacher. Multiboson Correlation Interferometry with Arbitrary Single-Photon Pure States. *Physical Review Letters*, 114(24):243601, June 2015. doi:10.1103/PhysRevLett.114.243601. URL https://link.aps.org/doi/10.1103/PhysRevLett.114.243601.

[198] Aurél Gàbris. DHOM in DTQW experiment with PDC states, September 2018.

[199] Robert J. Gordon and Stuart A. Rice. Active Control Of The Dynamics Of Atoms And Molecules. *Annual Review of Physical Chemistry*, 48(1):601–641, October 1997. ISSN 0066-426X, 1545-1593. doi:10.1146/annurev.physchem.48.1.601. URL http://www.annualreviews.org/doi/10.1146/annurev.physchem.48.1.601.

[200] Thomas Legero, Tatjana Wilk, Markus Hennrich, Gerhard Rempe, and Axel Kuhn. Quantum Beat of Two Single Photons. *Physical Review Letters*, 93(7):070503, August 2004. doi:10.1103/PhysRevLett.93.070503. URL https://link.aps.org/doi/10.1103/PhysRevLett.93.070503.

[201] Rui-Bo Jin, Thomas Gerrits, Mikio Fujiwara, Ryota Wakabayashi, Taro Yamashita, Shigehito Miki, Hirotaka Terai, Ryosuke Shimizu, Masahiro Takeoka, and Masahide Sasaki. Spectrally resolved Hong-Ou-Mandel interference between independent photon sources. *Optics Express*, 23(22):28836–28848, November 2015. ISSN 1094-4087. doi:10.1364/OE.23.028836. URL https://www.osapublishing.org/oe/abstract.cfm?uri=oe-23-22-28836.

[202] Adrian J. Menssen, Alex E. Jones, Benjamin J. Metcalf, Malte C. Tichy, Stefanie Barz, W. Steven Kolthammer, and Ian A. Walmsley. Distinguishability and Many-Particle Interference. *Physical Review Letters*, 118(15):153603, April 2017. doi:10.1103/PhysRevLett.118.153603. URL https://link.aps.org/doi/10.1103/PhysRevLett.118.153603.

[203] A. Smirne, D. Egloff, M. G. Díaz, M. B. Plenio, and S. F. Huelga. Coherence and non-classicality of quantum Markov processes. *Quantum Science and Technology*, 4 (1):01LT01, November 2018. ISSN 2058-9565. doi:10.1088/2058-9565/aaebd5. URL https://doi.org/10.1088%2F2058-9565%2Faaebd5.

[204] Bassano Vacchini, Andrea Smirne, Elsi-Mari Laine, Jyrki Piilo, and Heinz-Peter Breuer. Markovianity and non-Markovianity in quantum and classical systems. *New Journal of Physics*, 13(9):093004, September 2011. ISSN 1367-2630. doi:10.1088/1367-2630/13/9/093004. URL https://iopscience.iop.org/article/10.1088/1367-2630/13/9/093004/meta.

[205] Carl M. Bender and Stefan Boettcher. Real Spectra in Non-Hermitian Hamiltonians Having $\mathsc{P}\mathsc{T}$ Symmetry. *Physical Review Letters*, 80(24):5243–5246, June 1998. doi:10.1103/PhysRevLett.80.5243. URL https://link.aps.org/doi/10.1103/PhysRevLett.80.5243.

[206] Alois Regensburger, Christoph Bersch, Mohammad-Ali Miri, Georgy Onishchukov, Demetrios N. Christodoulides, and Ulf Peschel. Parity–time synthetic photonic lattices. *Nature*, 488(7410):167–171, August 2012. ISSN 1476-4687. doi:10.1038/nature11298. URL https://www.nature.com/articles/nature11298.

[207] William T. M. Irvine, Juan F. Hodelin, Christoph Simon, and Dirk Bouwmeester. Realization of Hardy's Thought Experiment with Photons. *Physical Review Letters*, 95(3):030401, July 2005. doi:10.1103/PhysRevLett.95.030401. URL https://link.aps.org/doi/10.1103/PhysRevLett.95.030401.

[208] Clive Emary, Neill Lambert, and Franco Nori. Leggett–Garg inequalities. *Reports on Progress in Physics*, 77(1):016001, December 2013. ISSN 0034-4885. doi:10.1088/0034-4885/77/1/016001. URL https://doi.org/10.1088%2F0034-4885%2F77%2F1%2F016001.

[209] T. C. Ralph, N. K. Langford, T. B. Bell, and A. G. White. Linear optical controlled-NOT gate in the coincidence basis. *Physical Review A*, 65(6):062324, June 2002. doi:10.1103/PhysRevA.65.062324. URL https://link.aps.org/doi/10.1103/PhysRevA.65.062324.

[210] L. Rigovacca and C. Di Franco. Two-walker discrete-time quantum walks on the line with percolation. *Scientific Reports*, 6:22052, February 2016. ISSN 2045-2322. doi:10.1038/srep22052. URL https://www.nature.com/articles/srep22052.

[211] Aurél Gàbris and Bálint Kollár. Witnessing entanglement in the asymptotic dynamics of a two-photon percolation quantum walk, March 2015.

[212] P. Lazaridis, G. Debarge, and P. Gallion. Time–bandwidth product of chirped sech^2 pulses: application to phase–amplitude-coupling factor measurement. *Optics Letters*, 20(10):1160–1162, May 1995. ISSN 1539-4794. doi:10.1364/OL.20.001160. URL https://www.osapublishing.org/ol/abstract.cfm?uri=ol-20-10-1160.

10 Acknowledgements

The work presented here would not have been possible without the invaluable support from numerous people, which consists both in providing foundations on which my work is built or directly collaborating with me during the time I wrote this thesis. While the expertise of people working previously or in different groups on related topics is acknowledged via the respective citations, this chapter is dedicated to thanking in a less formal way those I have been with in more direct contact.
First of all, I would like to thank Christine Silberhorn who set up the group "Integrated Quantum Optics" and thus provided the environment which enabled the creation of this thesis. Even more importantly, she provided guidance, input and motivation crucially contributing to the successful completion of this thesis.
Thomas Zentgraf has been willing familiarise himself with the topics of quantum networks and quantum walks in order to be the second examiner. I also want to thank Wolf Gero Schmidt and Matthias Reichelt who agreed to complete the evaluation committee.
Sonja Barkhofen is heading the "Quantum Walks" subgroup and has thus been working with me on all the projects presented in this thesis. Apart from providing invaluable contributions in conceptualising, setting up and analysing the experiments, she has also shown great patience in regard to incoherent briefings, a anarchic programming "style" and "pragmatic" problem solving. Fabian Elster left the subgroup rather shortly after I started working on my thesis (correlation does not equal causality!), but still left helpful building blocks for setting up the experiments (the logging function is explicitly exempt from being helpful!). Syamsundar De, on the other hand, joined towards the end and provided important contributions for finalising the experiments. Lennart Lorz wrote this Bachelor- and Master-Thesis on quantum walks during my time and thus helped in a great way in carrying out the experiments involving topological phenomena. Linda Sansoni and Regina Kruse gave valuable input for the project involving the implementation of projective measurements.
Not only members of the "Quantum Walks" subgroup, but from the whole "Integrated Quantum Optics" group have contributed to the completion of this thesis. To start with, Evan Meyer-Scott was always willing to share his expertise in quantum optics, helped me in debugging the experiment and getting into QuTip and enjoyed the peculiar German traffic regulations. Speaking of which, Georg Harder was working together with me in setting up an engineered PDC source. Johannes Tiedau collaborated in writing code for the analysis of coincidence counts and seems be great fan of Python as well. "Ultrafast" Vahid Ansari and Benjamin Brecht provided code and expertise for the investigation of the spectral properties of PDC processes. The technology-crew, i.e. Christof Eigner, Laura

Padberg and Raimund Ricken, coated what needed to be coated without asking to many questions. Jan Sperling put a lot of effort into the final paper and gave an amazing tour of Rostock. Melanie Engelkemeier accomplished the daunting feat of learning Blender and thus furnished great pictures. Tim Bartley made invaluable contributions to winning the monthly ranking of the pub quiz and pointed out the best coupling lenses. In the secretary office, Petra Bobe, Nadine Schwarz, Irmgard Zimmermann and especially Rita Prevor saved me from the pitfalls of bureaucracy. Harald Herrmann had a CD for almost any purpose.
My office mates Markus Allgaier, Sebastian Brauner, Jano Gil López, Marcello Massaro, René Pollmann (almost office mate), Nidhin Prasannan, Matteo Santandrea and Michael Stefzsky deserve among others thanks for a great working atmosphere, teaching me a basic vocabulary of Italian swearwords and sharing my enthusiasm for the greatest movie of all times.
The tribute for a very friendly working environment and fruitful goes as well to the members of the group not mentioned here explicitly.
My fellow students from my undergraduate studies who I am still in contact with might be happy to read their names as well, so I want to thank Anna Bauer, Dennis Deutsch, Andreas Lücke, Sergej Neufeld, Michael Rüsing and Franziska Zeuner for the great times we have had back in the days and occasionally still have today.
Last but least, I thank my family for lifelong support, contributing a precedent for a successful defence and providing for at least a day a cute office mascot.
The length of this list does not guarantee that it is exhaustive, so I would also like those that I might have forgotten. And a big thanks to everyone again!

A Appendix: Equivalence of Coherent Light and Single Photons for a Single Initial Position

Parts of this appendix can be found in [22]. It is based on the work found in [21].
The objective of our experimental work is the investigation of the evolution of the wave function of a photonic walker, i.e. a single photon. In the following we will show that by investigating coherent pulses of indistinguishable photons in the same state $|\Psi\rangle$, we will be able to observe the same evolution as for single photons.

We start by defining the creation operator $\hat{a}_i^\dagger$ which creates a photon in the i-th mode of the vacuum state $|0\rangle$:

$$\hat{a}_i^\dagger|0\rangle = |0_1, 0_2, ..., 1_i, 0_{i+1}, ..., 0_{n\times 2}\rangle \tag{A.1}$$

Here, we consider again a space $\mathcal{H} = \mathcal{H}_\mathrm{x} \otimes \mathcal{H}_\mathrm{c}$ with the dimension $n \times 2$.

The evolution of a single photon can be described with the evolution operator $\hat{U}_n$ for the n-th step and the creation operator $\hat{a}_0^\dagger$ of the initial state:

$$\hat{U}_n\hat{a}_0^\dagger|0\rangle = \sum_i A_i(n)\hat{a}_i^\dagger|0\rangle \tag{A.2}$$

$A_i(n)$ denotes the probability amplitude of the i-th mode in step n. Accordingly, the probability $P(m,n)$ to measure the walker in mode m in the n-th step, is given by the following expression:

$$P(m,n) = |\langle 1_m| \sum_i A_i(n)\hat{a}_i^\dagger|0\rangle|^2 = |\langle 1_m| \sum_i A_i(n)|1_i\rangle|^2 = |A_m(n)|^2 \tag{A.3}$$

In order to simulate the evolution of a single photon with coherent light, the presence of one photon must not influence the evolution of another. Thus, we take a look at the evolution of the wave function for p photons which is given by the following term:

$$\frac{1}{\sqrt{p!}}(\hat{U}_n\hat{a}_0^\dagger)^p|0\rangle = \frac{1}{\sqrt{p!}}(\sum_i A_i(n)\hat{a}_i^\dagger)^p|0\rangle \tag{A.4}$$

To see whether the probability distribution for the outcome of the experiment is altered by additional photons, we determine the probability $P(m,n)$ of a measurement event in the m-th mode of step n for the simplest case of $p=2$. Both photons are initially in the same mode, but we consider that the other photon (indexed $i^{'}$) might be in m as well as in any other mode in the n-th step.

$$\begin{aligned} P(m,n) &= |\sum_{j\neq m}\langle 1_m,1_j|\frac{1}{\sqrt{2}}(\sum_i A_i(n)\hat{a}_i^\dagger)(\sum_{i'} A_{i'}(n)\hat{a}_{i'}^\dagger)|0\rangle|^2 \\ &+ |\langle 2_m|\frac{1}{\sqrt{2}}(\sum_i A_i(n)\hat{a}_i^\dagger)(\sum_{i'} A_{i'}(n)\hat{a}_{i'}^\dagger)|0\rangle|^2 \\ &= \sum_{j\neq m}|A_j(n)|^2|A_m(n)|^2 + |A_m(n)|^4 \\ &= |A_m(n)|^2\sum_j |A_j(n)|^2 = |A_m(n)|^2 \end{aligned} \tag{A.5}$$

With the term above we see that the probability for a measurement event in mode m is unaffected by the presence of another photon. Knowing that an additional photon does not have an effect, the statement can be extended to arbitrarily large number of indistinguishable photons that are initially in the same mode of $|\Psi\rangle$.

In the next step, we examine the evolution of coherent states. In the photon number representation these can be derived from the vacuum state in the following way with α being the eigenvalue of the creation operator:

$$|\alpha\rangle = e^{-|\alpha|^2/2}\cdot e^{\alpha\hat{a}_i^\dagger}|0\rangle = e^{-|\alpha|^2/2}\sum_{p=0}^{\infty}\alpha^p\frac{\hat{a}_i^{\dagger p}}{p!}|0\rangle \tag{A.6}$$

Again, all photons are created in the same mode. A quantum walk with a coherent state is described by altering the term above by including the evolution operator $\hat{U}_n$ analogue to equation (A.2) which describes the evolution of a single photon.

$$e^{-|\alpha|^2/2}\cdot e^{\alpha\hat{U}(n)\hat{a}_0^\dagger}|0\rangle = e^{-|\alpha|^2/2}\cdot e^{\alpha\sum_i A_i\hat{a}_i^\dagger}|0\rangle = e^{-|\alpha|^2/2}\sum_{p=0}^{\infty}\frac{\alpha^p}{p!}(\sum_i A_i(n)\hat{a}_i^\dagger)^p|0\rangle \tag{A.7}$$

The term is of the same form as equation (A.4) which allows us to determine the probability of a measurement event independent of the presence of another photon. Consequently, we

can determine $P(m,n)$ analogue to equation A.5:

$$P_\alpha(m,n) = |\langle 1_m|e^{-|\alpha|^2/2}\cdot\alpha\sum_i A_i(n)\hat{a}_i^\dagger|0\rangle|^2 = e^{-|\alpha|^2}\cdot|\alpha|^2|A_m(n)|^2 \tag{A.8}$$

Thus, the probability distribution of measurement events depending on the mode m and the step n is in a coherent pulse in principle independent of the other photons, if all photons are in the same initial state $|\Psi\rangle$. The difference to a quantum walk conducted with single photons is merely a pre-factor depending on α, which affects the overall probability of a measurement events, but not their distribution over the modes. The relation found here is of great significance for our experimental work as it shows that quantum walks of single photons can be simulated with coherent light. Consequently, the experiment does not require a single photon source, saving a lot of time and resources when setting it up. The results obtained for a single occupied input position do not mean that there is never a difference between a quantum walk conducted with coherent light and a quantum walk with single photons. When considering coincidences in a quantum walk initialised at more than one position, qualitative differences between coherent states and single photons arise. The coincidence probability $P_{\mathrm{Coinc,s}}(m,m')$ between modes m and m' for two photons a and b initialised at different positions is given by the following expression:

$$\begin{aligned} P_{\mathrm{Coinc,s}}(m,m') &= |\,\langle 1_m,1_{m'}|\sum_i A_i\hat{a}_i^\dagger\sum_j B_j\hat{b}_j^\dagger\,|0,0\rangle\,|^2 \\ &= |\,\langle 1_m,1_{m'}|\,A_mB_{m'}\hat{a}_m^\dagger\hat{a}_{m'}^\dagger + A_{m'}B_m\hat{a}_{m'}^\dagger\hat{a}_m^\dagger\,|0,0\rangle\,|^2 \\ &= |A_{m'}B_m + A_mB_{m'}|^2 \end{aligned} \tag{A.9}$$

In contrast, a coherent state exhibits the following coincidence probability $P_{\mathrm{Coinc,c}}(m,m')$:

$$P_{\mathrm{Coinc,c}}(m,m') = e^{-2|\alpha|^2}\frac{|\alpha|^4}{2}|A_mB_{m'} + A_{m'}B_m + \frac{1}{2}A_mA_{m'} + \frac{1}{2}B_mB_{m'}|^2 \tag{A.10}$$

We see that the coincidence probability for a coherent state is significantly altered due to the fact that here coincidences can originate from the same source.
In conclusion, the difference between coherent, i.e. classical, states and single photons, i.e. quantum states, is found in the coincidence probabilities, which are related to second-order coherences.

B Appendix: Parity of Interfering State

B.1 Interfering State with Even Parity

In the following we will show how the parity of the interfering state affects the visibilities of HOM-dips in either a time-bin resolving or a time-bucket detection scheme. For this purpose we consider ideal single photon states. In order to account for realistic parameters concerning the photon-number statistics of the source, we resort to numerical simulations in QuTip. Note that we always refer to the parity of the interfering state after it has been transformed in the network and not to the parity of the state initially sent into the network.
In our experimental setting we obtain an interfering state $|E\rangle$ with even parity by sending a horizontally and a vertically polarised photon that are spaced two positions apart into the setup (see Figure 8.2, (a)). The coin operation $\hat{C}_{\mathrm{QWP}}$ applied during the evolution is conducted by a quarter-wave plate (QWP), while the final interference coin $\hat{C}_{\mathrm{HWP}}$ is implemented with a half-wave plate (HWP). The routing of the photons is carried out with the reflection operation $\hat{R}$:

$$\begin{aligned} \hat{C}_{\mathrm{QWP}} &= \frac{1}{\sqrt{2}} \begin{pmatrix} \cos(\theta) & -i\sin(\theta) \\ -i\sin(\theta) & \cos(\theta) \end{pmatrix} \qquad \hat{C}_{\mathrm{HWP}} = \frac{1}{\sqrt{2}} \begin{pmatrix} \cos(\theta) & \sin(\theta) \\ \sin(\theta) & -\cos(\theta) \end{pmatrix} \\ \hat{R} &= \begin{pmatrix} 0 & -i \\ -i & 0 \end{pmatrix} \end{aligned} \tag{B.1}$$

The state $|E\rangle$ before the application of the final interference coin can consequently be written in the following way:

$$\begin{aligned} |E\rangle &= \frac{1}{\sqrt{4}} \left(-\hat{a}^{\dagger}_{-1,H}\hat{b}^{\dagger}_{-1,V} - \hat{a}^{\dagger}_{1,H}\hat{b}^{\dagger}_{1,V} + \hat{a}^{\dagger}_{-1,H}\hat{b}^{\dagger}_{1,V} + \hat{a}^{\dagger}_{1,H}\hat{b}^{\dagger}_{-1,V} \right) |0\rangle_A \otimes |0\rangle_B \\ &= \frac{-1}{\sqrt{2}} \left(\hat{a}^{\dagger}_{-1,H} - \hat{a}^{\dagger}_{1,H} \right) |0\rangle_A \otimes \frac{1}{\sqrt{2}} \left(\hat{b}^{\dagger}_{-1,V} - \hat{b}^{\dagger}_{1,V} \right) |0\rangle_B \end{aligned} \tag{B.2}$$

In our notation the two subsystems A and B refer to the two input photons. The first creation operator in each term of the sum acts on subsystem A, the second on subsystem B. Since we are assuming an ideal single photon source, all of the two photon terms in the expression above have to originate from contributions of both input photons.
The application of the final interference coin $\hat{C}_{\mathrm{HWP}}$ transforms the state in the following

way:

$$
\begin{aligned}
&\mathbb{1}_x \otimes \hat{C}_{\mathrm{HWP}} \left|E\right\rangle \\
&= \frac{1}{\sqrt{16}}[(\hat{a}^\dagger_{-1,H} + \hat{a}^\dagger_{-1,V}) \cdot (\hat{b}^\dagger_{-1,H} - \hat{b}^\dagger_{-1,V}) \\
&+ (\hat{a}^\dagger_{1,H} + \hat{a}^\dagger_{1,V}) \cdot (-\hat{b}^\dagger_{1,H} + \hat{b}^\dagger_{1,V}) + (-\hat{a}^\dagger_{-1,H} - \hat{a}^\dagger_{-1,V}) \cdot (-\hat{b}^\dagger_{1,H} + \hat{b}^\dagger_{1,V}) \\
&+ (\hat{a}^\dagger_{1,H} + \hat{a}^\dagger_{1,V}) \cdot (\hat{b}^\dagger_{-1,H} - \hat{b}^\dagger_{-1,V})] \left|0\right\rangle_A \otimes \left|0\right\rangle_B \\
&= \frac{1}{\sqrt{16}}[(\hat{a}^\dagger_{-1,H}\hat{b}^\dagger_{-1,H} - \hat{a}^\dagger_{-1,H}\hat{b}^\dagger_{-1,V} + \hat{a}^\dagger_{-1,V}\hat{b}^\dagger_{-1,H} - \hat{a}^\dagger_{-1,V}\hat{b}^\dagger_{-1,V} - \hat{a}^\dagger_{1,H}\hat{b}^\dagger_{1,H} \\
&+ \hat{a}^\dagger_{1,H}\hat{b}^\dagger_{1,V} - \hat{a}^\dagger_{1,V}\hat{b}^\dagger_{1,H} - \hat{a}^\dagger_{1,V}\hat{b}^\dagger_{1,V} + \hat{a}^\dagger_{-1,H}\hat{b}^\dagger_{1,H} + \hat{a}^\dagger_{-1,V}\hat{b}^\dagger_{1,H} - \hat{a}^\dagger_{-1,H}\hat{b}^\dagger_{1,V} \\
&- \hat{a}^\dagger_{-1,V}\hat{b}^\dagger_{1,V} + \hat{a}^\dagger_{1,H}\hat{b}^\dagger_{-1,H} + \hat{a}^\dagger_{1,V}\hat{b}^\dagger_{-1,H} - \hat{a}^\dagger_{1,H}\hat{b}^\dagger_{-1,V} - \hat{a}^\dagger_{1,V}\hat{b}^\dagger_{-1,V})] \left|0\right\rangle_A \otimes \left|0\right\rangle_B
\end{aligned}
\tag{B.3}
$$

As can be seen upon closer inspection, the state exhibits even parity, i.e. the signs of the positions can flipped without changing the overall state.
The above expression contains 16 individual terms, but only a certain number of them is relevant when detecting coincidences in either a time-bin resolving or a time-bucket detection scheme. In a time-bin resolving scheme we only record coincidences between the two polarisation modes of a certain position. Consequently, the relevant (renormalised) state $\left|E\right\rangle_{\mathrm{tbr}}$ in this scenario is the following:

$$
\left|E\right\rangle_{\mathrm{tbr}} = \frac{1}{\sqrt{4}}\left[-\hat{a}^\dagger_{-1,H}\hat{b}^\dagger_{-1,V} + \hat{a}^\dagger_{-1,V}\hat{b}^\dagger_{-1,H} + \hat{a}^\dagger_{1,H}\hat{b}^\dagger_{1,V} - \hat{a}^\dagger_{1,V}\hat{b}^\dagger_{1,H}\right]\left|0\right\rangle_A \otimes \left|0\right\rangle_B \tag{B.4}
$$

In case the photons in A and B are perfectly indistinguishable all of these terms cancel each other out, which results in a HOM-dip which full visibility for this detection scheme. In a time-bucket detection scheme, we also consider coincidences between two polarisation that belong to different positions and end up with the following additional terms $\left|E\right\rangle_{\mathrm{diff,tb}}$:

$$
\begin{aligned}
\left|E\right\rangle_{\mathrm{diff,tb}} &= \frac{1}{\sqrt{8}}[-\hat{a}^\dagger_{-1,H}\hat{b}^\dagger_{-1,V} + \hat{a}^\dagger_{-1,V}\hat{b}^\dagger_{-1,H} + \hat{a}^\dagger_{1,H}\hat{b}^\dagger_{1,V} - \hat{a}^\dagger_{1,V}\hat{b}^\dagger_{1,H} \\
&+ \hat{a}^\dagger_{-1,V}\hat{b}^\dagger_{1,H} - \hat{a}^\dagger_{-1,H}\hat{b}^\dagger_{1,V} + \hat{a}^\dagger_{1,V}\hat{b}^\dagger_{-1,H} - \hat{a}^\dagger_{1,H}\hat{b}^\dagger_{-1,V}]\left|0\right\rangle_A \otimes \left|0\right\rangle_B
\end{aligned}
\tag{B.5}
$$

Again, all of these coincidence terms cancel out in case the two photons are indistinguishable. It can be concluded that also a time-bucket detection scheme leads to HOM-dips with full visibilities for an interfering state with even parity.

B.2 Interfering State with Odd Parity

In a next step we analyse interfering states with odd parity which can be prepared by sending two photons with the same input polarisation (in this case horizontal polarisation) into the setup (see Figure 8.2, (b)). In this scenario we obtain the following state $|O\rangle$ before the final interference coin:

$$\begin{aligned} |O\rangle &= \frac{1}{\sqrt{4}}\left(i\hat{a}^\dagger_{-1,H}\hat{b}^\dagger_{-1,V} - i\hat{a}^\dagger_{1,H}\hat{b}^\dagger_{1,V} + i\hat{a}^\dagger_{-1,H}\hat{b}^\dagger_{1,V} - i\hat{a}^\dagger_{1,H}\hat{b}^\dagger_{-1,V}\right)|0\rangle_A \otimes |0\rangle_B \\ &= \frac{1}{\sqrt{2}}\left(-\hat{a}^\dagger_{-1,H} + \hat{a}^\dagger_{1,H}\right)|0\rangle_A \otimes \frac{-i}{\sqrt{2}}\left(\hat{b}^\dagger_{-1,V} + \hat{b}^\dagger_{1,V}\right)|0\rangle_B \end{aligned} \tag{B.6}$$

The application of the final interference coin $\hat{C}_{\mathrm{HWP}}$ transforms it into the following expression $|O\rangle_{\mathrm{aftercoin}}$:

$$\begin{aligned} &|O\rangle_{\mathrm{aftercoin}} = \mathbb{1}_x \otimes \hat{C}_{\mathrm{HWP}}\,|O\rangle \\ &= \frac{1}{\sqrt{16}}(-\hat{a}^\dagger_{-1,H} - \hat{a}^\dagger_{-1,V})\cdot(-i\hat{b}^\dagger_{-1,H} + i\hat{b}^\dagger_{-1,V}) \\ &+ (\hat{a}^\dagger_{1,H} + \hat{a}^\dagger_{1,V})\cdot(-i\hat{b}^\dagger_{1,H} + i\hat{b}^\dagger_{1,V}) + (-\hat{a}^\dagger_{-1,H} - \hat{a}^\dagger_{-1,V})\cdot(-i\hat{b}^\dagger_{1,H} + i\hat{b}^\dagger_{1,V}) \\ &+ (\hat{a}^\dagger_{1,H} + \hat{a}^\dagger_{1,V})\cdot(-i\hat{b}^\dagger_{-1,H} + i\hat{b}^\dagger_{-1,V})\,|0\rangle_A \otimes |0\rangle_B \\ &= \frac{1}{\sqrt{16}}(i\hat{a}^\dagger_{-1,H}\hat{b}^\dagger_{-1,H} - i\hat{a}^\dagger_{-1,H}\hat{b}^\dagger_{-1,V} + i\hat{a}^\dagger_{-1,V}\hat{b}^\dagger_{-1,H} - i\hat{a}^\dagger_{-1,V}\hat{b}^\dagger_{-1,V} - i\hat{a}^\dagger_{1,H}\hat{b}^\dagger_{1,H} \\ &+ i\hat{a}^\dagger_{1,H}\hat{b}^\dagger_{1,V} - i\hat{a}^\dagger_{1,V}\hat{b}^\dagger_{1,H} + i\hat{a}^\dagger_{1,V}\hat{b}^\dagger_{1,V} + i\hat{a}^\dagger_{-1,H}\hat{b}^\dagger_{1,H} + i\hat{a}^\dagger_{-1,V}\hat{b}^\dagger_{1,H} - i\hat{a}^\dagger_{-1,H}\hat{b}^\dagger_{1,V} \\ &- i\hat{a}^\dagger_{-1,V}\hat{b}^\dagger_{1,V} - i\hat{a}^\dagger_{1,H}\hat{b}^\dagger_{-1,H} - i\hat{a}^\dagger_{1,V}\hat{b}^\dagger_{-1,H} + i\hat{a}^\dagger_{1,H}\hat{b}^\dagger_{-1,V} + i\hat{a}^\dagger_{1,V}\hat{b}^\dagger_{-1,V})\,|0\rangle_A \otimes |0\rangle_B \end{aligned} \tag{B.7}$$

Again, we can identify the terms $|O\rangle_{\mathrm{tbr}}$ that lead to coincidences in a time-bin resolving detection scheme:

$$|O\rangle_{\mathrm{tbr}} = \frac{1}{\sqrt{4}}\left(-i\hat{a}^\dagger_{-1,H}\hat{b}^\dagger_{-1,V} + i\hat{a}^\dagger_{-1,V}\hat{b}^\dagger_{-1,H} + i\hat{a}^\dagger_{1,H}\hat{b}^\dagger_{1,V} - i\hat{a}^\dagger_{1,V}\hat{b}^\dagger_{1,H}\right)|0\rangle_A \otimes |0\rangle_B \tag{B.8}$$

All of these terms cancel each other out in case of perfect indistinguishability, so that we could observe a HOM-dip with full visibility.
In a time-bucket detection scheme the state $|O\rangle_{\mathrm{tb}}$ incorporates additional terms in respect to $|O\rangle_{\mathrm{tbr}}$, which we denote $|O\rangle_{\mathrm{diff}}$. They are given by the following expression:

$$|O\rangle_{\mathrm{diff}} = \frac{1}{\sqrt{4}}\left(+i\hat{a}^\dagger_{-1,V}\hat{b}^\dagger_{1,H} + i\hat{a}^\dagger_{1,H}\hat{b}^\dagger_{-1,V} - i\hat{a}^\dagger_{-1,H}\hat{b}^\dagger_{1,V} - i\hat{a}^\dagger_{1,V}\hat{b}^\dagger_{-1,H}\right)|0\rangle_A \otimes |0\rangle_B \tag{B.9}$$

In contrast to the other expressions for coincidences seen so far, the individual terms do not cancel each other out in case of indistinguishability, but actually interfere constructively. We see how this affects the ratio of coincidence counts to overall counts, when also writing down the bunching terms $|O\rangle_{\mathrm{diff,b}}$:

$$\begin{aligned}|O\rangle_{\mathrm{diff}} + |O\rangle_{\mathrm{diff,b}} = \frac{1}{\sqrt{8}}[&+i\hat{a}^{\dagger}_{-1,V}\hat{b}^{\dagger}_{1,H} + i\hat{a}^{\dagger}_{1,H}\hat{b}^{\dagger}_{-1,V} - i\hat{a}^{\dagger}_{-1,H}\hat{b}^{\dagger}_{1,V} - i\hat{a}^{\dagger}_{1,V}\hat{b}^{\dagger}_{-1,H} \\ &+i\hat{a}^{\dagger}_{-1,H}\hat{b}^{\dagger}_{1,H} - i\hat{a}^{\dagger}_{1,H}\hat{b}^{\dagger}_{-1,H} - i\hat{a}^{\dagger}_{-1,V}\hat{b}^{\dagger}_{1,V} + i\hat{a}^{\dagger}_{1,V}\hat{b}^{\dagger}_{-1,V}]\,|0\rangle_A \otimes |0\rangle_B\end{aligned} \tag{B.10}$$

In case of indistinguishability the bunching terms $|O\rangle_{\mathrm{diff,b}}$ all cancel each other out, while the coincidence terms survive. We consequently end up with a coincidence probability that is increased by a factor of 2 for indistinguishable photons in respect to distinguishable photons. In the experiment we thus expect to observe not a dip, but a peak. Since $|O\rangle_{\mathrm{tbr}}$ and $|O\rangle_{\mathrm{diff,tb}}$ contribute with the same weight to the overall state in the time-bucket detection scheme this peak is thus expected to offsets the dip present for the time-bin resolving detection. We end up with coincidence terms $|O\rangle_{\mathrm{coin,distin}}$ for distinguishable case resp. $|O\rangle_{\mathrm{coin,indistin}}$ for the indistinguishable case that both lead to a coincidence probability of 50 %:

$$\begin{aligned}|O\rangle_{\mathrm{coin,distin}} = \frac{1}{\sqrt{16}}[&i\hat{a}^{\dagger}_{-1,V}\hat{b}^{\dagger}_{-1,H} - i\hat{a}^{\dagger}_{-1,H}\hat{b}^{\dagger}_{-1,V} - i\hat{a}^{\dagger}_{1,V}\hat{b}^{\dagger}_{1,H} - i\hat{a}^{\dagger}_{1,H}\hat{b}^{\dagger}_{1,V} \\ &- i\hat{a}^{\dagger}_{1,V}\hat{b}^{\dagger}_{-1,H} + i\hat{a}^{\dagger}_{1,H}\hat{b}^{\dagger}_{-1,V} + i\hat{a}^{\dagger}_{-1,V}\hat{b}^{\dagger}_{1,H} - i\hat{a}^{\dagger}_{-1,H}\hat{b}^{\dagger}_{1,V}]\,|0\rangle_A \otimes |0\rangle_B\end{aligned} \tag{B.11}$$

$$|O\rangle_{\mathrm{coin,indistin}} = \frac{1}{\sqrt{16}}[2i\hat{a}^{\dagger}_{1,H}\hat{a}^{\dagger}_{-1,V} - 2i\hat{a}^{\dagger}_{1,V}\hat{a}^{\dagger}_{-1,H}]\,|0\rangle_A \otimes |0\rangle_B \tag{B.12}$$

C Appendix: Processing Time Lists

The time lists consist of lines with five entries, of which four define the delays for the four output signals, while the fifth one determines the time after which the delay generator starts processing a new line. The signal causing this jump to a new line is called inhibit and is put on the bus connecting the delay generators. This inhibit is consequently the same for all delay generators. As we found out that spacings between two inhibit signals of more than 4.6 μs might compromise the reliable operation of the delay generators, we limit the maximum distance of two inhibit signals to this value.
Once the delay generator has completed one run through the timelist, a reset signal has to be sent so that the timelist is processed again from the beginning when the next trigger signal arrives. The time at which a reset signal is sent relative to a trigger signal is provided by the reset parameter. In addition, we have to specify a so called "burst" parameter specifying the number of lines in the timelist. Making sure that the reset process works reliably requires a careful tweaking of the relevant parameters: To start with, the length of the last inhibit period in the timelist needs to have minimum length of 2 μs in which the reset signal has to be centered. Furthermore, we need to repeat the last line of the timelist once, which is done by setting the burst parameter to a value exceeding the number of lines in the timelist by one. As the inhibit is the same for all delay generators, they also have to share a common value of the reset and of the burst parameter.
The delays as well as the inhibits are timed by a clock signal. As the delay generators calculate the timings of the inhibit as multiples of the clock period, avoiding deviations of the actual output times from the desired one requires setting the values of the inhibit to multiples of the clock period. The delays, on the other hand, are determined as multiples of the clock period plus an additional delay independent of the clock period, so that they can be set to almost arbitrary values with a precision of 0.1 ns. Constraints on the delays, however, still arise from the fact that there has to be a minimal time difference of at least one clock period to the previous inhibit and also a distance of around 50 ns to the subsequent inhibit.
All delay generators are timed with the same master clock, inhibit, reset and burst parameter. Still, our experiments rely on the possibility to switch different positions with different EOMs. We can fulfil this requirement by having all four EOMs conduct operations at the same positions. However, we still have the freedom to vary the exact timings of switchings at a certain position. If we send to one EOM signals for engaging two switches at the same time (see [22]), we conduct a so called "empty" switching in which ideally no effective voltage in applied to the EOM crystal at all. In practice, however, the two switches might exhibit a slightly different response, so that the crystal is subjected to

an effective voltage for a short time. To avoid even a small influence on the photons of the quantum walk during this interval, empty switchings are offset by 5 ns in regard to the positions where we would expect pulses of the quantum walk.
This way of composing timelists for the different EOMs relies on having a common notation assigning positions for all four EOMs. In our framework, the pulses picked by EOM 1 (see Figure 4.1) constitute the reference point. These pulses then travel through the either the short or the long fibre which we account for by either lowering or increasing their position index by one. EOMs 2 and 3 are placed behind these fibres, so that addressing a certain position with them corresponds to switching shortly after the photons have left the fibre. When addressing the same positions with EOM 4, we have to account for the time it takes photons to travel from EOMs 2 and 3 to EOM 4 which is placed in the feedback arm. Furthermore, we have to consider the offset resulting from the fact that EOM 1 is placed outside the loop. Consequently, a certain position is offset by up to 13.5 ns between different EOMs. In order to avoid that these offsets lead to a violation of the constrains regarding the spacing of delays and inhibits, we compensate these offsets by inserting additional cables with a length of up to 2.7 m.

D Appendix: Software in Use

There is an extensive library of software used to numerically predict the outcome of experiments, control EOM switchings and analyse recorded data. It is the product of joint effort in our group with the contributions from Fabian Elster, Sonja Barkhofen (numerics and analysis of quantum walks), Johannes Tiedau (earlier versions of coincidence detection), Evan Meyer-Scott (simulations in QuTip) and Vahid Ansari as well as Benjamin Brecht (numerics of source properties) deserving particular mention.

D.1 Accessing EOMs

The code for operating four EOMs in parallel can found on the IQO network folder in the subfolder ".../QW_Data/Code/Controlling_fourEOMs_and_Stage". The script "stage_EOM_control.py" is able to operate delay stage as well as four synchronised EOMs and to record data with the AIT TDC. In order to so, it accesses several other scripts and files. Figure D.1 shows how these are related.

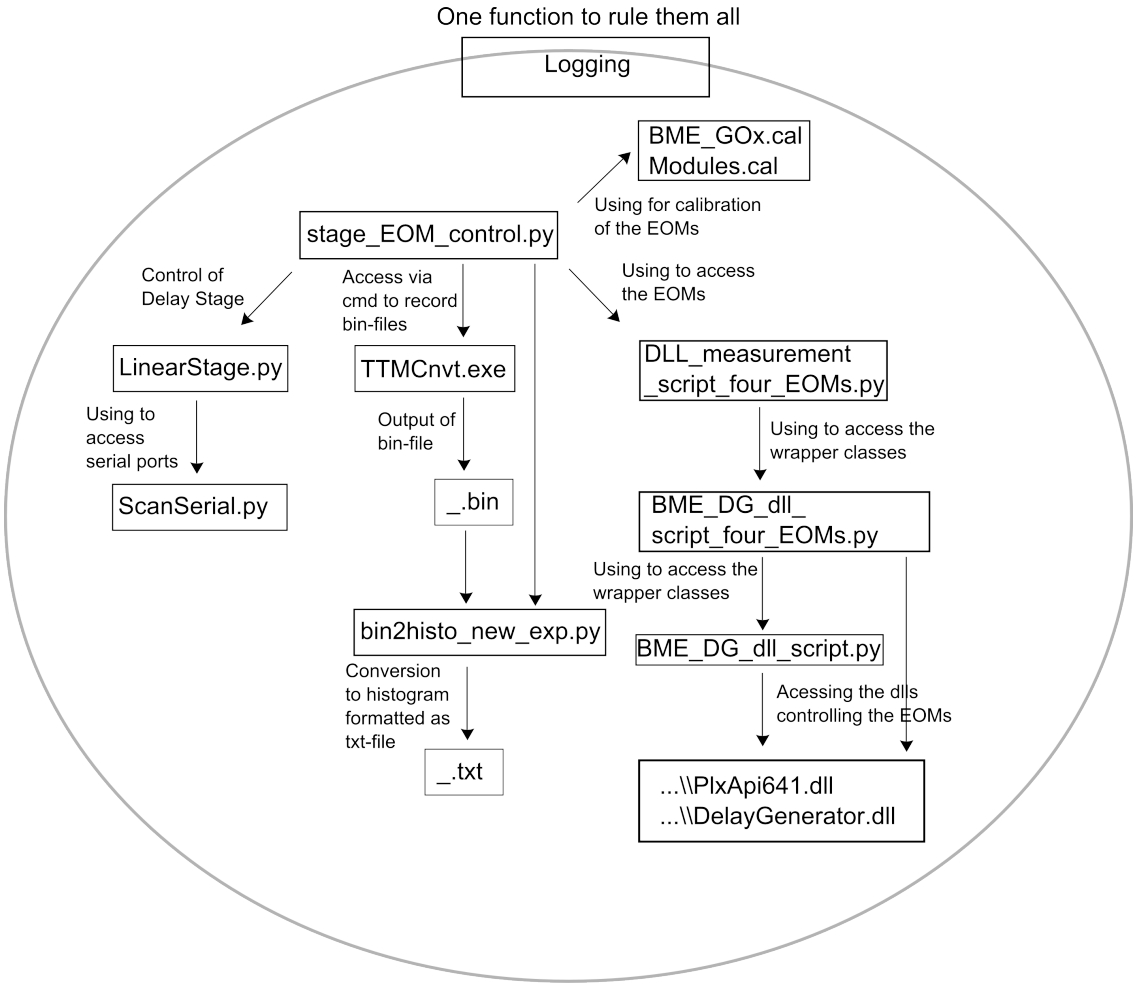

Figure D.1: Map of how "stage_EOM_control.py" uses other scripts and files to achieve simultaneous control of EOM and delay stage while also being able to record data with the AIT TDC.

We can see in Figure D.1 how calibration files ("*.cal") and dlls are employed in accessing the EOM or more precisely the delay generator card controlling the EOMs. In addition, time lists play a crucial role in the EOM's operation. They consist of a number of rows proportional to the step number and five columns, out of which the first four columns determine the switching times in microseconds relative to the starting time of a certain row for the four switches "A_on", "B_on", "A_off" and "B_off" (in this order). The fifth column gives the value of the "inhibit" which is the time (again in microseconds) that the delay generator remains in a certain row. Consequently, an actual switching time relative to the start of the time list is calculated as the entry for a certain switch in a certain row plus the sum of the inhibits in the preceding rows. Note that the time list are

read starting from the bottom. Trial-and-error has lead to the conclusion that a reliable operation requires the last inhibit to have a length of at least 2 microseconds which the actual (empty) switching times being at the beginning of the inhibit period.

D.2 Generating Time Lists for the EOMs

The switching times of the EOM are given by the step and positions spacings in the actual experiment, i.e. the fibre length. The code to generate time lists depending on these parameters is found in the folder "...QW_Data/Code/Generating_EOM_time_lists". The script "timing_calculation_no_log.py" calculates the required switching times. Note that while this file managed to shake off the shackles of logging, it relies on "save_settings_tofile_no_log.py" (found in the same folder) for proper operation. "EOM_switchings_new_experiment.py" eventually casts the switching times into files that can either be read by the software controlling the delay generator ("*_out.fpm"-files) or humans ("*_human_readable.txt"-files). The former are written in five-column-format described above such that obtaining times relative to the start time of the list requires adding up entries, while the latter gives the switching times directly. At which positions the EOMs switch is determined by pulse-list-files ("*_pulses_*.txt") which assigns either empty switchings (two switches firing at the same time, so that effectively no voltage is applied to the crystal, marked by 'e' in list), "transmissions" (two switches firing with a delay so a voltage is applied during this time, marked by 't') or "reflections" (the same as "transmission" but with inverted order of switches, so that the voltage is applied in the opposite direction). The names are derived from the fact that when the EOM switches a transmissive coin for a certain voltage, it will switch a reflective coin when the inverse voltage is applied.
When operating multiple EOMs with multiple delay generator cards connected via a common bus, they can all be controlled by different time lists. Constrains arise, however, due to the fact that a common inhibit is sent to all cards via the bus. Consequently, a stable operation requires all cards to switch at the same positions and the freedom regarding each individual card is limited to the type of switchings. Since, however, an empty switching is equivalent to not switching, these constrains do not severely impair the flexibility of switching different patterns. The creation of time lists for the individual EOMs is conducted by reading in different pulse lists discerned by an identifier for the EOM in the name of the pulse list, e.g. "*_pulses_EOM1.txt". This identifier is then transferred into the name of the created time list, so that it can be used to automatically assign the proper list to each of the delay generators resp. EOMs.

D.3 Data Analysis - Analysing histograms from bin-files

In order to decide how the recorded data can be analysed, we first have to determine with which device it is to be recorded. So far, we have used three different time taggers

(time-to-digital converters: TDC): a qutools quTau (called quTau in the following), an AIT TTM 8000 (called AIT in the following) and a Swabian Instruments Time Tagger 20 (called Swabian in the following). The software for data analysis is found in the folder "...QW_Data/Code/Numerics_and_Data_analysis".
The quTau and the AIT TDC output bin-files which entries give a time-stamp relative to the start of the data run as well as the corresponding channel in which the click resp. trigger event has been recorded. Since we repeat experimental runs with f_{frep}, we want, however, histograms giving the accumulated number of clicks in time-bins relative to the trigger events. The script "bin2histo_new_exp.py" carries out this task by conducting array operations: It converts the bin-files into arrays with absolute arrival times (i.e. relative to the start of the data run) for each of the channels, including the trigger channel. Then we successively shift the index of the array for the trigger events by a number ranging from 1 up to the maximum number of counts between two trigger events. After each shift the values in the array for the trigger channel are subtracted from values in the other arrays, yielding arrays with arrival times relative to the trigger for each of the channels with click events. The built-in histogram function of numpy can then be used to obtain arrival time histograms for each of the channels, which are saved into a txt-file.
The resulting txt-files containing the histograms can be analysed using the script "Data-Analysis_no_log.py". Note that adapted versions of this program exist, e.g. for the analysis of topologically protected edge states ("...QW_Data/Measuring_Eigenvalues/Scripts/ DataAnalysis_eigen- values_pub_settings.py"). By translating the arrival times into step and position numbers and normalising for the number of counts in a certain step, we are able to determine the probabilities of the individual positions within a step. In order to compare these values with numerical predictions, the script "theory_1D_dtqw_no_log.py" is employed, implementing matrix transformations on the state vectors. With the help of this software we are able to account for a wide range of experimental imperfections related to e.g. coupling efficiencies, coin angles, detection efficiencies, etc. "DataAnalysis_no_log.py" can plot bar charts for the comparison of numerical and experimental probabilities within a certain step and quantify either the distance or the similarity between the two sets of data. Furthermore, this script is able to conduct Monte-Carlo-Scans. These scans determine errors for numerical data by trying all combinations of either positive or negative deviations of a fixed amount from the expected value of a certain parameter. Other versions of the data analysis code such as "DataAnalysis_eigenvalues_pub_settings.py" carry out actual Monte-Carlo simulations by generating a number (e.g. 1000) of random parameter sets within a given uncertainty range and recording the maximum deviation from a reference set of parameters. The mentioned version of the software is also able to optimise the set of assumed parameters such the distance between numerical and experimental data becomes minimal. This feature is helpful in determining unknown experimental parameters, e.g. the exact value of a certain coupling. Note that the file "save_settings_tofile_no_log.py" is also required for the data analysis.

D.4 Data Analysis - Live analysis of Coincidences

The Swabian Instruments TDC comes with a handy API ("...QW_Data/Swabian_Scripts/Swabian Instruments/Time Tagger/API) that allows i.a. for the live detection of coincidences between channels. This feature makes the TDC the weapon of choice for multi-photon experiments. Several scripts ("...QW_Data/Code/Live_coincidence_detection/get_4_fold*.py) exemplify how this can be done: We create virtual channels having multiple functions. To start with, they can be delayed versions of actual channels. Another possibility are coincidence channels which contain only coincidences between two or more specified channels within a certain time interval. The combination of delayed and coincidence virtual channels allows to implement time gating by delaying the trigger channel such that it gates counts within a certain time window. A new virtual channel with the coincidences between the delayed trigger and the original channel will then constitute a gated channel that can again be used for operations in regard to additional channels, e.g. the detection of three- or four-fold coincidences. Please see the manual of the TDC ("...QW_Data/Swabian_Scripts/Swabian Instruments/Time Tagger/Time Tagger User Manual.pdf") for further possibilities of the API. Achieving time gating by delaying virtual channels requires finding the proper delays. To this purpose, the brower-based GUI ("...QW_Data/Swabian_Scripts/Swabian Instruments/Time Tagger/TimeTaggerServer/TimeTaggerServer.exe") can be used for displaying histograms and extracting timings. It should also be possible to implement histograms via the API, but it has not been tested yet. Furthermore, live measurements of Klyshko-efficiencies, generation probabilities and $g^{(2)}$-values can be conducted with the help of virtual channels (see "...QW_Data/Code/Live_coincidence_detection/g2_181213.py" and "*/klyshko_gated_181212.py" for examples).

D.5 Numerical Simulations in QuTip

In order to simulate the outcome of multi-photon interference experiments, we use the Python toolbox QuTip [154]. An account on the physical aspects of the modelled systems can be found in 5.6.
The corresponding software can be found in the folder "...QW_Data/Code/Numerics_in_QuTip" with the subfolder "*/iqoQUTIP" containing libraries that define operators, components, etc.

E Appendix: The Pump

As we can see from (3.6), the JSA does not only depend on the phase-matching function $\Phi(\lambda_s, \lambda_i)$, but also on the the pump distribution $\alpha(\lambda_s, \lambda_i)$.
So far, we have assumed that the pump for PDC process has an ideal Gaussian profile, while a sekanshyperbolicus shape in time and frequency is a more realistic assumption [135]. Furthermore, the pump pulses are not necessarily Fourier-limited but might exhibit a chirp, i.e. an additional phase that depends quadratically on the frequency. In the framework used here [212], the strength of a chirp is quantified by the phase-amplitude-coupling factor α, which relates phase κ and pulse intensity $P(t)$ in the following way:

$$\frac{d\kappa(t)}{dt} = \frac{\alpha}{2}\frac{1}{P}\frac{dP}{dt} \tag{E.1}$$

With this parameter, the chirp-dependent normalised pulse shape in frequency can be written in the following way:

$$\frac{|E(\omega)|^2}{|E(0)|^2} = \frac{\mathrm{sech}[\pi/2(\omega\tau + \alpha)] \cdot \mathrm{sech}[\pi/2(\omega\tau - \alpha)]}{\mathrm{sech}^2[\pi/2 \cdot \alpha]} \tag{E.2}$$

The time parameter $1.763\tau = \Delta t$ in the above equation is related to the FWHM temporal width Δt of the pulse.
The time-bandwidth product (TBP) for the FWHM widths in time Δt, frequency Δf and wavelength $\Delta\lambda$ depend on each other in the following way:

$$\Delta t \cdot \Delta f = \Delta t \frac{c}{\lambda^2}\Delta\lambda = \frac{2}{\pi^2}\mathrm{arcosh}(\sqrt{(2)}) \cdot \mathrm{arcosh}[\cosh(\pi \cdot \alpha + 2)] \tag{E.3}$$

In the above expression, terms can be rephrased as $\mathrm{arcosh}(x) = ln(x + \sqrt{x^2 - 1})$ and $\cosh = 1/2(e^x + e^{-x})$. Assuming a unchirped pulse, i.e. $\alpha = 0$, we obtain a value of 0.315 for the time-bandwidth product.
When running the pump laser in the ps-mode, we measure both $\Delta t_{\mathrm{ac,ps}}$ =2.25 ps with an autocorrelator and $\Delta\lambda_{\mathrm{exp,ps}}$ =0.4 nm with a spectrometer. The measured temporal duration $\Delta t_{\mathrm{ac,ps}}$ has to be multiplied with a deconvolution factor of 0.65 in order to obtain the actual temporal duration $\Delta t_{\mathrm{exp,ps}}$ =2.25 ps·0.65 =1.4625 ps. These values yield a TBP of 0.3 which is close to the value of 0.315 obtained according to (E.3) for an unchirped pulse. This tells us that the pump pulses can be considered to be unchirped when operating

the pump laser in the ps-mode.
Running the numerical simulation of the PDC process with the same parameters as in section 5.4.3, i.e. for a 16 mm long KTP-sample, the numerically obtained visibilities differ only to a negligible extent from the ones calculated for a Gaussian pump: For the unfiltered HOM-dip visibility we determine a value of 0.72 (compared to 0.74 for a Gaussian pump) and for the filtered case a value of 0.95 (compared to 0.95 for a Gaussian pump).
While we do not assume a chirp for the pump pulses when the pump laser in the ps-mode, we get a different picture when running in the pump laser in fs-mode and using a 4f-line to filter down the pump to an appropriate spectral width. In this case, we measure $\Delta t_{\mathrm{ac,fs}}$ =4.8 ps, corresponding to $\Delta t_{\mathrm{exp,ps}}$ =4.8 ps·0.65 = 3.12 ps and $\Delta \lambda_{\mathrm{exp,fs}}$ =0.3 nm, resulting in TBP of 0.47 (comparing to a value of 0.3 for the ps-mode).
It is not clear whether this increase is caused entirely by a chirp or by change in the pulse form caused by the 4f-line. Assuming that the TBP can be explained by a chirp, this number would correspond to an α of 0.7. At least in numerical simulations this amount of chirp increases the unfiltered visibility to 0.74 and the filtered one to 0.96, as the broadening of the pulse due to chirping leads to a more symmetric JSI. Since the experiment is conducted in the ps-mode where no chirp seems to be present, we skip a more accurate treatment of chirps.

F Appendix: Implementing Seeded PDC

In the following, we will briefly describe how to implement seeded PDC input states in order to investigate effects of the loop on the observed visibilities.
Energy conservation yields the following relation between pump wavelength λ_{p}, the seed wavelength λ_{seed} and the DFG wavelength λ_{DFG}:

$$\frac{1}{\lambda_{\mathrm{DFG}}} = \frac{1}{\lambda_{\mathrm{p}}} - \frac{1}{\lambda_{\mathrm{seed}}} \tag{F.1}$$

The pump wavelength λ_{p} is set to 770.3 nm and the seed wavelength λ_{seed} to 1542 nm, which results in a calculated DFG wavelength λ_{DFG} of 1539.2 nm. Note that the values for λ_{p} and λ_{seed} are those measured with a spectrometer resp. set at the laser controller. They are adjusted by optimising the counts transmitted through DWDM filters centered around 1539.8 nm, which is slightly different from the calculated value for λ_{DFG}. Since the DWDM filters exhibit a high accuracy of their center wavelength, it is likely that there is some inaccuracy in the wavelength set for the pump and the seed laser.
In order to measure the DFG signal, we need to separate it not only from the pump light but also from the seed field. As λ_{p} is far away from λ_{DFG}, the pump can blocked with a combination of a silicon plate and a bandpass filter (Semrock 1538/82 nm) transmitting for (1540 $\pm$ 40) nm. The small difference between λ_{seed} and λ_{DFG} makes filtering more delicate for the seed. We concatenate two DWDM filter centered around 1539.8 nm, one with a full transmission window $\Delta\lambda_f/2$ of 0.45 nm and one with 0.9 nm, in each of the two fibres leading to the detectors. In addition, two 1550/3 nm bandpass filters with FWHM bandwith of 8.8 nm are inserted, one angle-tuned to a center wavelength of 1539.8 nm after the KTP chip and another tuned to a center wavelength of 1542 nm in front of the KTP chip. The latter one is transmissive for the seed and serves to filter out amplified stimulated emission (ASE) originating from the seed laser that might otherwise be transmitted through the other filters.
The spectral filtering is complemented by filtering in the polarisation: Seed and DFG field are in orthogonal polarisations and can thus be separated by PBSs of which we use three in a row to optimise the discrimination between the two fields.
While the seed is provided by a cw-Laser ("Tunics") the pump pulses are picked by an EOM out of the pulse train put out by the MIRA laser system, so that the synchronisation between source and loop works in the same way as for the PDC input.
With the described scheme we are able to investigate achievable visibilities virtually independent from spectral characteristics and mean photon number.

G Appendix: Equivalence of Split-step Definitions

Here, we show that the theoretical concept of a split-step-QW can be implemented with our setup in a straight-forward way. We make use of this fact for the experiments requiring the implementation of a split-step protocol [75, 76].
In the theoretical framework of a split-step-QW, we assume that a unitary U with the following sequence of operations (to be defined later in the text) is applied on the wavefunction (see e.g. [46]):

$$U = S^H_{\uparrow} \cdot R_2 \cdot S^V_{\downarrow} \cdot R_1 \tag{G.1}$$

Here, as in the following, we omit the head symbols on the operators. $S^H_{\uparrow}$ denotes the partial shift operation displacing only the horizontal component and $S^V_{\downarrow}$ the partial shift of the vertical component:

$$\begin{aligned} S^H_{\uparrow} &= \sum_x \left(|x+2,H\rangle\langle x,H| + |x,V\rangle\langle x,V|\right) = \sum_x \left(|x+2\rangle\langle x| \begin{pmatrix} 1 & 0 \\ 0 & 0 \end{pmatrix} + |x\rangle\langle x| \begin{pmatrix} 0 & 0 \\ 0 & 1 \end{pmatrix}\right) \\ S^V_{\downarrow} &= \sum_x \left(|x,H\rangle\langle x,H| + |x-2,V\rangle\langle x,V|\right) = \sum_x \left(|x\rangle\langle x| \begin{pmatrix} 1 & 0 \\ 0 & 0 \end{pmatrix} + |x-2\rangle\langle x| \begin{pmatrix} 0 & 0 \\ 0 & 1 \end{pmatrix}\right) \end{aligned} \tag{G.2}$$

We interpret the shift conducted by these two operators as a shift by two positions in order to obtain compatibility with the shift operation as carried out in our experiment.
We show that the sequence described by G can be experimentally simulated with the shift operation S. We do so by verifying the following relation:

$$S^H_{\uparrow} \cdot R_2 \cdot S^V_{\downarrow} \cdot R_1 = S \cdot R_2 \cdot S \cdot R_1 \tag{G.3}$$

S is defined as follows:

$$\begin{aligned} S &= \left(\sum_x |x+1, H\rangle\langle x, H| + |x-1, V\rangle\langle x, V| \right) \\ &= \sum_x \left(|x+1\rangle\langle x| \begin{pmatrix} 1 & 0 \\ 0 & 0 \end{pmatrix} + |x-1\rangle\langle x| \begin{pmatrix} 0 & 0 \\ 0 & 1 \end{pmatrix} \right) \end{aligned} \tag{G.4}$$

We first calculate explicitly the left side of equation G.3:

$$\begin{aligned} 2S^H_{\uparrow} \cdot R_2 \cdot S^V_{\downarrow} \cdot R_1 &= \sum_y (|y+2\rangle\langle y| \begin{pmatrix} 1 & 0 \\ 0 & 0 \end{pmatrix} + |y\rangle\langle y| \begin{pmatrix} 0 & 0 \\ 0 & 1 \end{pmatrix}) \cdot \begin{pmatrix} \cos(\theta_2) & \sin(\theta_2) \\ \sin(\theta_2) & -\cos(\theta_2) \end{pmatrix} \\ &\quad \cdot \sum_x (|x\rangle\langle x| \begin{pmatrix} 1 & 0 \\ 0 & 0 \end{pmatrix} + |x-2\rangle\langle x| \begin{pmatrix} 0 & 0 \\ 0 & 1 \end{pmatrix}) \cdot \begin{pmatrix} \cos(\theta_1) & \sin(\theta_1) \\ \sin(\theta_1) & -\cos(\theta_1) \end{pmatrix} \\ &= \sum_y \sum_x \begin{pmatrix} \cos(\theta_2)|y+2\rangle\langle y| & \sin(\theta_2)|y+2\rangle\langle y| \\ \sin(\theta_2)|y\rangle\langle y| & -\cos(\theta_2)|y\rangle\langle y| \end{pmatrix} \\ &\quad \cdot \begin{pmatrix} \cos(\theta_1)|x\rangle\langle x| & \sin(\theta_1)|x\rangle\langle x| \\ \sin(\theta_1)|x-2\rangle\langle y| & -\cos(\theta_1)|x-2\rangle\langle x| \end{pmatrix} \\ &= \begin{pmatrix} a & c \\ b & d \end{pmatrix} \cdot \begin{pmatrix} a^* & c^* \\ b^* & d^* \end{pmatrix} = \sum_y \sum_x \begin{pmatrix} aa^* + cb^* & ac^* + cd^* \\ ba^* + db^* & bc^* + dd^* \end{pmatrix} \end{aligned} \tag{G.5}$$

We now determine the four entries of the matrix:

$$\begin{aligned} aa^* + cb^* &= \cos(\theta_2)\cos(\theta_1)|y+2\rangle\langle y|x\rangle\langle x| + \sin(\theta_2)\sin(\theta_1)|y+2\rangle\langle y|x-2\rangle\langle x| \\ &= \cos(\theta_2)\cos(\theta_1)|x+2\rangle\langle x| + \sin(\theta_2)\sin(\theta_1)|x\rangle\langle x| \\ \\ ba^* + db^* &= \sin(\theta_2)\cos(\theta_1)|y\rangle\langle y|x\rangle\langle x| - \cos(\theta_2)\sin(\theta_1)|y\rangle\langle y|x-2\rangle\langle x| \\ &= \sin(\theta_2)\cos(\theta_1)|x\rangle\langle x| - \cos(\theta_2)\sin(\theta_1)|x-2\rangle\langle x| \\ \\ ac^* + cd^* &= \cos(\theta_2)\sin(\theta_1)|y+2\rangle\langle y|x\rangle\langle x| - \sin(\theta_2)\cos(\theta_1)|y+2\rangle\langle y|x-2\rangle\langle x| \\ &= \cos(\theta_2)\sin(\theta_1)|x+2\rangle\langle x| - \sin(\theta_2)\cos(\theta_1)|x\rangle\langle x| \\ \\ bc^* + dd^* &= \sin(\theta_2)\sin(\theta_1)|y\rangle\langle y|x\rangle\langle x| + \cos(\theta_2)\cos(\theta_1)|y\rangle\langle y|x-2\rangle\langle x| \\ &= \sin(\theta_2)\sin(\theta_1)|x\rangle\langle x| + \cos(\theta_2)\cos(\theta_1)|x-2\rangle\langle x| \end{aligned} \tag{G.6}$$

Similarily, we determine the right side of equation G.3

$$
\begin{aligned}
2S \cdot R_2 \cdot S \cdot R_1 = \sum_y \sum_x & \left(|y+1\rangle\langle y| \begin{pmatrix} 1 & 0 \\ 0 & 0 \end{pmatrix} + |y-1\rangle\langle y| \begin{pmatrix} 0 & 0 \\ 0 & 1 \end{pmatrix} \right) \cdot \begin{pmatrix} \cos(\theta_2) & \sin(\theta_2) \\ \sin(\theta_2) & -\cos(\theta_2) \end{pmatrix} \\
& \cdot \left(|x+1\rangle\langle x| \begin{pmatrix} 1 & 0 \\ 0 & 0 \end{pmatrix} + |x-1\rangle\langle x| \begin{pmatrix} 0 & 0 \\ 0 & 1 \end{pmatrix} \right) \cdot \begin{pmatrix} \cos(\theta_1) & \sin(\theta_1) \\ \sin(\theta_1) & -\cos(\theta_1) \end{pmatrix} \\
= \sum_y \sum_x & \begin{pmatrix} \cos(\theta_2)|y+1\rangle\langle y| & \sin(\theta_2)|y+1\rangle\langle y| \\ \sin(\theta_2)|y-1\rangle\langle y| & -\cos(\theta_2)|y-1\rangle\langle y| \end{pmatrix} \\
& \cdot \begin{pmatrix} \cos(\theta_1)|x+1\rangle\langle x| & \sin(\theta_1)|x+1\rangle\langle x| \\ \sin(\theta_1)|x-1\rangle\langle y| & -\cos(\theta_1)|x-1\rangle\langle x| \end{pmatrix} \\
= \sum_y \sum_x & \begin{pmatrix} ee^* + gf^* & eg^* + gh^* \\ fe^* + hf^* & fg^* + hh^* \end{pmatrix}
\end{aligned}
\tag{G.7}
$$

The entries of the matrix are determined in the following way:

$$
\begin{aligned}
ee^* + gf^* &= \cos(\theta_2)\cos(\theta_1)|x+1\rangle\langle x|y+1\rangle\langle y| + \sin(\theta_2)\sin(\theta_1)|x+1\rangle\langle x|y-1\rangle\langle y| \\
&= \cos(\theta_2)\cos(\theta_1)|y+2\rangle\langle y| + \sin(\theta_2)\sin(\theta_1)|y\rangle\langle y| \\
\\
fe^* + hf^* &= \sin(\theta_2)\cos(\theta_1)|x-1\rangle\langle x|y+1\rangle\langle y| - \cos(\theta_2)\sin(\theta_1)|x-1\rangle\langle x|y-1\rangle\langle y| \\
&= \sin(\theta_2)\cos(\theta_1)|y\rangle\langle y| - \cos(\theta_2)\sin(\theta_1)|y-2\rangle\langle y| \\
\\
eg^* + gh^* &= \cos(\theta_2)\sin(\theta_1)|x+1\rangle\langle x|y+1\rangle\langle y| - \sin(\theta_2)\cos(\theta_1)|x+1\rangle\langle x|y-1\rangle\langle y| \\
&= \cos(\theta_2)\sin(\theta_1)|y+2\rangle\langle y| - \sin(\theta_2)\cos(\theta_1)|y\rangle\langle y| \\
\\
fg^* + hh^* &= \sin(\theta_2)\sin(\theta_1)|x-1\rangle\langle x|y+1\rangle\langle y| + \cos(\theta_2)\cos(\theta_1)|x-1\rangle\langle x|y-1\rangle\langle y| \\
&= \sin(\theta_2)\sin(\theta_1)|y\rangle\langle y| + \cos(\theta_2)\cos(\theta_1)|y-2\rangle\langle y|
\end{aligned}
\tag{G.8}
$$

As G.6 and G.8 yield the same expressions, we have shown that we are able to implement the split-step protocol with our setup. The only point in the derivations that is not complete straight-forward is interpreting a shift in the split-step protocol as a shift by two positions in our setup.